AN OPTIMUM DESIGN OF A SUBSONIC AIRCRAFT WING DUE TO THE AERODYNAMIC LOADING

2023
MASTER THESIS
MECHANICAL ENGINEERING

Ibtisam Jaafar ISMEAL ISMEAL

Thesis Advisor
Assist. Prof. Dr. Mehmet BAKIRCI
Prof. Dr. Muhsin JABER JWEEG

AN OPTIMUM DESIGN OF A SUBSONIC AIRCRAFT WING DUE TO THE AERODYNAMIC LOADING

Ibtisam Jaafar ISMEAL ISMEAL

Thesis Advisor

Assist. Prof. Dr. MEHMET BAKIRCI

Prof. Dr. Muhsin JABER JWEEG

T.C.

Karabük University

Institute of Graduate Programs

Department of Mechanical Engineering

Prepared as

Master Thesis

KARABÜK

January 2023

I certify that in my opinion, the thesis submitted by Ibtisam Jaafar ISMEAL ISMEAL titled “AN OPTIMUM DESIGN OF A SUBSONIC AIRCRAFT WING DUE TO THE AERODYNAMIC LOADING” is fully adequate in scope and in quality as a thesis for the degree of Master of Science.

Assist. Prof. Dr. Mehmet BAKIRCI .....
Thesis Advisor, Department of Mechanical Engineering

Prof. Dr. Muhsin JABER JWEEG .....
Thesis Advisor, Department of Mechanical Engineering

This thesis is accepted by the examining committee with a unanimous vote in the Department of Mechanical Engineering as a Master of Science thesis. /01/2023

Examining Committee Members (Institutions)	Signature
Chairman : Prof. Dr. Bilge DEMIR (KBU)	.....
Member : Prof. Dr. Muhsin JABER JWEEG (FUC)	.....
Member : Assoc. Prof. Dr. Fuat KARTAL (YBU)	.....
Member : Assist. Prof. Dr. Mehmet BAKIRCI (KBU)	.....

The degree of Master of Science by the thesis submitted is approved by the Administrative Board of the Institute of Graduate Programs, Karabük University.

Prof. Dr. Müslüm KUZU .....
Director of the Institute of Graduate Programs

This thesis contains information that I have gathered and presented in a manner that is consistent with academic regulations and ethical principles, and I affirm that I have appropriately cited any and all sources that are not my own work.

Ibtisam Jaafar ISMEAL ISMEAL

ABSTRACT

M. Sc. Thesis

AN OPTIMUM DESIGN OF A SUBSONIC AIRCRAFT WING DUE TO THE AERODYNAMIC LOADING

Ibtisam Jaafar ISMEAL ISMEAL

Karabük University
Institute of Graduate Programs
The Department of Mechanical Engineering

Thesis Advisor.
Assist. Prof. Dr. Mehmet BAKIRCI
Prof. Dr. Muhsin JABER JWEEG
January 2023, 163 pages

Aircraft designers are mainly interested in finding the level of pressure, stresses and deformations of the parts of the aircraft, especially the wing, as in many aviation accidents, the failure of the wing was the main cause of disasters, as it is considered the main surface that generates the necessary lift for the aircraft. In addition to its other functions in controlling the transverse stability. In this work, the numerical study was achieved to obtain the optimum wing aerodynamic and structural design parameters for high strength and minimum weight for the L.39 A/C wing. The analysis is concerned with the effect of the aerodynamic design parameter as well as the structural design parameters. In the aerodynamic study, the volume method was used to predict the pressure distribution of the wing in the subsonic potential flow. The singularity strength which satisfies the boundary condition of the tangential flow at the control point for a given Mach number and the angle of attack was determined

by solving a system the governing differential equation. The design has been a design wing 3D geometry model by using the Software SOLIDWORKS 2020 and the second step was processing the governing differential equations for airflow over a wing by ANSYS FLUENT 2022 R1 version solver by utilizing a Finite Volume Element. Finally, the third stage was the post.processing step in which calculate the aerodynamic characteristics like pressure distribution. In the structural study, the wing was modeled as Honeycomb with different thicknesses using the Software SOLIDWORKS 2020. Numerical investigations were carried out for deformation and stress by ANSYS FLUENT 2022 R1. The results were compared with other researchers used other models, such as the using of ribs and stringers in the interior stricture of the wing, The current results were found to be reliable and acceptable from the design point view on the high stiffness /weight ratio. The result of this work can be used for a new wing configuration and further development of the considered aircraft.

Key Words : Aerodynamics, Subsonic Aircraft Wing optimum design, high stiffness / weight ratio, honeycomb geometry, CFD, Mach.

Science Code : 91410

ÖZET

Yüksek Lisans Tezi

AERODİNAMİK YÜKLEME NEDENİYLE BİR SUBSONİK UÇAK KANATININ OPTİMUM TASARIMI

Ibtisam Jaafar ISMEAL ISMEAL

Karabük Üniversitesi
Lisansüstü Eğitim Enstitüsü
Makine Mühendisliği Anabilim Dalı

Tez Danışmanı:
Dr. Öğr. Üyesi Mehmet BAKIRCI
Prof. Dr. Muhsin JABER JWEEG
Ocak 2023, 163 sayfa

Uçak tasarımcıları, esas olarak uçağın parçalarının, özellikle de kanadının basınç seviyesini, gerilmelerini ve deformasyonlarını bulmakla ilgilenirler, birçok havacılık kazasında olduğu gibi, kanadın arızalanması, ana sebep olarak kabul edildiğinden, felaketlerin ana nedeniydi. uçak için gerekli kaldırma kuvveti oluşturan yüzey. Enine stabiliteyi kontrol etmedeki diğer işlevlerine ek olarak. Bu çalışmada, L.39 A/C kanadı için yüksek mukavemet ve minimum ağırlık için optimum kanat aerodinamiği ve yapısal tasarım parametrelerini elde etmek için sayısal çalışma gerçekleştirilmiştir. Analiz, aerodinamik tasarım parametresinin yanı sıra yapısal tasarım parametrelerinin etkisi ile ilgilidir. Aerodinamik çalışmada, ses altı potansiyel akışında kanadın basınç dağılımını tahmin etmek için hacim yöntemi kullanılmıştır. Belirli bir Mach sayısı ve hücum açısı için kontrol noktasındaki teğetsel akışın sınır koşulunu karşılayan tekillik kuvveti, bir sistem yöneten

diferansiyel denklem çözülerek belirlendi. Tasarım, SOLIDWORKS 2020 Yazılımı kullanılarak bir tasarım kanadı 3D geometri modeliydi ve ikinci adım, bir Sonlu Hacim Elemanı kullanarak ANSYS FLUENT 2022 R1 sürüm çözücüsü tarafından bir kanat üzerindeki hava akışı için geçerli diferansiyel denklemleri işlemekti. Son olarak, üçüncü aşama, basınç dağılımı gibi aerodinamik özelliklerin hesaplandığı işlem sonrası adımdır.Yapısal çalışmada kanat, SOLIDWORKS 2020 Yazılımı kullanılarak farklı kalınlıklarda Honeycomb olarak modellenmiştir. ANSYS FLUENT 2022 R1 ile deformasyon ve gerilme için sayısal incelemeler yapılmıştır. Sonuçlar, kanadın iç darlığında nervür ve kiriş kullanımı gibi diğer araştırmacıların kullandığı diğer modeller ile karşılaştırıldı. Mevcut sonuçlar, yüksek rijitlik/ağırlık oranı açısından tasarım açısından güvenilir ve kabul edilebilir bulundu. Bu çalışmanın sonucu, yeni bir kanat konfigürasyonu ve söz konusu uçağın daha da geliştirilmesi için kullanılabilir.

Anahtar Kelimeler : Aerodinamik, Ses Altı Uçak Kanadı optimum tasarımı, yüksek rijitlik/ağırlık oranı, bal peteği geometrisi, CFD, Mach.

Bilim Kodu **:** 91410

ACKNOWLEDGMENT

Finally, I can only pray to God Almighty to grant us guidance, chastity, People do not reach the garden of success without going through the stations of fatigue, failure and despair, and the one who has a strong will does not prolong standing in these stations, The first to whom to give thanks and praise during the night and the end of the day is the Highest, the Kahar, the First and the Last, the Apparent and the Inward, Who showers us with his countless blessings, blesses us with His endless provision, and illuminates our paths. Upon us, when He sent among us His servant and Messenger, Muhammad bin Abdullah, may God's prayers and peace be upon Him and His family, He sent him with his clear Qur'an, so He taught us what we did not know and urged us to seek knowledge wherever it was found. All praise and thanks are due to God for granting us success and inspiring us with patience and the eagerness for that which confronts us to accomplish this humble work, and thanks go to every teacher who helped me with his knowledge, from the first stages of this study until this moment. I also extend a word of thanks to Assist. Prof. Dr. mehmet bakirci and prof. Dr. muhsin jaber jweed. I wish them all the best and much success. I also thank the Head of the Department of Mechanical Engineering, Prof. Dr. Kamil ARSLAN, and his staff for the assistance they have given me. Thanks also go to my colleagues, wishing them the best ranks and success, I dedicate the fruit of my humble effort to those who gave me life, hope, and upbringing with passion for knowledge and knowledge, and to those who taught me to climb the ladder of life with wisdom, patience, and loyalty to them, my dear mother, Abu Muhammad Mahdi, my sisters, and my brother. Finally, to my dear country, Iraq, and my second country, Turkey, and whoever had a role, from near or far, in completing this study, I ask the Lord Almighty to reward everyone with the best reward in this world and the Hereafter. Finally, I can only pray to god almighty to grant us guidance, chastity, wealth, health, safety, and who inspires me with more determination and strength to upgrade my scientific thesis and study the PhD, Inshallah.

CONTENTS

Page

Page

Page

Page

LIST OF FIGURES

Page

Page

Page

Page

Page

Page

Page

Page

Page

Page

Page

Page

Page

Page

LIST OF TABLES

Page

SYMBOLS AND ABBREVITIONS INDEX

SYMBOL

S : Wing area

b : Span

Ct : Tip chord length

Cr : Root chord length

AR : Aspect ratio

λ : Taper ratio

MAC : Mean Aerodynamic chord

α : Angle of attack

M : Mach number

P : Pressure

$c/4$: Quarter chord line

L.E : Leading edge

$V.M$: Von Mises

V : Poisons` ratio

P_k : represents the gradients of mean velocity by turbulence kinetic energy

P_b : represents the buoyancy by turbulence kinetic energy

K : turbulent kinetic energy

Ɛ : turbulent dissipation

ABBREVITIONS

FSI : Fluid Structure Interaction

CFD : The Computational Fluid Dynamics

PART 1

INTRODUCTION

1.1. GENERAL

Today, the world is witnessing a great development in the field of aviation, as this science has taken a privileged position for what it is of great importance in achieving important and great achievements for all mankind. Building structures modern aircraft are among the basic and important things that have taken a wide interest from scientists and researchers, as this building requires careful design and careful selection of the structure and the metal component of it achieves high durability relative to weight, high safety in addition to achieving a long life, and the lowest cost to manufacture and maintain parts. Designers are primarily concerned with obtaining accurate and reasonable estimates of parts. The main and important of the aircraft, which is exposed to air loads. These shed loads the aircraft is periodically represented by the operations of take.off and landing and the carrying out of the main duties of the aircraft like maneuvers.

In many of the aviation accidents recorded as a result of failure, it was the failure of the wing and its parts .A large proportion, as the wing is the main surface that generates the necessary lift for the aircraft and is responsible for controlling it and transverse stability of the aircraft. It may sometimes be used as a means of mounting engines Aircraft, as well as spare fuel tanks in addition to the presence of bomb carriers and missiles. For all of the above, air loads have a clear effect on the wing.

obtaining the best wing sectional shape has captured the attention of designers in recent years. Therefore, the issue of the distribution of air loads represents a field of interest to both aerodynamic scientists and stress analysts. The specialists in the field of aerodynamics, as they are interested in the characteristics that affect the

performance, stability or control features of the aircraft, are interested in determining the external installation system of the aircraft in order to obtain the best specifications.

As for the stress analysts, they are interested in the distribution of loads and their impact on the various internal parts of the airframe, and finding the level of stress that the shell and the longitudinal and transverse stiffening pieces bear, in order to ensure their resistance to bending and torsion stresses resulting from aerodynamic forces. That specialists in the field of aerodynamics who do the distribution of aerodynamic loads or obtain the aerodynamic data lab needs to be aware of the use of this information and the amount of accuracy required. In general, it is necessary to obtain the distribution of loads along the wing, and this distribution depends on the shape of the plane of the wing for the purpose of structural analysis to ensure the safety of the structure from anaerobic effects that could lead to failure.

1.2. AERODYNAMIC LOADING

The primary function of theoretical and experimental aerodynamics is to predict and measure the aerodynamic forces and moments on a body. In many cases, this implies the prediction and measurement of the pressure distribution along a given surface. Furthermore, a prediction of pressure distribution on the surface frequently requires knowledge of the complete flow field around the surface. Moreover, the determination of the optimum wing design parameters requires the development of different wing geometry relations and the estimation of the complete aerodynamic data of the aircraft. The aerodynamic characteristics of a given configuration and the flight condition are used as input data for determining the optimum pressure distribution.

The loads on the wing have a number of different origins. The correct determination of this load is needed for efficient wing construction so as to obtain the necessary strength with maximum weight.saving. The following forces operate on the aircraft during flight as well as during take.off and landing [1].

- Aerodynamic forces, which are caused by the flow over and around the wing (distributed load).
- Weight of wing construction (distributed load).
- Inertial forces caused by the aircraft mass during maneuvers
- (distributed and point loads).
- Concentrated loads (point loads); caused by components or items of equipment attached to the wing.
- Concentrated loads, which are not linked to the mass (engine.
- thrust).

As the aircraft moves through the air, the flow produces pressure of various intensities, which act on the wing upper surface primarily as positive pressure. The upper surface is therefore also referred to as the suction surface and the lower surface as the pressure surface. Together the different pressures on the wing form a pressure distribution and shear stress distribution. No matter how complex the wing shape may be, the aerodynamic forces and moments on the wing are due entirely to these two basic sources. The only mechanism nature has for communicating a force a body moving through a fluid are the pressure and shear stress distributions on the body surface. The net effect of these distributions integrated over the complete wing surfaces is a resultant aerodynamic force and moment. Aerodynamic forces, primarily the LIFT and DRAG forces, are produced by an aircraft's velocity through the atmosphere, and the wing is the primary source of these forces. The wing is an airplane's surface that supports the aircraft by providing pressure distribution through a dynamic reaction on the air. With varied wing angles of attack and flight conditions, the pressure distribution on the wing changes. At high angles of attack and with flap deflections, the resultant pressure moves towards the leading edge.

When a result, the wing is subjected to varying pressure distributions, and it must be constructed torsionally robust so that it does not twist enough to influence its aerodynamic qualities as the load varies. The field of air load distribution is concerned with both aerodynamicist properties that affect the airplane's performance, stability, and control characteristics. The load distributions that will depict the most severe situations for various parts of the airplane's interior structure are normally the

focus of the aerodynamicist. It's first important to figure out how the loads are distributed across the wingspan.

The geometry of the wing planform, the aero foil section, the wing twist along the span, and the size and position of the wing flaps or ailerons all affect the spanwise distribution. In recent years, theoretical and experimental investigations, combined with developments in computer technology, have resulted in the capacity to determine the aerodynamic parameters of an entire airplane with amazing accuracy.

1.3. STRUCTURAL MODELING

Commercial airplane structures are designed with the goal of lowering weight (and thus operating costs) while maintaining adequate strength. As a result, thin panels must be stabilized to sustain tensile and compressive loads in tension, torsion, and bending, as well as a combination of the two [2]. A traditional wing box design has thin panels with skin that is stiffened via stringers, as can be seen from **Figure 1.1**. The outer structure of the wing box is made up of ribs, spars, and skin/stringer panels, which are all machined separately. The ribs keep the structure, whereas transferring the local air load to a wing box. The spars and panels bear global bending and torsion load values [3].

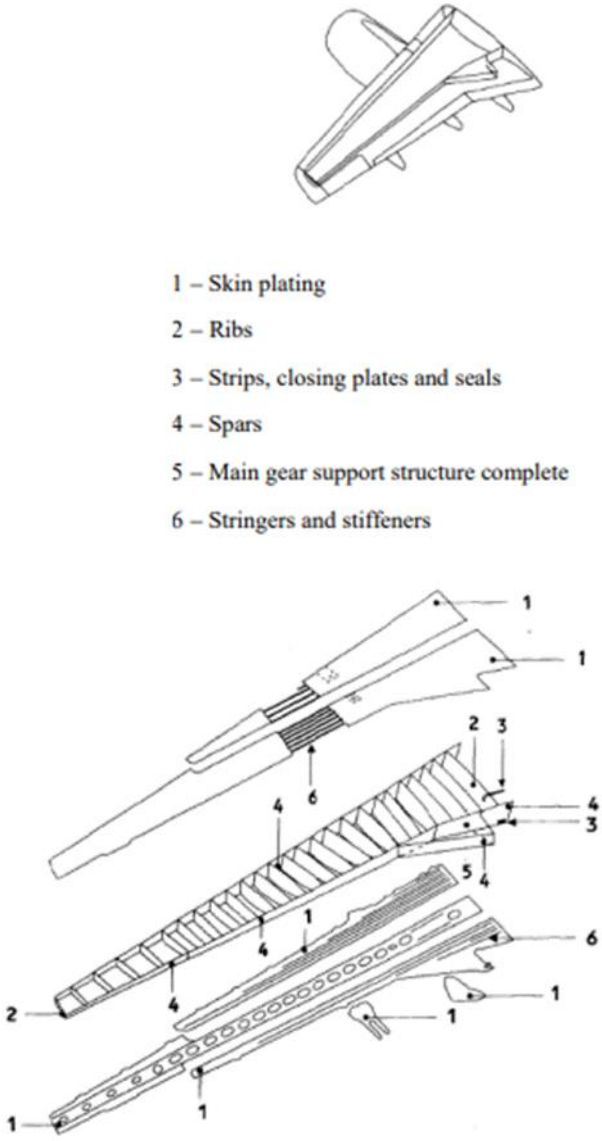

Figure 1.1. Scheme of outer wing structure of the British Aerospace [1].

Skin/stringer panels have been generally made via machining stiffeners from the thick blanks and after that fastening them to sheet. In addition, the resulting panels are rigid and light, yet they are costly to produce because of the high costs of machining and wasteful material use. Also, they are anisotropic in bending plane (that is, they aren't equally stiff along all bending axes) [4]. Actually, using twin skins that have stabilizing medium between them might frequently yield better results when it comes to the stability of thin sheets.

The sandwich structures can be described as "structural components that are consist of 2 strong and stiff skins that are divided by light.weight core", according to their definition (Gibson and Ashby, 1988). The lightweight core divides the skins, which causes increase in the moment of panel inertia, whereas lowering its weight. Therefore, the structure can endure bending as well as buckling loads [5]. As indicated before, conventional stiffened skins are made up of several stiffeners. On the other hand, sandwich constructions, have a consistent stiffness distribution throughout the panel. The number of parts in assemblies is decreased due to integral stiffening, leading to less logistics, part production, and assembly effort. The Havilland Mosquito night bomber of WWII was the first aircraft in British aviation to use sandwich constructions. Vultee BT.15 fuselage had a fiber.glass.reinforced polyester front and glass.fabric honeycomb with balsa wood core when it was manufactured in 1943 [6]. The composite sandwich structures have been increasingly commonly utilized in airplane designs (Airbus A.380 – as can be seen from Hata! Başvuru kaynağı bulunamadı. **Figure 1.2)**. Honeycomb sandwich covers 46% of an external Boeing757/767 surface, and fuselage cylindrical shell of the Boeing 747 is mostly made of Nomex honeycomb sandwich. Currently, sandwich structures are exclusively employed as secondary constructions in commercial aircraft. To be relevant to the fundamental structures (which means the structural components required for sustaining the design of the ultimate ground and flight loads), the sandwich structures should guarantee that any damages to a component throughout its service life doesn't lead to failure before the damage is discovered. This would have to be shown through suitable analyses and tests, along with specification of the maximal permissible damages as well as their visibility . which is where adaptability comes into play. Eye inspection and acoustic pulse.echo tests aren't usually enough to detect structural flaws in sandwich systems. This might involve frequent non.destructive testing (NDT) of the components, whereas also considering the in.service life economic requirements. The capacity to fail.safe, the materials' toughness, and the capability for withstanding impact damages are all key reasons to use a sandwich panel as a primary construction material.

1 – Spoilers/ailerons

2 – Vertical tail plane: fin tip & fairings, dorsal fin, leading & trailing edge panels

3 – Horizontal tail plane: fairing, leading & trailing edge panels

4 – Fuselage belly fairing

5 – Flap track fairings

6 – Pylons/nacelles: secondary structure, access panels

7 – Nose landing gear doors

8 – Cabin: floor panels

9 – Wing: leading & trailing edge panels, access panels

Figure 1.2. Example A 380 sandwich panel application [2].

Metal foams can be described as novel form of material with high E 1/3/ values, in which E represent the foam's Young's modulus and foam's density. With a purpose of decreasing mass, Lu and Ashby (2003) derive such material index for a panel with defined width, length, and stiffness. The larger the value of E 1/3/ for a given stiffness, the lighter a panel can be. Therefore, E1/3/ specifies bending stiffness regarding light.weight panels and recommends using metal foams as rigid and light panels [7]. Furthermore, metal foam sandwich panels are similar in weight to waffle.stretched aluminum panels, yet they are less expensive to produce (Ashby et al., 2000).

Metal foams also have high values of σ_y 1/2/, in which y represent the elastic limit of foam. The light. weight panel bending. Strength is measured using this material index created by Lu and Ashby (2003) for panel with defined width, length, and strength for a purpose of reducing mass. The larger the value of σ_y1/2/ for a given mass, the more powerful a panel will be. Therefore, for certain mass, the metal foam panel has been found to be stronger compared to a solid panel of the same material. Furthermore, sandwich panels with a restricted strength foam core might be lighter than traditional stringer.stiffened panels [8].

Therefore, metal foam can have a low density while still providing great strength and stiffness of bending; they make good cores for light.weight sandwich structures. Mechanical properties can also demonstrate isotropy (unlike honeycombs). They have a significant capability for absorbing energy under practically continuous pressure and might be curved easily [9]. The stress rises quickly with a strain as foam smashes in a compressive stress.strain plot, showing that the metal foam core sandwich panel's integrity isn't essentially compromised in the case where it is under any impact. The open.cell foams don't retain the moisture (they're less prone to the corrosions when compared to the honeycomb core) and might be employed in a number of applications, including the combination of the fuel storage with load. Bearing structures.

In an aircraft design it is always required to determine the strain and stress distribution on any structural component subjected to a given set of loads. The stress analysis is necessary to determine the strength of various aircraft structural components, whereas the strain distribution may be necessary to determine the aeroelastic behavior of these components. One of the important structural components of the aircraft which the designers deal with is the wing, that surface which supports the aircraft by means of the dynamic reactions on the air namely the lift force which is the major source of the aerodynamic forces. The stress analyst is intended to find the type and amount of stress on the aircraft structure. the stress analysis is the solution for the state of stress at a point or points under a given set of conditions. That is to make a stress analysis of a structural part means to establish the kinds and magnitudes of the stresses at all points of interest under all loading conditions. For many years, structural analysis approaches, as well as complete handbooks and nomograms, were employed in aircraft structural design. Those techniques are now considered obsolete. Rather, finite element computer algorithms are currently used to do practically all significant structural analyses. The finite element method (F.E.M.) depends on the idea of breaking down an aircraft's structure into many small elements, similar to gridding. Different approximations of the end constrains and deflection forms for the element are used to create equations characterizing the structural behavior of the finite element. The element equations are after that connected with the use of matrix algebra to derive the total structure's

response to a particular external loading condition. The enormous size of the matrices employed in F.E.M analysis necessitates using computers for all but the simplest applications.

1.4. OBJECTIVES OF PRESENT WORK

The goal of the current work is to design and analysis of a light weight aircraft wing using a honeycomb structure and can resist aerodynamic loading. A comparison study will be achieved in using a previous work dealing with the wing design with ribs and stringers. To achieve the above objective, the following steps are followed.

- Aerodynamic study should be achieved for a selected airfoil for the L39 Jet Trainer wing as a case study. Different Mach numbers, different angle of attack, using the NACA 64 A 012 Estimation of pressure distribution. The maximum developed Pressure model is chosen for structural analysis.
- The structural study investigates the effectiveness of using lightweight structure using the honeycomb internal structure shape. The assessment of ability of the structure depends upon the stresses and deformation developed due to the aerodynamic loading.
- Investigating the effects of honeycomb parameters (cell size, and wall thickness) in order to decide the best distribution of honeycomb shape internal stiffeners and the number of cells.
- The results of stresses and deformations of the wing structure are obtained for the different configurations of the wing of the L39 Jet Trainer. three types of cells will be suggested to model the wing structure.
  a. Effects of Mach no.
  b. Effect of skin thickness.
  c. Effect of core thickness.
- Comparison of the results. The result is the decision of the optimum light weight wing structure compared to using the ribs and stringers.

1.5. WORK PLAN

- The plan will cover a suggestion of a wing model to be examined aerodynamically, or analytically to estimate the pressure distribution using ANSYS FLUENT Software.
- A numerical investigation will be carried out to predict the stress distribution using new Design for airfoil by SOLIDWORKS Software and FSI Workbench (2022R1) package. The selected wing NACA 64A 012 type will be studied extensively in order to obtain.
- The aerodynamic results are obtained using different flow velocities and then the structural analysis using the light weight (honeycomb) as in internal structure is investigated using three suggested configuration of the wing ,1 cell ,6 cells and 9 cells.

The level of stresses and deformations are predicted . The results are compared using wings strengthened by heavy structures (rib) and stringers).

The thesis is arranged as follows.

Chapter two covers a literature review which will give a general idea about the investigations that had been done in the field of aerodynamics and structure analyses. Chapter three is devoted to aerodynamic analysis and explains the geometrical design parameters the chapter is ended with a brief description of the ANSYS and SOLIDWORK programs.

Chapter four introduces the Finite Element method, as well as the structure design considerations. This chapter will explain the relations and procedures carried out during the process of optimization.

Chapter five contains a discussion and illustrations of the obtained results. It explains and discusses how the optimized configuration is selected.

Finally, chapter six lists the concluding remarks drawn from the present investigation and the future work recommendations.

PART 2

LITERATURE SURVEY

The available literature that deals with the flight vehicles aerodynamic and structural design are few, consequently seeking an optimum design for such vehicles embraces a much wider range of problems and aims, which follow from the necessity to satisfy the required mission Optimization of the shape of a structure yields a great load capacity for a given amount of material or a given cost, if the concepts are such as minimum deformability or maximum durability can be introduced, so one can seek the least cost forms of the structure for a given load capacity deformability or durability.

Generally modern flight vehicles designed for subsonic flight often require a specified configuration of lifting surfaces with specified flying characteristics. The desire for improved and optimum design characteristics of aircraft leads to extend the study of predicting the aerodynamic characteristics of such configurations in this flight region.

One of the most attractive areas where optimization can be applied beside the structural synthesis is the aerodynamic shape optimization. It is worth to review the literature regarding this.

2.1. AERODYNAMIC PART

After the Wright brothers created the first aircraft at the turn of the century, a novel discipline of engineering and science referred to as "Aeronautics" was established. Approximately 4 decades later, a fully automated digital computer has been created, which had a significant impact on such novel branch. When Prandtl established his renowned lifting line theory around the turn of the century, the

aerodynamics regarding potential flow over bodies and wings has been first explored. This aided in the later development of all the theories and techniques employed now to address issues of this nature. Recently, computational fluid dynamics (C.F.D.) has advanced significantly. It was argued that impacts of the computational aerodynamics on the future aircraft design techniques will be significant due to variations of conventional approaches of aerodynamic designs, improvements in numerical algorithm efficiency and computer power over the time, and the increasing value of the energy resources needed to power large wind tunnels. Wind.tunnel testing was used for many years to develop aircraft configurations, with flow calculation methods making only a small contribution due to their simplicity and limitations. Each alternative configuration required the construction of a wind.tunnel model, which came at a cost and with a delay. Additionally, testing only give partial information.

S.A. Powers and D.F. Salter [10], The design of an air foil for a high.performance jet trainer was explored by the researchers. The airfoil design specifications and the aircraft performance specifications were discussed. The model of pressure distribution was described. The findings of transforming the pressure distribution model into an air foil using the airfoil design program were discussed. They came to the conclusion that this investigation demonstrates that specialty airfoils can be created at affordable prices to satisfy unique needs.

J.B. Malone[11], The researcher provided details of an iterative design generation for creating wing geometries with specific surface pressure distributions. A version of well.known surface.transpiration approach for simulating effects of the boundary layer was used in the design process. It was aimed to find a velocity distribution that minimized the discrepancy between computed and desired pressure and was normal to the aircraft surface. Numerical optimization was utilized for determining the distribution of the transpiration for particular initial geometry of the wing, which was after that applied to the configuration. For a number of example design issues, the application of this iterative process with sub.sonic surface.singularity panel approach was demonstrated. Malone came to the conclusion that methodologies for surface. singularity aerodynamic analysis could be used with the iterative design

procedure that was devised. Results had been given after process had been applied to available panel approach. This design process ought to offer an efficient tool for creating aircraft geometries with unique pressure distributions.

Gary B. Cosentino and Terry Holst [12], a dependable and quick program of the transonic wing flow field analysis was created by the researchers. A modified quasi.Newton unconstrained technique of optimization was linked with the program to produce a new design tool. The program's effectiveness decreased the amount of time needed for standard wing design. Utilizing lift.to.drag ratio as the objective function to be minimized, which was previously believed to be too unreliable for numerical optimization, generated considerable success, providing the designs of the wing with practically shock.free (i.e. 0.wave.drag) distributions of the pressure and suitable forms of the wing sector. They came to the conclusion that a new tool for aircraft designers concerned with effective aircraft operation at transonic flight speeds was created in the form of this program.

Per Krantz and Sven G. Hedman [13], To a computer program system utilized for the optimization of airfoils, the researchers included two new features. An approximate optimization approach, an aerodynamic code for transonic and subsonic viscous flow, and a geometry package for the airfoil's description are all included in the system. The additions were developed to broaden the application of airfoil optimization in practice. A geometry package that determines the airfoil shape, an aerodynamic module for potential flow computation, and subroutines for approximate optimization with quick convergence characteristics are all included in the program systems. A few chosen design variables were used in the optimization procedure. The potential for using constraints at off.design had been taken into consideration.

K. Appa [14].investigated the constant pressure panel approach for computing the generalized aerodynamic forces on lifting surfaces in invoiced flow. A formulation of the aerodynamic effects coefficient was used to link the panel pressure distributions and normal wash. The formulation rendered the analysis of the wake superfluous.

Low supersonic mach numbers were used for computation. The pressures panel approach described in this study was comparable to the doublet.lattice method utilized in subsonic flow in terms of the fundamental data and panel structure. The outcomes reported in this research show how the current technique for arbitrary planforms is accurate and computationally effective. The researchers came to the conclusion that since this technique was comparable to the double.lattice method code used in subsonic analysis, it could be seamlessly incorporated into that code, making aunifite code available for both supersonic and subsonic analysis.

Peter M. Goor Jian and Guru P. Guruswamy [15]. made some researches. in the domain of computational aeroelastic effects on airfoils and wings in unsteady transonic flows. Transonic, unsteady, small disturbance potential equation's results were reported. Unsteady transonic flow across wings and airfoils was calculated in a few different ways and displayed. An experimental flow over a NACA0012 airfoil that had significant shock movement, was compared to the calculation. In terms of flow over the wings, initially computations of the flow over the transport wing were demonstrated, and then the computations of the flow over low aspect ratio wing have been put to comparison with experimental findings. Lastly, the impact of changing sweep on aeroelastic damping was investigated. Which was done by comparing aerodynamic estimates of flow over variable.sweep wing with the experimentation.

2.2. STRUCTURAL PART

"When modern individual constructs massive load.bearing structures, they use dense materials such as concrete, steel, and glass," Ashby once said, the same phenomenon happens in nature with cellular materials such as bone, wood, and coral. Many scholars are now focusing their research on cellular material in general, and honeycomb structure in particular, as a result of these citations. Some of these are linked to the impacts of various honeycomb parameters on the honeycomb structure's static behavior. Others are looking at the dynamic behavior of this structure by changing the sandwich parameters. These studies and researches can be classified in the following ways to obtain a better understanding of them.

This section shows the most essential literature on static behaviors regarding the honeycomb sandwich panels, and that involves behaviors of such structures under the most common conditions of the load, like 3.point bending, buckling, and compression.

Fadhel Duaa [16]. had presented an experimental and computational study of the bending behaviors regarding honeycomb sandwich panels with different shapes of the cores (in other words, circular, hexagonal, and square) and 2 types of facing, one aluminum and the other one is composite. A 3.point bending testing has been used in the present work. In comparison to the other core shapes, the square honeycomb core had the highest load, which increased due to the increase in facing thickness, and aluminum skin facing had a larger value of the load when compared to composite skin facing.

In a numerical comparison work of the hexagonal and square honeycomb sandwich panel response under evenly distributed stresses, Ch.Naresh.utilized the same approach. To demonstrate the material impact of the core and face, the simulation used stainless steel, aluminum, and copper. According to the findings, the Al.Al sandwich panel with the square honeycomb structures had displayed higher deflection compared to SS.Cu panel, while having low stress values.

Guangyong Sun et al.[17], crushing behavior related to a honeycomb sandwich structure was investigated via experiments. In addition, the numerical model for the capturing of some specific deformation and failure features in the process of the crushing was developed using experimental data to ensure its validity. A 3.point bending test has been performed on Al honeycomb sandwich panel in the present study. Utilizing a variety of the honeycomb parameters, the effect of foil thickness, cell size, and core height on crush behavior was examined. A greater beak load value is predicted by increasing core height and face thickness, along with lowering cell size.

K. P. Toradmal et al [18], the 3.point bending of honeycomb sandwich panels was the subject of research. In this work, GFRP has been used as face sheet material

alongside metallic equivalents, such as the aluminum as well as stainless.steel alloys. Poly.propylene, a common material, was used for the core. According to the results, the GFRP–polypropylene core had a high ultimate load value.

V. Matta et al [19], the Taguchi approach was used to test the shear modulus and flexural stiffness of an Aluminum honeycomb core sandwich structure. It was determined what effect sheet thickness, core height and cell size have on the level of the bending stress. The results showed that increasing sheet thickness and core height enhanced flexural stiffness and shear modulus, but increasing cell size had the opposite effect.

Rao et al [20]. The strength of the sandwich structures under bending loads with a variety of the face materials was studied theoretically. Titanium, aluminum, and high.tensile steel have been utilized in this work. It has been discovered that titanium alloy had superior sandwich construction qualities.

Santosh et al [21]. Using PCTPE (i.e. the Plasticized Copolyamide Thermoplastic Elastomer) nylon as core material and HDPE (i.e. High.density poly.ethylene reinforced) as face material rather than metallic that is limited in several applications, enhanced energy absorption of the honeycomb structure under the compressive loads. The cell size has been varied from 10mm to 36mm for exploring influence of the size of the cell on honeycomb structure compressive behaviors. The specific energy absorption for a 10 mm cell was 1.15 kJ/kg during an out of plane test, however this reduced to 69 percent for a 36 mm cell.

E. S. Arbintarso et al [22]. The bending stress of a GFRP sandwich construction was investigated for a light.weight vehicle. There have been 3 different adhesives used to adhere the face and core (polyaminoamidebisphenol.A resin, plastic steel epoxy resin, and thermosetting resin). The research demonstrated that a lightweight chassis vehicle's honeycomb sandwich panel design with three adhesives might withstand considerable bending stress.

Jianmei He and Kentrao T [23], the researchers provided an experimental investigation on honeycomb sandwich panel compression properties in relation to different design parameters like cell size, foil thickness, and size of the sample (i.e. width, length, and height dimension) regarding the honeycomb structure. Sandwich samples were constructed via bonding Al honeycomb cores and 1mm thick CFRP laminate faces, and compression tests were performed on them. It could be seen that when the foil thickness and core height decrease, the yield stress increases.

M. Al.Waily and M. A. Al.Shammari [24], the researchers presented aa numerical and analytical examination regarding honeycomb sandwich structure buckling behavior. The general equation related to buckling the orthotropic plates with buckling loads in x.orientation for different honeycombs characteristics is used to get the analytic evaluations of buckling loads of simply supported plate. It was discovered that increasing the honeycomb core height and thickness increased the buckling behavior for honeycomb sandwich plate structures, however increasing the honeycomb core incline side size caused a decrease in the buckling load for honeycomb sandwich plate structures.

C. Zhao etal [25], the impact of the length.to.thickness ratio on lateral compression buckling performances was investigated numerically and experimentally by the researchers. To conduct the buckling test, a total of 4 honeycomb panel samples have been developed with varying thicknesses and lengths. Three of four test sections were 300 mm long and 10mm, 15mm, and 20mm thick, while the 4th has been 10mm thick and 500mm long. The result reveals that as honeycomb core thickness increased, the lateral compressive buckling load also increased, and the discrepancy between the findings of the actual test results and finite element analyses of the models of the honeycomb panel was 6% or less.

The static behavior does not appear to be sufficient to characterize the honeycomb sandwich panels efficiently, and additional information about dynamic behavior is required.

Muhsin J.Jweeg [26]. The vibration analysis of a honeycomb sandwich combination plate was given an analytical answer. The motion differential equation for vibration analyses of the honeycomb sandwich combination plate was solved to determine natural plate's frequency with a variety of the design parameters. Utilizing a range of design parameters, the impact of cell angle, core height, and cell size on basic natural frequency was examined. Natural frequency is linearly.proportionate to the parameter of the honeycomb, with an exception of thickness of the face, where the proportionality is inverse.

Harish et al [27]. The impact of the honeycomb thickness on the vibration response of sandwich panels was studied using experiments with various boundary conditions. Free vibration analysis has been performed on C.F.C.F and C.F.F.F in this work. It was revealed that the impact of core height on the basic natural frequency of the honeycomb sandwich panels is considerable. As the height of the core rises, so does frequency.

Ch. Naresh et al [28]. The natural honeycomb sandwich panels' frequency was numerically examined as a function of cell shapes, core and face sheet material combinations. The impact of core and face sheet material has been underlined in the work, which used hexagonal and square core forms.

S. Zghal and R. Nasri [29]. The vibration analyses of Honeycomb cored laminated sandwich beams was examined. An experimental evaluation regarding the 2 sandwich beams with Al and Nomex cores has been suggested. For clamped.free boundary conditions, the vibration tests were conducted using the forced vibration approach. In a set of the tests, the excitation and response points have been modified. The experimental data were used to determine the vibration parameters of honeycomb sandwich beams with regard to damping factors, natural frequencies, and vibration amplitudes.

Levent Ugur et al [30]. Finite and experimental element analytic methods have been used to look at the behavior of aluminum honeycomb structures under the low.speed impacts. The ASTM D7766 standard was utilized for conducting low.velocity impact

tests on the honeycomb structures that were created. The impact force was investigated as a function of cell width and height. The maximal impact force values in the honeycomb composite constructions have been found to grow as cell width and height decrease. The experimental and finite element approach results are roughly 85 percent in agreement.

Paulius et al [31]. The impact energy absorption of honeycomb core sandwich structures has been investigated experimentally as well as numerically. A woven glass fiber poly.vinylester resin composite face sheet and a poly.propylene hexagonal honeycomb core were used to create the sandwich panel. The impact of a geometrical parameter on the dynamic behaviors under the impact load has been studied.

G. Şakar [32]. Experiments and numerical simulations were conducted to investigate free vibration analysis of an Al honeycomb sandwich beam. For clamped free boundary condition, we got the natural frequency and mode forms with varied values. The lower and upper face sheet thickness, core material, foil thickness, cell angle, and cell diameter all had an impact on the vibration characteristics. The first natural frequency fell as the cell width rose in this study. On the first natural frequency, the cell angle (θ) has no impact. The initial natural frequency was raised by increasing the foil thickness and core height. The core height of the sandwich beam was shown to be the most beneficial parameter for reducing natural frequency.

M.Marythraza et al [33], the numerical model was created by the researchers to explore the vibration properties of honeycomb sandwich panels in spacecraft structures. The honeycomb panel was subjected to modal analysis. Analytical and FEM simulations are used to establish the panel's natural frequencies for simply supported and clamped boundary conditions. MSC PATRAN/NASTRAN was used to run FEM simulations. The analytical and FEM results are matching well. The panel's natural frequency must be separated from the natural frequencies of the launch vehicle and the spacecraft. The panel's natural frequency (stiffness requirement) must be more than 40 Hz in order to be uncoupled from spacecraft's fundamental natural frequency values, ranging between 12Hz and 15Hz. The launch

vehicle's fundamental natural frequencies are still in the region of less than 5 Hz. The honeycomb panel appears to match the natural frequency criterion, according to the research.

Zhengfeng Bai [34], the researchers utilized the same method to examine modal analysis for small satellite systems as M.Marythraza et al [33]. The findings show that finite element approach has been considered as a practical and valuable modal analysis tool, allowing for the calculation of normal frequency and the prediction of modal forms. Furthermore, the mode forms could be used for determining the satellite structural vibratory weakness parts. Until present, several honeycomb sandwich plate equivalent approaches were examined.

Abbadi et al [35]. The vibration analyses of laminated sandwich beams with the Honeycomb cores have been investigated. It is proposed to conduct experimental evaluation of 2 sandwich beams with Nomex and Al cores. The vibration tests have been carried out utilizing the forced vibration method for clamped.free boundary conditions. Excitation and response points have been varied in a series of the measurements. The vibration properties of the honeycomb sandwich beam in terms of the natural frequencies, vibration amplitudes and damping factors have been performed using experimental results.

2.3. CONCLUDING REMARKS

The comparison of approach's findings with certain previously published findings demonstrated how well the proposed way of study may predict the aerodynamic properties regarding a subsonic wing. The researchers came to the conclusion that the higher order technique was the most effective in treating the subsonic flow problems' sensitivity to numerical approaches. It is evident from the preceding analysis that there’s a lack of insights in literature regarding work pertaining to the effects of aerodynamic loading on the developed structures in light weight structural application.

In present study, The goal of the current work is to design and analysis of a light weight aircraft wing using a honeycomb structure and can resist aerodynamic loading. A comparison study will be achieved in using wing design with ribs and stringers. To achieve the above objective, the following steps are followed.

- Aerodynamic study should be achieved for a selected airfoil for the L39 Jet Trainer wing as a case study. Different Mach numbers, different angle of attack, using the NACA 64 A 012 Estimation of pressure distribution and the calculation of lift and drag forces are achieved.
- Structural Analysis is using the pressure predicted in (1), the deformation, stresses
- Structural Analysis is achieved using the pressure distribution predicted numerically. The finite element will be adopted employing the light weight structure.
    a. the wing is modeler using three types of configurations , one cell, 6 cells and 9 cells.
- Comparison of the results. The result is the decision of the optimum light weight wing structure compared to using the ribs and stringers.

PART 3

AERODYNAMIC THEORETICAL CONSDERATIONS

3.1. INTRODUCTION

As the need for excellent aeronautical performance grows, so does the requirement for precise aerodynamic estimations. Furthermore, precise accurate aerodynamic data (pressure distribution) is regarded as a vital input data for detailed structural design. Typically, the essential data is gathered via wind tunnel testing or provided by modern computational methods (C.F.D). Wind tunnel tests are usually extremely dependable. However, this is exceedingly expensive and necessitates advanced modeling, setting, and measuring approaches. Furthermore, it is a lengthy procedure. Computational fluid dynamics (C.F.D.) necessitates the use of a high.speed computer as well as effective computational methods.

The creation of the (C.F.D) in the early 1970s was prompted by the fact that wind.tunnel testing had become increasingly costly and time.consuming, as well as a reduction in relative computation cost, time, and better algorithms. Several computational methods for determining the potential flow field around realistic aircraft forms have been developed over the last decade. These computational tools give us the capacity to precisely model the aerodynamic interference impacts of arbitrary shape, like lifting surfaces.

In this chapter a fluid flow of the physical domain has been solve, using three.dimensional partial differential governing equations which are based on the continuity and momentum equations represented by N.S equation. A 3D wing are simulated with a finite volume method using ANSYS FLUENT Multiphysics 2020R1 commercial program solver of incompressible Navier.Stocks equations with (k.ε) turbulence model is used to simulate.

3.2. WING LOADING

An aircraft's wing is a critical component that determines its aerodynamic characteristics. Distributed air loads or aerodynamic forces, inertia loads, and, in many cases, concentrated forces from other key elements linked to the wing are all forces that the wing is susceptible to. The aerodynamic forces arise when the air flowing past the wing must be diverted from its original course, and this flow deflection causes changes in the airspeed, causing the pressure imposed by the air on the wing to differ from the pressure exerted by the undistributed stream. Also, because of the viscosity of air, frictional forces try to impede its flow; as a result of these processes, the wing is subjected to an aerodynamic force and moment.

Because of the differential pressure distribution caused by wing camber, wing incidence, or a combination of the two, the resulting aero.dynamic force acts at a center of the pressure. The position of pressure center shifts as the pressure distribution changes with speed or wing incidence. In addition, the chordwise pressure distribution defines where the resultant aerodynamic load is located in the wing cross.section, while the spanwise pressure distribution specifies where it’s located in relation to the wing root. The wing should be constructed for the most stressful combination of conditions since the location and direction of wing forces change with changing flight situations. In every scenario, a wing structure will be subjected to bending, twisting, and axial forces. Understanding the aerodynamic properties of aero foils is the beginning point for designing finite wings and, eventually, the entire aircraft.

3.3. WING CHARACTERISTICS

The important characteristics to be determined in the preliminary design of the wings are the number of wings, airfoil section, wing area, principle dimensions and the type of construction. These characteristics cannot be determined separately, as each effects the others, and the only way to come a final decision is to make trail performance computations with combinations of the various quantities that the designer believes from his experience will give the desired results. The

understanding of the aerodynamic properties of airfoils serves as the starting point for designing finite wings and, eventually, the entire aircraft.

The aerodynamic and structural analysis in this thesis is based on the advanced jet trainer aircraft (L.39) was selected as a case study in the present work testing and their characteristics and specifications. The wing required data was listed below in Table 3.1 [36] .

Table 3.1. The wing data.

Aircraft weight	**6500 Kg**
Span	9.12 m
Gross area	18.8 m^2
Quarter chord line sweepback angle	$1^0 45$
Leading edge sweepback angle	$6^0 26$
Taper ratio	0.475
Aspect ratio	4.4
Mean aerodynamic chord	2.15 m
Tip chord	1.33 m
Root chord	2.8 m
Profile	NACA 64A 012
Geometric shape	Trapezoidal

3.3.1. The Airfoil Section

Till lately, wing section development was nearly exclusively empirical. A sharp trailing edge and rounded leading edge were found to be desirable in early tests. The steady evolution of wing theory tended to isolate the wing section problem from planform influences, resulting in a more systematic experimental approach. Various wing sections' families were tested in 1929, yet the NACA's work was excellent. Separating the impacts of camber and thickness distribution further systematized the NACA experiments. In this thesis, the wing section is chosen arbitrarily as NACA 64A 012 for all the test cases of the wings. The details of this NACA section are

given in Figure 3.1 [37] and Figure 3.2 which will be used later on as input data in the analytical finite element program data and also in the modeling of the wings by the ANSYS program.

APPENDIX I

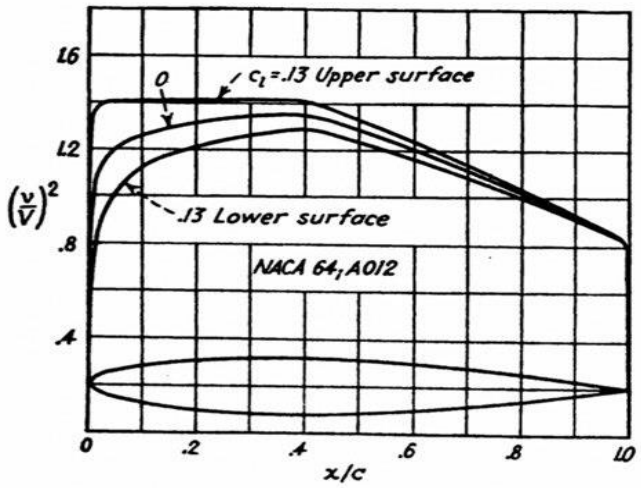

x (per cent c)	y (per cent c)	$(v/V)^2$	v/V	$\Delta v_a/V$
0	0	0	0	2.408
0.5	0.961	0.792	0.890	1.720
0.75	1.158	0.893	0.945	1.515
1.25	1.464	1.006	1.003	1.254
2.5	2.018	1.127	1.062	0.941
5.0	2.788	1.201	1.096	0.681
7.5	3.364	1.235	1.111	0.560
10	3.839	1.257	1.121	0.478
15	4.580	1.288	1.135	0.383
20	5.132	1.308	1.144	0.325
25	5.534	1.324	1.151	0.281
30	5.809	1.336	1.156	0.249
35	5.965	1.346	1.160	0.221
40	5.993	1.354	1.164	0.199
45	5.863	1.326	1.152	0.177
50	5.605	1.289	1.135	0.157
55	5.244	1.250	1.118	0.139
60	4.801	1.207	1.099	0.123
65	4.289	1.164	1.079	0.108
70	3.721	1.118	1.057	0.094
75	3.118	1.071	1.035	0.080
80	2.500	1.023	1.011	0.068
85	1.882	0.974	0.987	0.056
90	1.263	0.925	0.962	0.042
95	0.644	0.873	0.934	0.029
100	0.025	0	0	0

L.E. radius: 0.994 per cent c
T.E. radius: 0.028 per cent c

NACA 64₁A012 Basic Thickness Form

Figure 3.1. NACA 64A012 Basic Thickness Form [37].

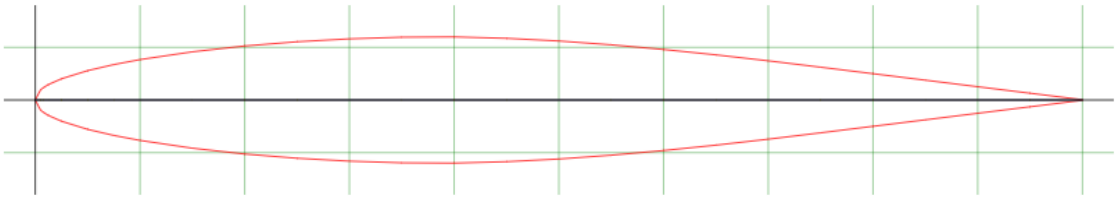

Figure 3.2. Wing Airfoil section NACA 64A012.
http://airfoiltools.com/airfoil/details?airfoil=n64012a-il

3.3.2. Wing Area (Planform)

When viewed from directly above, the wing planform is specified as the shape of the wing. Therefore, the area of the wing is same as planform area Planform area (S) is directly associated with the taper ratio λ and aspect ratio (AR), as

$$S = \frac{b}{2}(Ct+Cr) \tag{3.1}$$

where b represents wing span, Ct is wing tip chord and Cr is root chord of the wing.

3.3.3. Wing Aspect Ratio (AR)

The AR represents wing planform narrowness measure, or ratio of wing span to average geometric chord. It gives a direct measure of wing span for a given wing area.

$$AR= \frac{b^2}{s} \tag{3.2}$$

3.3.4. The Wing Taper Ratio (λ)

The taper ratio (λ) of the wing represents ratio of wing root chord to wing tip chord, i.e

$$\lambda= \frac{c_t}{c_r} \tag{3.3}$$

The span.wise lift distribution is greatly influenced by taper ratio. As the spanwise position of a half wing's center of pressure advances in direction of wing root lowers, so does root bending moment owing to the lift.

3.3.5. Mean Aerodynamic Chord (MAC)

which is defined as.

$$MAC = \frac{2}{3} C_R \frac{(1+\lambda+\lambda^2)}{(1+\lambda)} \quad (3.4)$$

3.3.6. Quarter Chord Line Sweep Angle (Λc/4)

$$\tan \Lambda_{c/4} = \tan (\Lambda_{L.E} .0.5(\frac{C_R - C_T}{b_w}) \quad (3.5)$$

The characteristics defined below and illustrated in Figure 3.3 are usually classed as planform characteristics [38].

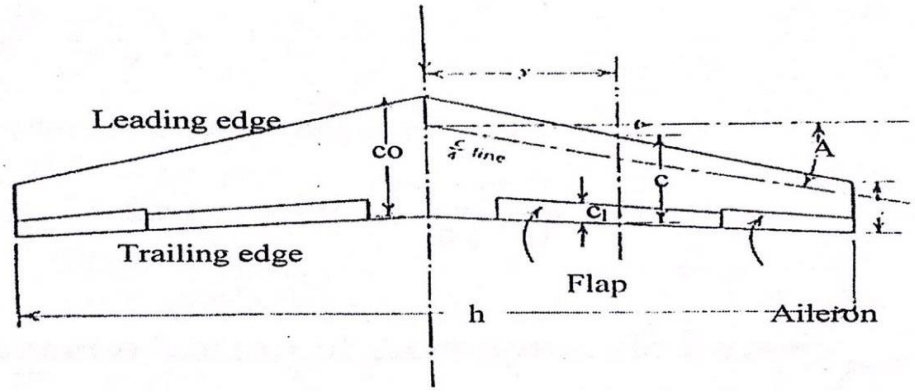

Figure 3.3. Wing planform characteristics [38].

3.4. CHARACTERIZATION OF AERODYNAMIC FORCE

The motion of the air around the aircraft produces pressure and velocity variation, which produce the aerodynamic forces and moments. With the invicid flow field known, the velocity distribution across the viscous boundary layer, and hence the

tangential shear forces can be calculated. The normal and tangential forces, which act on the surface due to the fluid motion around the airfoil, are shown in Figure 3.4.

The magnitude of the forces and moments that act on the surface depend on the combined effect of many different variables. The parameter that govern the magnitude of the aerodynamic forces and moments include the following [39].

- Configuration geometry
- Angel of attack.
- Free stream velocity
- Density of the air
- Reynolds number (viscous effect)
- Mach number (compressibility effect).

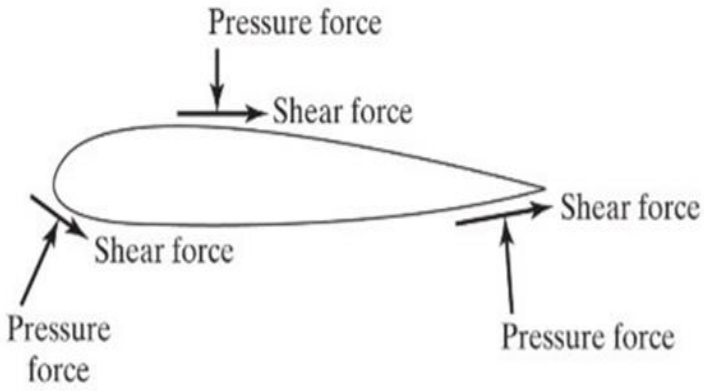

Figure 3.4. Normal (or pressure) and tangential (or shear) forces on an airfoil surface [39].

3.4.1. Pressure Distribution on an Airfoil

The pressure on the surface of an airfoil in flight is not uniform, Figure 3.5 shows some typical pressure distribution for a given section at various angles of attack. Looking at the sketch of zero angle of attack (a=0), it is seen that there are small regions at the leading edge and trailing edge where Cp is positive but that over most of the section Cp is negative. At the trailing edge the pressure coefficient decreases. The reduced pressure on the upper surface is tending to draw the airfoil upwards while that on the lower surface has the opposite effect. With the pressure distribution

as sketch in Figure 3.5, the effect on the upper surface is the larger and there is a resultant upward force on the airfoil, which is the lift [40].

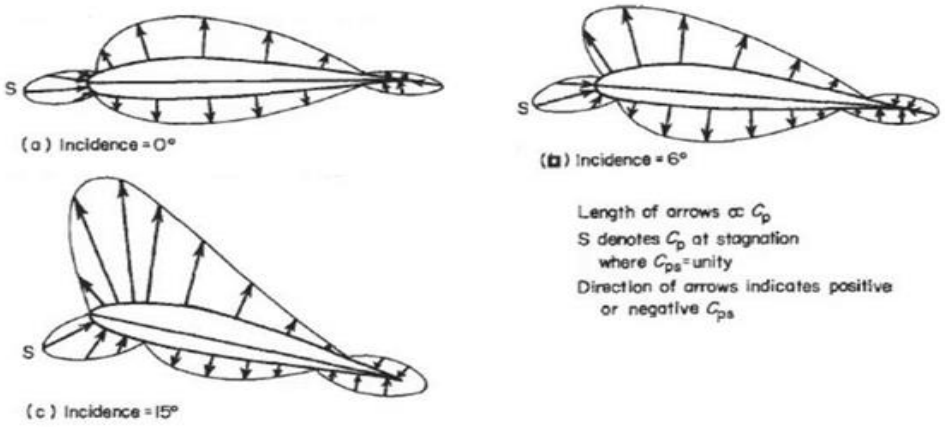

Figure 3.5. Typical pressure distributions on an airfoil section [40].

3.4.2. Pressure Distribution Around the Wing

For a wing of finite span, the high.pressure air under the wing spills out a round the wing tips toward the low.pressure regions above the wing. As a consequence of the tendency of the pressure acting on the top surface near the tip of the wing to equalize with those on the bottom surface, the lift force per unit span decreases towards the tip. Figure 3.6 represents an aerodynamic load distribution. As indicated in Figure 3.6 a) there is a chordwise variation in the pressure differential between the lower surface and the upper surface. The resultant lift force acting on a section (unit span) is obtained by integrating the pressure distribution over the chord length.

The spanwise variation in the lift force is shown in Figure 3.6 b). As a result of the spanwise pressure variation, the air on the upper surface flows inboard toward the root. Similarly, on the lower surface, air will tend to flow outward toward the tips. The resultants flow a round the wing of finite span is three dimensional having both chordwise and spanwise velocity components.

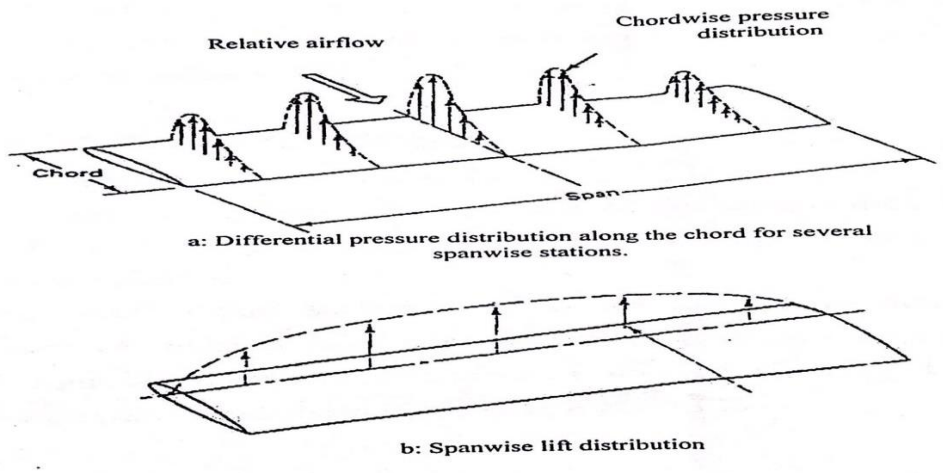

Figure 3.6. Aerodynamic load distribution for rectangular wing in subsonic airstream.

3.5. THE GOVERNING EQUATIONS

The governing equations that equations describe the three dimensional flow over a wing are (Verestage & Malalasekera, 1995) [41].

- Conservation of Mass

Applying mass conservation law on a three.dimensional control volume, the conservation equation is.

$$\frac{\partial}{\partial x_i}\, u_i = 0 \tag{3.4}$$

- Momentum Equations

$$u_j \frac{\partial u_i}{\partial x_j} = -\frac{1}{\rho}\frac{\partial p}{\partial x_i} + \frac{\partial}{\partial x_j}\left(\vartheta \frac{\partial u_i}{\partial x_j} - u_i u_j\right) \tag{3.5}$$

3.5.1. k.ε Turbulence Model

k.ε model of turbulence can be described as 2.equation model of the kinetic energy (k) as well as its rate of dissipation (ε). Turbulent viscosity is related to the local

values of ρ, ε, and k via the expression in this model. Realizable k.ε is a step forward from the ordinary k.ε model. The realizable k.ε model is divided into two equation groups, each of which requires the solution of two extra amounts. rate of dissipation ε and turbulent kinetic energy k.

For the turbulent kinetic energy (k);

$$\frac{\partial(\rho k)}{\partial t} + \frac{\partial(\rho k u_j)}{\partial x_j} = \frac{\partial}{\partial x_j}\left[\left(\mu + \frac{\mu t}{\sigma x}\right)\frac{\partial k}{\partial x_j}\right] + P_k + P_b - \rho\epsilon - Y_M + S_k.... \quad (3.6)$$

For turbulent dissipation (ε);

$$\frac{\partial(\rho\epsilon)}{\partial t} + \frac{\partial(\rho\epsilon u_j)}{\partial x_j} = \frac{\partial}{\partial x_j}\left[\left(\mu + \frac{\mu t}{\sigma\epsilon}\right)\frac{\partial\epsilon}{\partial x_j}\right] + \rho C_1 S_\epsilon - C_{2\rho}\frac{\epsilon^2}{k+\sqrt{v\epsilon}} + C_{1\epsilon}\frac{\epsilon}{k}C_{3\epsilon}P_b + S\epsilon \quad (3.7)$$

Where;

$C_1 = \max[0.43, \frac{\eta}{\eta+5}]$, $\eta = S\frac{k}{\epsilon}$, $S = \sqrt{2S_{ij}S_{ij}}$

P_K. represents the gradients of mean velocity by turbulence kinetic energy.

P_b. represents the buoyancy by turbulence kinetic energy.

The Modelling of turbulent viscosity

$$\mu_t = \rho C\mu \frac{k^2}{\epsilon}$$

Where;

$$C_\mu = \frac{1}{A_O + A_S\frac{kU^*}{\epsilon}}$$

$U^* = \sqrt{S_{ij}S_{ij} + \Omega_{ij}\Omega_{ij}}$

$\Omega_{ij} = \Omega_{ij} - 2\epsilon_{ijk}\omega_k$

$\Omega_{ij} = \Omega_{ij} - \epsilon_{ijk}\omega_k$

Where rep Ω_{ij} resents the absolute vorticity with angular velocity ωk.

The values of constants in equations are represented as.

$A_O = 4.040$, $A_S = \sqrt{6}\cos\phi$

$\phi = \frac{1}{3}\cos^{-1}(\sqrt{6}W)$, $W = \frac{S_{ij}S_{jk}S_{ki}}{\tilde{S}^3}$, $\tilde{S} = \sqrt{S_{ij}S_{ij}}$,

$S_{ij} = \frac{1}{2}\left(\frac{\partial u_j}{\partial x_i} + \frac{\partial u_i}{\partial x_j}\right)$

$C_\mu = 0.09\sigma_k = 1\sigma_\epsilon = 1.3\ C_{1\epsilon} = 1.44\ C_{2\epsilon} = 1.92$

3.5.2. Boundary Conditions

The significance of the boundary conditions are to reproduce the experimental conditions. In the commercial program ANSYS FLUENT 2022R1, the boundary conditions of the present study used are;

- Inlet Velocity Boundary Condition

The inlet velocity boundary was specified using a normal inflow velocity inlet boundary condition. In this study, the inlet velocity was specified at several Mach (0.2,0.4,0.6,0.8) and for several different angles (0^O,2^O,4^O,6^O,8^O,12^O) for each angle, a run was made for the previously mentioned velocity.

- B. Wall Boundary Conditions

No slip condition specified for the wing surfaces. The domain was modeled using symmetric boundary conditions that are a zero shear at wall slip. condition, in order to minimize a number of mesh nodes that would be needed to analyze the created boundary layer on the wind tunnel walls.

- C. Outlet Boundary Conditions

The outlet boundary was modelled by using a pressure outlet boundary condition. The outlet pressure was set to atmospheric pressure.

3.5.3. Numerical Solution

The Computational Fluid Dynamics (CFD) consists of three main steps. The first is the pre.processing which are a 3D geometry model by using the Software SOLIDWORKS 2020. The second step was processing the governing differential equations for air flow over a wing by ANSYS FLUENT 2022 R1 version solver by utilizing a Finite Volume Element. Finally, the third stage was the post.processing step in which calculate the aerodynamic characteristics like pressure distribution.

3.5.4. SOLIDWORKS Software

SOLIDWORKS Software is used to design the wing and the computational domain. The wing model is designed at the present work with the actual dimension divided by the root chord length of the wing. The size of the computational domain chosen extends one of the wing root chord lengths in front of and back the trailing edge of the wing because the distance behind the wing should be suitable to be the area of separation of flow and does not affect the flow of air. The distance between the upper boundaries and the flyover of the wing lengths is a set of wing root chords. The distance between the lower boundaries and the flyover of the wing lengths is set and the distance between the tip of the wing and the side wall of the domain is set at one of the wing root chords because the large domain needs a lot of iterations to solve the many numbers of mesh cells and gives approximately the same results for the selected domain. The computational domain was formed with appropriate dimensions as shown in Figure 3.7.

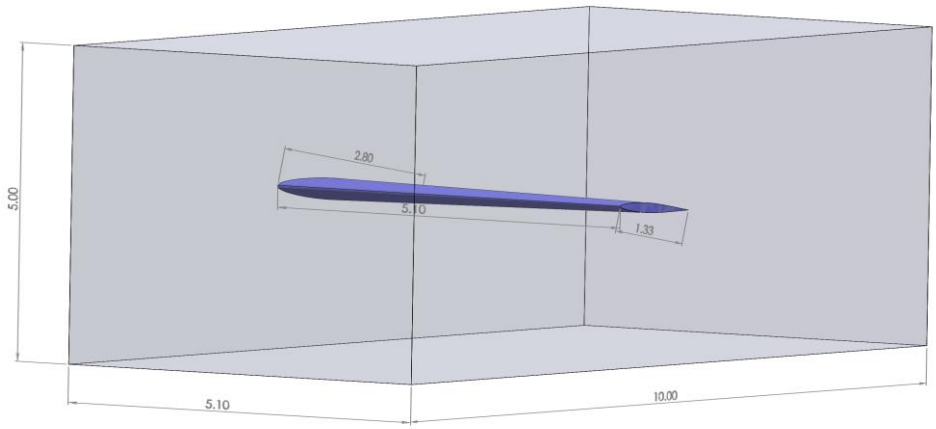

Figure 3.7. Design the geometry by Solidworks.

3.5.5. ANSYS FLUENT Software

FLUENT (2022R1) is a commercial CFD software used to generate the mesh and analysis the fluid flow around the wing. FLUENT utilizes the discretized domain constructed in SOLIDWORKS to solve the governing equations of the control volume in the present study.

3.5.5.1. Mesh Generation

A mesh is defined as dividing the model's geometry into simple shapes of small units, by using tetrahedral meshing with finer sizing, the grid was generated. Because the large domain needs a lot of iterations to solve the many numbers of mesh cells and gives approximately the same results for the selected domain. For the study of three.dimensional, the number of nodes and elements has been chosen between 5531204 and 5341329 (see Figure 3.9), and chosen mesh metric (see Figure 3.10); the selection of the number of elements depends on the grid independence test (see Figure 3.8). The difference between the soft and chosen grids is less than 0.1% and the Mesh of the domain with wing model 3D is shown in Figure 3.8. the smallest cells are generated near the adjacent surface of the wing, and the larger cells are located near the boundary domain (see Figure 3.8).

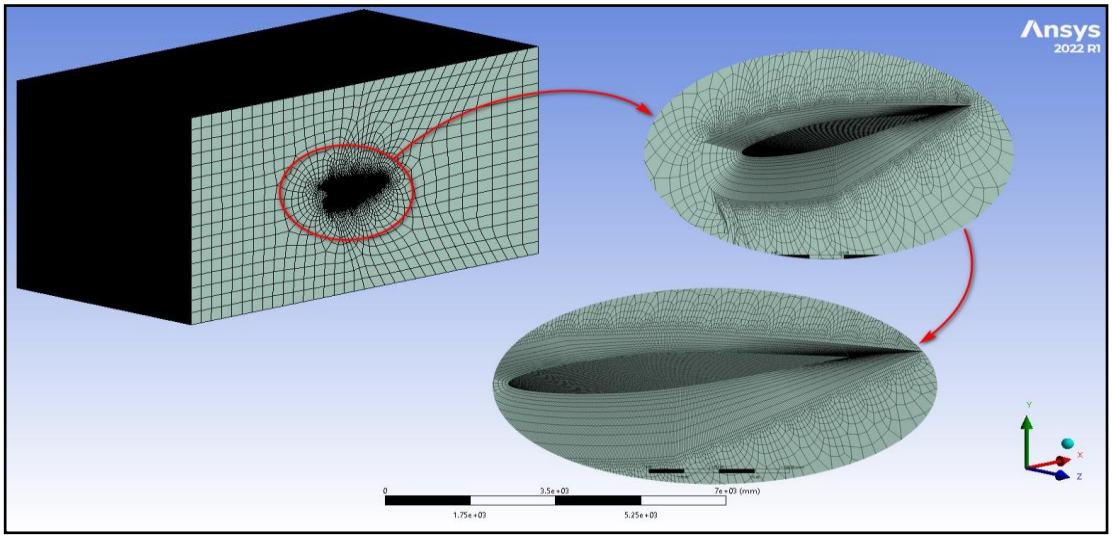

Figure 3.8. Mesh generation.

Statistics	
Nodes	5531204
Elements	5341329

Figure 3.9. Number of nodes and elements are used in mesh.

In order to know the quality of the mesh, whether it is good or not, we used the Sequence method from the Mesh Metric box, where we found the Skewness number (0.29964), which is an excellent mesh see Figure 3.10.

Mesh Metric	Skewness
Min	2.6822e-004
Max	0.99947
Average	0.29964
Standard Deviation	0.22634

Figure 3.10. Skewness mesh metrics.

3.5.5.2. Numerical Algorithm

The ANSYS FLUENT 2022 R1 uses the following steps to obtain the pressure distribution Around the airfoil.

- Generation the geometry and domain.
- Generation the mesh of geometry.
- Set up the steady flow, pressure.based solver type and absolute velocity formulation.
- 4. Specification of the properties of the fluid used such as air density and viscosity and the boundary conditions as mentioned above.
- The solution method of the problem is the pressure.velocity coupling simple scheme.
- Initialization the solution and run calculations.
- calculation The pressure distribution.
- Analysis the problem after specifying the convergence criteria and the iterations number.

PART 4

STRUCTURAL CONSIDERATIONS

4.1. INTRODUCTION

For determining the optimal overall aircraft structural configuration with regard to a given mission requirement, the preliminary sizing of an aircraft's primary structure necessitates the consideration of a significant number of design variables. The primary disciplines that must interact during the design process are aerodynamics, geometry, load, weight, strength, and structural design.

4.2. SOURCE LOADING

The loads carried by the aircraft come from a variety of sources. Both during landing and takeoff along with throughout flight, such loads are active on the aircraft.
Figure 4.1 explains these loads. For effective wing design, such loads must be accurately determined in order to achieve the required strength while minimizing weight [42]. Regarding the structural design, the inquiry is focused on the optimization of the wing taking into account the strength.weight tradeoff. The aerodynamic design provides certain insight into the wing's structural shape.

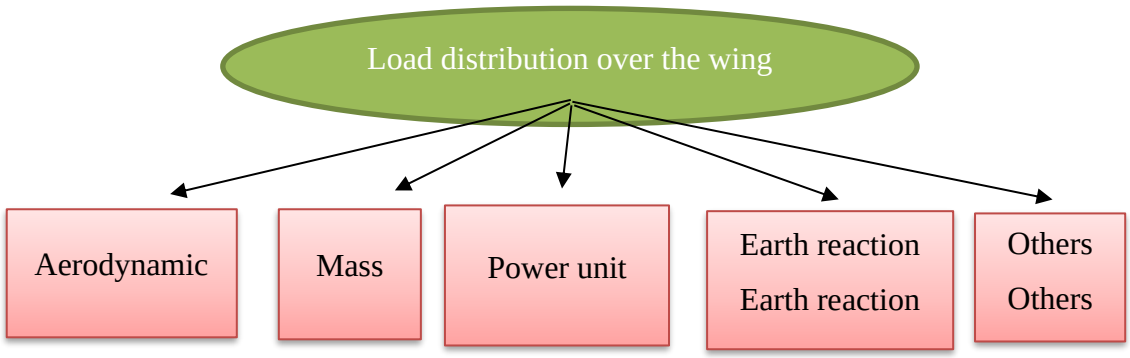

Figure 4.1. Loads on the wing [42].

4.3. WING STRUCTURAL ARRANGEMENT

The wing cross.section should have a streamlined shape for aerodynamic purposes. Throughout flight, aerodynamic forces and moments change in direction, magnitude and location; as a result, the necessary structure should be able to effectively withstand loads that cause tension. A portion of the airfoil surface could be covered with a metal skin for providing forsional resistance, and at least one internal metal web could be added to create a single closed cell or a multiple closed cell wing cross.section. Although the external skin surface regarding subsonic aircraft is rather thin, it is effective at resisting torsional shear stresses and tension, yet not at resisting compressive stresses brought on by wing bending. The inside of surface skin is joined by spanwise stiffening units, also known as stringers or Longerous, for providing strength efficiency. Chordwise ribs are incorporated to retain the skin's surface in the airfoil shape and act as a medium for air pressures on the surface to be transferred to the cellular beam structure. Figure 4.2 and Figure 4.3 show the typical structural configurations of wing cross.sections [43].

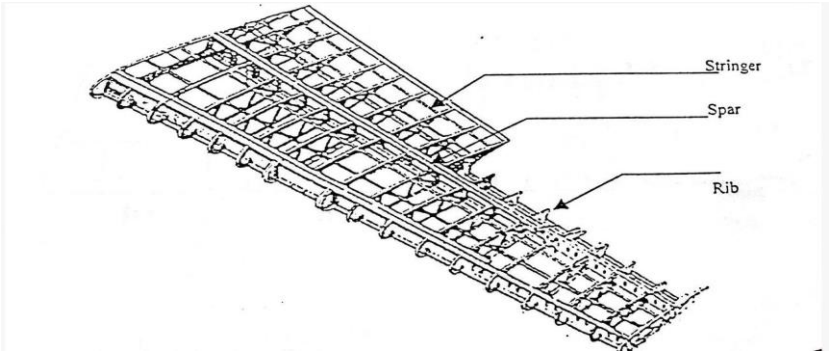

Figure 4.2. Spar Wing Construction [43].

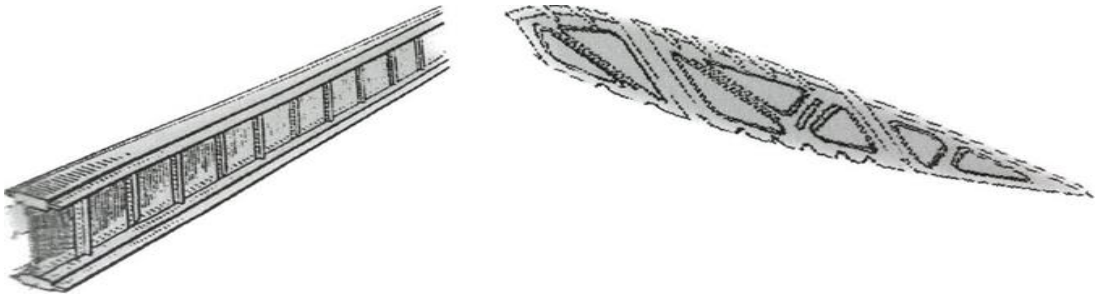

Figure 4.3. Typical structural arrangements of wing cross.section [43].

4.4. LIGHT WEIGHT STRUCTURES

The most cutting.edge, dependable materials are required in the aerospace sector to provide optimal safety, strength, and longevity in demanding applications. Aerospace materials should be heat resistant so that structural changes are kept to a minimum throughout the extreme and abrupt temperature variations that take place at both high.altitude and high.speed flights [44], as well as lightweight for ensuring optimal aerodynamics and the safety of passengers and pilots. All of the aforementioned conditions could be successfully met by honeycomb, especially aluminum honeycomb. As seen in Figure 4.4, sandwich panels are utilized in the bulkheads, floors, and even the wings and skin [45].

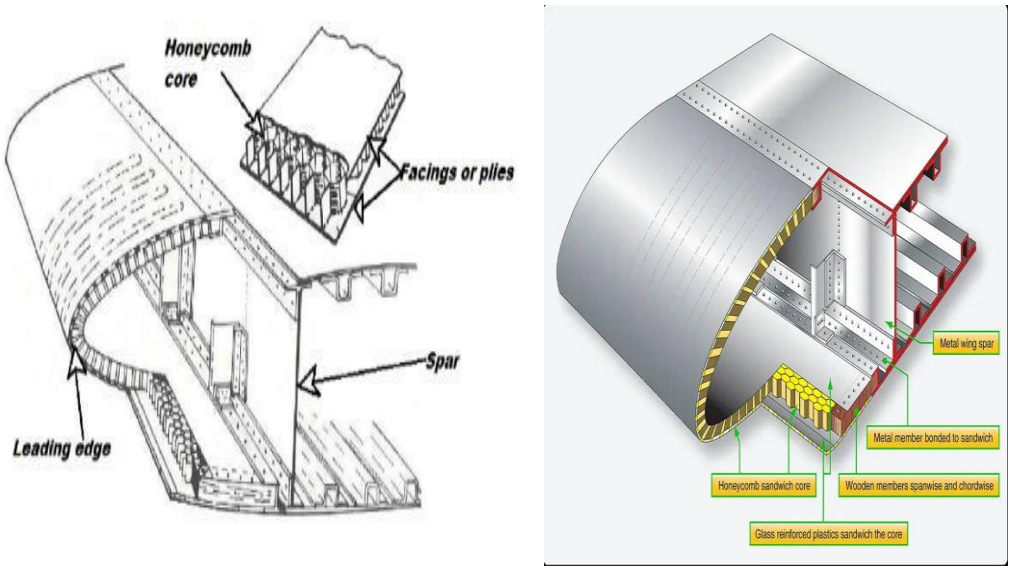

Figure 4.4. application of honeycomb in aircraft structure [45].

4.4.1. Honeycomb

With regard to sandwich structures, honeycomb cores are available in a range of materials, including paper and card for applications needing low strength and stiffness and low loads (like interior doors for homes) and high strength and stiffness, incredibly lightweight sections for aviation structures, are available for honeycomb cores used in sandwich structures. Honeycombs can be formed into composite structures which are both flat and curved without needing a lot of mechanical force or heat. [46] A honeycomb's typical shape is shown in Figure 4.5. The cells could be hexagonal, triangular, or square. Examples of honeycomb include glass fiber reinforced plastic, aluminum, and honeycomb made of Kraft paper, among others. Aluminum and carbon honeycomb cores are used in this experiment. Sandwich composites are excellent materials for adding features beyond load.bearing capacity. Those composite structures have a light, stiff structure and two faceplates that are separated by core material in order to boost their bending stiffness. Figure 3.6 is a representative illustration of a sandwich structure with attached faceplates. A core is often set up as a grid of cells with a variety of possible geometrical structures, like polygonal or circular cross.sections [47]. Here, our attention will be on hexagonal arrangements of the honeycomb which have been sized in order to preserve significant bending stiffness in sandwich panels.

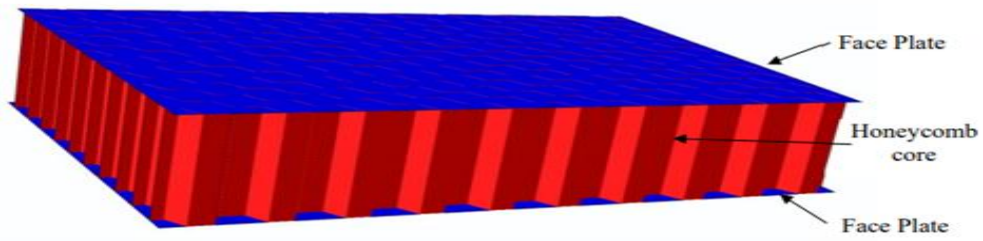

Figure 4.5. A schematic of a typical sandwich structure.

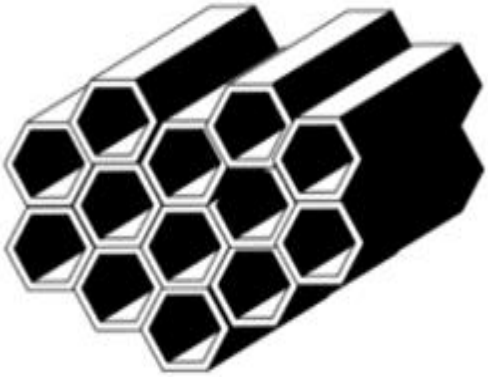

Figure 4.6. honeycomb core [46].

Honeycomb characteristics are anisotropic, meaning that they differ between out.of.plane and in.plane strengths and stiffnesses. The walls of the cells first bend and deformation is linear elastic in a case where a honeycomb is squeezed in.plane, that is, when stress acts orthogonal to cell axis, plane X1 X2 has been depicted in Figure 4.7.

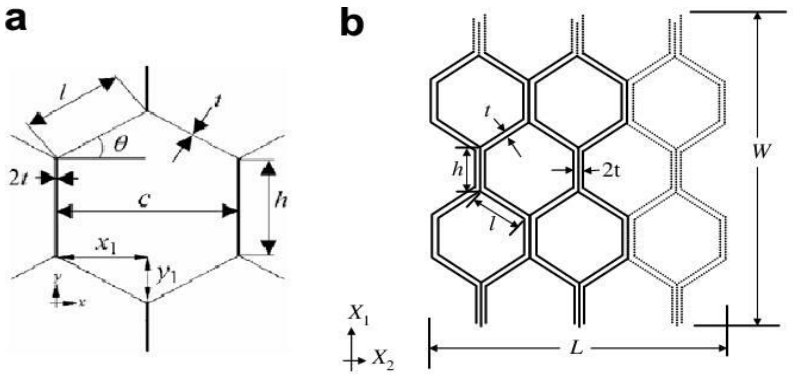

Figure 4.7. Definitions of parameters for a honeycomb cell [47].

FEM is usually utilized in order to study composite structures. Composite sandwich structures, on the other hand, represent a modeling problem due to the fact that their core region is made up of several cells with complex geometries. While some analyses, like the simulation of the sequential propagation of the failure within core, might call for detailed finite element modelling of small representative core region in order to ascertain material responses in the propagation of the damage, other sandwich composite behavior simulations that involve full panel might call for the modelling of sizable number of the core cells, which makes the explicit simulation be

expensive computationally. As a result, a few types of homogenization technique is required for replacing core for simpler solid layer with equal (i.e. effective) material characteristics. Numerous studies that avoided the explicit modelling regarding honeycomb structure were published that give different analytical approaches for figuring out the mechanical characteristics of the homogenized core geometry. The analysis of unit cell that represents one repeating element in the honeycomb geometry often yields effective material properties for honeycomb structures.

The 1D isotropic beam analysis method by Gibson *et al*. [48] is the most widely used model of unit cell for determining effective characteristic determinations. Gibson makes an assumption that the honeycomb deformations' linear.elastic response and the consequent core characteristics are solely dependent on the bending of the core cell walls. The stretching and shearing of cell walls were studied as additional deformation modes [49]. The FEM has been used in numerous previous publications for estimating effective material characteristics regarding honeycomb architectures. To anticipate homogenized the effective material characteristics for the multi.functional honeycomb sandwich cores, analytical equations must be developed. The core of multifunctional sandwich composites could after that be sized using such analytical equations in the design process to account for anticipated energy needs as well as desired service loads. Figure 4.8 provides an illustration of the homogenization approach used in this study. Gibson's method is utilized for obtaining similar elastic characteristics that are related to full core configurations so that they could be utilized in uniform solid material representations. This method has been carried out in 2 steps. (a) determining single effective modulus for multi.layer wall that is utilized in core; (b) using Gibson's method. The finite element modeling regarding a sandwich core is after that made simpler by using the homogenized core. Figure 4.9 illustrates this process.

This study's two goals are to improve Gibson analysis through expanding it to include multi.layer isotropic walls and to confirm this approach through the comparison of analytical results for the referencing of the FEM simulations that

explicitly describe multi.layer honeycomb design. All analyses are predicated on the assumption of small deformations and a solely linear elastic response.

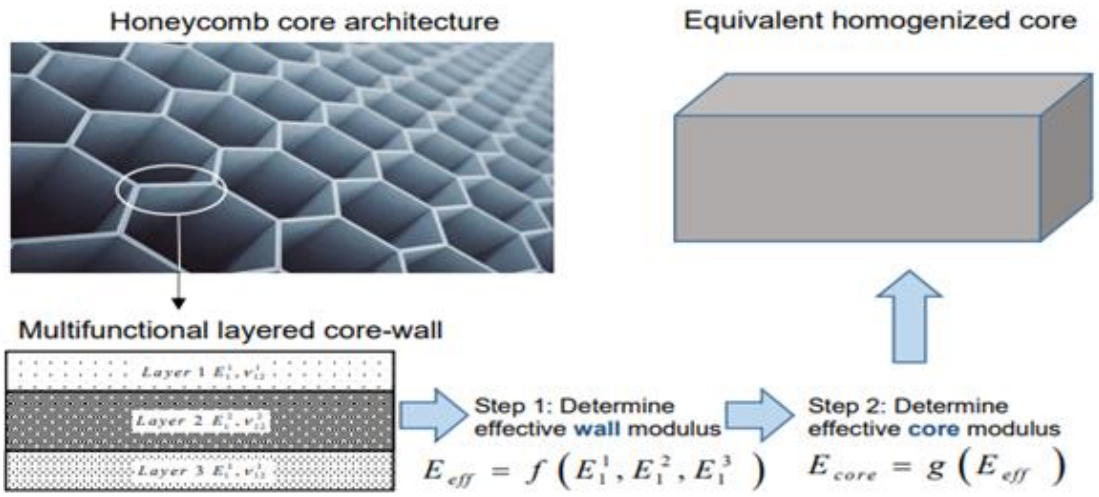

Figure 4.8. Overview of homogenization methodology sought in the current investigation.

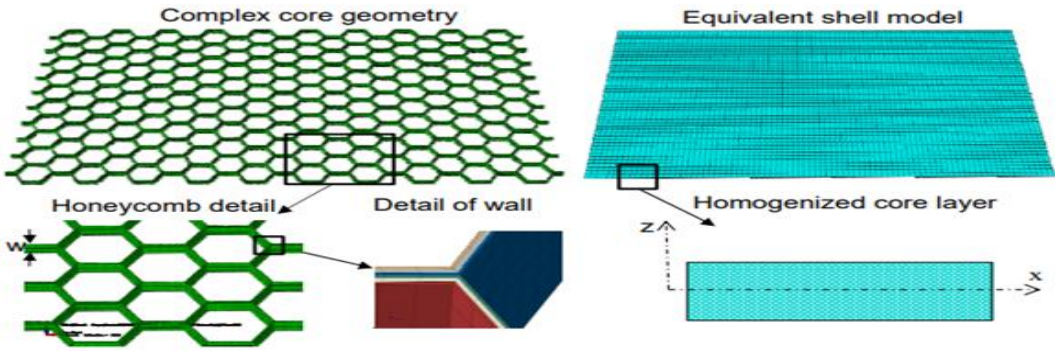

Figure 4.9. Simplified modeling of complex core geometry.

4.4.2. Material Properties of the Sandwich Panels

In this step, the material properties of the sandwich panels were input and the material sections were assigned. The material properties used in this analysis for carbon fibers, and Al 7075.T6 materials are listed in

Table 4.1 and Table 4.2, 3D deformable shell geometry was used to model the skins and the honeycomb core. The composite shell material section was assigned for the skins and the honeycomb core. The skin thickness was to be (2,3,4 mm) and the Core

thickness was set to be (2,4,6 mm) which is the thickness of the laminated skins and the laminated honeycomb core layer.

Table 4.1. Material properties of aluminum (Al 7075 T6).

Material (Al7075 T6)	Number	Unit
Elastic Modulus	72000	N/mm^2
Poisson's Ratio	0.33	N/A
Shear Modulus	26900	N/mm^2
Mass Density	2810	kg/m^3
Tensile Strength	570	N/mm^2
Yield Strength	505	N/mm^2
Thermal Expansion Coefficient	2.36E.05	/K
Thermal Conductivity	130	W/(m·K)
Specific Heat	960	J/(kg·K)

Table 4.2. Material properties of Carbon fiber laminates.[50]

Material (carbon fiber Laminates)	Number	Unit
Elastic Modulus	140	Gpa
Poisson's Ratio	0.22	N/A
Mass Density	1760	kg/m^3

4.4.3. Fluid.Structure Interaction (FSI)

The FSI represents Multi.physics study of the way that the structures and the fluids interact. Fluid flow could be exerting pressure and/or thermal load on structure. Those loads could lead to some structural deformations, which are sufficiently significant for changing the actual fluid flow. The undesired impacts on one's product could be increasing with the increase of fluid.structure interaction level. With the simulation of ANSYS one can acquire a more detailed understanding about phenomena that occur with one's product for the purpose of ensuring the safety, longevity and reliability. ANSYS includes broad variety of the solutions for all challenges of the FSIs that one could be facing for providing the required fidelity level. The simple problems of fluid.structure interactions may be entirely solved

completely within the ANSYS CFD. Which has been referred to as the rigid motions of the body, which can be represented by impeller that rotates in mixing tank. With an increase of the interaction of fluid.structure and problem requires more thorough assessment, ANSYS has easy.to use automated solution that is referred to as the one.way coupling, which can solve preliminary CFD or ANSYS Mechanical simulations and automatically transfer and map data to another system. One of the examples of that would be the simulation of fluid flow around the flow meter of the cone and transferring that data automatically for calculation of resultant structural responses. For the most tightly coupled and complex problems of the fluid.structure interactions, System Coupling can be utilized for performing 2.way coupled FSI simulation. Fluid as well as structural simulations have been set up and solved in a simultaneous manner. At the time where it is being solved, the data is transferred in an automatic manner between both solvers for purpose of achieving accurate and robust results. One of the examples of that would be the calculation of the flow about rigid airplane wing and transfer of pressure loads for solving the structural deformations, which would be transferred back to the simulation of the CFD for the purpose of calculating flow once more, and that process would be repeated.

Figure 4.10**Hata! Başvuru kaynağı bulunamadı.** depicts FSI flowchart. The MFS (i.e. Multi.field solver) provides infrastructure for the FSI in the ANSYS, where it couples it with FLUENT with no scheme of third party coupling. The settings of the coupling specify conditions of convergence. Targets have been setup in the fluent.Pre. Displacements/Loads are updated between ANSYS and FLUENT solvers. Typical inner loops, which are referred to as coefficient loopsin FLUENT and equilibrium iterations in the ANSYS, have been utilized in order converge field within solver.

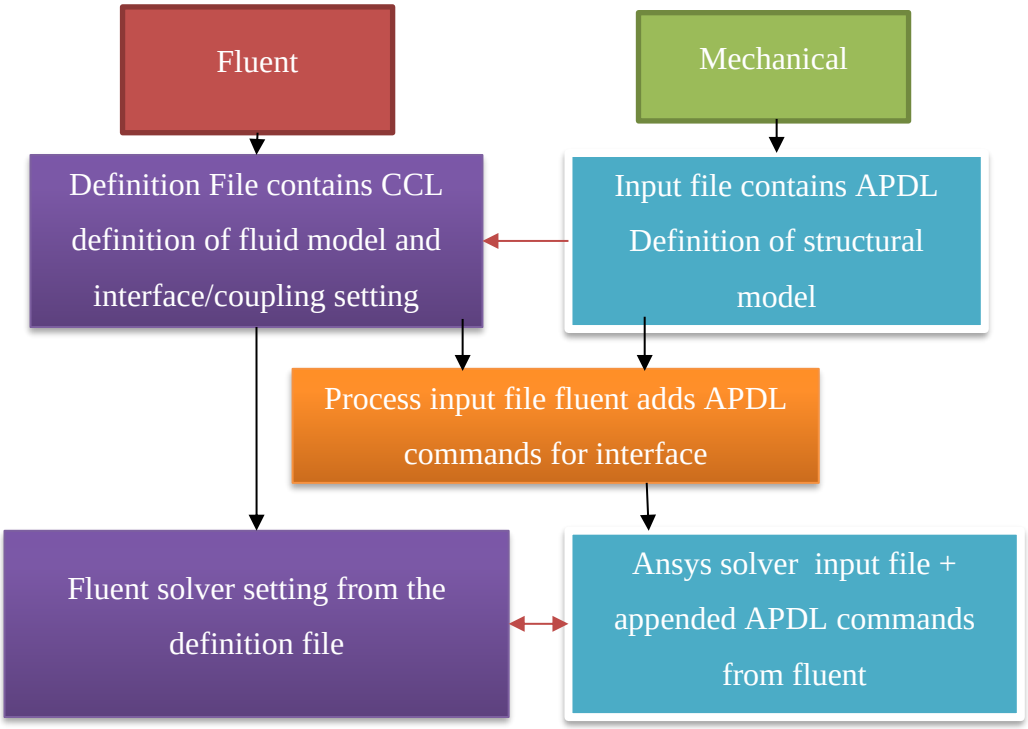

Figure 4.10. Flowchart of the FSI procedure.

Figure 4.11 depicts FSI loop iterations. The iterations of the field Loop are terminated in a case where field reaches the target of convergence (or maximal number of the iterations in the fluent). The stagger loop iterations are stopped when loads/displacements reach the convergence target values or the case of reaching maximal number of the loops. Individual field solvers and displacements/loads are converged prior to beginning the following time step. FLUENT field loop doesn't require being converged each one of the stagger loops.

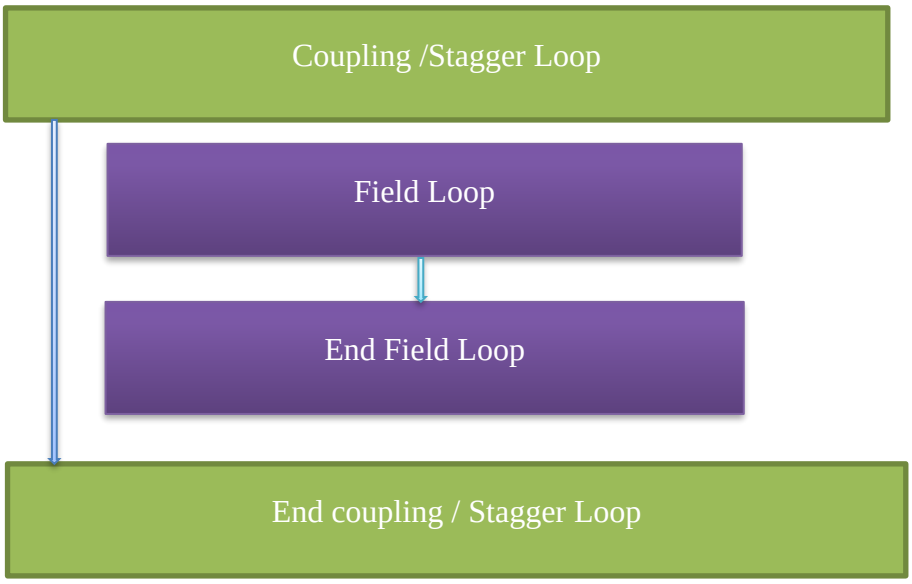

Figure 4.11. FSI `s iteration Loop.

4.4.4. Finite Element Method

The first step to solve the structures is to make a parameter from the fluent function, and it is a function of the setup, the parameter is the pressure that we extracted from the fluent, see Figure 4.12, The second step is to add the material , which is (Al 7075.T6), and the third step is to generate the Mesh, and then add the Fixed support side (root area), and the last step is to make a run and show the results.

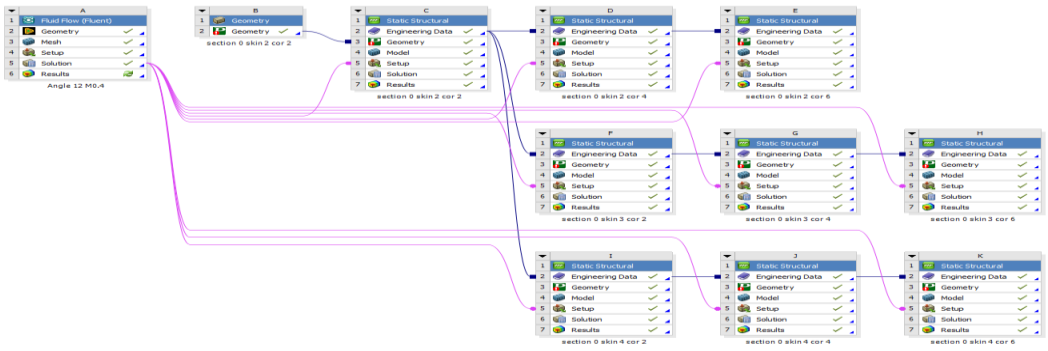

Figure 4.12. Processing of program solver

4.4.4.1. Mesh Generation

A mesh is defined as dividing the model's geometry into simple shapes of small units, by using tetrahedral meshing with finer sizing, the grid was generated. Because the large domain needs a lot of iterations to solve the many numbers of mesh cells, it gives approximately the same results for the selected domain. For the study of three.dimensional geometry, the number of nodes and elements has been chosen between 1849211 and 941171 (see Figure 4.14), and depending on the chosen mesh metric, the selection of the number of elements depends on the grid independence test (see Figure 4.13). The smallest cells are generated near the adjacent surface of the wing, and the larger cells are located near the boundary domain (see Figure 4.13).

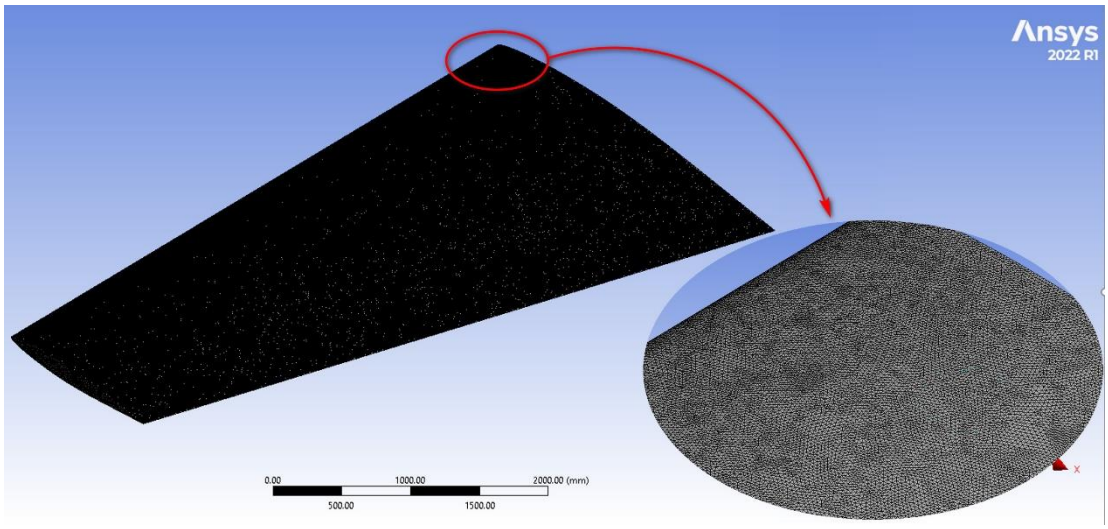

Figure 4.13. Mesh generation

Statistics	
Nodes	1849211
Elements	941171

Figure 4.14. Number of nodes and elements are used in mesh.

4.4.4.2. Numerical Algorithm

Using the FSI package follows the Fluid structure interaction is applied to obtain the deformation and stresses using the ANSYS FLUNT 2022 R1 computer package while followers the procedure presented in the flow chart shown in Figure 4.15.

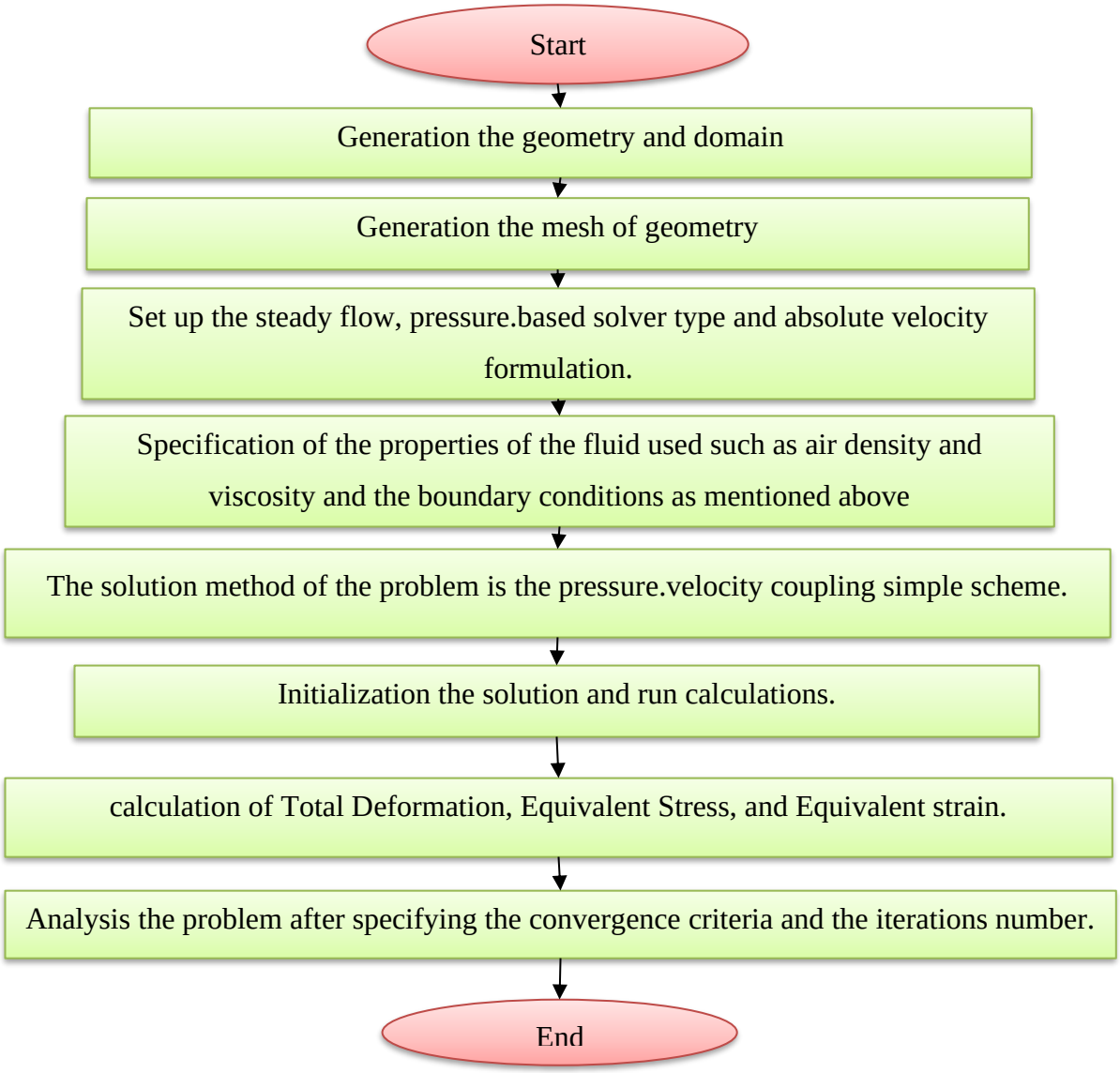

Figure 4.15. Flow chart Diagram of program solver

PART 5

RESULT AND DISCUSSION

In this chapter, the results are divided into two section, Aerodynamic to predict the pressure distribution and the structural analysis to find the displacement and stress levels.

5.1. AERODYNAMIC RESULTS

The cases to be investigated are shown in Figure 5.1.

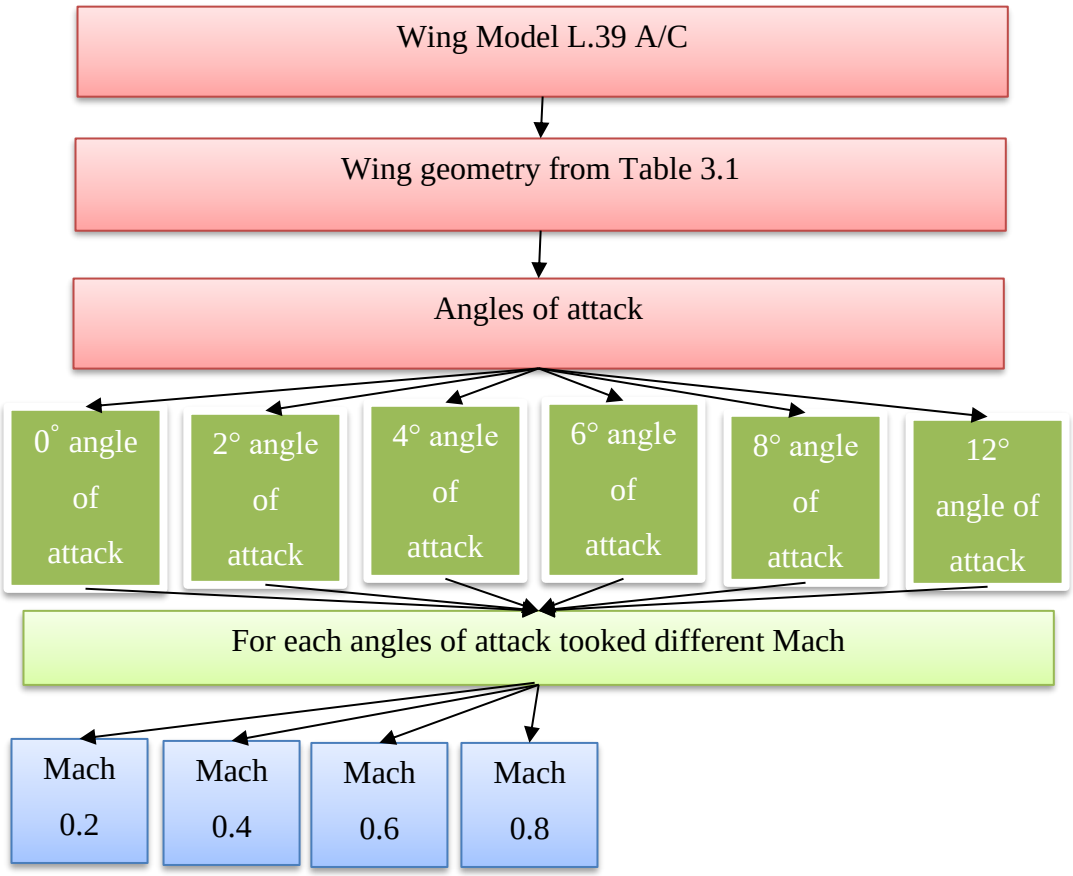

Figure 5.1.The flow chart of the suggested cases of the aerodynamic study

The program used was ANSYS FLUENT 2022R1 the computer package fluent was used to model the A/c wing using the airfoil NACA shown in Table 3.1 .

5.1.1. Flow Pattern at Different Mach Numbers

The variation of the pressure distribution in the chordwise direction for the upper and lower wing surfaces was obtained with a small difference while increasing the Mach number values. shows Figure 5.2 the pressure distribution on the wing at a constant angle of attack (0°) at Mach numbers (0.2and0.4) at different locations and Mid location. while showing Figure 5.4 (c) the pressure distribution on the upper surface of the wing at an angle of attack (2°) at Mach number (0.2) and showing the Mid location for the upper wing in Figure 5.4 (e) and Figure 5.4 (d) shows the pressure distribution for the lower surface at different location and showing the Mid location for the lower wing in Figure 5.4 (f) at the same angle of attack and at the same Mach numbers And so are the rest of the angles . In order to show the effect of changing the Mach numbers, at a certain constant angle of attack, in the behavior of the pressure distribution, another constant angle of attack (4°,6°,8°12°,) is considered, hence figure shows the variation in the Total pressure. Comparing the results from Figure 5.2 to **Hata! Başvuru kaynağı bulunamadı.**, it is clear that, fixing the angle of attack gives no change in pressure distribution, and there was a small variation in the Total pressure, when increasing the Mach number, this is due to; the flow has nearly a similar pattern in the upper and lower wing surfaces, which leads to a similar pressure distributions.

The variation of the pressure distribution in the chordwise direction for the upper and lower wing surfaces was obtained with a small difference during increasing the Mach number values. Figure 5.24shows the pressure distribution for the selected wing section at zero angle of attack, while shows Figure 5.25 (a) the pressure distribution on the upper surface of the wing at constant angle of attack (2°) at different Mach numbers (0.2,0.4,0.6 and 0.8).and Figure 5.25 (b) shows the pressure distribution for the lower surface at the same angle of attack and at the same Mach numbers taken in Figure 5.25 (a) And so are the rest of the angles . In order to show the effect of changing the Mach numbers, at a certain constant angles of attack, in the behavior of

the pressure distribution, another constant angle of attack (4°,6°,8°12°,) is considered, hence figure shows the variation in the Total pressure. Comparing the results from Figure 5.24 to Figure 5.29, it is clear that, fixing the angle of attack gives no change in pressure distribution, and there was a small variation in the Total pressure, when increasing the Mach number, this is due to; the flow has nearly a similar pattern in the upper and lower wing surfaces, which leads to a similar pressure distributions.

5.1.2. Spanwise Pressure Distribution

In order to have a complete idea about the pressure distribution in that direction. This is an essential result to be considered during the structural analysis since the load distribution is of great importance in these analyses, for example, Figure 5.35**Hata! Başvuru kaynağı bulunamadı.** (a) and Figure 5.35 (b) shows the pressure distributions for upper and lower surfaces in the spanwise direction for angles of attack equal (12) at different Mach numbers between (0.2 to 0.8) , the step of four Mach numbers for the selected wing configuration. It can be seen that the distribution of the pressure was non.uniform. Also, it was clear that increasing the angle of attack, increases the pressure value which reaches its maximum, at the lower surface, for the angle of attack (12°) at the mid.span of the leading edge, see Figure 5.35 (a).

5.1.3. At Angle 0°

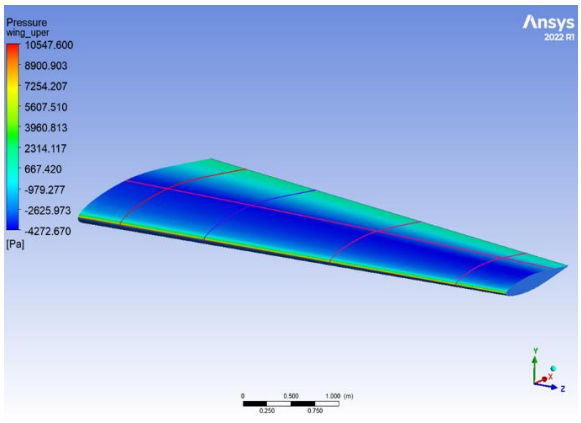

Figure(a).Contour (total pressure) at different locations for angle 0° at Mach 0.4

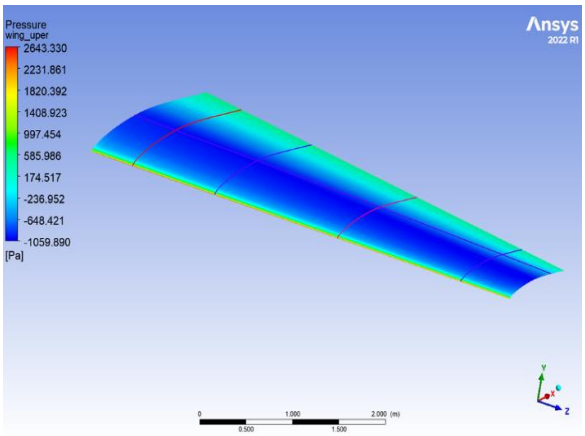

Figure (b).Contour (total pressure) at different locations for angle 0° at Mach 0.2

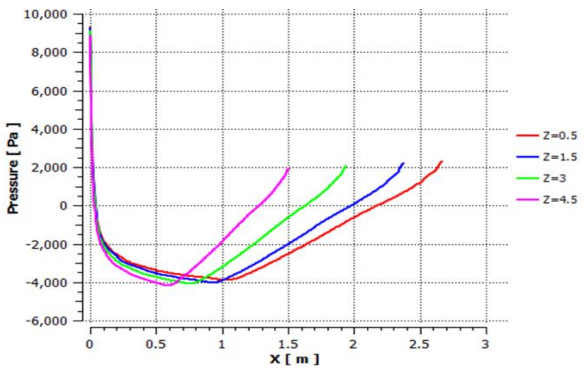

Figure (c). (total pressure) at different locations for angle 0° at Mach 0.4

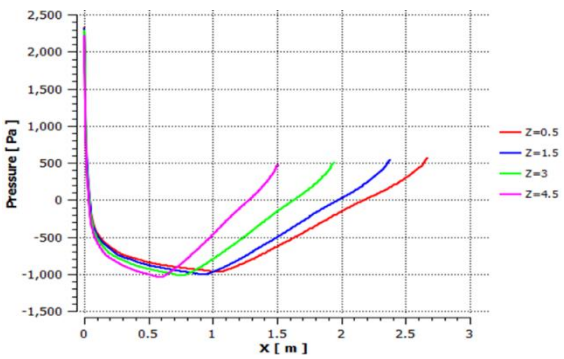

Figure (d). (total pressure) at different locations for angle 0° at Mach 0.2

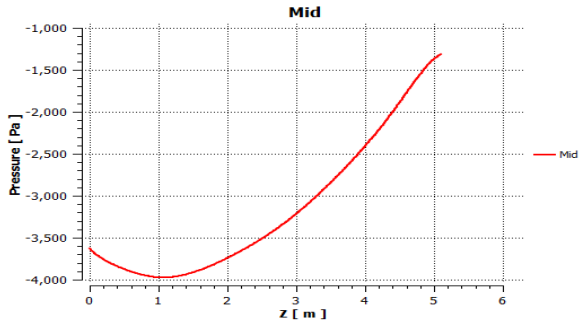

Figure (e). Spanwise (total pressure) at Middle locations for angle 0° at Mach 0.4

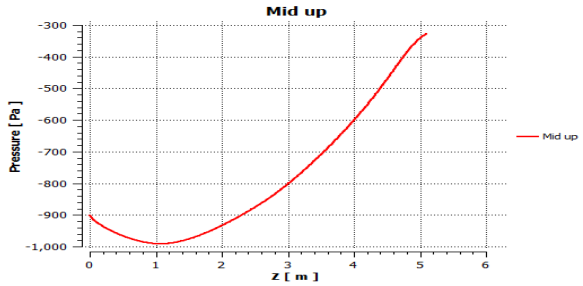

Figure (f). Spanwise (total pressure) at middle locations for angle 0° at Mach 0.2

Figure 5.2. Pressure distribution for angle of attack 0° at different Mach numbers for upper and lower surface

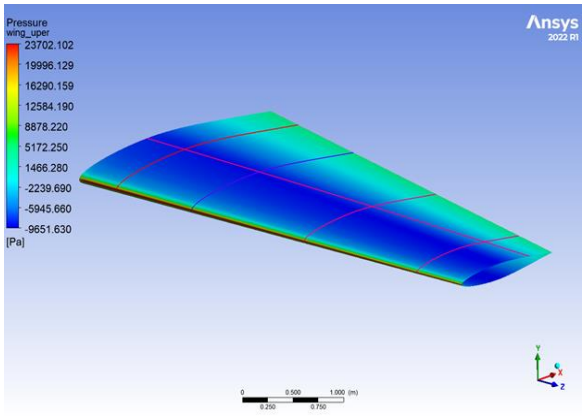

Figure (a). Contour (total pressure) at different locations for angle 0° at Mach 0.6

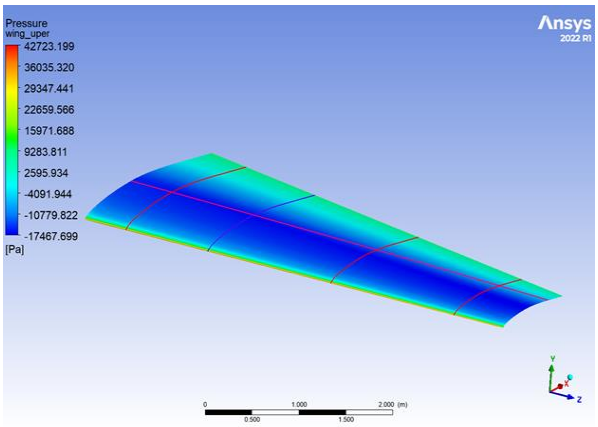

Figure (b). Contour (total pressure) at different locations for angle 0° at Mach 0.8

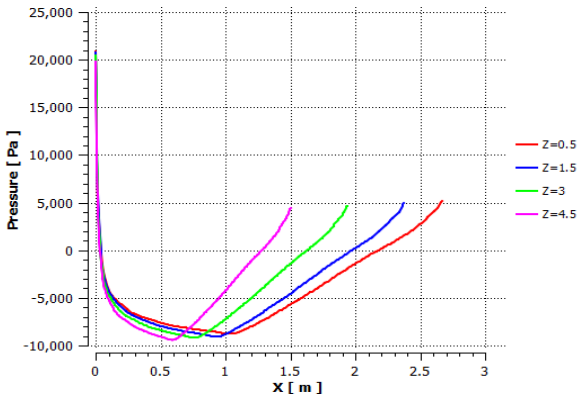

Figure (c). (total pressure) at different locations for angle 0° at Mach 0.6

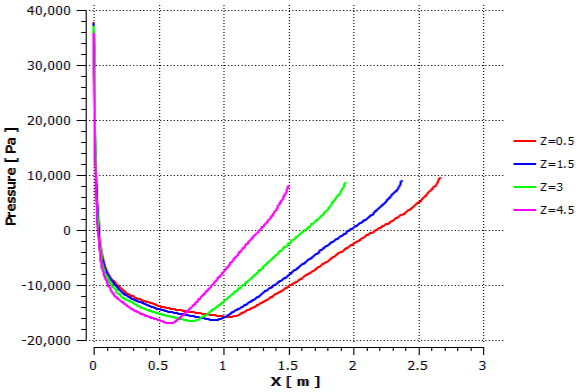

Figure(d). (total pressure) at different locations for angle 0° at Mach 0.8

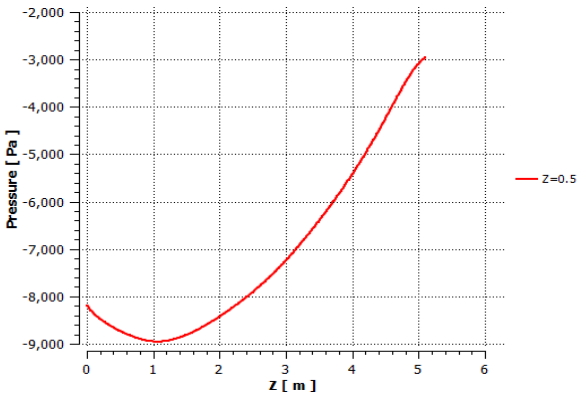

Figure (e). Spanwise (total pressure) at middle locations for angle 0° at Mach 0.6

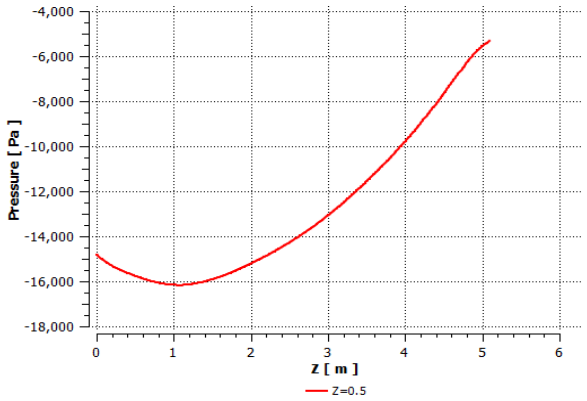

Figure (f). Spanwise (total pressure) at middle locations for angle 0° at Mach 0.8

Figure 5.3. Pressure distribution for angle of attack 0° at different Mach numbers for upper and lower surface

5.1.4. At Angle 2°

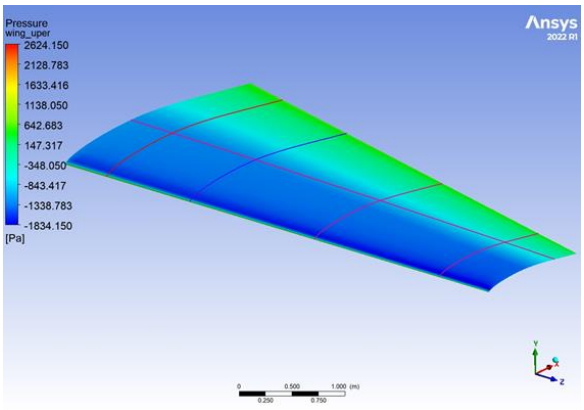

Figure (a). Contour (total pressure) at different locations for angle 2° at Mach 0.2 (Upper surface)

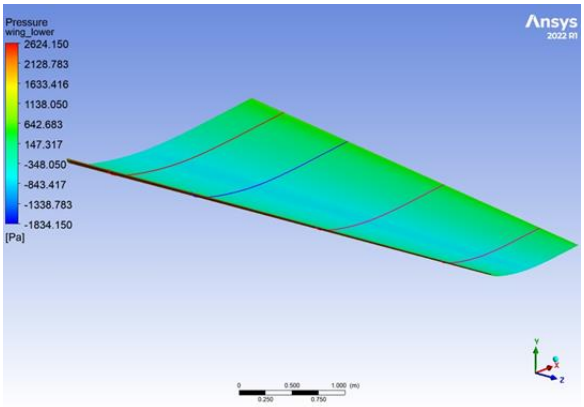

Figure (b). Contour (total pressure) at different locations for angle 2° at Mach 0.2 (Lower surface)

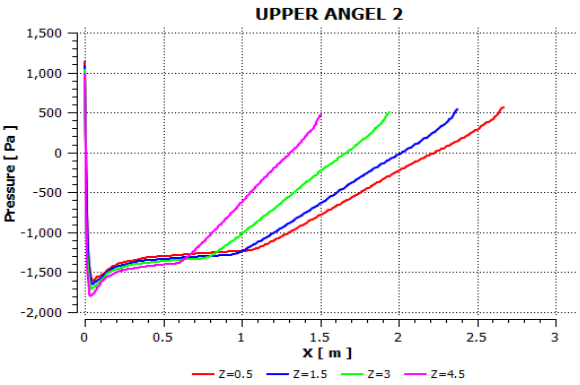

Figure (c). (total pressure) at different locations for angle 2° at Mach 0.2(Upper surface)

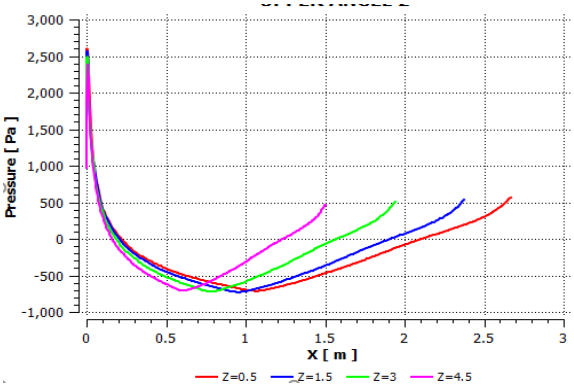

Figure(d). (total pressure) at different locations for angle 2° at Mach 0.2(Lower surface)

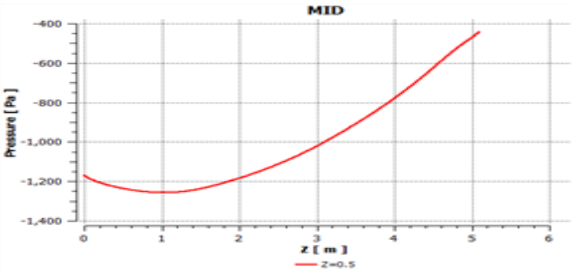

Figure(e). Spanwise (total pressure) at middle locations for angle 2° at Mach 0.2 (Upper surface)

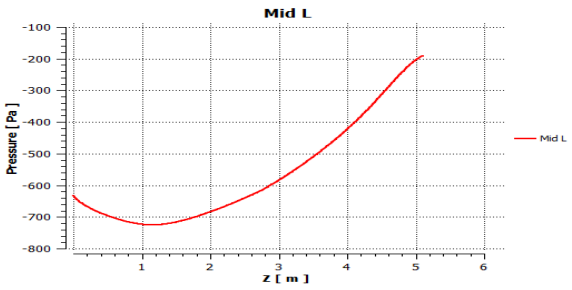

Figure(f). Spanwise (total pressure) at middle locations for angle 2° at Mach 0.2 (Lower surface)

Figure 5.4. Pressure distribution for angle of attack 2° at different Mach numbers for upper and lower surface

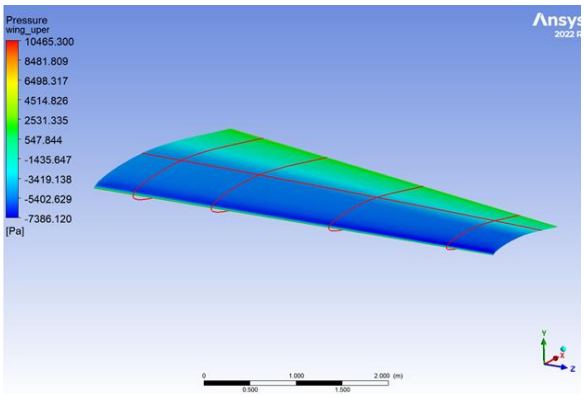

Figure (a). Contour (total pressure) at different locations for angle 2° at Mach 0.4 (upper surface)

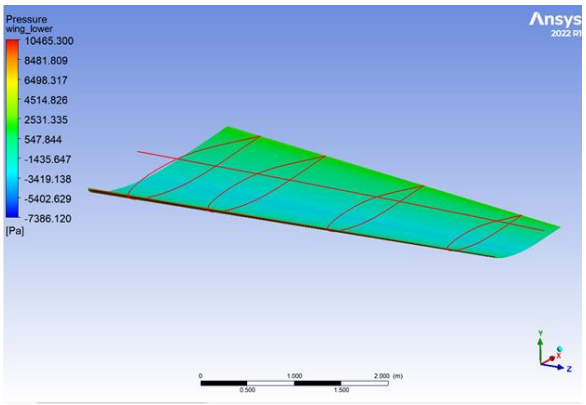

Figure (b). Contour (total pressure) at different locations for angle 2° at Mach 0.4 (Lower surface)

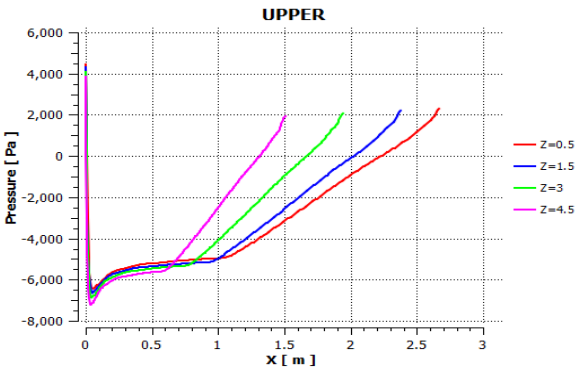

Figure (c). (total pressure) at different locations for angle 2° at Mach 0.4 (Upper surface)

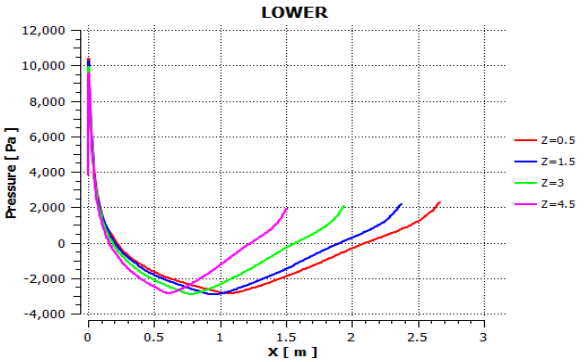

Figure (d). (total pressure) at different locations for angle 2° at Mach 0.4 (Lower surface)

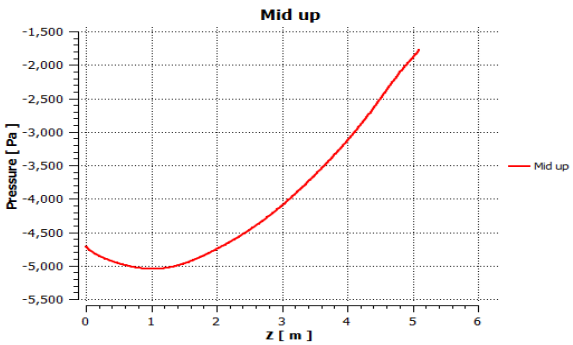

Figure (e). Spanwise (total pressure) at middle locations for angle 2° at Mach 0.4 (Upper surface)

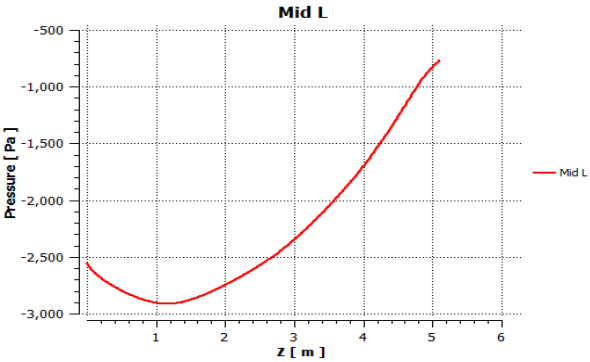

Figure (f). Spanwise (total pressure) at middle locations for angle 2° at Mach 0.4 (Lower surface)

Figure 5.5. Pressure distribution for angle of attack 2° at different Mach numbers for upper and lower surface

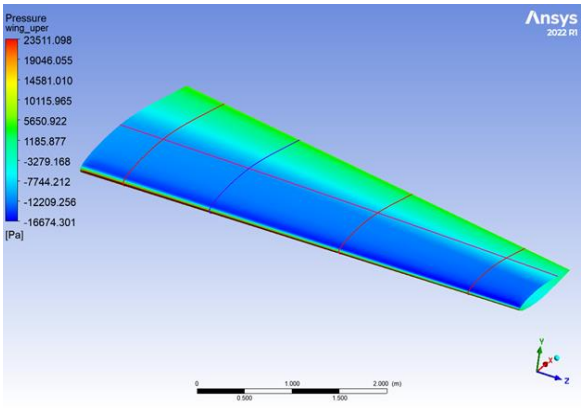

Figure (a). Contour (total pressure) at different locations for angle 2° at Mach 0.6 (Upper surface)

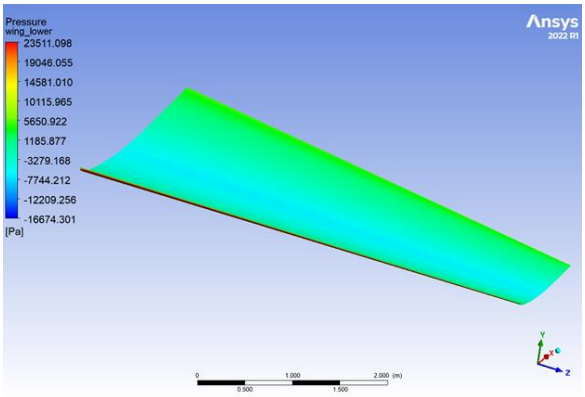

Figure (b). Contour (total pressure) at different locations for angle 2° at Mach 0.6 (Lower surface)

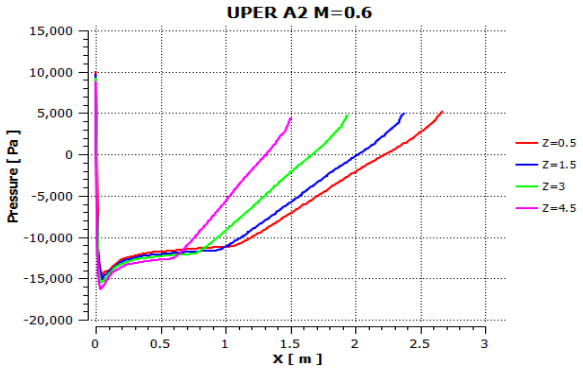

Figure (c). (total pressure) at different locations for angle 2° at Mach 0.6 (Upper surface)

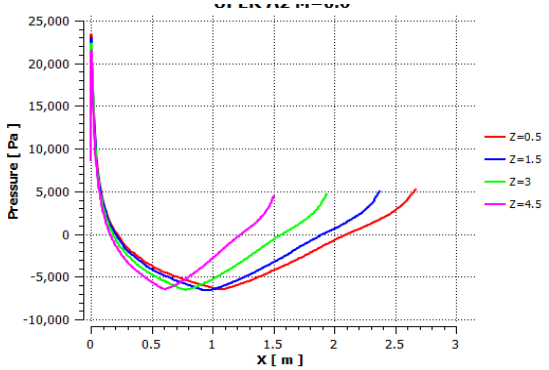

Figure(d). (total pressure) at different locations for angle 2° at Mach 0.6 (Lower surface)

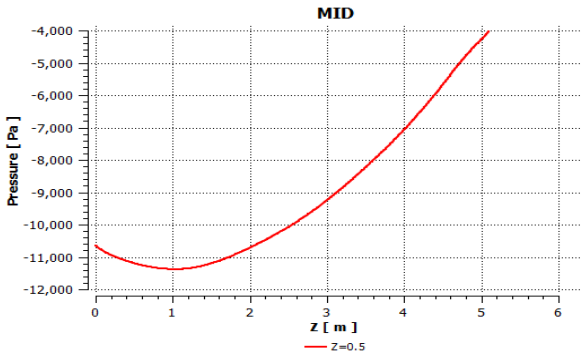

Figure (e). Spanwise (total pressure) at middle locations for angle 2° at Mach 0.6 (Upper surface)

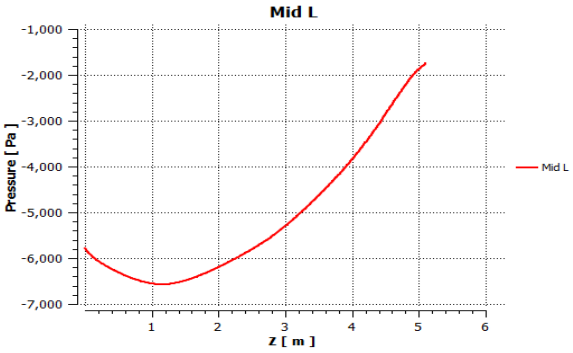

Figure (f). Spanwise (total pressure) at middle locations for angle 2° at Mach 0.6 (Lower surface)

Figure 5.6. Pressure distribution for angle of attack 2° at different Mach numbers for upper and lower surface

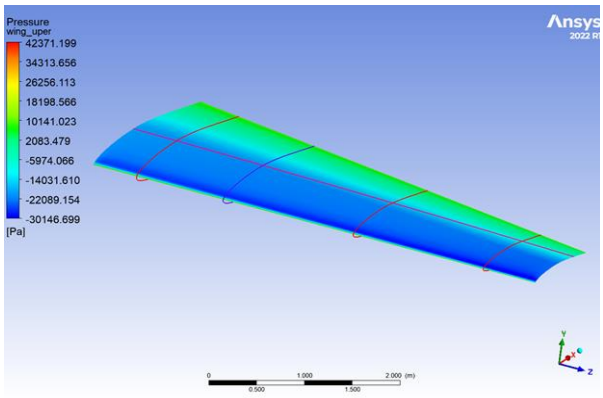

Figure (a). Contour (total pressure) at different locations for angle 2° at Mach 0.8 (Upper surface)

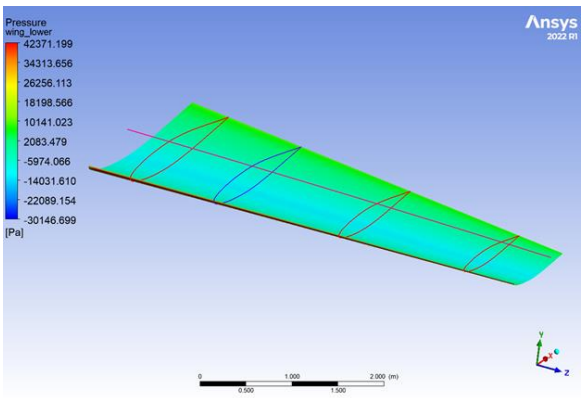

Figure (b). Contour (total pressure) at different locations for angle 2° at Mach 0.8 (Lower surface)

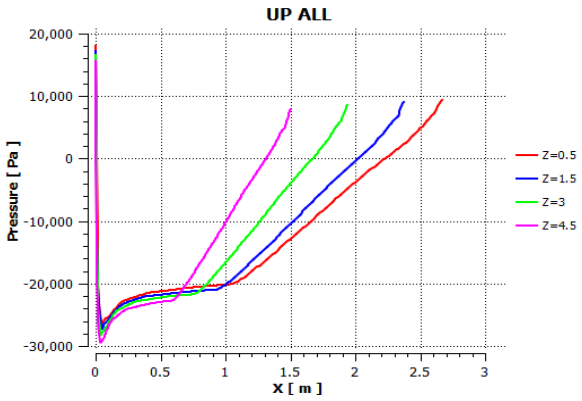

Figure (c). (total pressure) at different locations for angle 2° at Mach 0.8 (Upper surface)

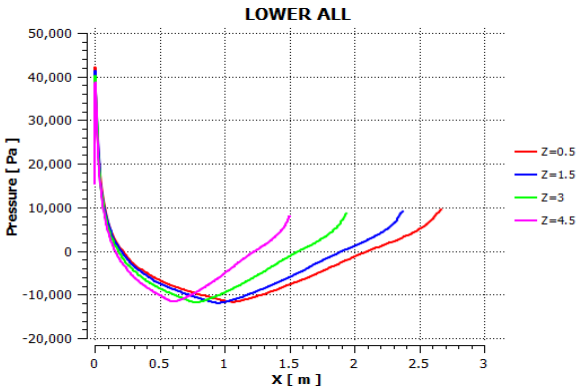

Figure (d). (total pressure) at different locations for angle 2° at Mach 0.8 (Lower surface)

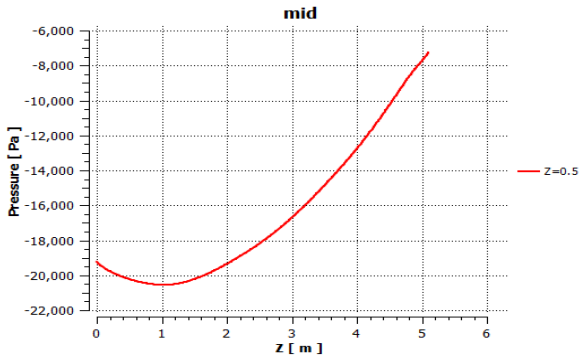

Figure(e). Spanwise (total pressure) at middle locations for angle 2° at Mach 0.8 (Upper surface)

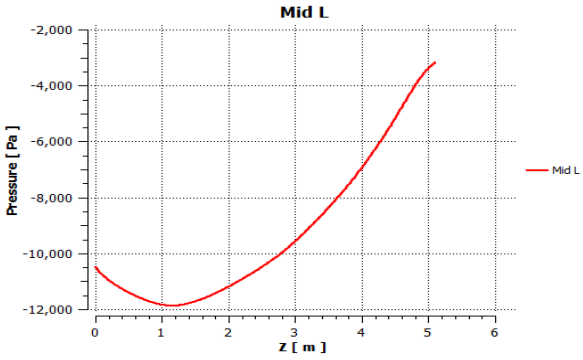

Figure (f). Spanwise (total pressure) at middle locations for angle 2° at Mach 0.8 (Lower surface)

Figure 5.7. Pressure distribution for angle of attack 2° at different Mach numbers for upper and lower surface

5.1.5. At Angle 4°

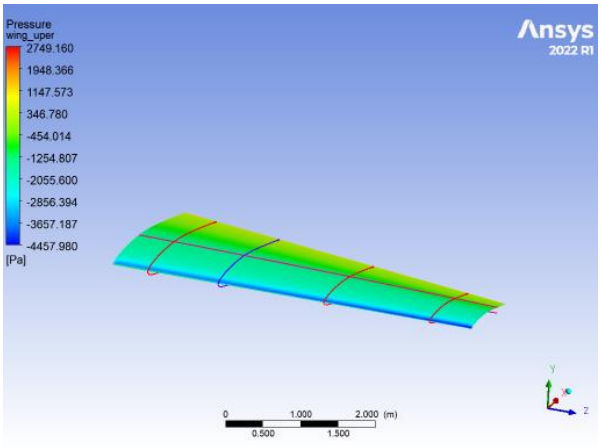

Figure (a). Contour (total pressure) at different locations for angle 4° at Mach 0.2 (Upper surface)

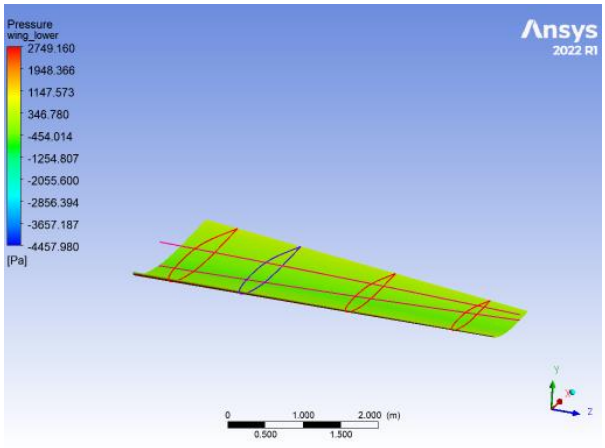

Figure (b). Contour (total pressure) at different locations for angle 4° at Mach 0.2 (Lower surface)

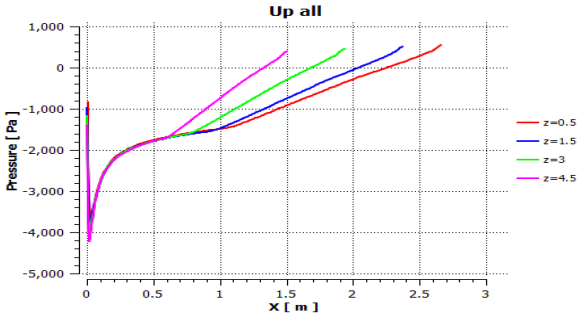

Figure (c). (total pressure) at different locations for angle 4° at Mach 0.8 (Upper surface)

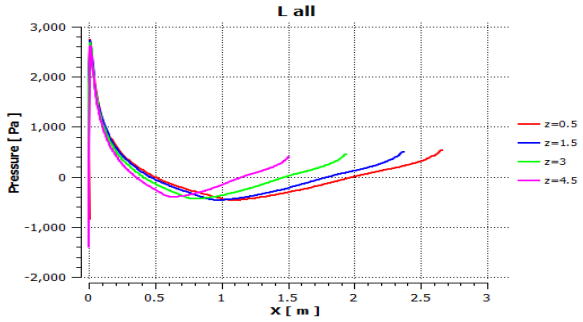

Figure (d). (total pressure) at different locations for angle 4° at Mach 0.2 (Lower surface)

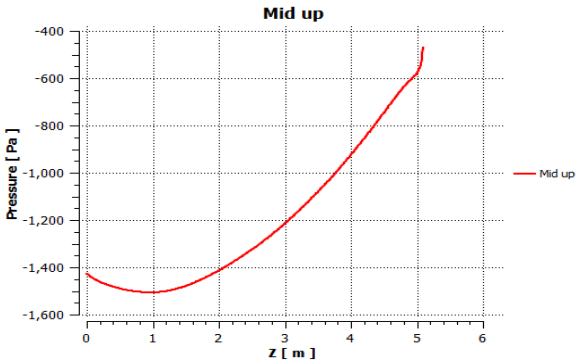

Figure (e). Spanwise (total pressure) at middle locations for angle 4° at Mach 0.2 (Upper surface)

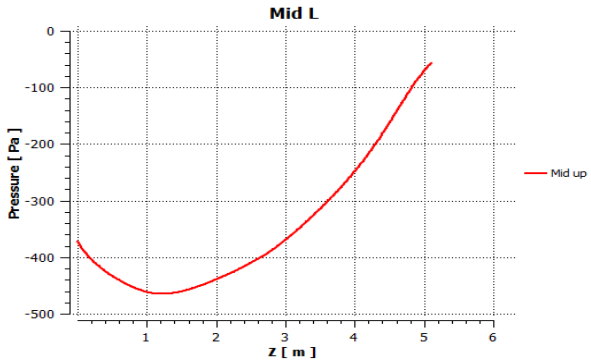

Figure (f). Spanwise (total pressure) at middle locations for angle 4° at Mach 0.2 (Lower surface)

Figure 5.8. Pressure distribution for angle of attack 4° at different Mach numbers for upper and lower surface

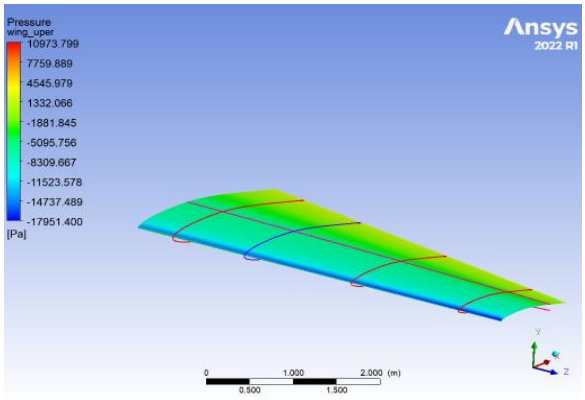

Figure (a). Contour (total pressure) at different locations for angle 4° at Mach 0.4 (Upper surface)

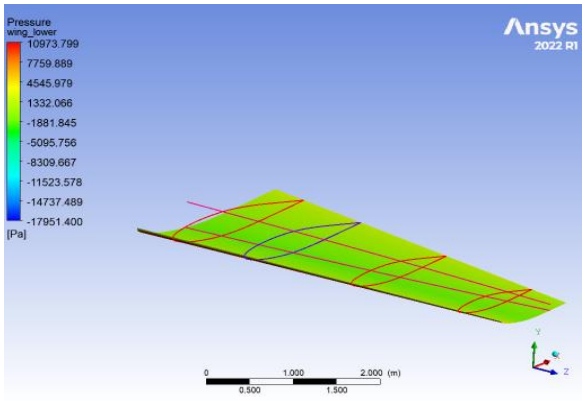

Figure (b). Contour (total pressure) at different locations for angle 4° at Mach 0.4 (Lower surface)

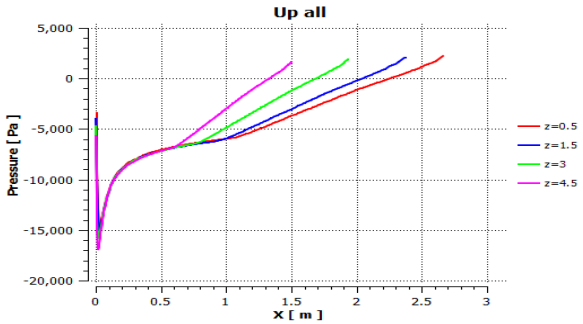

Figure (c). (total pressure) at different locations for angle 4° at Mach 0.4 (Upper surface)

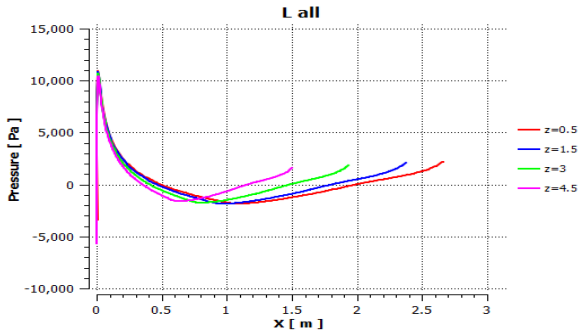

Figure (d). (total pressure) at different locations for angle 4° at Mach 0.4 (Lower surface)

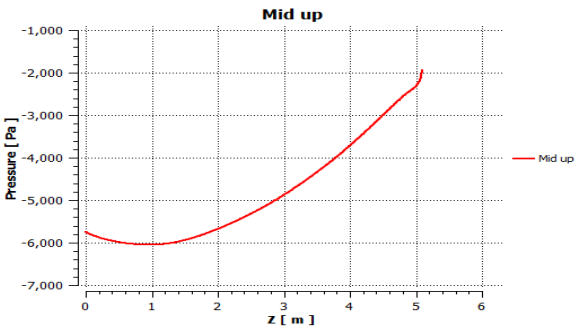

Figure (e). Spanwise (total pressure) at middle locations for angle 4° at Mach 0.4 (Upper surface)

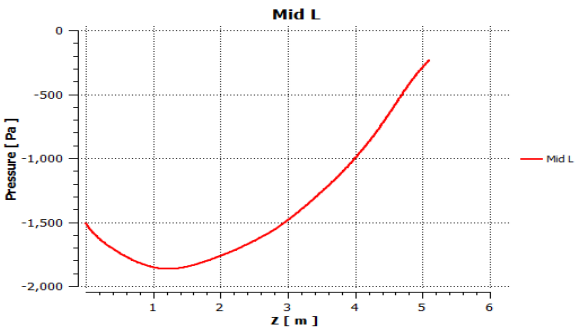

Figure (f). Spanwise (total pressure) at middle locations for angle 4° at Mach 0.4 (Lower surface)

Figure 5.9. Pressure distribution for angle of attack 4° at different Mach numbers for upper and lower surface

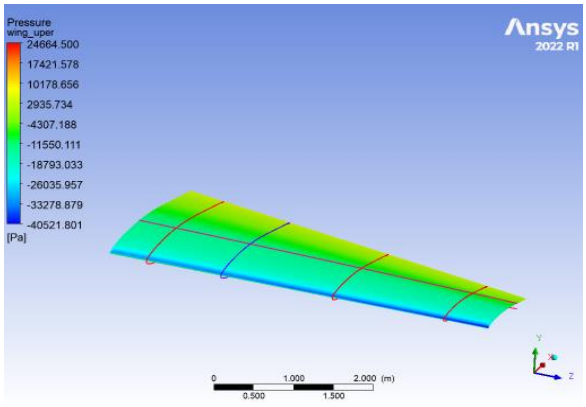

Figure (a). Contour (total pressure) at different locations for angle 4° at Mach 0.6 (Upper surface)

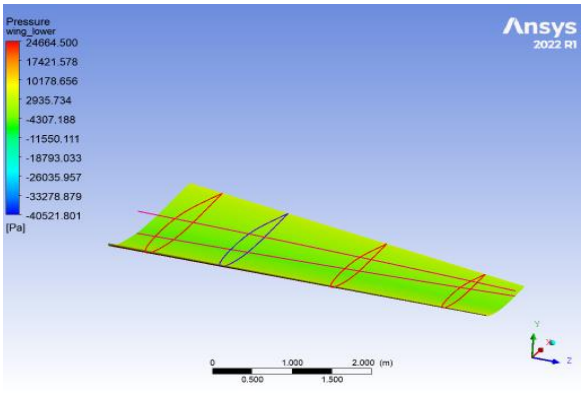

Figure (b). Contour (total pressure) at different locations for angle 4° at Mach 0.6 (Lower surface)

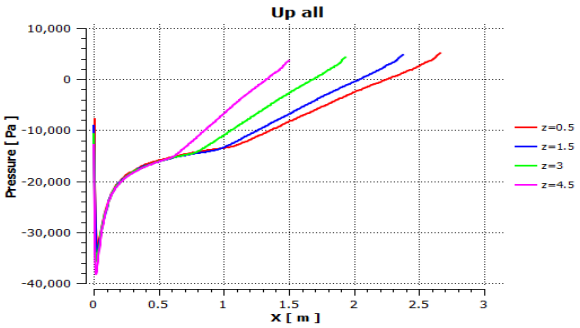

Figure (c). (total pressure) at different locations for angle 4° at Mach 0.6 (Upper surface)

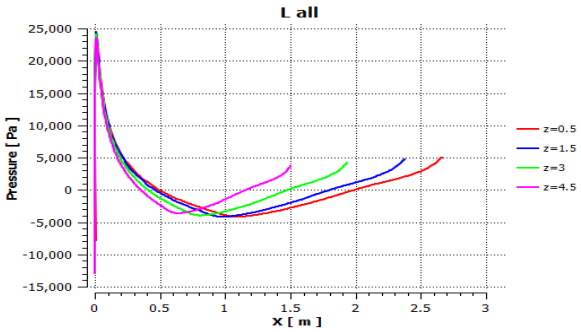

Figure (d). (total pressure) at different locations for angle 4° at Mach 0.6 (Lower surface)

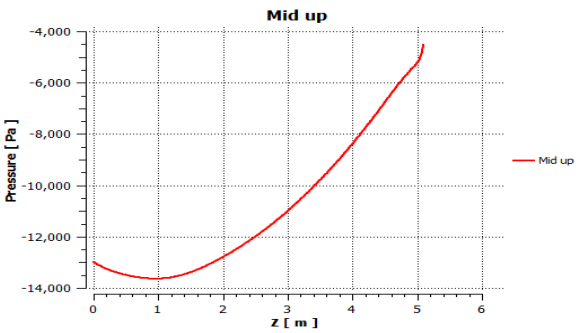

Figure (e). Spanwise (total pressure) at middle locations for angle 4° at Mach 0.6 (Upper surface)

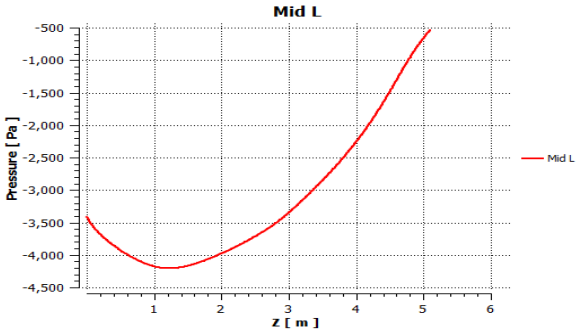

Figure (f). Spanwise (total pressure) at middle locations for angle 4° at Mach 0.6 (Lower surface)

Figure 5.10. Pressure distribution for angle of attack 4° at different Mach numbers for upper and lower surface

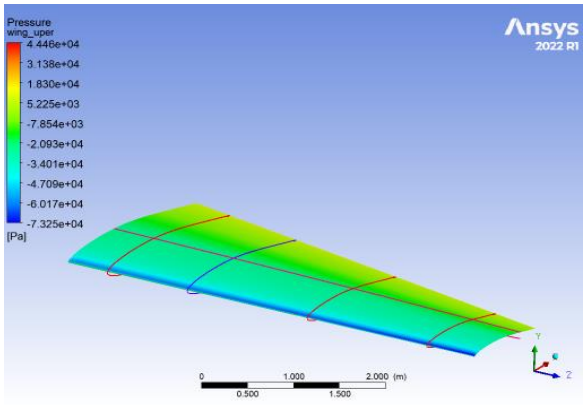

Figure (a). Contour (total pressure) at different locations for angle 4° at Mach 0.8 (Upper surface)

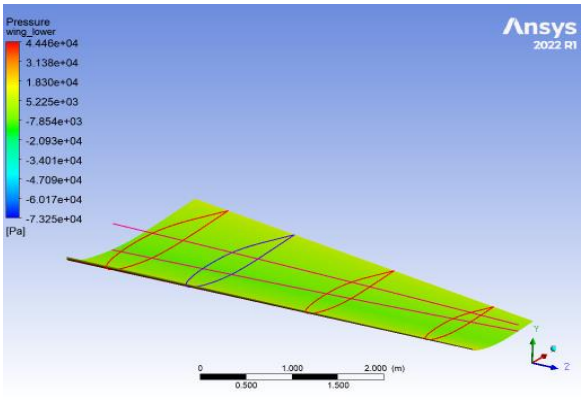

Figure (b). Contour (total pressure) at different locations for angle 4° at Mach 0.8 (Lower surface)

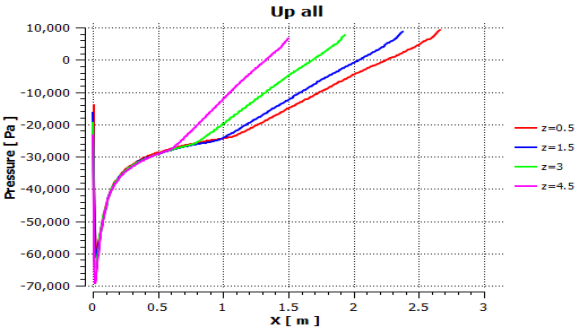

Figure (c). (total pressure) at different locations for angle 4° at Mach 0.8 (Upper surface)

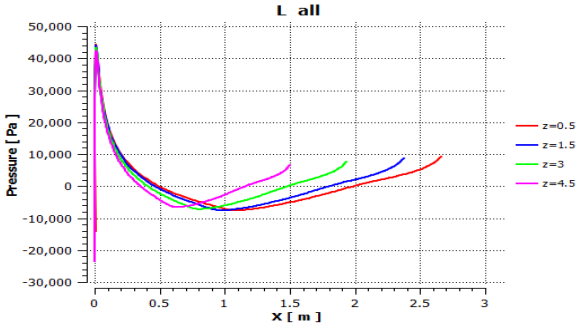

Figure (d). (total pressure) at different locations for angle 4° at Mach 0.8 (Lower surface)

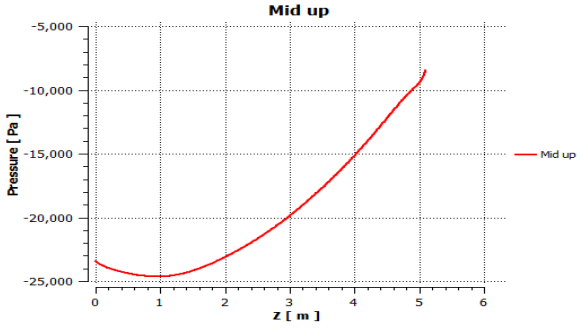

Figure(e). Spanwise (total pressure) at middle locations for angle 4° at Mach 0.8 (Upper surface)

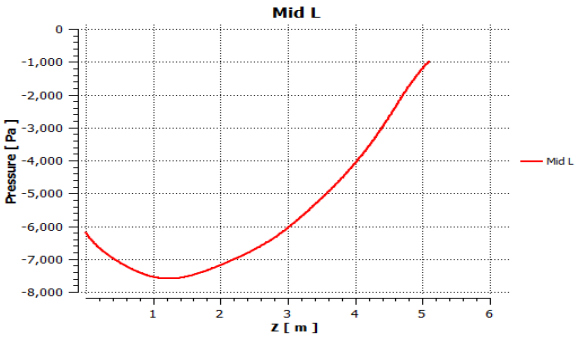

Figure (f). Spanwise (total pressure) at middle locations for angle 4° at Mach 0.8 (Lower surface)

Figure 5.11. Pressure distribution for angle of attack 4° at different Mach numbers for upper and lower surface

5.1.6. At Angle 6°

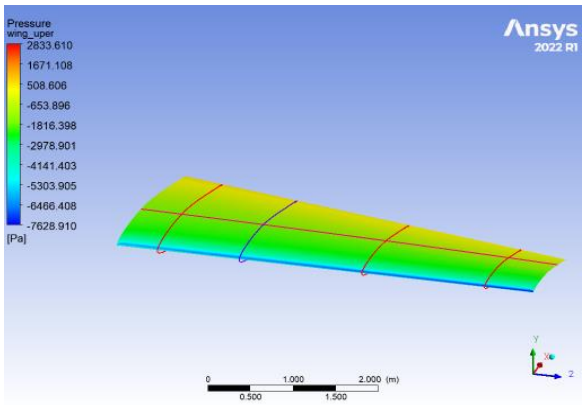

Figure (a). Contour (total pressure) at different locations for angle 6° at Mach 0.2 (Upper surface)

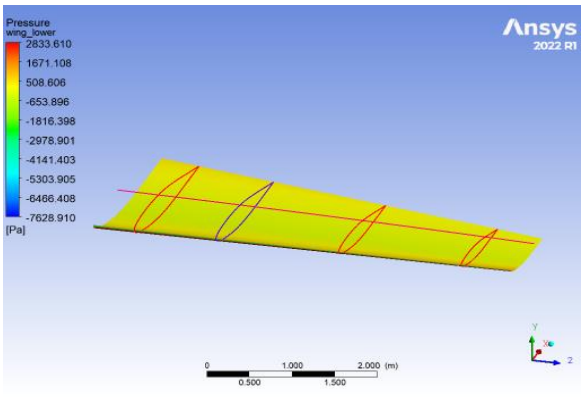

Figure (b). Contour (total pressure) at different locations for angle 6° at Mach 0.2 (Lower surface)

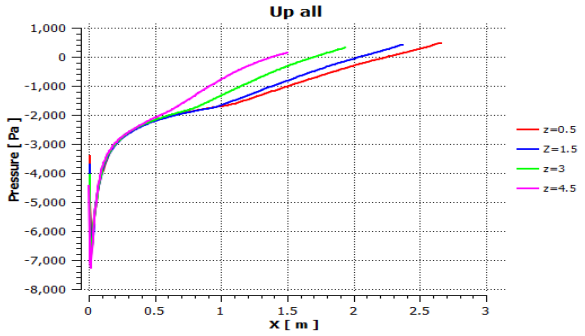

Figure (c). (total pressure) at different locations for angle 6° at Mach 0.2 (Upper surface)

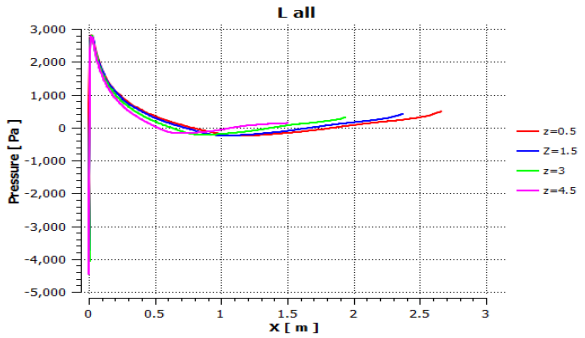

Figure (d). (total pressure) at different locations for angle 6° at Mach 0.2 (Lower surface)

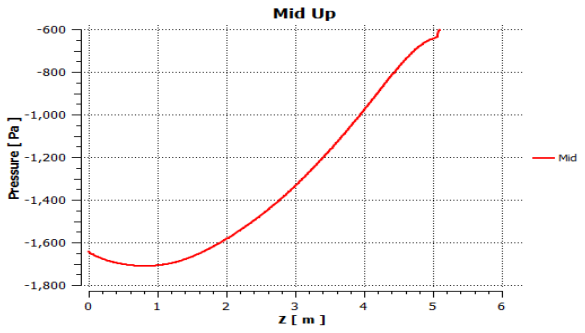

Figure (e). Spanwise (total pressure) at middle locations for angle 6° at Mach 0.2 (Upper surface)

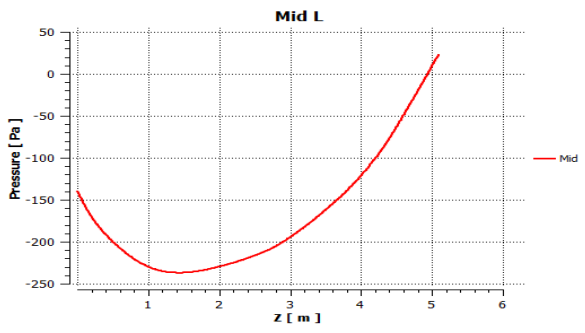

Figure (f). Spanwise (total pressure) at middle locations for angle 6° at Mach 0.2 (Lower surface)

Figure 5.12. Pressure distribution for angle of attack 6° at different Mach numbers for upper and lower surface

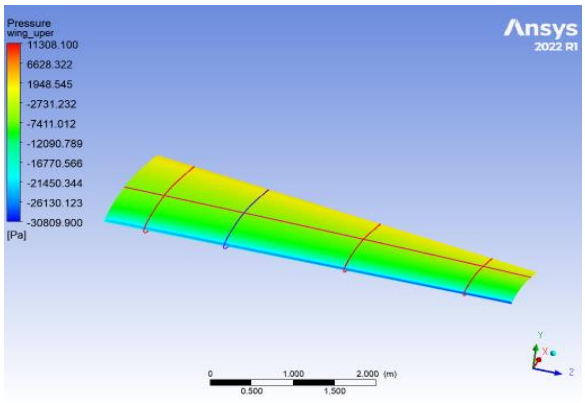

Figure (a). Contour (total pressure) at different locations for angle 6° at Mach 0.4 (Upper surface)

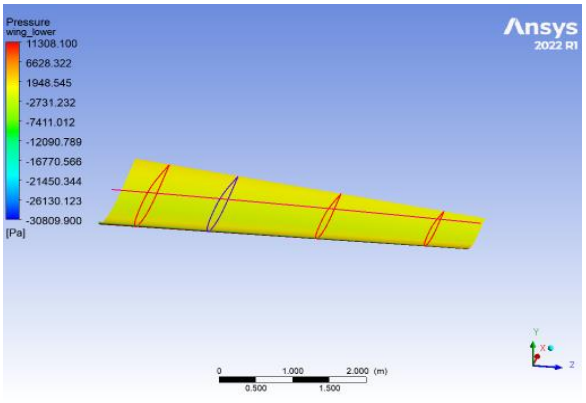

Figure (b). Contour (total pressure) at different locations for angle 6° at Mach 0.4 (Lower surface)

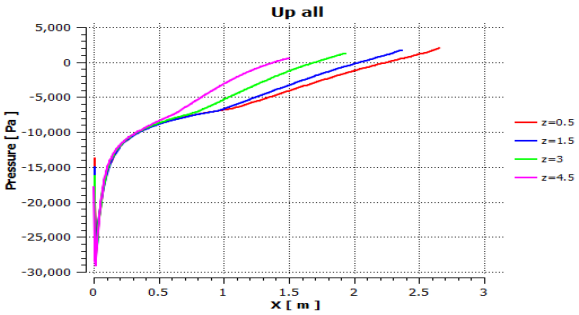

Figure (c). (total pressure) at different locations for angle 6° at Mach 0.4 (Upper surface)

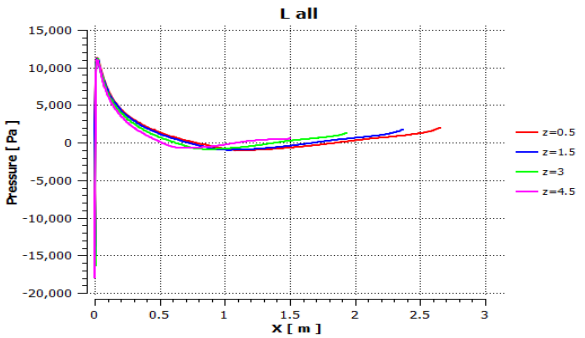

Figure (d). (total pressure) at different locations for angle 6° at Mach 0.4 (Lower surface)

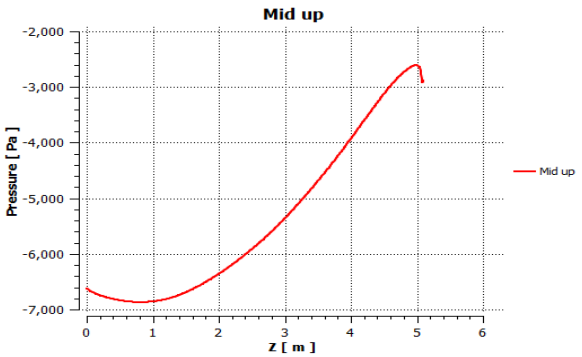

Figure (e) Spanwise (total pressure) at middle locations for angle 6°at Mach 0.4 (Upper surface)

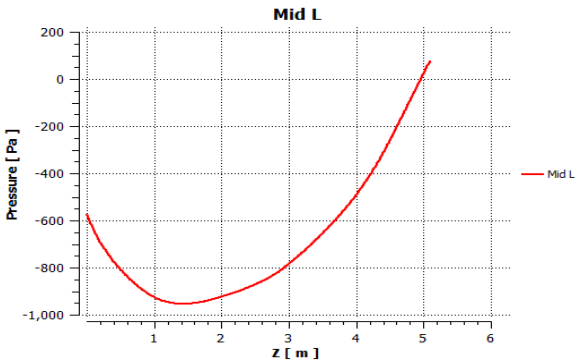

Figure (f). Spanwise (total pressure) at middle locations for angle 6° at Mach 0.4 (Lower surface)

Figure 5.13. Pressure distribution for angle of attack 6° at different Mach numbers for upper and lower surface

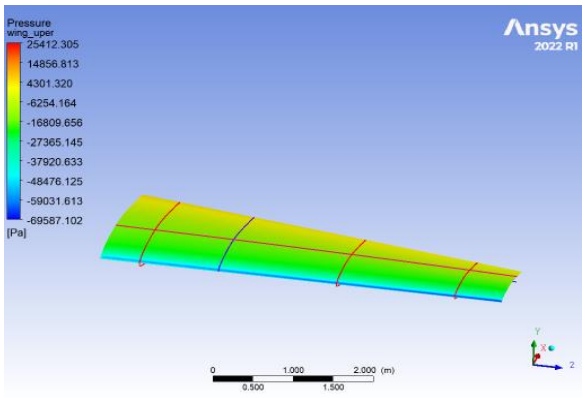

Figure (a). Contour (total pressure) at different locations for angle 6° at Mach 0.6 (Upper surface)

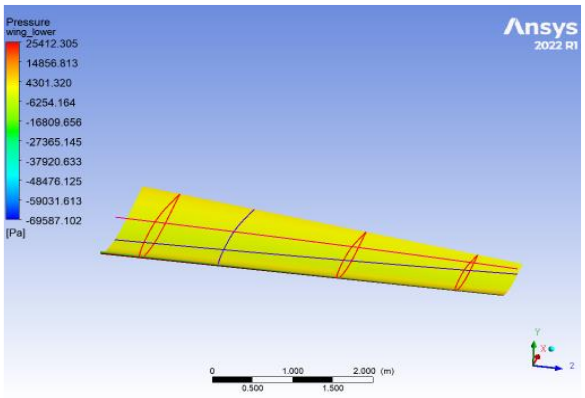

Figure (b). Contour (total pressure) at different locations for angle 6° at Mach 0.6 (Lower surface)

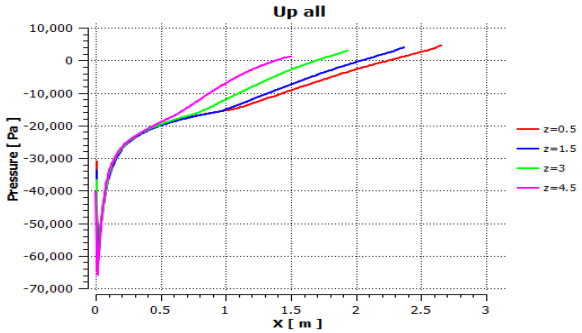

Figure (c). (total pressure) at different locations for angle 6° at Mach 0.6 (Upper surface)

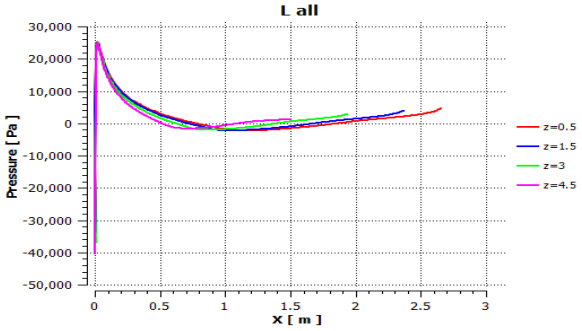

Figure (d). (total pressure) at different locations for angle 6° at Mach 0.6 (Lower surface)

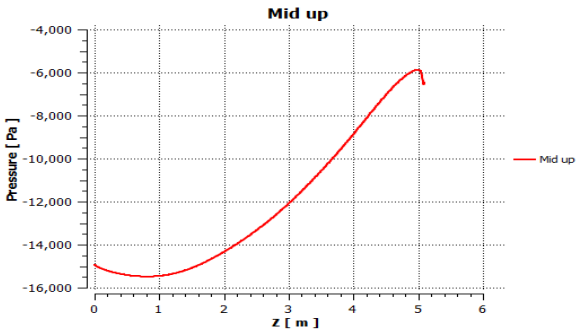

Figure (e). Spanwise (total pressure) at middle locations for angle 6° at Mach 0.6 (Upper surface)

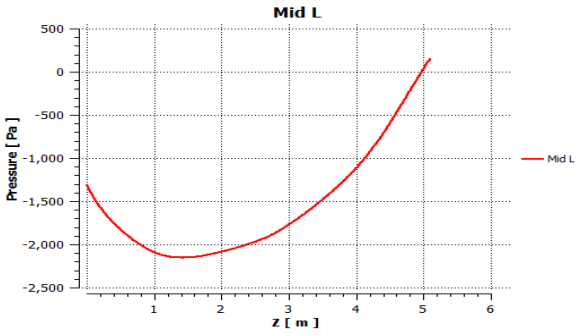

Figure (f). Spanwise (total pressure) at middle locations for angle 6° at Mach 0.6 (Lower surface)

Figure 5.14. Pressure distribution for angle of attack 6° at different Mach numbers for upper and lower surface

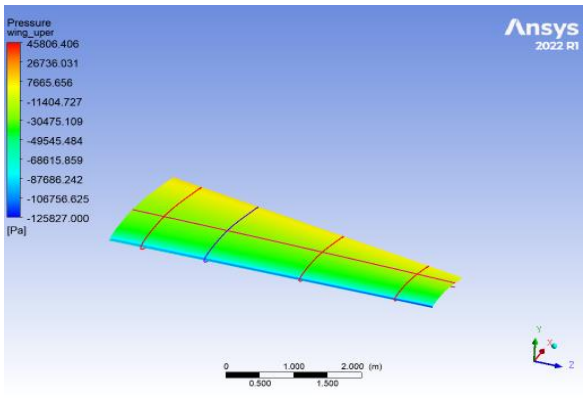

Figure (a). Contour (total pressure) at different locations for angle 6° at Mach 0.8 (Upper surface)

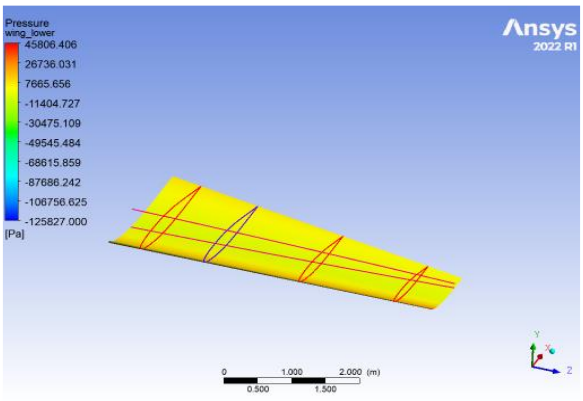

Figure (b). Contour (total pressure) at different locations for angle 6° at Mach 0.8 (Lower surface)

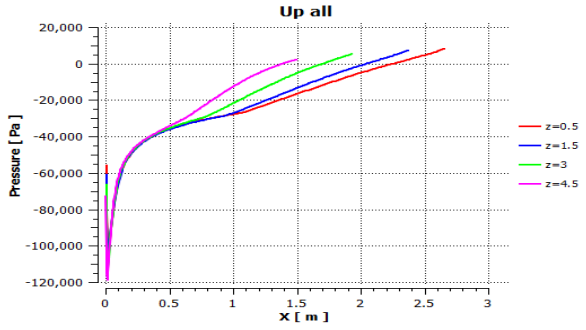

Figure (c). (total pressure) at different locations for angle 6° at Mach 0.8 (Upper surface)

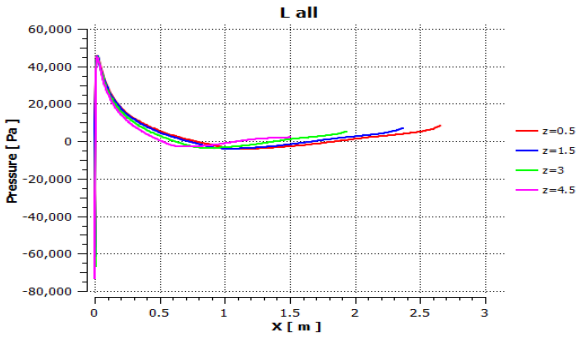

Figure (d). (total pressure) at different locations for angle 6°at Mach 0.8 (Lower surface)

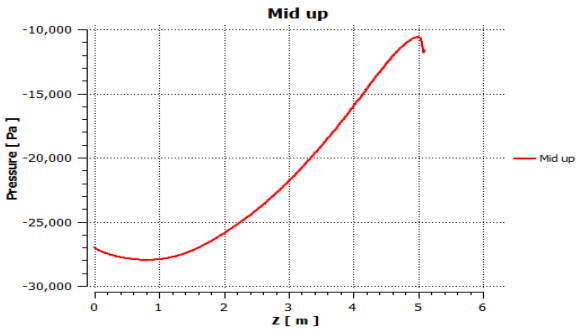

Figure (e). Spanwise (total pressure) at middle locations for angle 6° at Mach 0.8 (Lower surface)

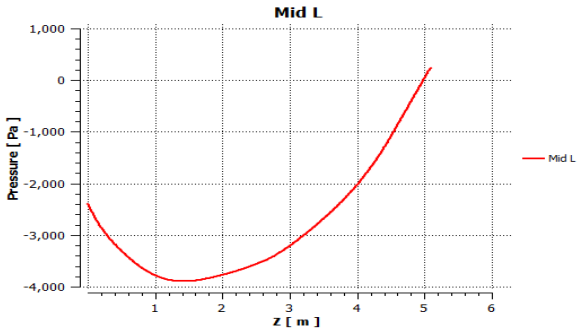

Figure (f). Spanwise (total pressure) at middle locations for angle 6° at Mach 0.8 (Lower surface)

Figure 5.15. Pressure distribution for angle of attack 6° at different Mach numbers for upper and lower surface

5.1.7. At Angle 8°

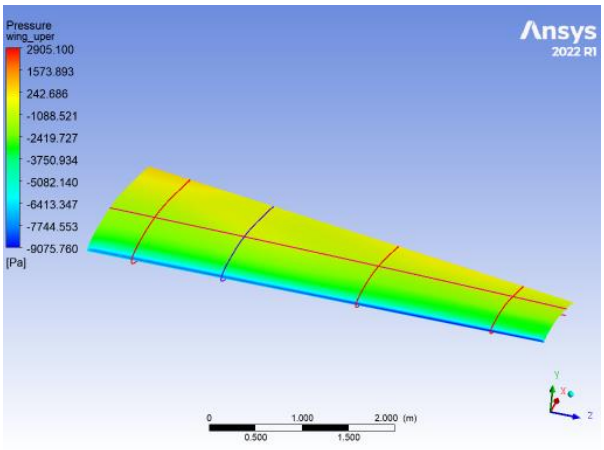

Figure (a). Contour (total pressure) at different locations for angle 8° at Mach 0.2 (Upper surface)

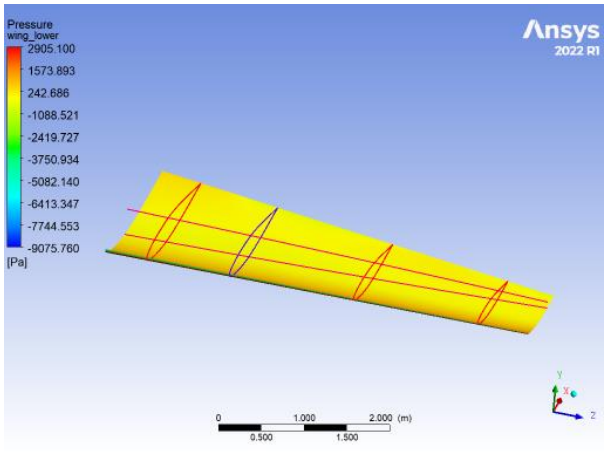

Figure (b). Contour (total pressure) at different locations for angle 8° at Mach 0.2 (Lower surface)

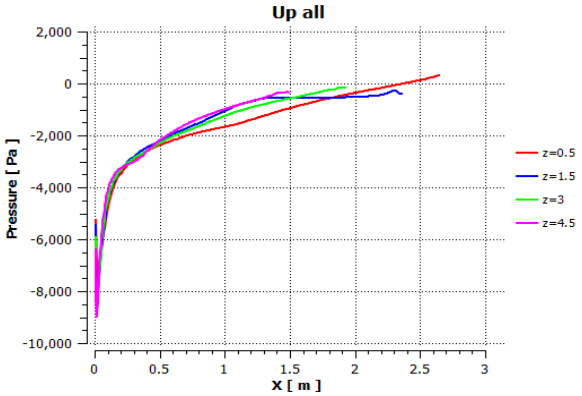

Figure (c). (total pressure) at different locations for angle 8° at Mach 0.2 (Upper surface)

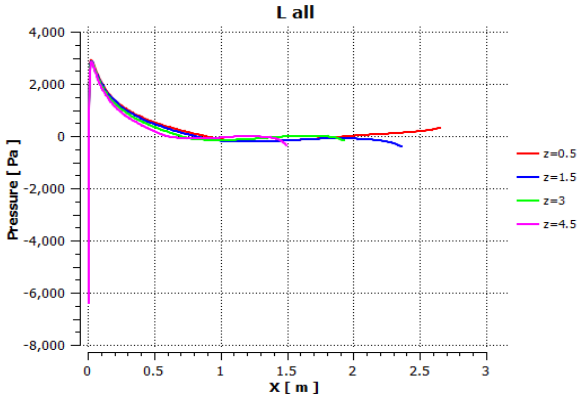

Figure (d). (total pressure) at different locations for angle 8° at Mach 0.2 (Lower surface)

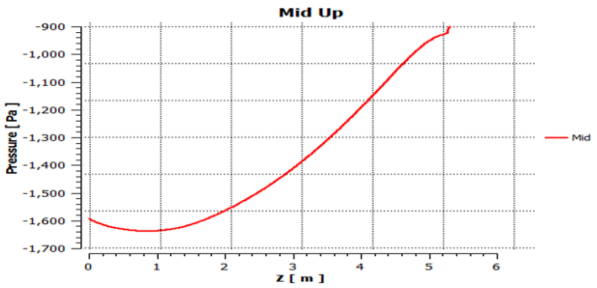

Figure (e). Spanwise (total pressure) at middle locations for angle 8° at Mach 0.2 (Upper surface)

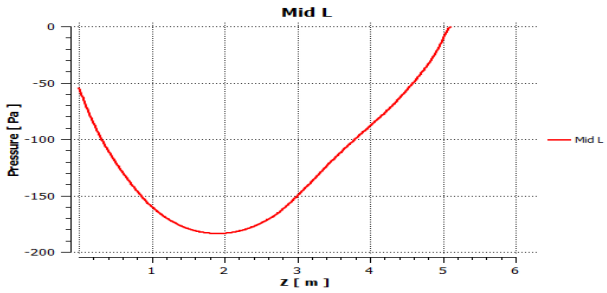

Figure (f). Spanwise (total pressure) at middle locations for angle 8° at Mach 0.2 (Lower surface)

Figure 5.16. Pressure distribution for angle of attack 8° at different Mach numbers for upper and lower surface

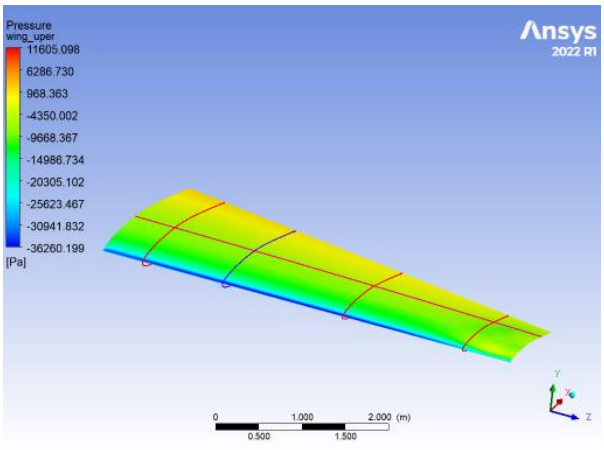

Figure (a). Contour (total pressure) at different locations for angle 8° at Mach 0.4 (Upper surface)

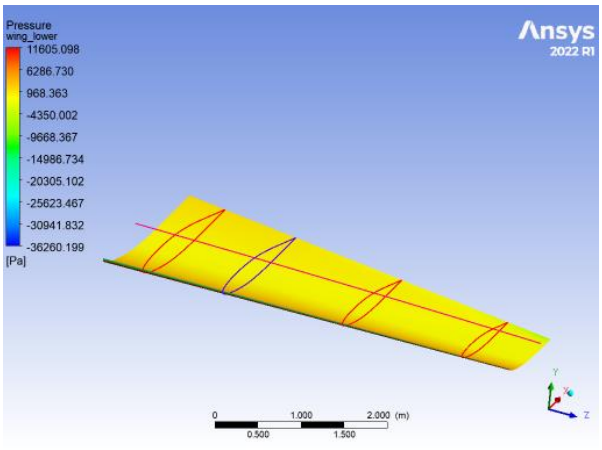

Figure (b). Contour (total pressure) at different locations for angle 8° at Mach 0.4 (Lower surface)

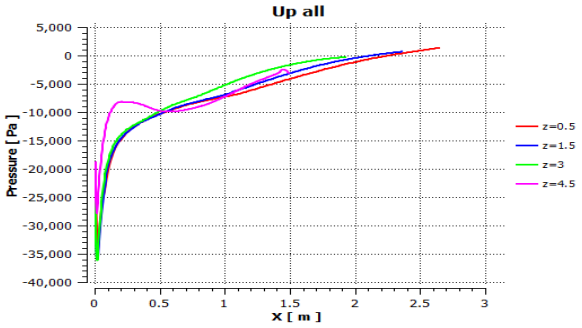

Figure (c). (total pressure) at different locations for angle 8° at Mach 0.4 (Upper surface)

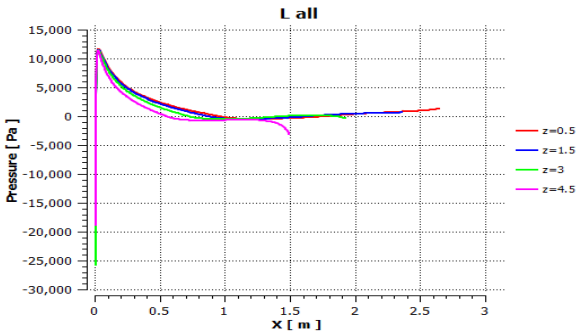

Figure (d). (total pressure) at different locations for angle 8° at Mach 0.4 (Lower surface)

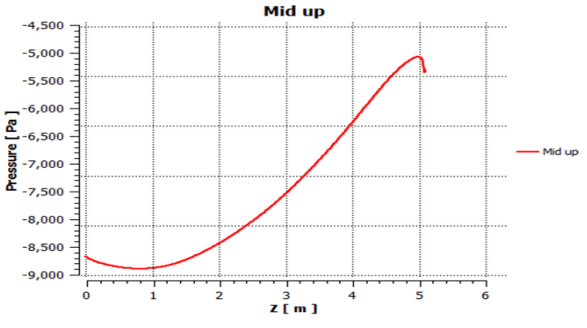

Figure (e). Spanwise (total pressure) at middle locations for angle 8° at Mach 0.4 (Lower surface)

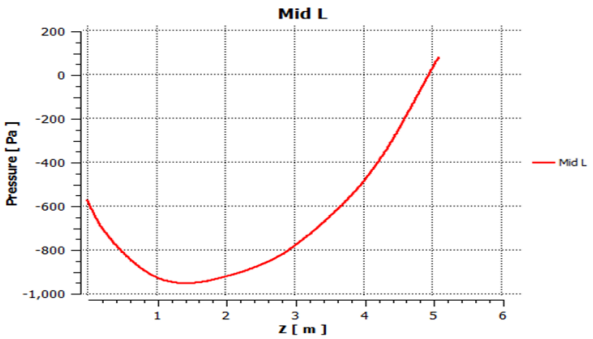

Figure (f). Spanwise (total pressure) at middle locations for angle 8° at Mach 0.4 (Upper surface)

Figure 5.17. Pressure distribution for angle of attack 8° at different Mach numbers for upper and lower surface

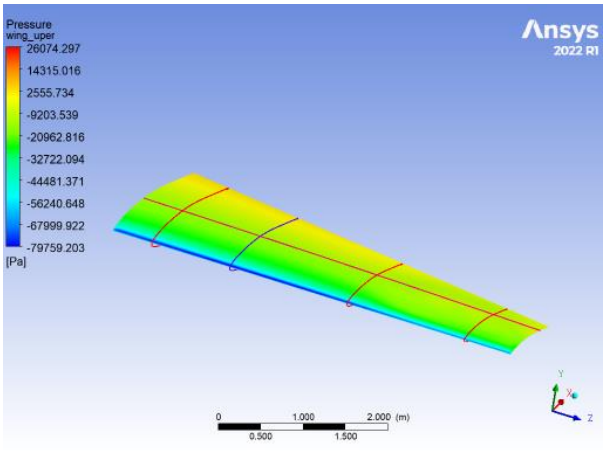

Figure (a). Contour (total pressure) at different locations for angle 8 ° at Mach 0.6 (Upper surface)

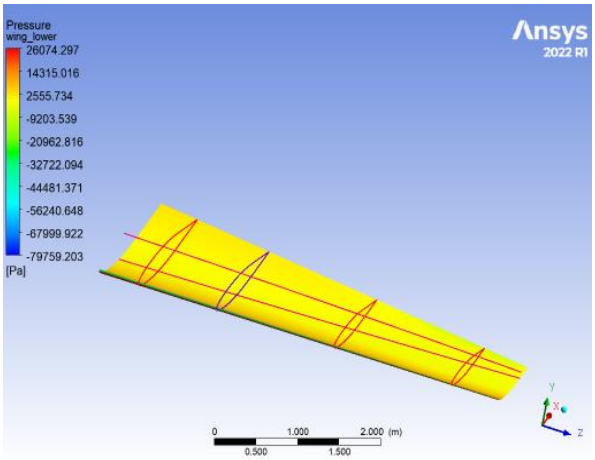

Figure (b). Contour (total pressure) at different locations for angle 8° at Mach 0.6 (Lower surface)

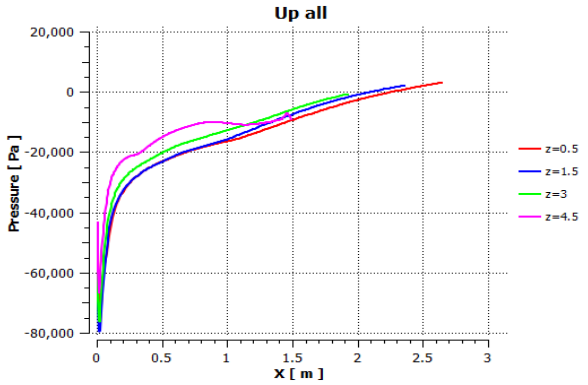

Figure (c). (total pressure) at different locations for angle 8 ° at Mach 0.6 (Upper surface)

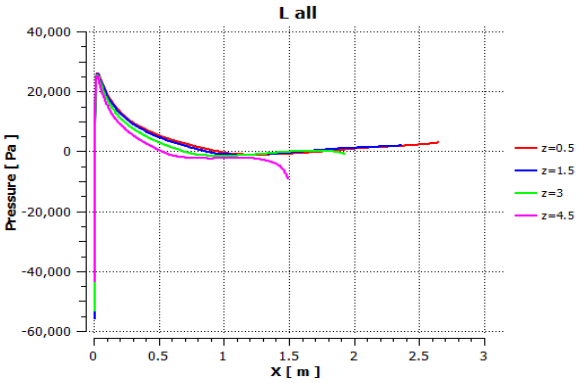

Figure (d). (total pressure) at different locations for angle 8° at Mach 0.6 (Lower surface)

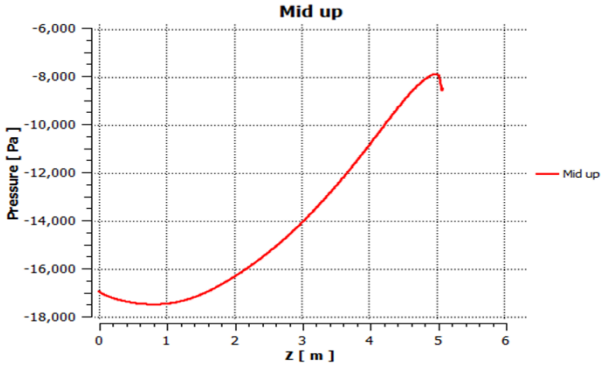

Figure (e). Spanwise (total pressure) at middle locations for angle 8 ° at Mach 0.6 (Upper surface)

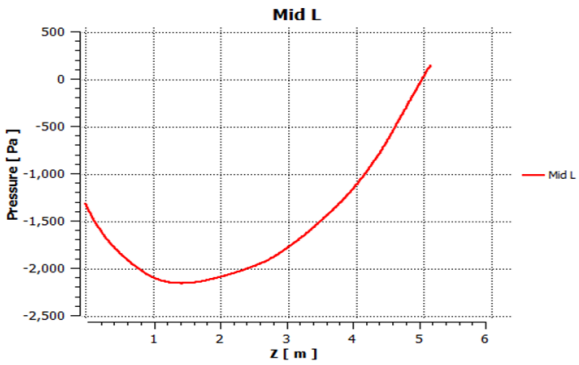

Figure (f). Spanwise (total pressure) at middle locations for angle 8° at Mach 0.6 (Lower surface)

Figure 5.18. Pressure distribution for angle of attack 8° at different Mach numbers for upper and lower surface

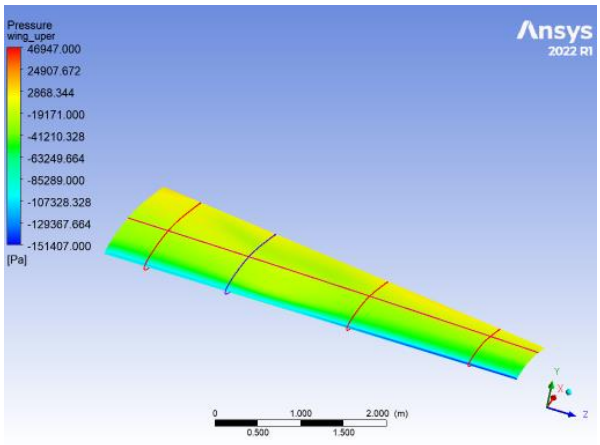

Figure (a). Contour (total pressure) at different locations for angle 8° at Mach 0.8 (Upper surface)

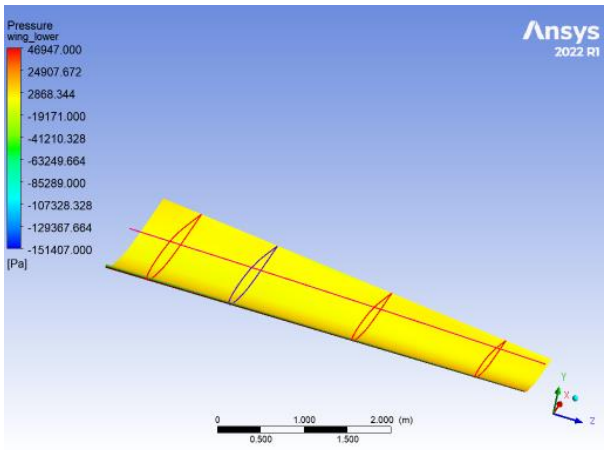

Figure (b). Contour (total pressure) at different locations for angle 8° at Mach 0.8 (Lower surface)

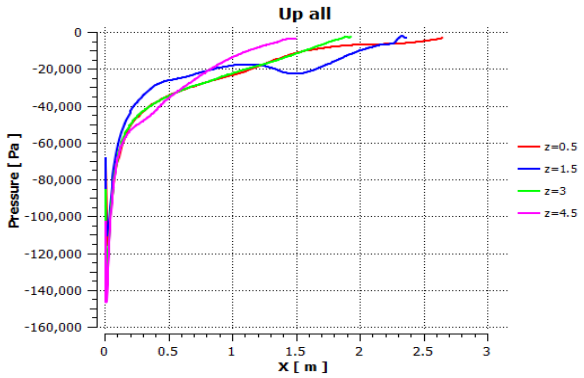

Figure (c). (total pressure) at different locations for angle 8° at Mach 0.8 (Upper surface)

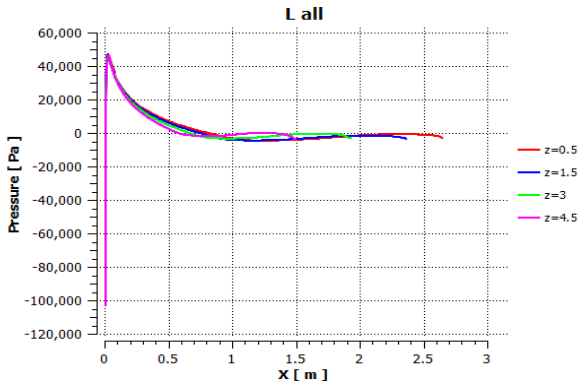

Figure (d). (total pressure) at different locations for angle 8° at Mach 0.8 (Lower surface)

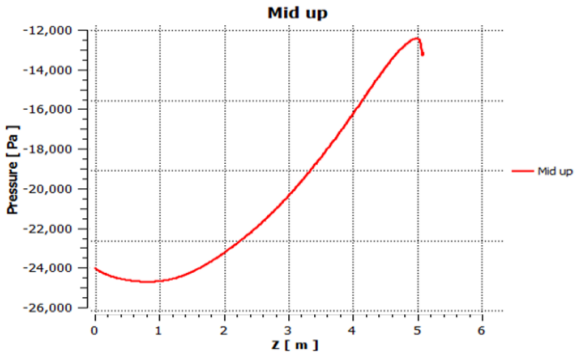

Figure(e). Spanwise (total pressure) at middle locations for angle 8° at Mach 0.8 (Upper surface)

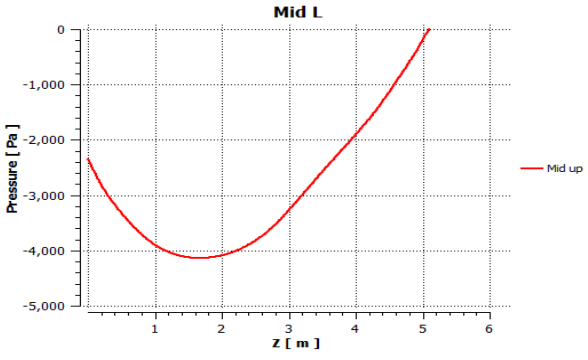

Figure (f). Spanwise (total pressure) at middle locations for angle 8° at Mach 0.8 (Lower surface)

Figure 5.19. Pressure distribution for angle of attack 8° at different Mach numbers for upper and lower surface

5.1.8. At Angle 12

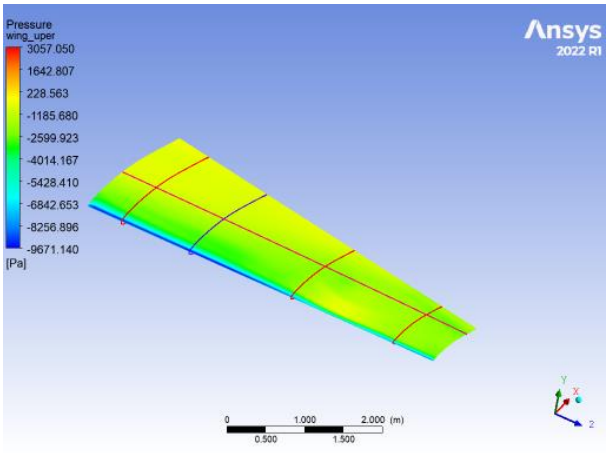

Figure (a). Contour (total pressure) at different locations for angle 12° at Mach 0.2 (Upper surface)

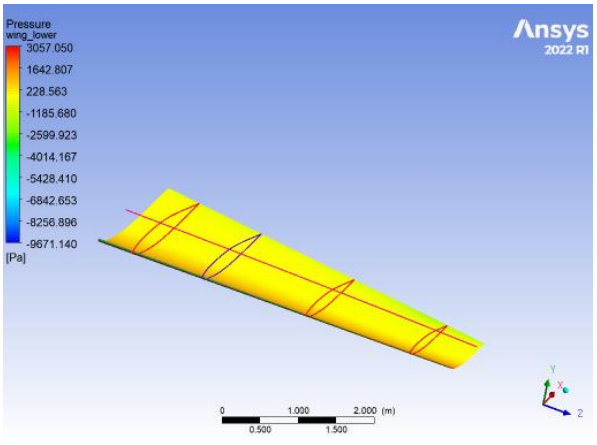

Figure (b). Contour (total pressure) at different locations for angle 12° at Mach 0.2 (Lower surface)

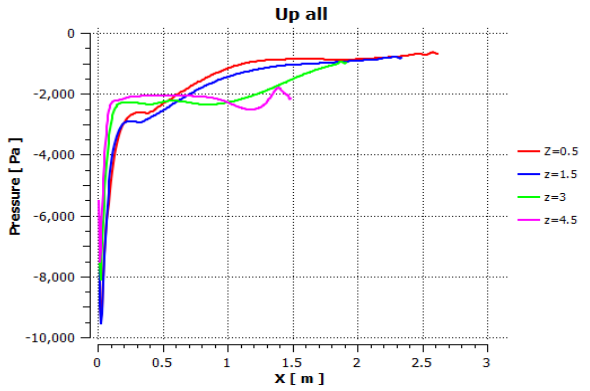

Figure (c). Chordwise (total pressure) at different locations for angle 12° at Mach 0.2 (Upper surface)

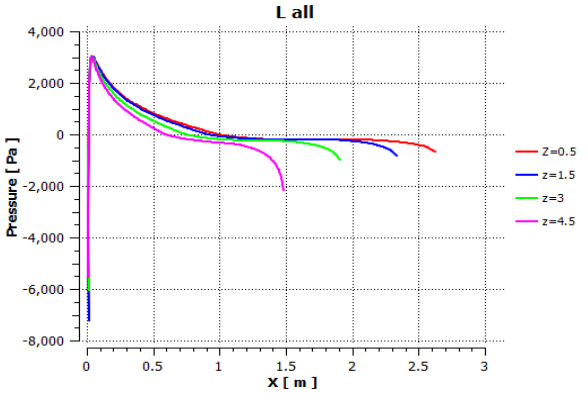

Figure (d). Chordwise (total pressure) at different locations for angle 12° at Mach 0.2 (Lower surface)

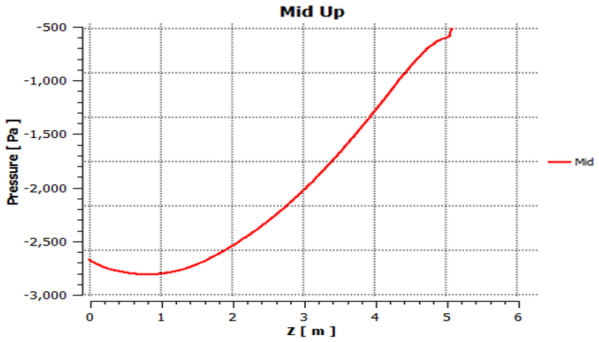

Figure (e). Spanwise (total pressure) at middle locations for angle 12° at Mach 0.2 (Upper surface)

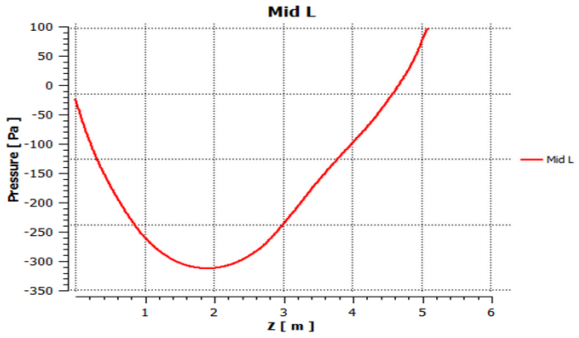

Figure (f). Spanwise (total pressure) at middle locations for angle 12° at Mach 0.2 (Lower surface)

Figure 5.20. Pressure distribution for angle of attack 12° at different Mach numbers for upper and lower surface

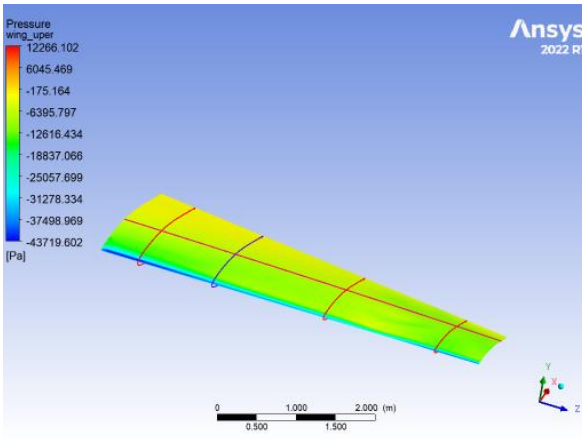

Figure (a). Contour (total pressure) at different locations for angle 12° at Mach 0.4 (Upper surface)

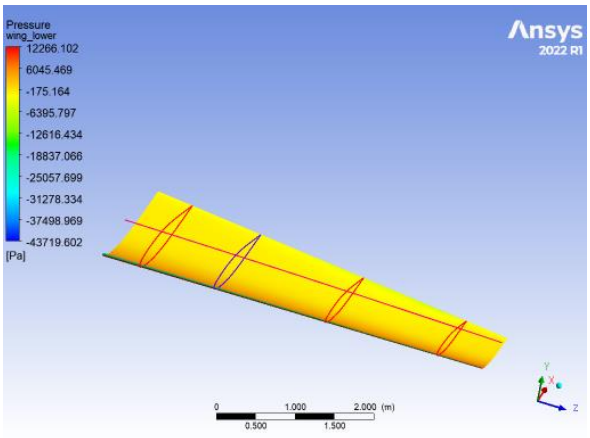

Figure (b). Contour (total pressure) at different locations for angle 12° at Mach 0.4 (Lower surface)

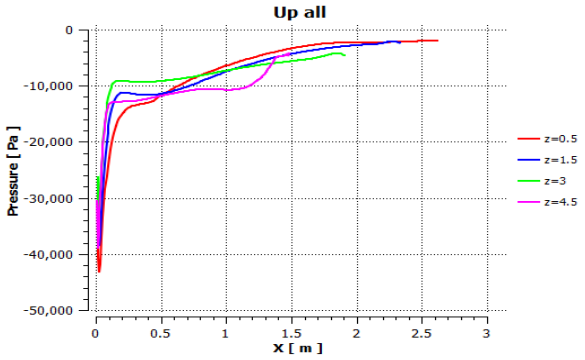

Figure (c). Chordwise (total pressure) at different locations for angle 12° at Mach 0.4 (Upper surface)

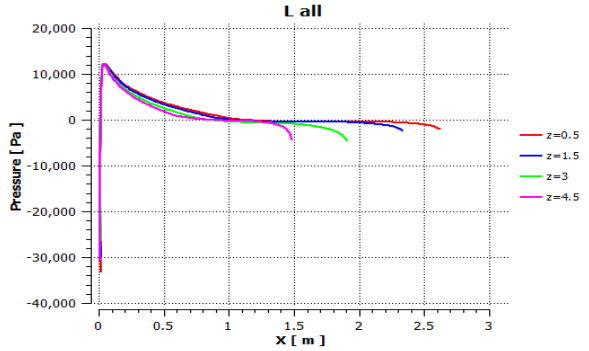

Figure (d). Chordwise (total pressure) at different locations for angle 12° at Mach 0.4 (Lower surface)

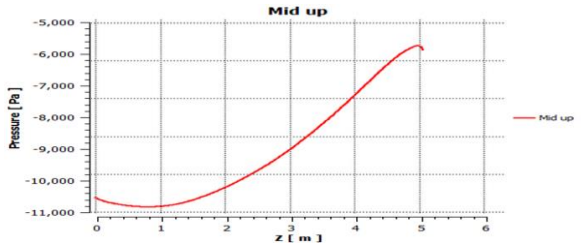

Figure (e). Spanwise (total pressure) at middle locations for angle 12° at Mach 0.4 (Upper surface)

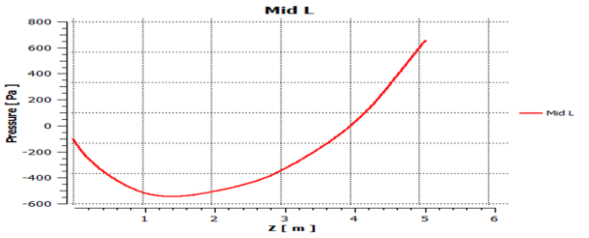

Figure (f). Spanwise (total pressure) at middle locations for angle 12° at Mach 0.4 (Lower surface)

Figure 5.21. Pressure distribution for angle of attack 12° at different Mach numbers for upper and lower surface

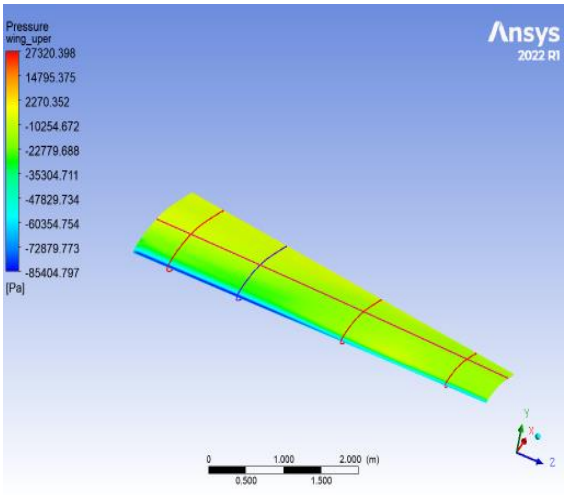

Figure (a). Contour (total pressure) at different locations for angle 12° at Mach 0.6 Upper surface)

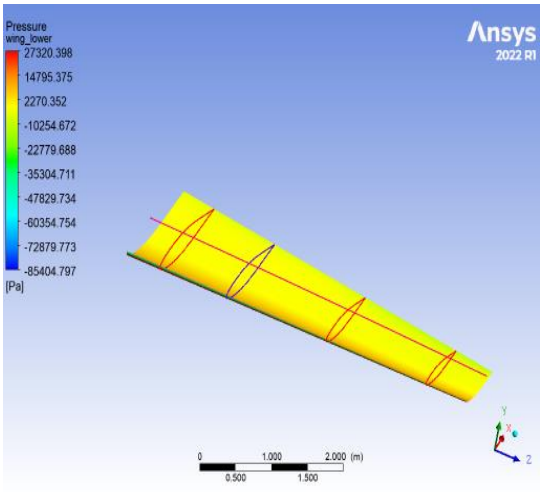

Figure (b). Contour (total pressure) at different locations for angle 12° at Mach 0.6 (Lower surface)

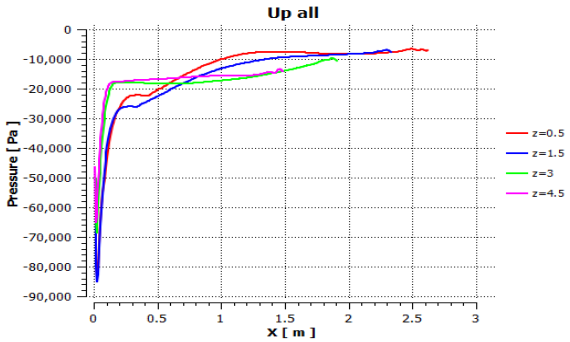

Figure (c). Chordwise (total pressure) at different locations for angle 12° at Mach 0.6 (Upper surface)

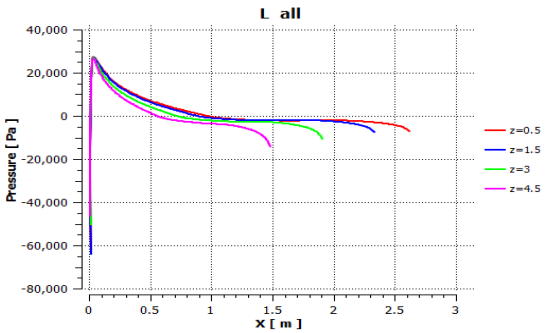

Figure (d). Chordwise (total pressure) at different locations for angle 12° at Mach 0.6 (Lower surface)

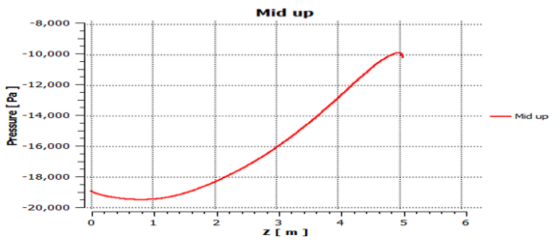

Figure (e). Spanwise (total pressure) at middle locations for angle 12° at Mach 0.6 (Upper surface)

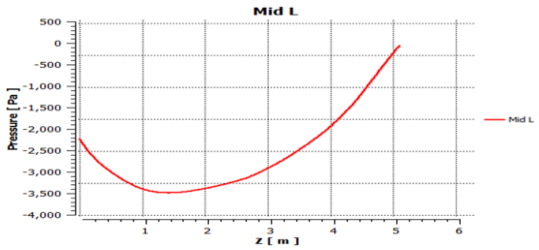

Figure (f). Spanwise (total pressure) at middle locations for angle 12° at Mach 0.6 (Lower surface)

Figure 5.22. Pressure distribution for angle of attack 12° at different Mach numbers for upper and lower surface

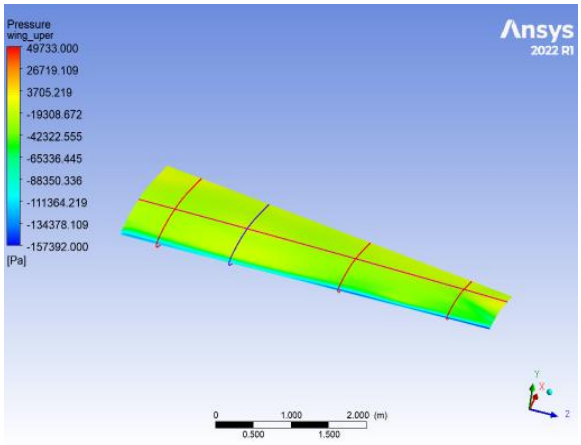

Figure (a). Contour (total pressure) at different locations for angle 12° at Mach 0.8 (Upper surface)

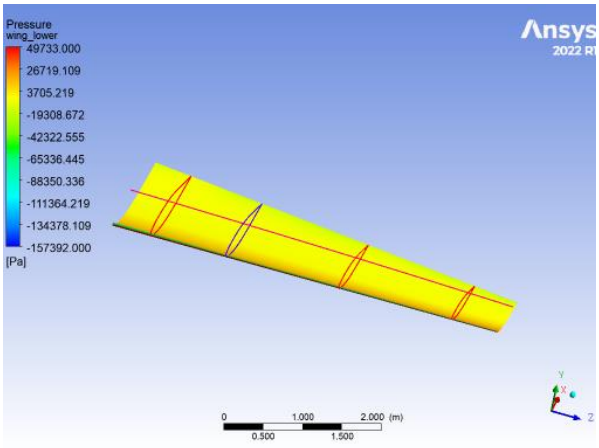

Figure (b). Contour (total pressure) at different locations for angle 12° at Mach 0.8 (Lower surface)

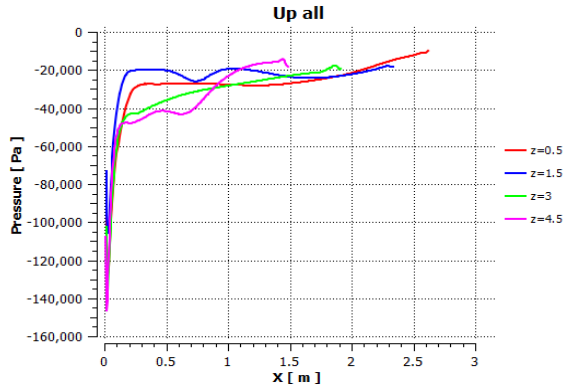

Figure (c). Chordwise (total pressure) at different locations for angle 12° at Mach 0.8 (Upper surface)

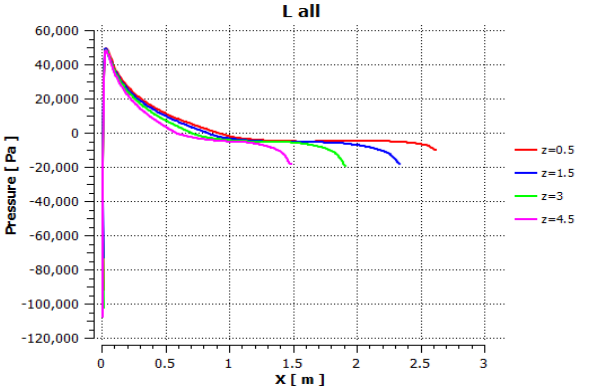

Figure (d). Chordwise (total pressure) at different locations for angle 12° at Mach 0.8 (Lower surface)

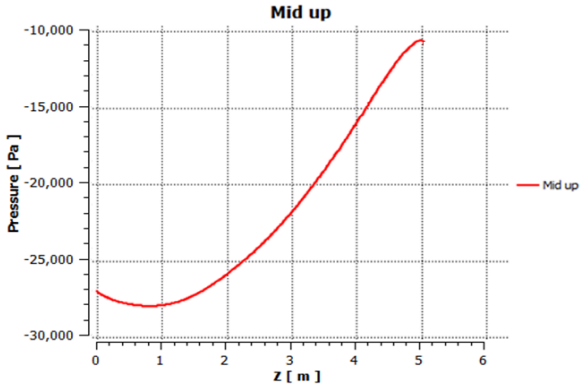

Figure (e). Spanwise (total pressure) at middle locations for angle 12° at Mach 0.8 (Upper surface)

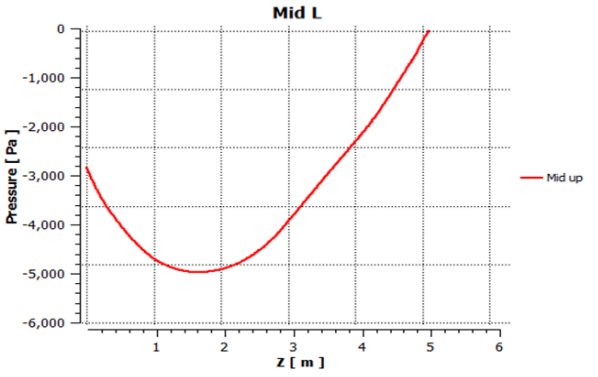

Figure (f). Spanwise (total pressure) at middle locations for angle 12° at Mach 0.8 (Lower surface)

Figure 5.23. Pressure distribution for angle of attack 8° at different Mach numbers for upper and lower surface

Now all the results obtained from the analysis will be displayed and at angles (0^{O},2 ^{O},4 ^{O},6 ^{O},8 ^{O},12 ^{O}) and every angle has four Mach (0.2,0.4,0.6,0.8).

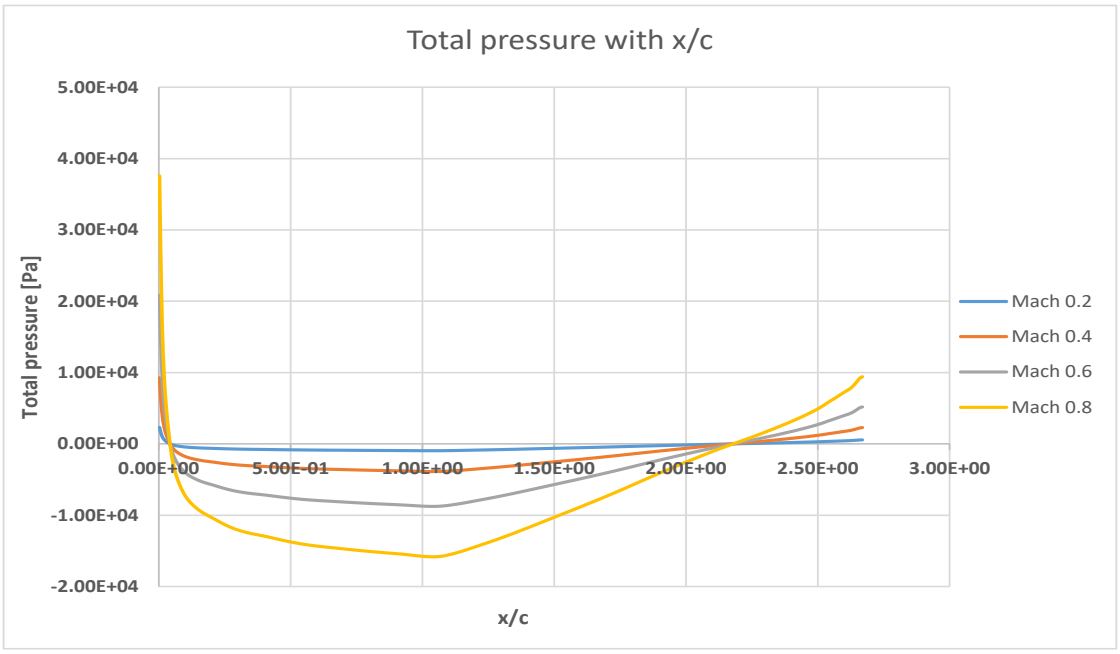

Figure 5.24. Chordwise Pressure distribution at different Mach and at angle 0°

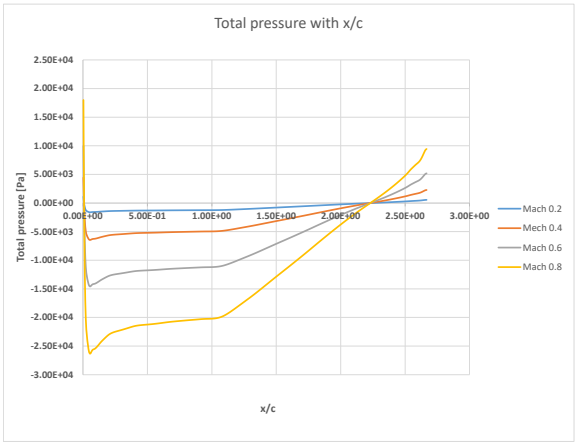

Figure (a). Chordwise Pressure distribution at different Mach and at angle 2° (Upper surface)

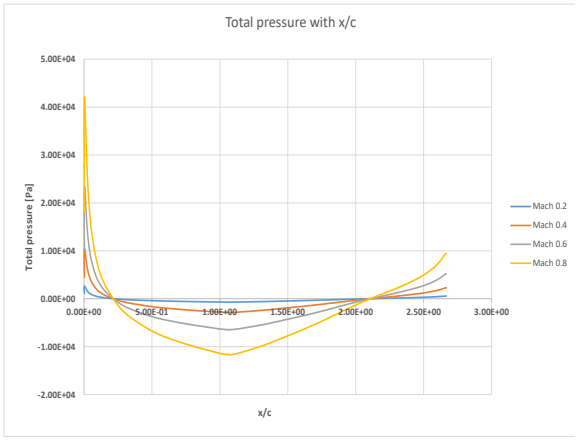

Figure (b). Chordwise Pressure distribution at different Mach and at angle 2° (Lower surface)

Figure 5.25. Chordwise Pressure distribution for angle of attack 2° at different Mach numbers for upper and lower surface

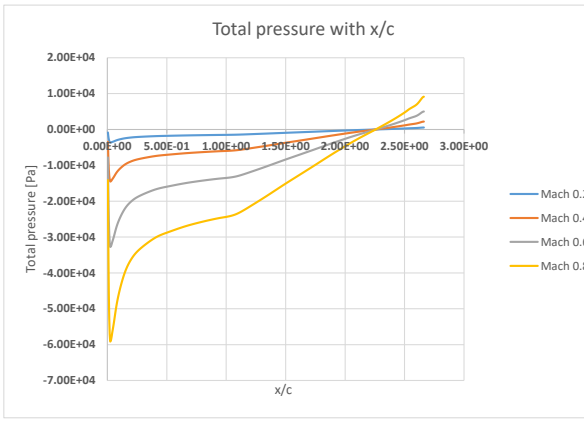

Figure (a). Chordwise Pressure distribution at different Mach and at angle 4° (Upper surface)

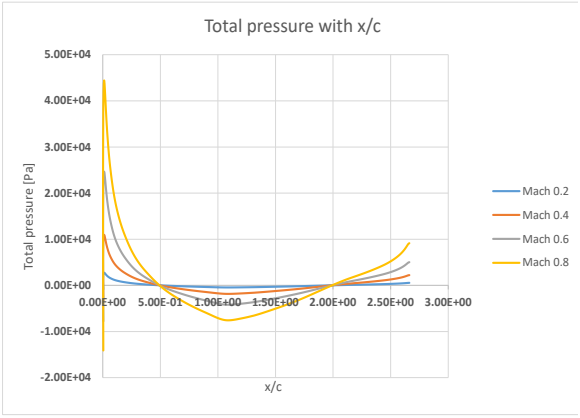

Figure (b). Chordwise Pressure distribution at different Mach and at angle 4° (Lower surface)

Figure 5.26. Chordwise Pressure distribution for angle of attack 4° at different Mach numbers for upper and lower surface

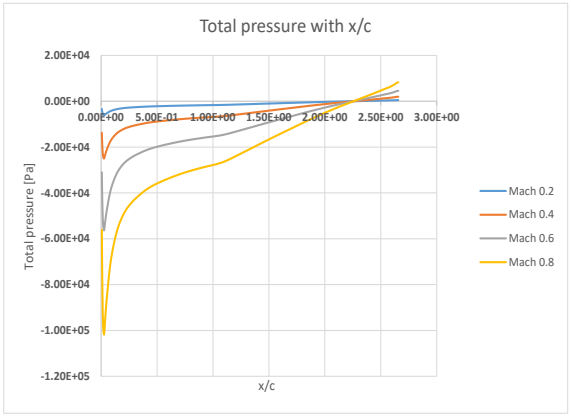

Figure (a). Chordwise Pressure distribution at different Mach and at angle 6° (Upper surface)

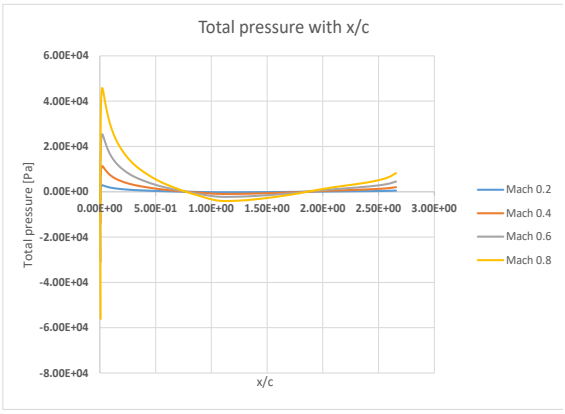

Figure (b). Chordwise Pressure distribution at different Mach and at angle 6° (Lower surface)

Figure 5.27. Chordwise Pressure distribution for angle of attack 6° at different Mach numbers for upper and lower surface

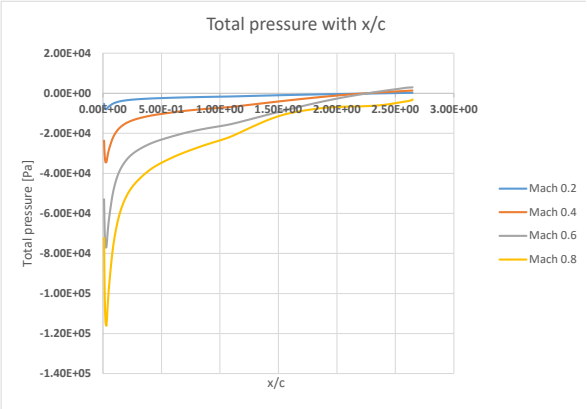

Figure (a). Chordwise Pressure distribution at different Mach and at angle 8 ° (Upper surface)

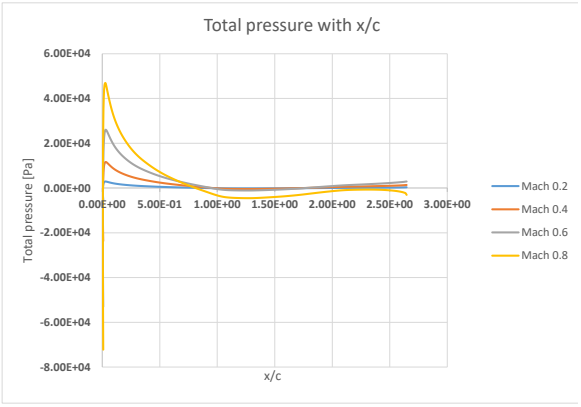

Figure (b). Chordwise Pressure distribution at different Mach and at angle 8° (Lower surface)

Figure 5.28. Chordwise Pressure distribution for angle of attack 8° at different Mach numbers for upper and lower surface

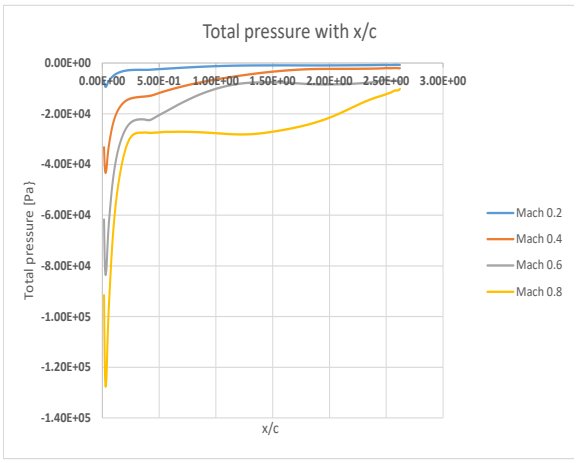

Figure (a). Chordwise Pressure distribution at different Mach and at angle 12° (Upper surface)

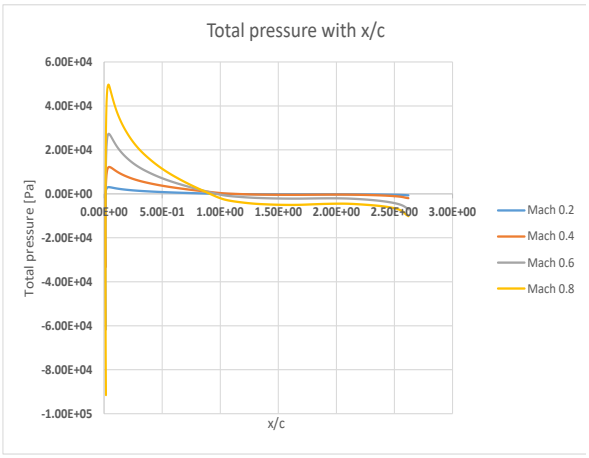

Figure (b). Chordwise Pressure distribution at different Mach and at angle 12° (Lower surface)

Figure 5.29. Chordwise Pressure distribution for angle of attack 12° at different Mach numbers for upper and lower surface

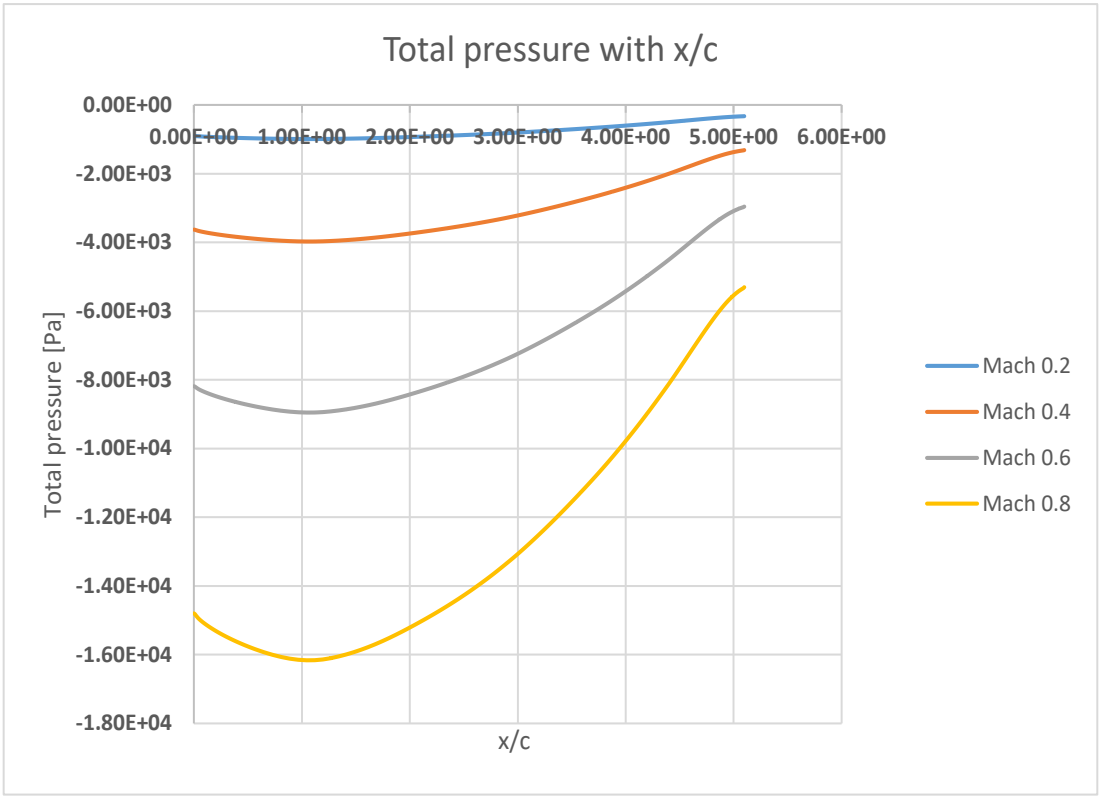

Figure 5.30. Spanwise Pressure distribution at different Mach and at angle 0°

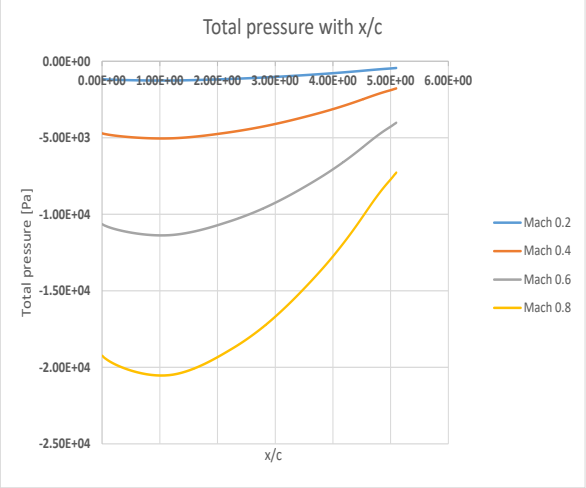

Figure (a). Spanwise Pressure distribution at different Mach and at angle 2° (Upper surface)

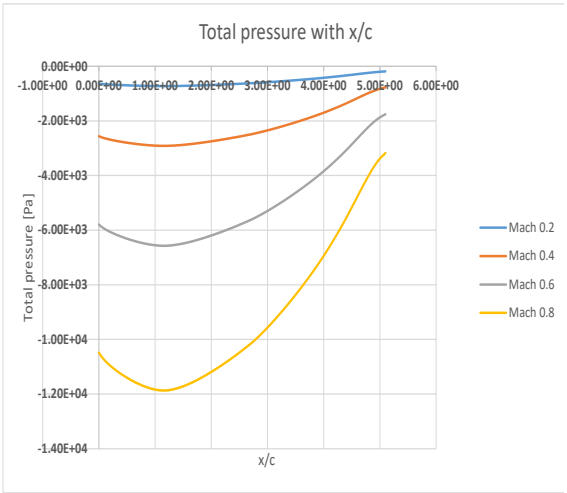

Figure(b).Spanwise Pressure distribution at different Mach and at angle 2° (Lower surface)

Figure 5.31. Spanwise Pressure distribution for angle of attack 2° at different Mach numbers for upper and lower surface

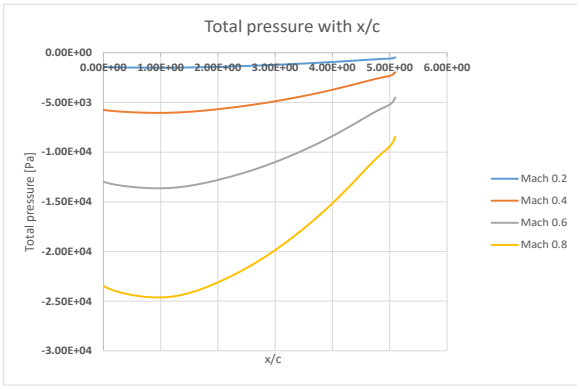

Figure (a). Spanwise Pressure distribution at different Mach and at angle 4° (Upper surface)

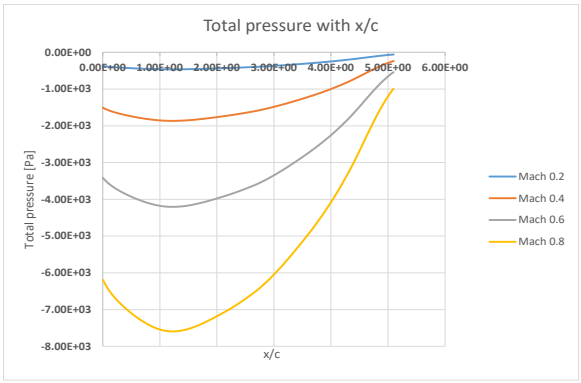

Figure (b). Spanwise Pressure distribution at different Mach and at angle 4° (Lower surface)

Figure 5.32. Spanwise Pressure distribution for angle of attack 4° at different Mach numbers for upper and lower surface

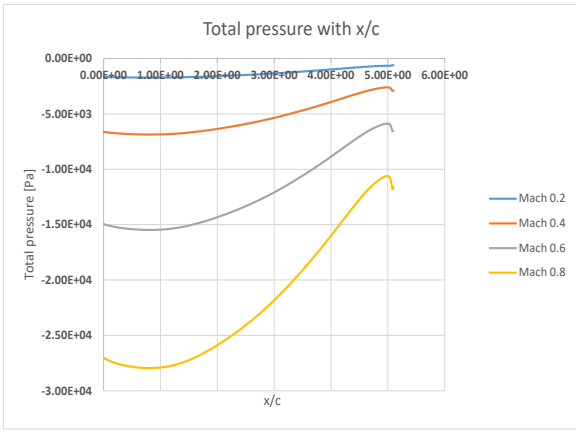

Figure (a). Spanwise Pressure distribution at different Mach and at angle 6° (Upper surface)

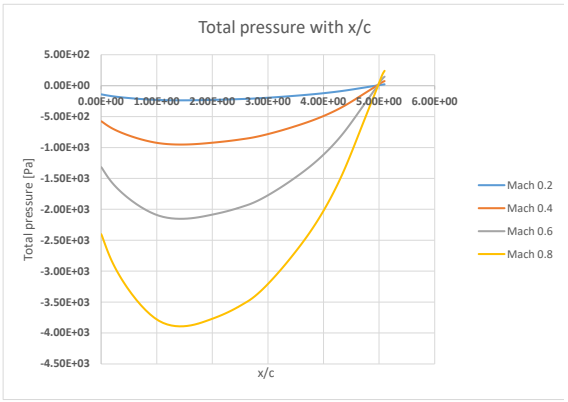

Figure (b). Spanwise Pressure distribution at different Mach and at angle 6° (Lower surface)

Figure 5.33. Spanwise Pressure distribution for angle of attack 6° at different Mach numbers for upper and lower surface

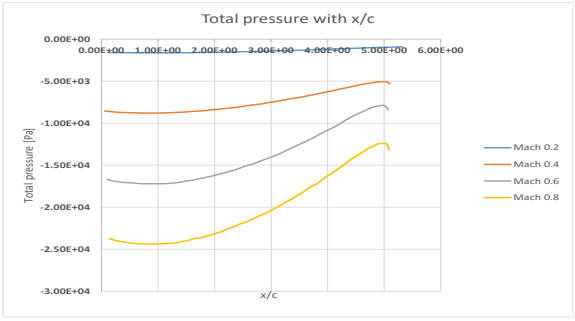

Figure (a). Spanwise Pressure distribution at different Mach and at angle 8 ° (Upper surface)

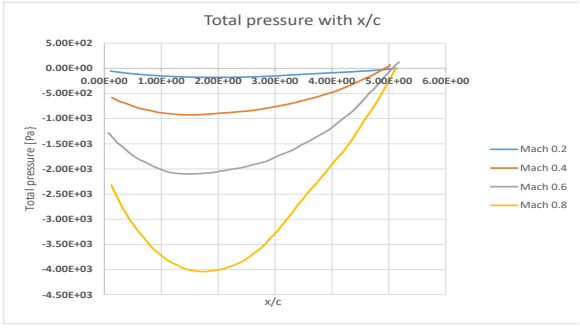

Figure (b). Spanwise Pressure distribution at different Mach and at angle 8 ° (Lower surface)

Figure 5.34. Spanwise Pressure distribution for angle of attack 8° at different Mach numbers for upper and lower surface

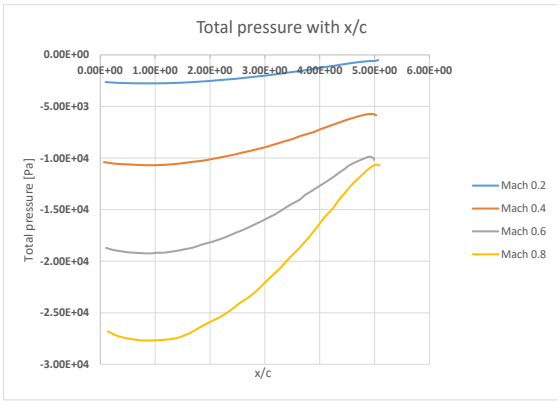

Figure(a). Spanwise Pressure distribution at different Mach and at angle 12° (Upper surface)

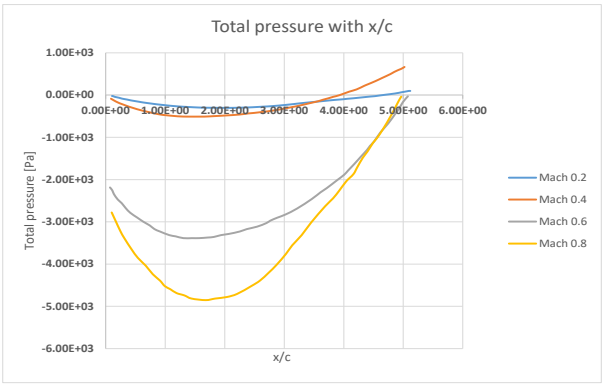

Figure (b). Spanwise Pressure distribution at different Mach and at angle 12 ° (Lower surface)

Figure 5.35. Spanwise Pressure distribution for angle of attack 12° at different Mach numbers for upper and lower surface

Table 5.1. (Distribution pressure on the upper and lower wing (pa units)) at different Mach.

Mach \ angle	Angle 0°	Angle 2°		Angle 6°		Angle 8°		Angle 12°		Angle 4°		Mach \ angle	T.H.Elsoni (Angle 4°)	
Pressure [Pa]	upper=lower	upper	lower	upper	lower	upper	lower	upper	lower	upper	lower	Pressure [Pa]	upper	lower
0.2	1354.5064	982.211	1914.09	-412	2147.18	-1002	2200	-1436.31	2339.56	367.577	2055.4	**0.4**	-2823.6	6211.9
0.4	5758.1949	4211.64	7962.91	-1581	8847.93	-4131	9136.44	-6091.53	9779.53	1618.92	8507.1			
0.6	13364.237	9806.39	18279.4	-3481	20212.1	-8940	20731.4	-12900.9	21801.1	3799.65	19477.2			
0.8	24615.468	18092.2	33426.2	-6189	36838.6	#####	37548.2	-12526.6	39435.2	7035.17	35552.2			

From Table 5.1 . it is seems that the total pressure has a largest value in using the angle of attack 12°, therefore the structural part will be based upon using this value. Tarik [51] used a computer.developed program for his results and approximately have a good agreement with a maximum discrepancy of (21%).

5.2. RESULT AND DISCUSSION STRUCTURAL

General airframe design requires knowledge of a large number of design variables in order to arrive at the best airframe structure and provide for the specific requirements to perform a particular task. The design requires many major engineering controls related to the geometry, as well as aerodynamics, related to weight and load, that is, structural design and durability, and in general, the load that affects the aircraft has several sources that affect the aircraft in flight in addition to the takeoff and landing states and that careful calculation of these loads is necessary in creating the best wing structural design with the highest strength and the lowest possible weight.

5.2.1. Detailed Case

The flow chart of the structural part is shown in Figure 5.36 and Figure 5.37. All the calculations are based upon the angle of attack $=\mathbf{12}^{\circ}$ since this of in the maximum pressure around the A/C wing model.

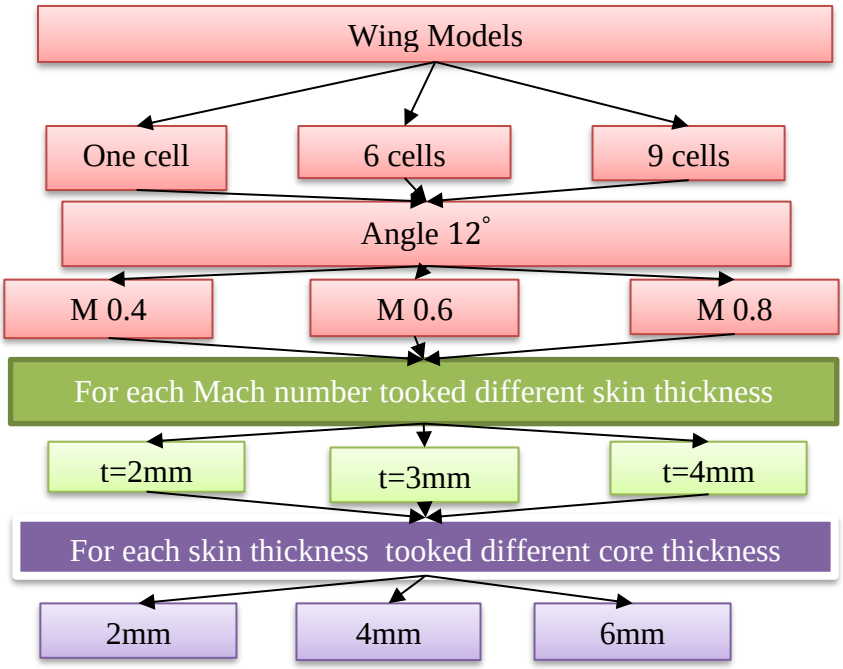

Figure 5.36. The flow chart of the suggested cases of the structural study

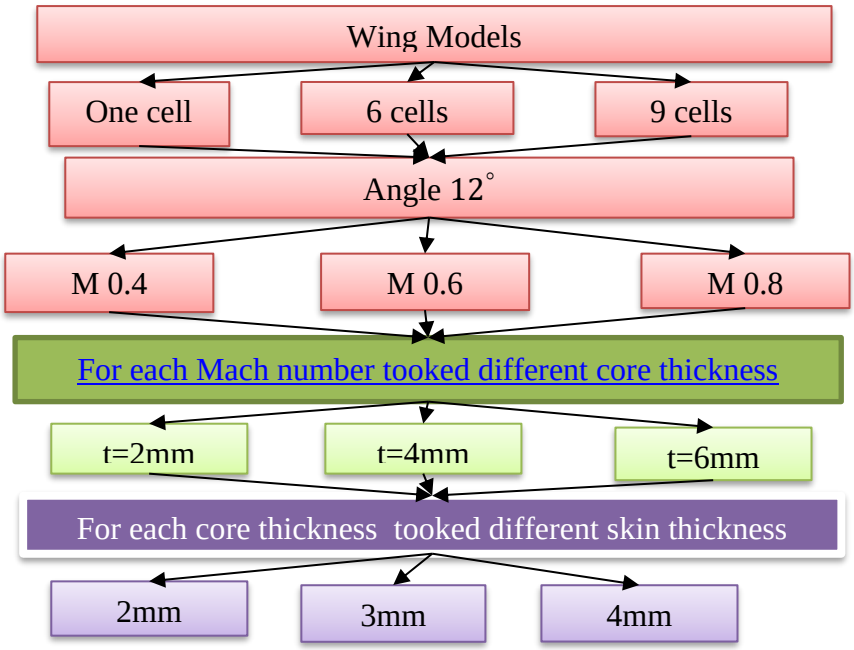

Figure 5.37. The flow chart of the suggested cases of the structural study

5.2.2. Structural Consideration

Firstly, a 12° angle of attack is adopted have, since the maximum resulted in deformations and stress and developed using this wing attitude. the pressure developed for the wing model is directly fed to the ANSYS package. The interaction of fluid.structure used wing will give results near to the exact modeling. Three types of models are used to investigate the static behavior using lightweight structures in comparison to the huge structure designed by previous investigations using ribs and stringers. The results will be compared using the analysis of the same wing.

5.2.3. Wing One Cell

The determination of displacements and stress using the different structural modeling are presented here. The finite element modeling was used by import the pressure distribution and applied on the wing structure .it corresponds with the real case this give the true picture of deformation and stresses on the wing skin.

The effects of design parameters of the wing structure are discussed as follows.

- Effects of skin thickness.
- Effects of number of cells
- Effects of core thickness (invariably of skin thickness)

5.2.3.1. (Effects of Skin Thickness)

Using the skin= 2mm and core thickness=2mm ,the maximum deformation= 154.28mm and the resulted Von Mises=210.17 MPa

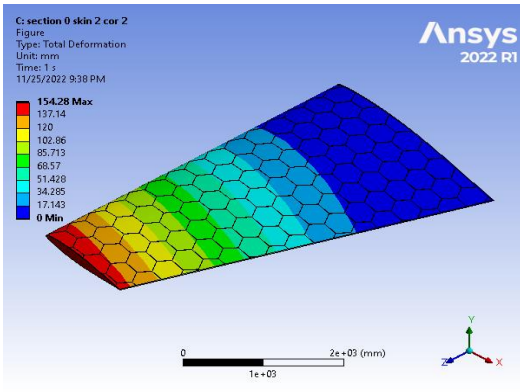

Figure 5.39. Contour Total Deformation at one cell skin 2 core 2 (Mach 0.4)

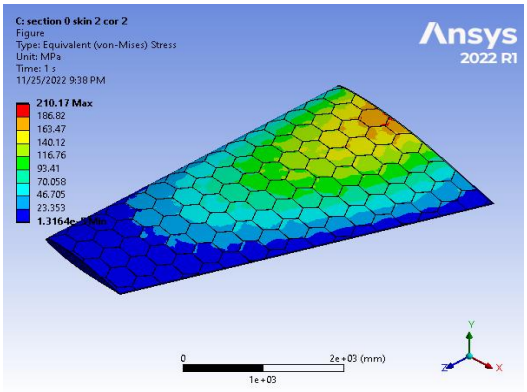

Figure 5.38. Contour Equivalent Stress at one cell skin 2 core 2 (Mach 0.4)

Increasing the skin thickness=3mm, the deformation = 106.41 mm and the resulted Von Mises =143.64MPa

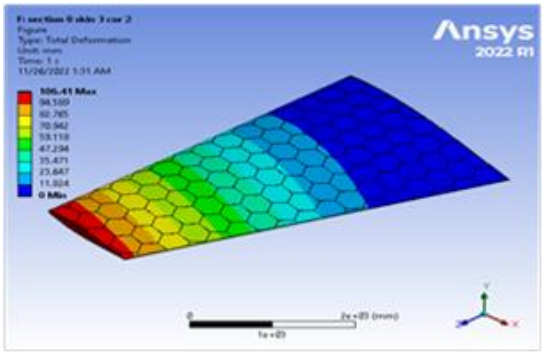

Figure 5.41.Contour Total Deformation at one cell skin 3 core 2 (Mach 0.4)

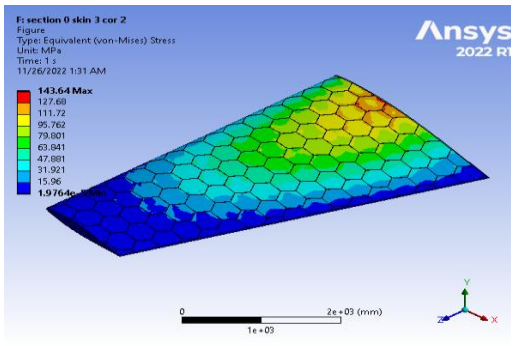

Figure 5.40. Contour Equivalent Stress at one cell skin 3 core 2 (Mach 0.4)

Table 5.2 shows the results of using different thickness (invariably of core). note in Table 5.2 that some of the points in red failed because the value exceeded Yield Strength=505 N/(mm)^2. And the least mass was (200.21Kg) and the larger mass was (421.71Kg) in using Material (Al7075 T6) . Table 5.2 shows us the change in the total Von Mises Stress was largest (793.92MPa) at skin thickness (2mm), core (4mm), and Mach 0.8 and which failed, while the lowest was stress (108.41MPa) at a skin thickness of (4mm), core (6mm) and Mach0.4. Also, this Table 5.2 shows that the largest Equivalent strain of (0.0075414 mm /mm) occurs in the model with the skin thickness (3mm) and core (2 mm) at Mach 0.8, while the least deviation is

(0.0010246mm/mm) obtained in the model with a skin thickness (2mm) and core (6mm) at Mach 0.8.

Table 5.2. Wing one cell at angle of attack **12**°.

Mach No	Skin thickness(mm)	Core thickness(mm)	Max deformation (mm)	Equivalent stress (MPa)	Equivalent strain (mm/mm)	Mass (kg)
0.4	2	2	154.28	210.17	0.003177	200.21
	3	2	106.41	143.64	20404	258.8
	4	2	81.681	110.74	0.001557	317.96
	2	4	146.39	217.08	0.003156	253.46
	3	4	101.88	140.54	0.002052	311.5
	4	4	78.785	108.41	0.001577	369.96
	2	6	138.16	195.19	0.002785	306.56
	3	6	98.262	137.65	0.001964	363.82
	4	6	76.48	104.37	0.001484	421.71
Mach No	Skin thickness(mm)	Core thickness (mm)	Max deformation (mm)	Equivalent stress (MPa)	Equivalent strain (mm/mm)	Mass (kg)
0.6	2	2	338.84	473.87	0.007152	200.1
	3	2	233.76	324.6	0.004612	258.8
	4	2	179.45	253.16	0.003528	317.96
	2	4	321.44	487.8	0.007093	253.46
	3	4	223.74	316	0.004617	311.5
	4	4	173.04	244.05	0.003549	369.96
	2	6	308.4	515.52	0.007238	306.56
	3	6	215.75	309.67	0.004423	363.82
	4	6	167.95	235.52	0.003338	421.71
Mach No	Skin thickness(mm)	Core thickness (mm)	Max deformation (mm)	Equivalent stress (MPa)	Equivalent strain (mm/mm)	Mass (kg)
0.8	2	2	547.06	774.53	0.011689	200.1
	3	2	377.45	530.72	0.007541	258.8
	4	2	289.77	413.8	0.005768	317.96
	2	4	518.87	793.92	0.011543	253.46
	3	4	361.19	514.4	0.007548	311.5
	4	4	279.36	398.98	0.005801	369.96
	2	6	489.42	718.16	0.010246	306.56
	3	6	348.26	503.78	0.007197	363.82
	4	6	271.12	358.11	0.005433	421.71

5.2.3.2. (Effects of Core Thickness)

Using the skin= 2mm and core thickness=2mm, the maximum deformation=338.84 mm and the resulted von mises=473.87 MPa

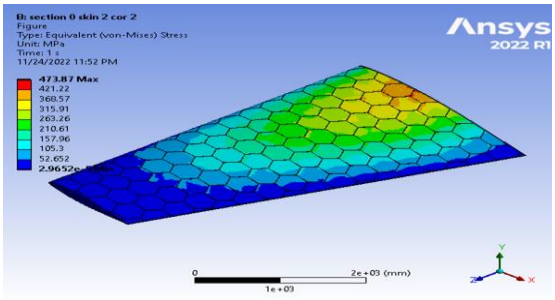

Figure 5.43. Contour Equivalent Stress at one cell skin 2 core 2 (Mach 0.6)

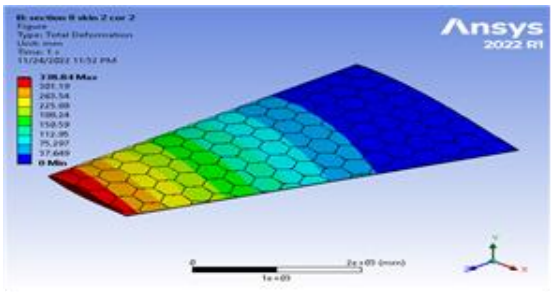

Figure 5.42.Contour Total Deformation at one cell skin 2 core 2 (Mach 0.6)

Increasing the skin thickness=3mm, the deformation = 233.76 mm and the resulted Von Mises = 324.6 MPa

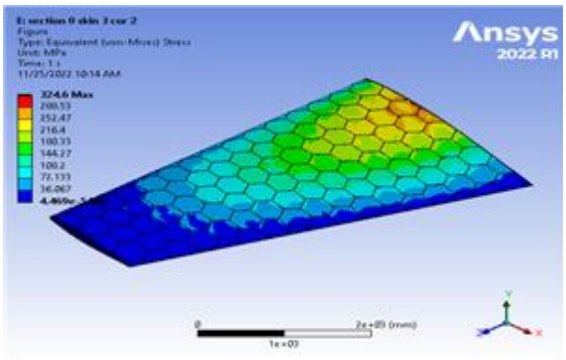

Figure 5.45. Contour Equivalent Stress at one cell skin 3 core 2 (Mach 0.6)

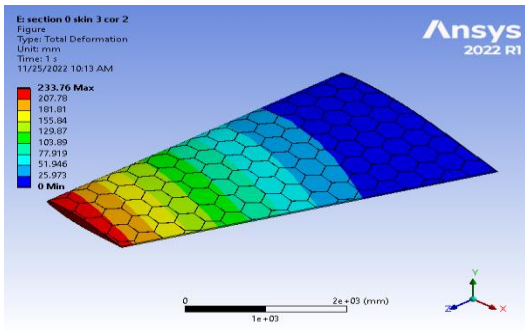

Figure 5.44. Contour Total Deformation at one cell skin 3 core 2 (Mach 0.6)

Table 5.3 shows the results of using different thickness.

Table 5.3. Wing :one cell at angle of attack**12**°

Mach No	skin thickness (mm)	Core thickness (mm)	Max deformation (mm)	Von mises stress (MPa)	Equivalent strain (mm/mm)	Mass (kg)
0.4	2	2	154.28	210.17	0.003177	200.2
	2	4	146.39	217.08	0.003156	253.5
	2	6	138.16	195.19	0.002785	306.6
	3	2	106.41	143.64	0.00204	258.8
	3	4	101.88	140.54	0.002052	311.5
	3	6	98.262	137.65	0.001964	363.8
	4	2	81.681	110.74	0.001557	318
	4	4	78.785	108.41	0.001577	370
	4	6	76.48	104.37	0.001484	421.7
Mach No	skin thickness(mm)	Core thickness(mm)	Max deformation (mm)	Von mises stress (MPa)	Equivalent strain (mm/mm)	Mass (kg)
0.6	2	2	338.84	473.87	0.00715	200.2
	2	4	321.44	487.8	0.00709	253.5
	2	6	308.4	515.52	0.007238	306.6
	3	2	233.76	324.6	0.00461	258.8
	3	4	223.74	316	0.00462	311.5
	3	6	215.75	309.67	0.00442	363.8
	4	2	179.45	253.16	0.00353	318
	4	4	173.04	244.05	0.00355	370
	4	6	167.95	235.52	0.00334	421.7
Mach No	skin thickness(mm)	Core thickness(mm)	Max deformation (mm)	Von mises stress (MPa)	Equivalent strain (mm/mm)	Mass (kg)
0.8	2	2	547.06	774.53	0.011689	200.21
	2	4	518.87	793.92	0.011543	253.46
	2	6	489.42	718.16	0.010246	306.56
	3	2	377.45	530.72	0.007541	258.8
	3	4	361.19	514.4	0.007548	311.5
	3	6	348.26	503.78	0.007197	363.82
	4	2	289.77	413.8	0.005768	317.96
	4	4	279.36	398.98	0.005801	369.96
	4	6	271.12	358.11	0.005433	421.71

Note in the Table 5.3 that some of the points in red failed because the value of the value exceeded Yield Strength=505N/ $(mm)^2$. And that the least mass was (200.21Kg) and the Larger mass was (421.71Kg). Table 5.3 shows us the change in the total Von Mises Stress is larger (793.92MPa) at skin thickness (2mm), core (4mm), and Mach 0.8 and which failed, while the lowest stress (108.41MPa) at a skin thickness of (4mm), core (6mm) and Mach0.4. Also, this Table 5.3 shows that the largest Equivalent strain of (0.0075414 mm /mm) occurs in the model with The skin thickness (3mm) and core (2 mm) at Mach 0.8, while the least deviation is (0.0010246mm/mm) obtained in the model with a skin thickness (2mm) and core (6mm) at Mach 0.8. The summary of the results which are extracted from the contours and shown in Table 5.3. some cases fail to the maximum stresses developed compared to the yield stress at the used Material (Al7075 T6) when a stress ratio less than 1. They are labelled in red colour. even the masses are low compared to the used mass in A/C design.

5.2.3.3. (Effects of Number Cells)

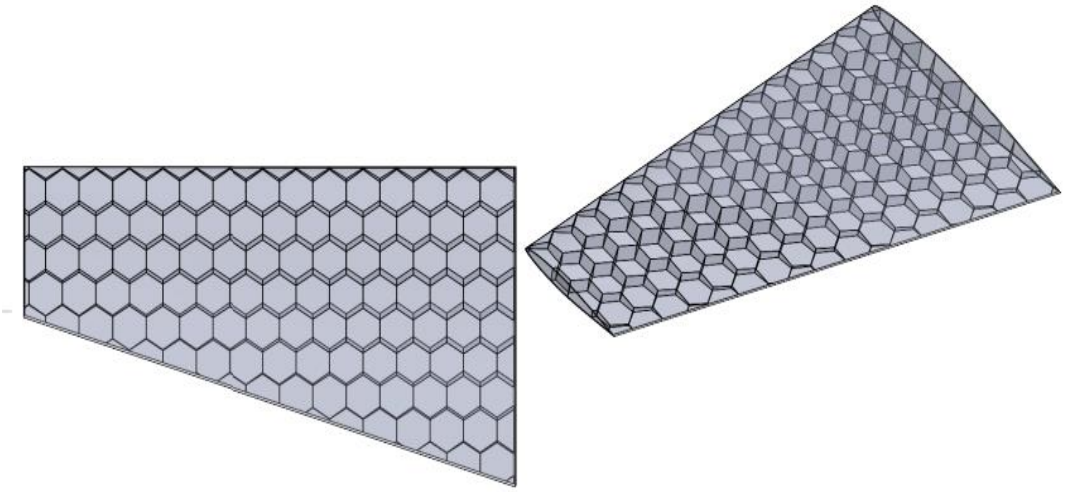

Figure 5.46. Wing. one cell

5.2.3.4. MACH (0.4), (0.6), (0.8)

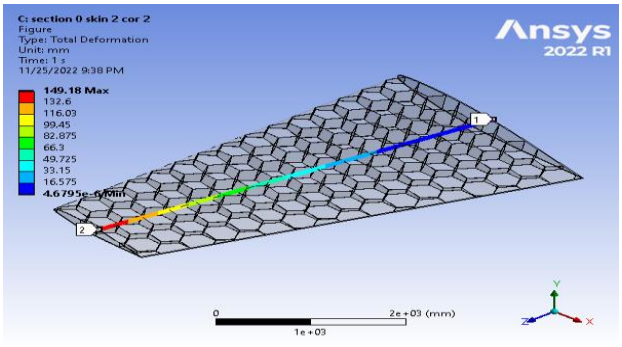

Figure 5.48. Contour Total Deformation at one cell skin 2 core 2 (Mach 0.4)

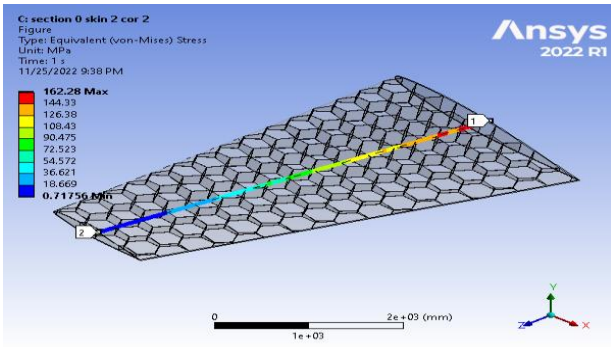

Figure 5.47. Contour Equivalent Stress at one cell skin 2 core 2 (Mach 0.4)

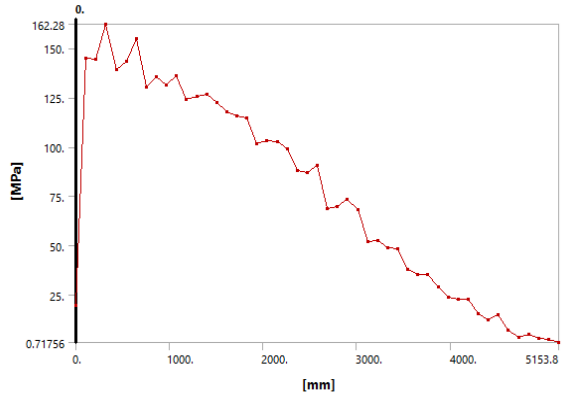

Figure 5.50. Equivalent Stress at section 1.2 skin 2 core 2 (Mach 0.4)

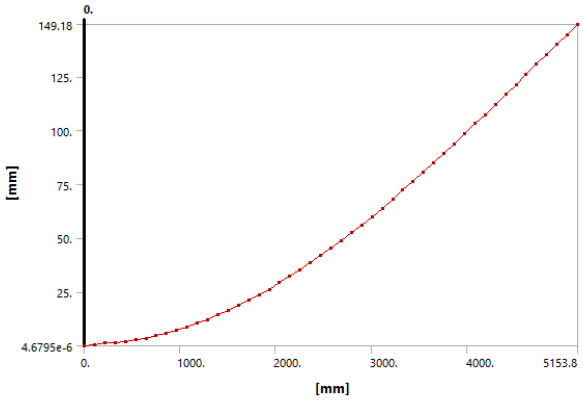

Figure 5.49. Variation of deformation at section 1.2 skin 2 core 2 (Mach 0.4)

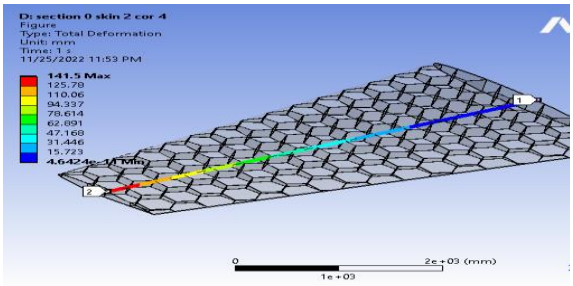

Figure 5.51. Contour Total Deformation at one cell skin 2 core 4 (Mach 0.4)

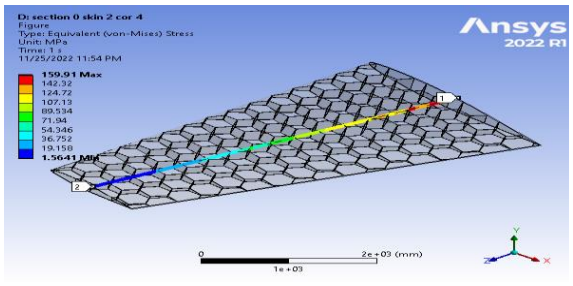

Figure 5.52. Contour Equivalent Stress at one cell skin 2 core 4 (Mach 0.4)

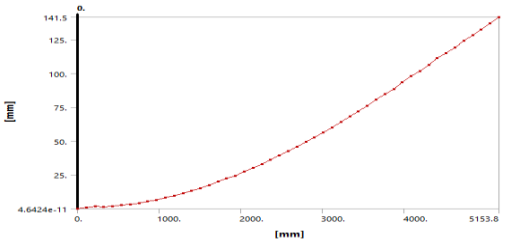

Figure 5.54. Variation of deformation at section 1.2 skin 2 core 4 (Mach 0.4)

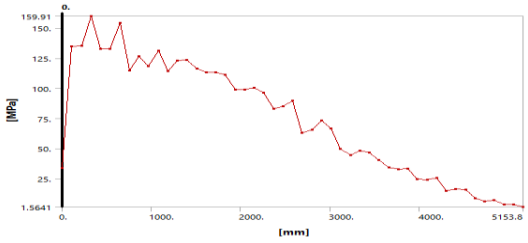

Figure 5.53. Equivalent Stress at section 1.2 skin 2 core 4 (Mach 0.4)

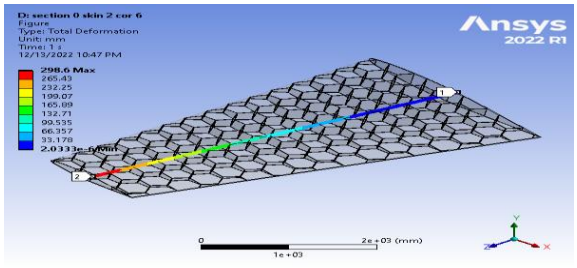

Figure 5.56. Contour Total Deformation at one cell skin 2 core 6(Mach 0.4)

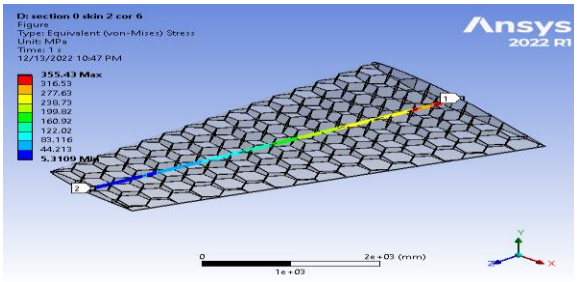

Figure 5.57. Contour Equivalent Stress at one cell skin 2 core 6(Mach 0.4)

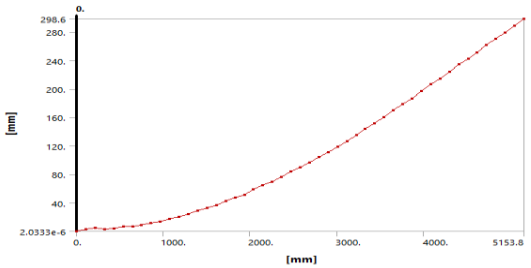

Figure 5.55. Variation of deformation at section 1.2 skin 2 core 6(Mach 0.4)

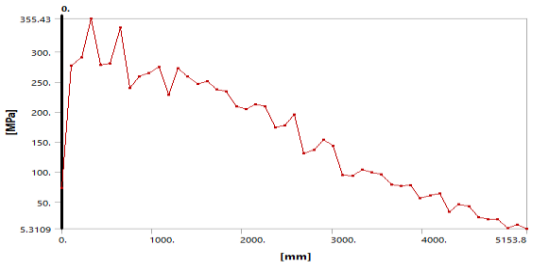

Figure 5.58. Equivalent Stress at section 1.2 skin 2 core 6(Mach 0.4)

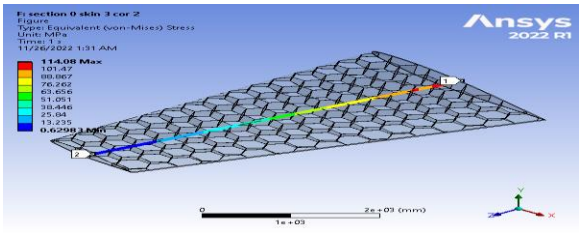

Figure 5.60. Contour Equivalent Stress at one cell skin 3 core 2 (Mach 0.4)

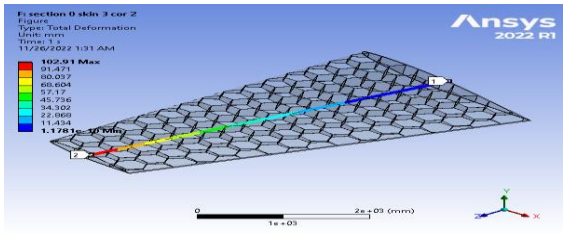

Figure 5.59. Contour Total Deformation at one cell skin 3 core 2 (Mach 0.4)

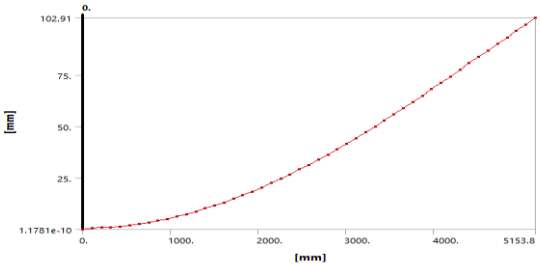

Figure 5.62. Variation of deformation at section 1.2 skin 3 core 2(Mach 0.4)

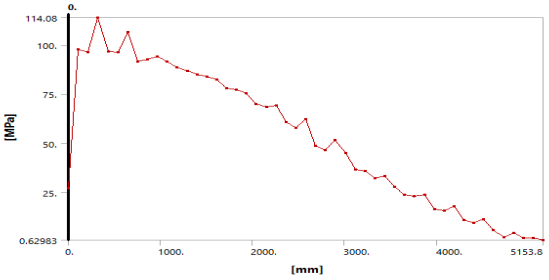

Figure 5.61. Equivalent Stress at section 1.2 skin 3 core 2 (Mach 0.4)

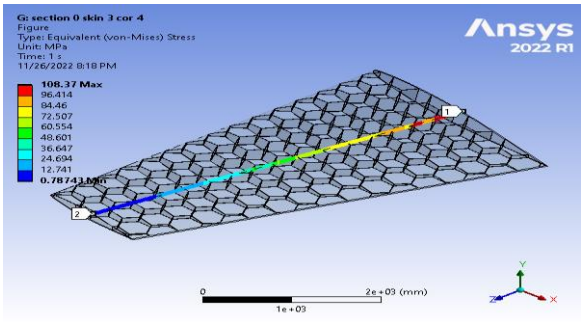

Figure 5.63. Contour Equivalent Stress at one cell skin 3 core 4 (Mach 0.4)

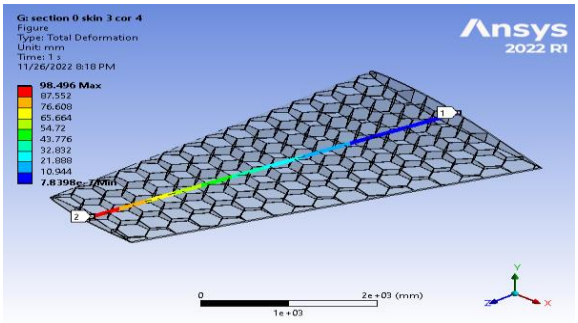

Figure 5.64. Contour Total Deformation at one cell skin 3 core 4 (Mach 0.4)

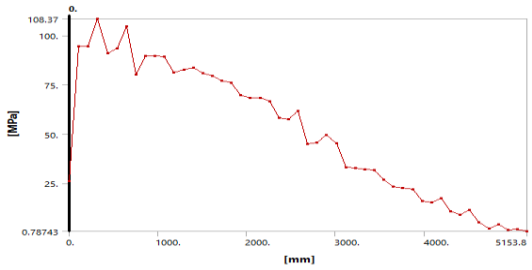

Figure 5.66. Equivalent Stress at section 1.2 skin 3 core 4 (Mach 0.4)

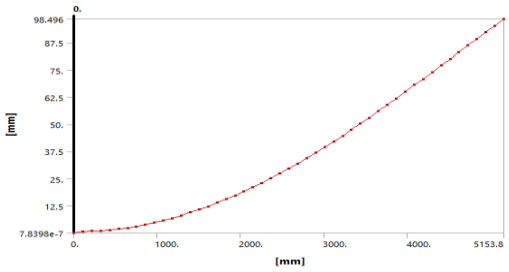

Figure 5.65. Variation of deformation at section 1.2 skin 3 core 4 (Mach 0.4)

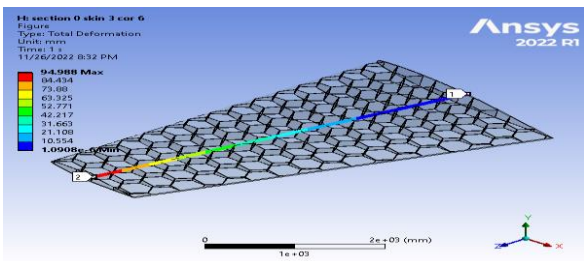

Figure 5.68. Contour Total Deformation at one cell skin 3 core 6 (Mach 0.4)

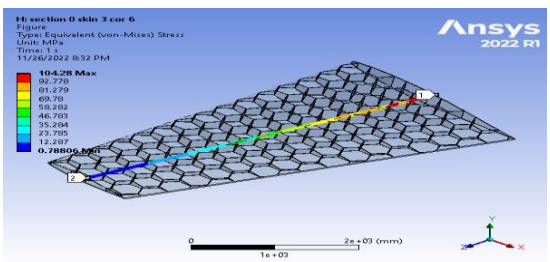

Figure 5.67. Contour Equivalent Stress at one cell skin 3 core 6 (Mach 0.4)

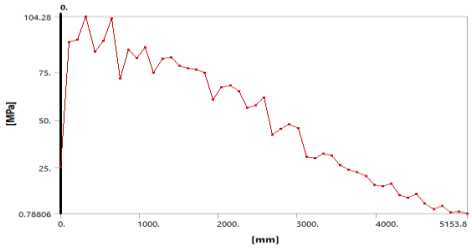

Figure 5.70. Equivalent Stress at section 1.2 skin 3 core 6 (Mach 0.4)

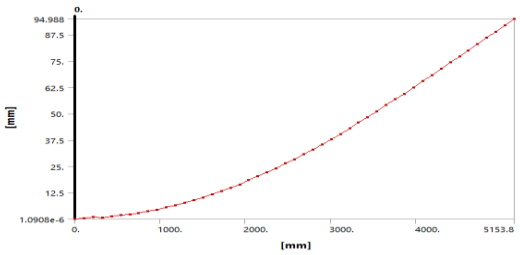

Figure 5.69. Variation of deformation at section 1.2 skin 3 core 6 (Mach 0.4)

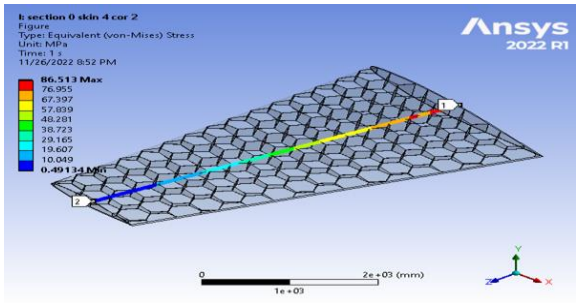

Figure 5.71. Contour Equivalent Stress at one cell skin 4 core 2 (Mach 0.4)

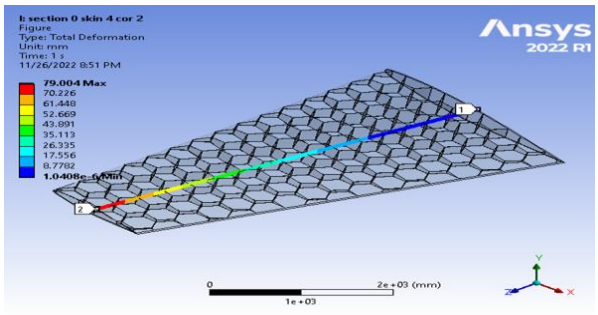

Figure 5.72. Contour Total Deformation at one cell skin 4 core 2 (Mach 0.4)

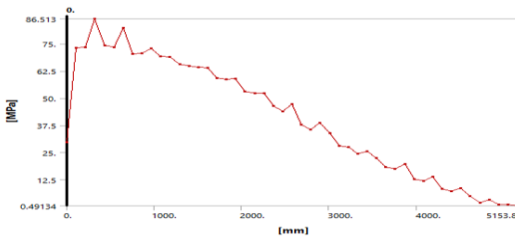

Figure 5.73. Equivalent Stress at section 1.2 skin 4 core 2 (Mach 0.4)

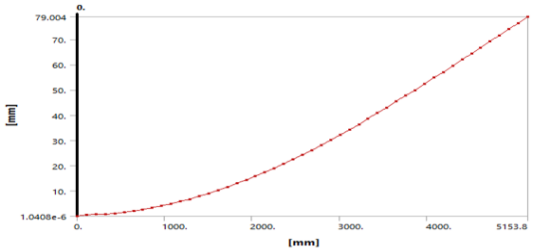

Figure 5.74. Variation of deformation at section 1.2 skin 4 core 2 (Mach 0.4)

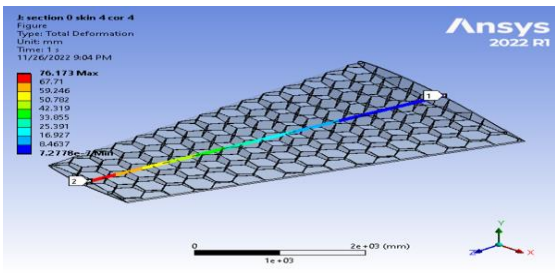

Figure 5.75. Contour Total Deformation at one cell skin 4 core 4

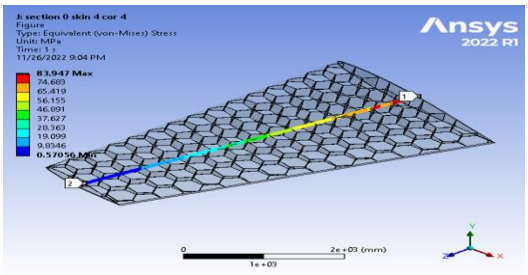

Figure 5.76. Contour Equivalent Stress at one cell skin 4 core 4 (Mach 0.4)

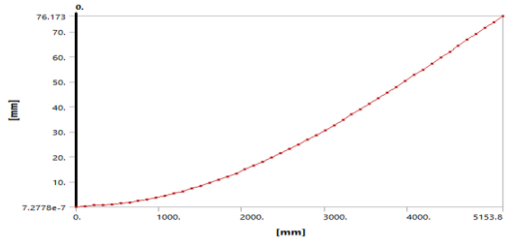

Figure 5.78. Variation of deformation at section 1.2 skin 4 core 4 (Mach 0.4)

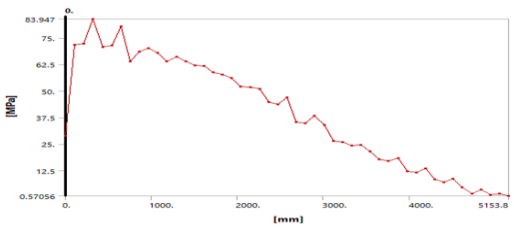

Figure 5.77. Equivalent Stress at section 1.2 skin 4 core 4 (Mach 0.4)

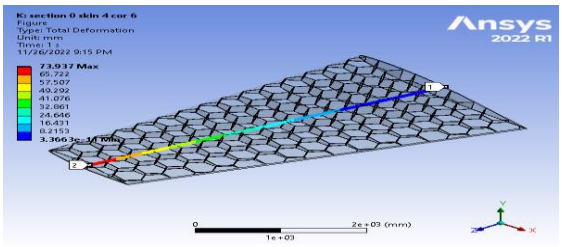

Figure 5.80. Contour Total Deformation at one cell skin 4 core 6(Mach 0.4)

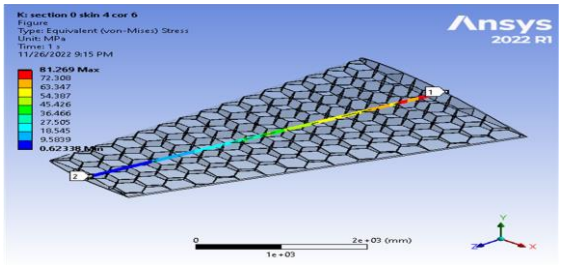

Figure 5.79. Contour Equivalent Stress at one cell skin 4 core 6(Mach 0.4)

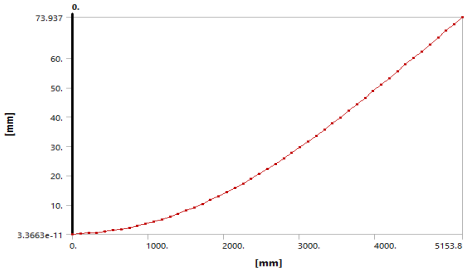

Figure 5.81. Variation of deformation at section 1.2 skin 4 core 6 (Mach 0.4)

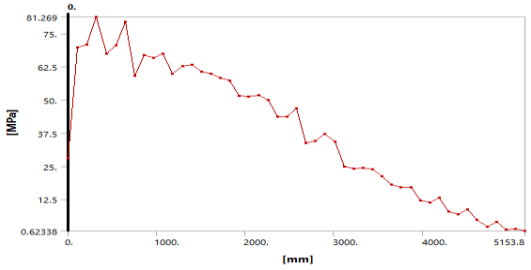

Figure 5.82. Equivalent Stress at section 1.2 skin 4 core 6 (Mach 0.4)

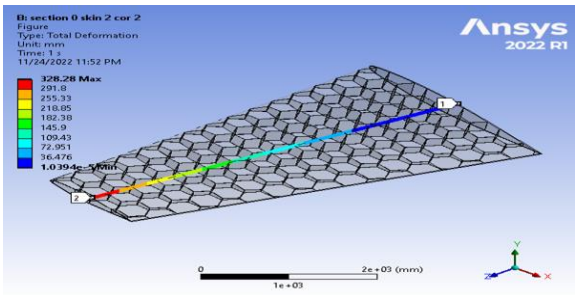

Figure 5.83. (Contour)Total Deformation at one cell skin 2 core 2 (Mach 0.6)

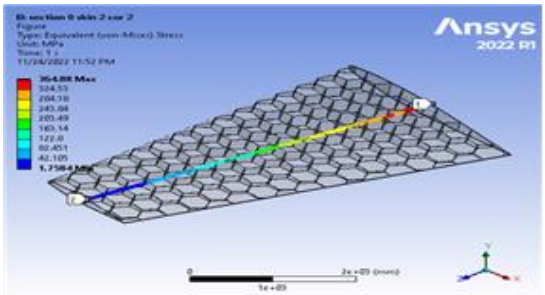

Figure 5.84. (Contour)Equivalent Stress at one cell skin 2 core 2 (Mach 0.6)

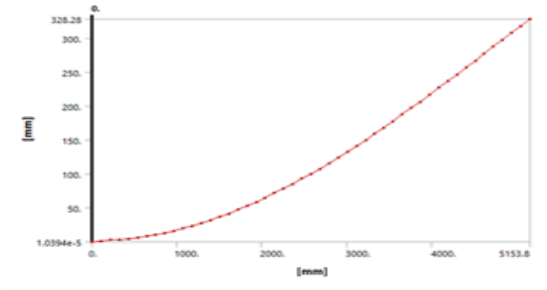

Figure 5.86. Variation of deformation at section 1.2 skin 2 core 2 (Mach 0.6)

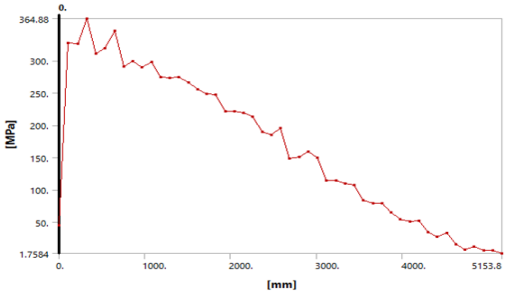

Figure 5.85. Equivalent Stress at section 1.2 skin 2 core 2 (Mach 0.6)

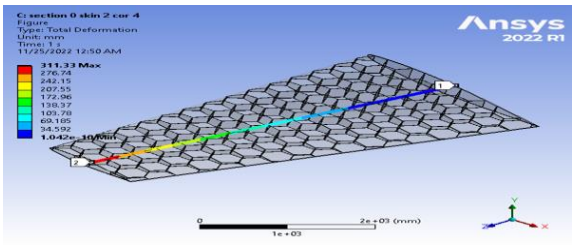

Figure 5.87. (Contour)Total Deformation at one cell skin 2 core 4 (Mach 0.6)

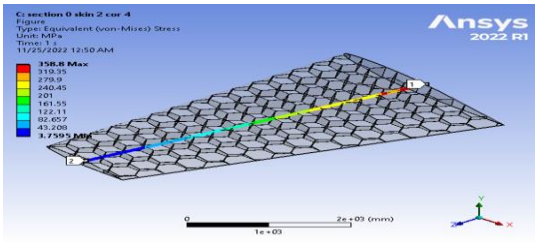

Figure 5.88. (Contour) Equivalent Stress at one cell skin 2 core 4 (Mach 0.6)

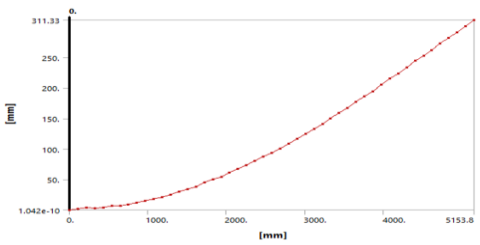

Figure 5.89. Variation of deformation at section 1.2 skin 2 core 4 (Mach 0.6)

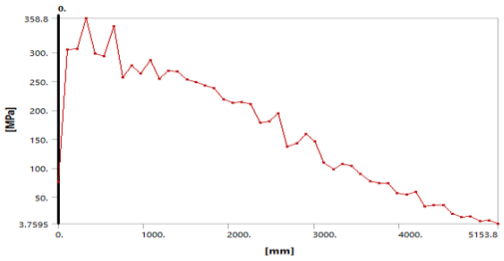

Figure 5.90. Equivalent Stress at section 1.2 skin 2 core 4 (Mach 0.6)

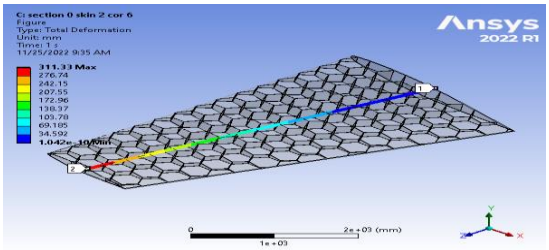

Figure 5.92. (Contour)Total Deformation at one cell skin 2 core 6 (Mach 0.6)

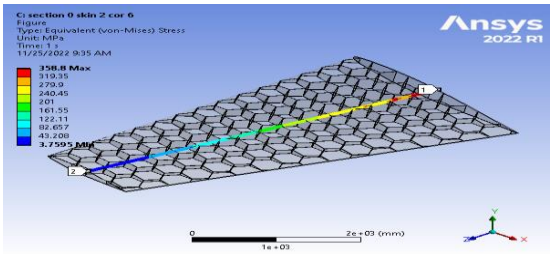

Figure 5.91. Contour Equivalent Stress at one cell skin 2 core 6 (Mach 0.6)

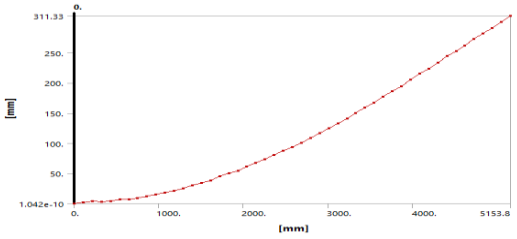

Figure 5.94. Variation of deformation at section 1.2 skin 2 core 6 (Mach 0.6)

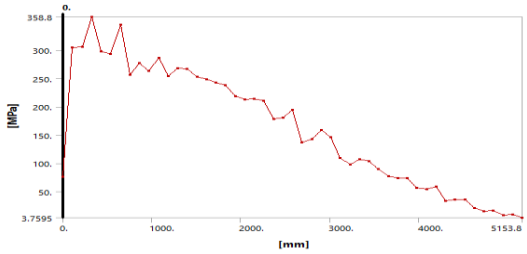

Figure 5.93. Equivalent Stress at section 1.2 skin 2 core 6 (Mach 0.6)

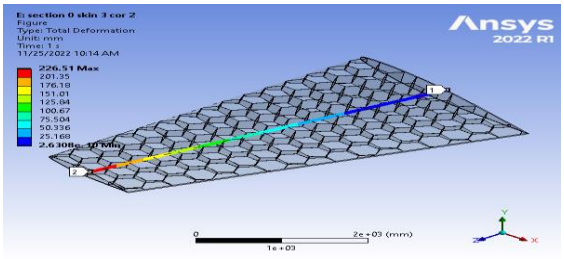

Figure 5.96. Contour Total Deformation at one cell skin 3 core 2 (Mach 0.6)

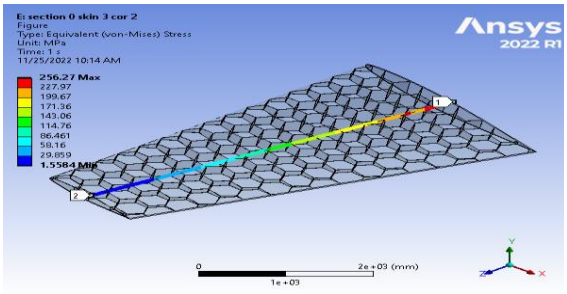

Figure 5.95. Contour Equivalent Stress at one cell skin 3 core 2 (Mach 0.6)

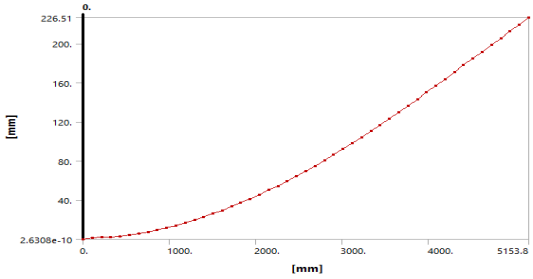

Figure 5.97. Variation of deformation at section 1.2 skin 3 core 2 (Mach 0.6)

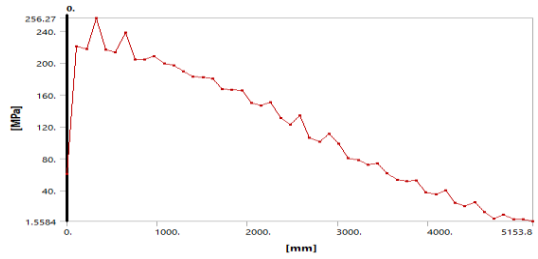

Figure 5.98. Equivalent Stress at section 1.2 skin 3 core 2 (Mach 0.6)

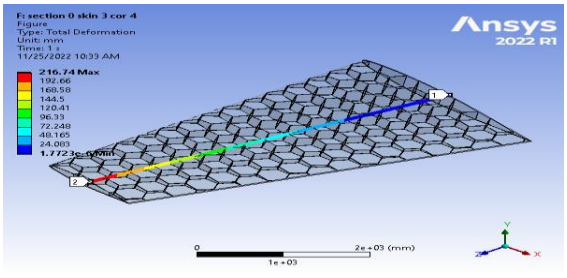

Figure 5.99. Contour Total Deformation at one cell skin 3 core 4 (Mach 0.6)

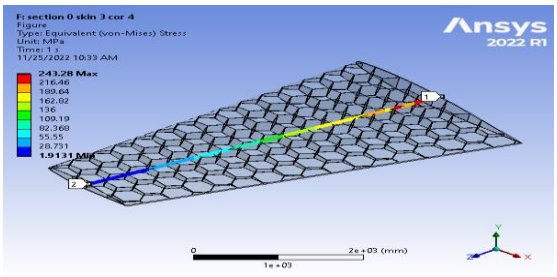

Figure 5.100. Contour Equivalent Stress at one cell skin 3 core 4 (Mach 0.6)

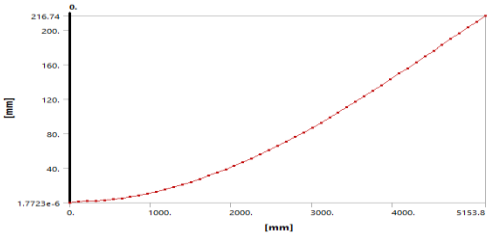

Figure 5.102. Variation of deformation at section 1.2 skin 3 core 4 (Mach 0.6)

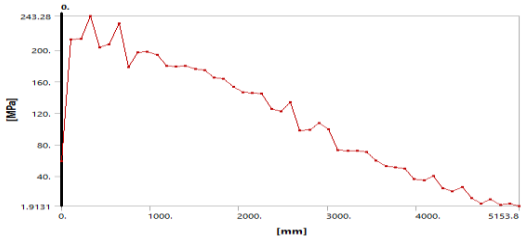

Figure 5.101. Equivalent Stress at section 1.2 skin 3 core 4 (Mach 0.6)

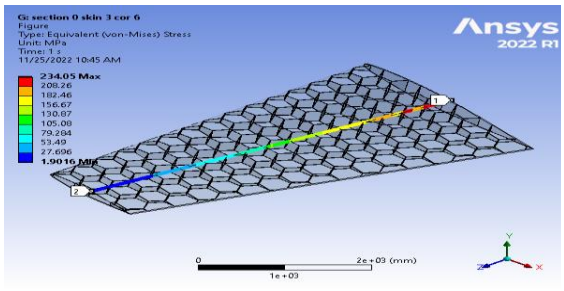

Figure 5.104. Contour Equivalent Stress at one cell skin 3 core 6 (Mach 0.6)

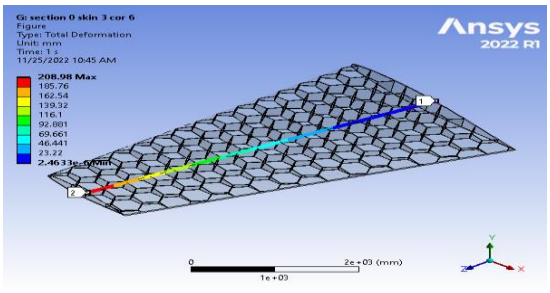

Figure 5.103. Contour Total Deformation at one cell skin 3 core 6 (Mach 0.6)

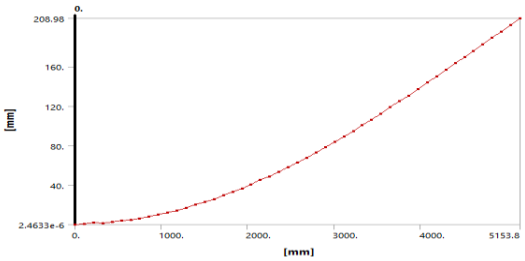

Figure 5.105. Variation of deformation at section 1.2 skin 3 core 6 (Mach 0.6)

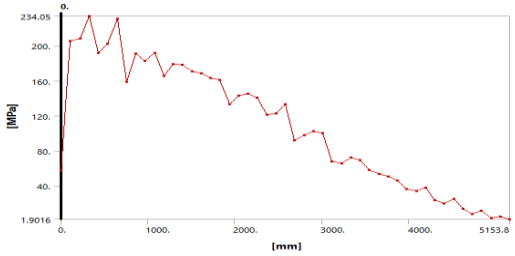

Figure 5.106. Equivalent Stress at section 0 skin 3 core 6 (Mach 0.6)

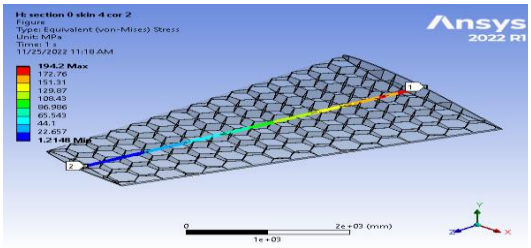

Figure 5.108. Contour Equivalent Stress at one cell skin 4 core 2 (Mach 0.6)

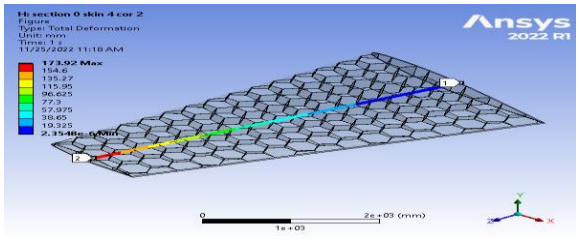

Figure 5.107. Contour Total Deformation at one cell skin 4 core 2 (Mach 0.6)

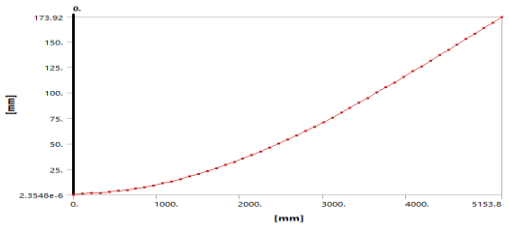

Figure 5.110. Variation of deformation at section 1.2 skin 4 core 2 (Mach 0.6)

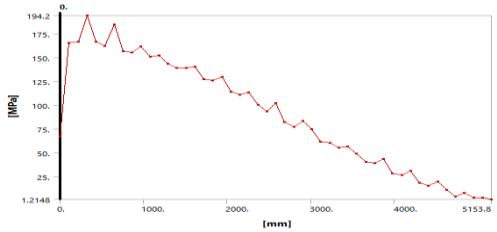

Figure 5.109. Equivalent Stress at section 1.2 skin 4 core 2 (Mach 0.6)

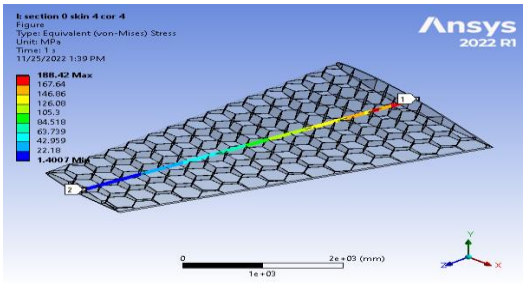

Figure 5.111. Contour Equivalent Stress at one cell skin 4 core 4 (Mach 0.6)

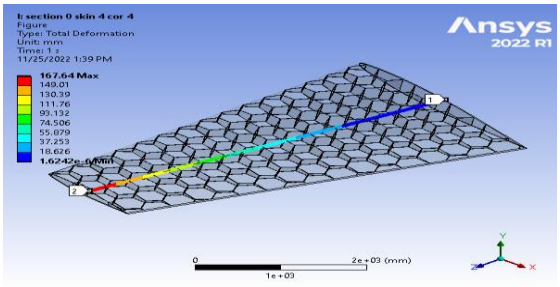

Figure 5.112. Contour Total Deformation at one cell skin 4 core 4 (Mach 0.6)

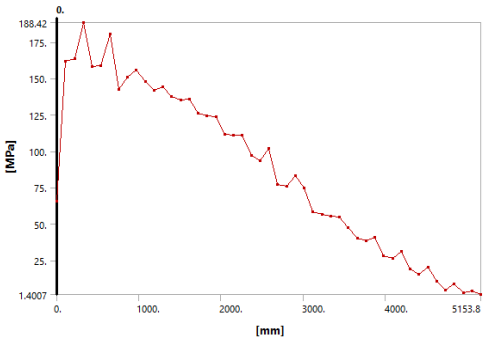

Figure 5.113. Equivalent Stress at section 1.2 skin 4 core 4 (Mach 0.6)

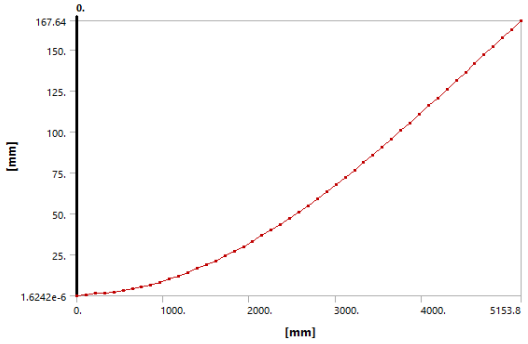

Figure 5.114. Variation of deformation at section 1.2 skin 4 core 4 (Mach 0.6)

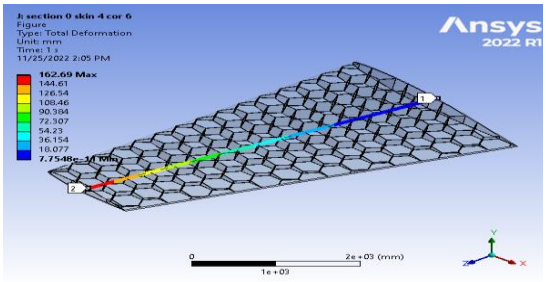

Figure 5.116. Contour Total Deformation at one cell skin 4 core 6 (Mach 0.6)

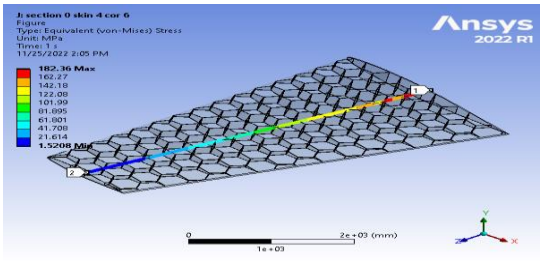

Figure 5.115. Contour Equivalent Stress at one cell skin 4 core 6 (Mach 0.6)

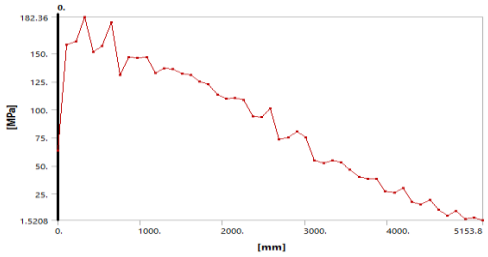

Figure 5.117. Equivalent Stress at section 1.2 skin 4 core 6 (Mach 0.6)

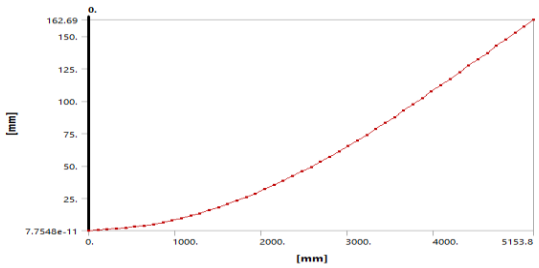

Figure 5.118. Variation of deformation at section 1.2 skin 4 core 6 (Mach 0.6)

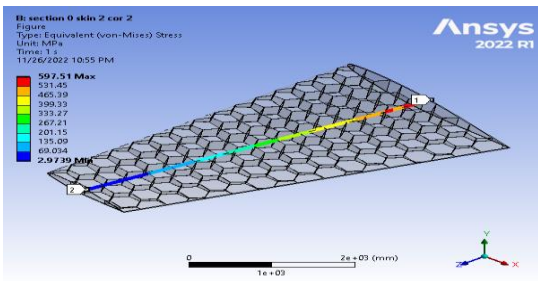

Figure 5.120. Contour Equivalent Stress at one cell skin 2 core 2 (Mach 0.8)

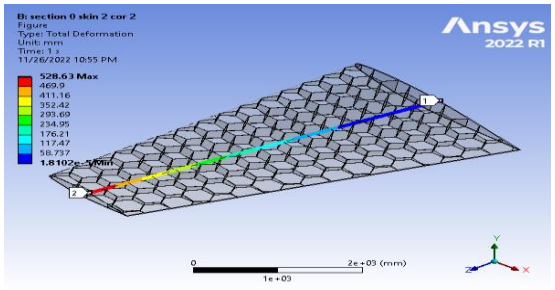

Figure 5.119. Contour Total Deformation at one cell skin 2 core 2 (Mach 0.8)

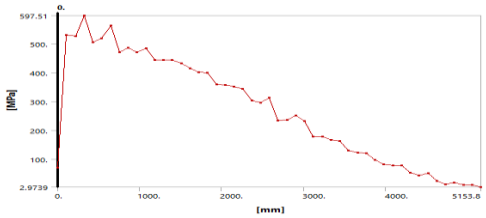

Figure 5.122. Equivalent Stress at section 1.2 skin 2 core 2 (Mach 0.8)

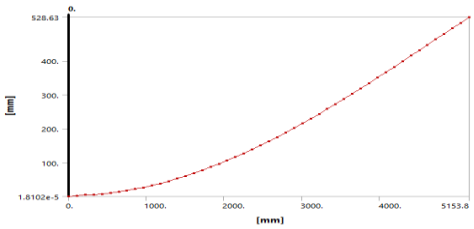

Figure 5.121. Variation of deformation at section 1.2 skin 2 core 2(Mach 0.8)

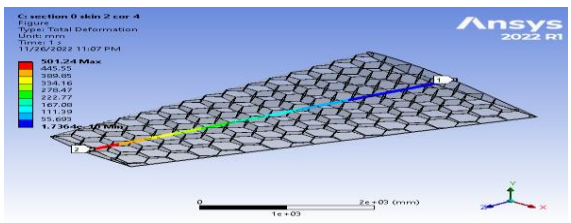

Figure 5.124. Contour Total Deformation at one cell skin 2 core 4 (Mach 0.8)

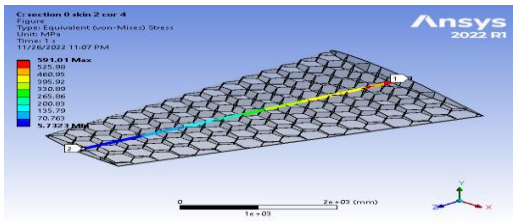

Figure 5.123. Contour Equivalent Stress at one cell skin 2 core 4 (Mach 0.8)

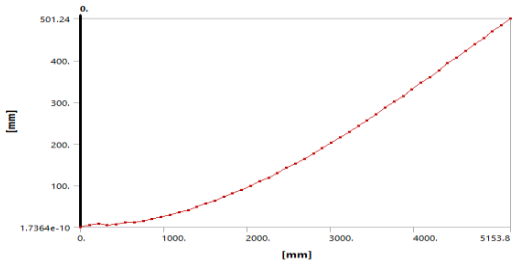

Figure 5.126. Variation of deformation at section 1.2 skin 2 core 4 (Mach 0.8)

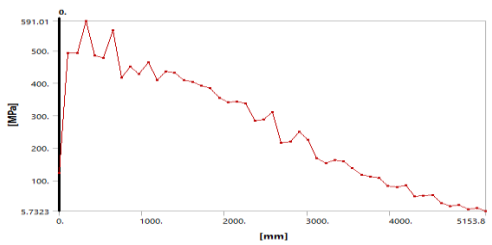

Figure 5.125. Equivalent Stress at section 1.2 skin 2 core 4 (Mach 0.8)

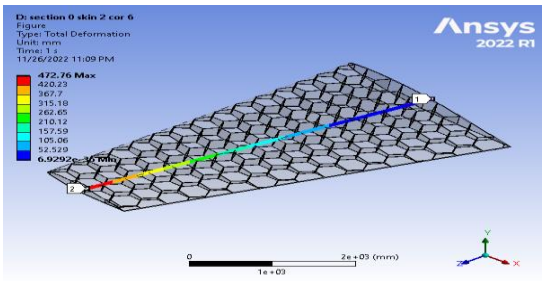

Figure 5.128. Contour Total Deformation at one cell skin 2 core 6 (Mach 0.8)

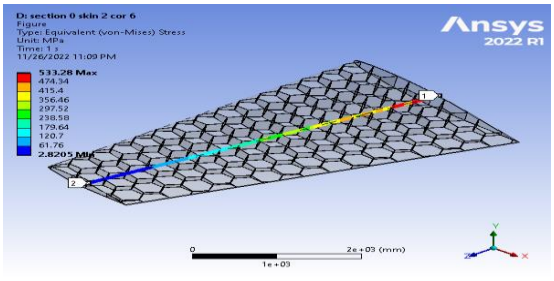

Figure 5.127. Contour Equivalent Stress at one cell skin 2 core 6 (Mach 0.8)

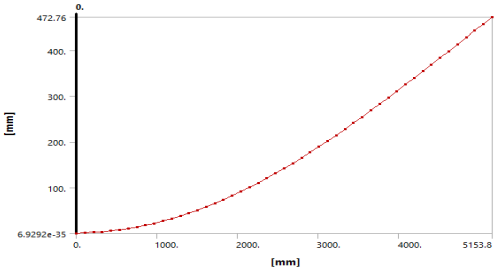

Figure 5.129. Variation of deformation at section 1.2 skin 2 core 6 (Mach 0.8)

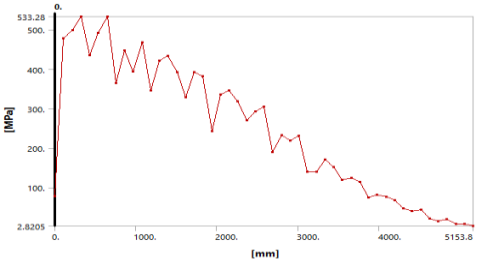

Figure 5.130. Equivalent Stress at section 1.2 skin 2 core 6 (Mach 0.8)

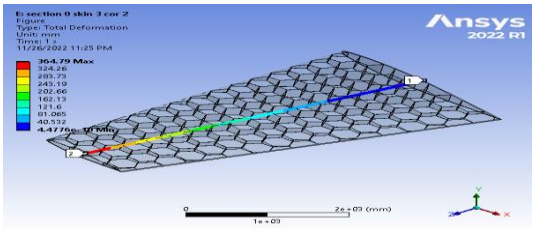

Figure 5.131. Contour Total Deformation at one cell skin 3 core 2 (Mach 0.8)

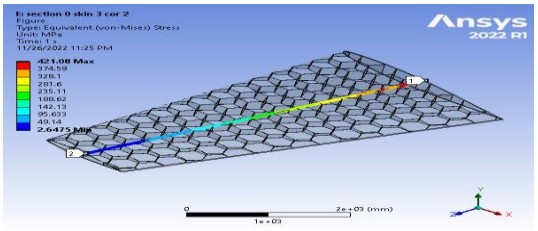

Figure 5.132. Contour Equivalent Stress at one cell skin 3 core 2 (Mach 0.8)

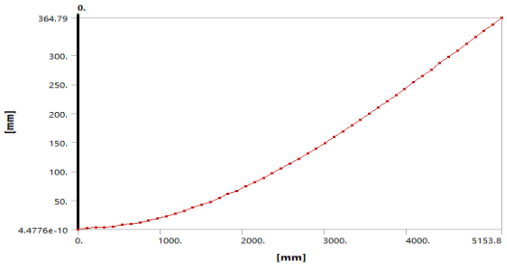

Figure 5.134. Variation of deformation at section 1.2 skin 3 core 2 (Mach 0.8)

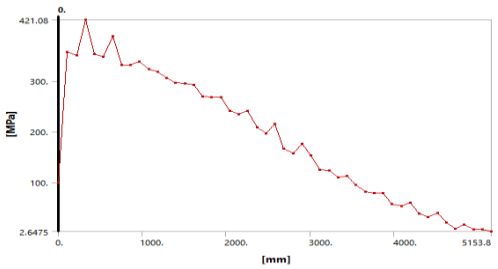

Figure 5.133. Equivalent Stress at section 1.2 skin 3 core 2 (Mach 0.8)

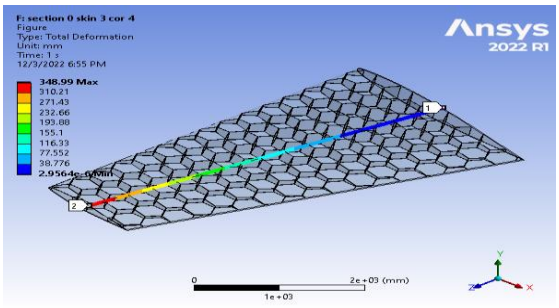

Figure 5.136. Contour Total Deformation at one cell skin 3 core 4 (Mach 0.8)

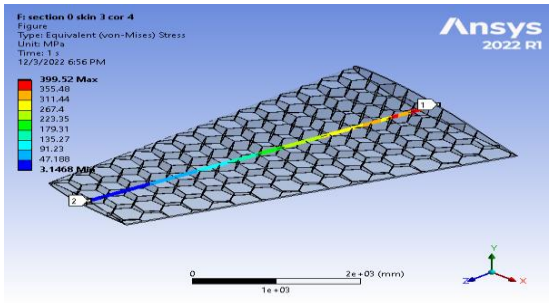

Figure 5.135. Contour Equivalent Stress at one cell skin 3 core 4 (Mach 0.8)

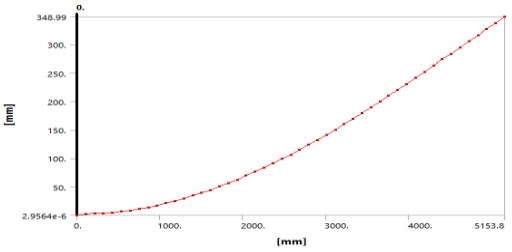

Figure 5.138. Variation of deformation at section 1.2 skin 3 core 4 (Mach 0.8)

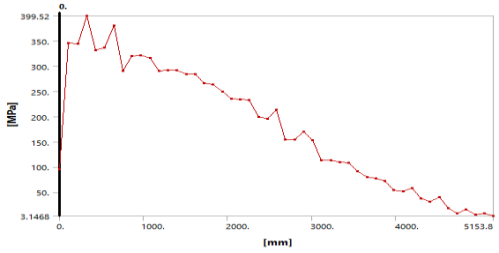

Figure 5.137. Equivalent Stress at section 1.2 skin 3 core 4 (Mach 0.8)

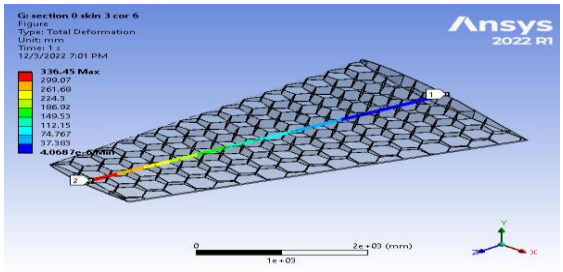

Figure 5.140. Contour Total Deformation at one cell skin 3 core 6 (Mach 0.8)

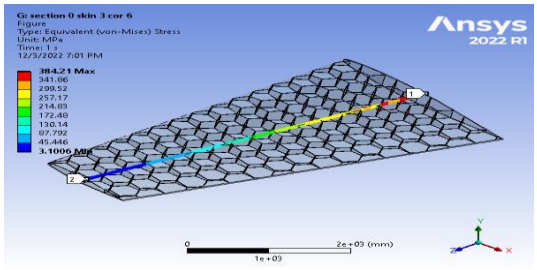

Figure 5.139. Contour Equivalent Stress at one cell skin 3 core 6 (Mach 0.8)

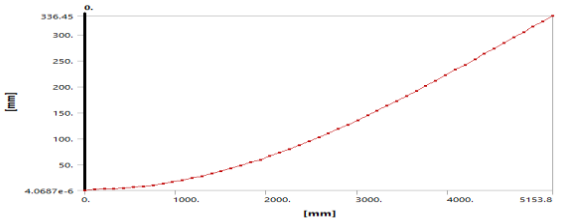

Figure 5.142. Variation of deformation at section 1.2 skin 3 core 6 (Mach 0.8)

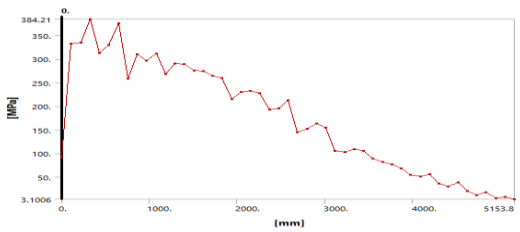

Figure 5.141. Equivalent Stress at section 1.2 skin 3 core 6 (Mach 0.8)

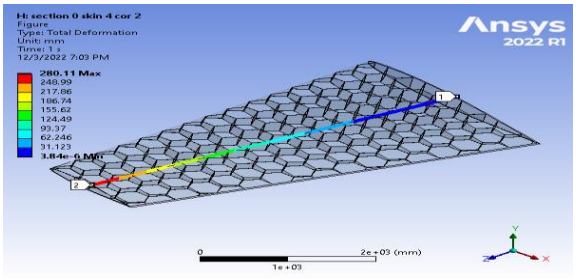

Figure 5.144. Contour Total Deformation at one cell skin 4 core 2 (Mach 0.8)

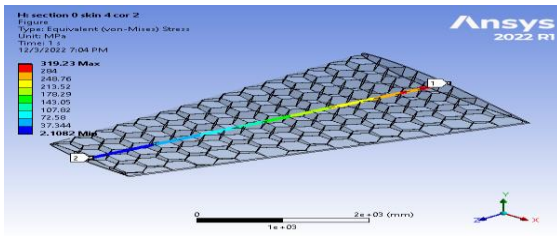

Figure 5.143. Contour Equivalent Stress at one cell skin 4 core 2 (Mach 0.8)

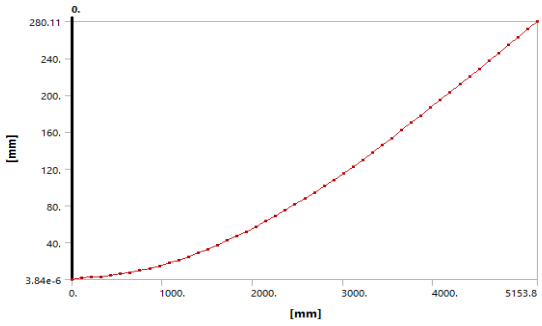

Figure 5.145. Variation of deformation at section 1.2 skin 4 core 2 (Mach 0.8)

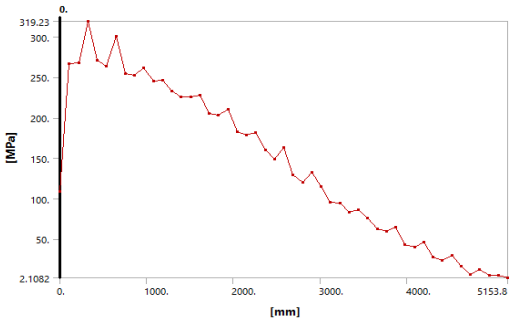

Figure 5.146. Equivalent Stress at section 1.2 skin 4 core 2 (Mach 0.8)

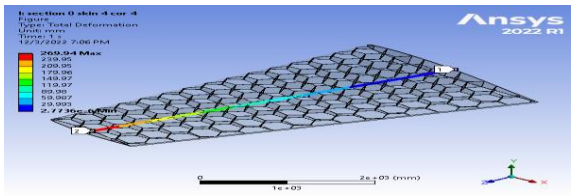

Figure 5.147. Contour Total Deformation at one cell skin 4 core 4 (Mach 0.8)

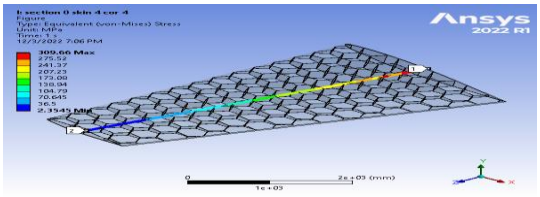

Figure 5.148. Contour Equivalent Stress at one cell skin 4 core 4 (Mach 0.8)

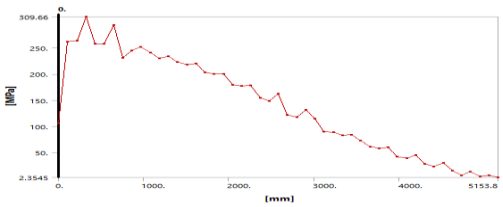

Figure 5.150. Contour Equivalent Stress at section 1.2 skin 4 core 4 (Mach 0.8)

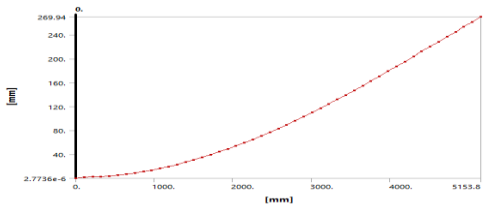

Figure 5.149. Variation of deformation at section 1.2 skin 4 core 4 (Mach 0.8)

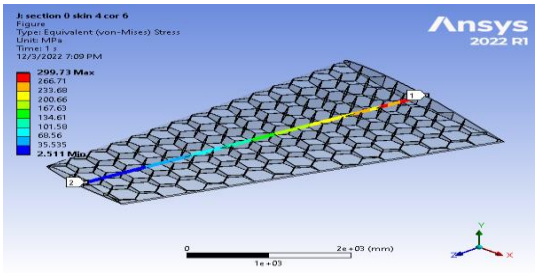

Figure 5.151. Contour Equivalent Stress at one cell skin 4 core 6 (Mach 0.8)

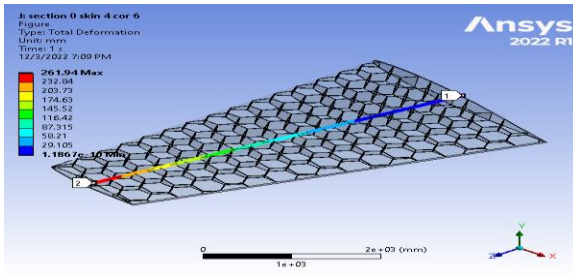

Figure 5.152. Contour Total Deformation at one cell skin 4 core 6 (Mach 0.8)

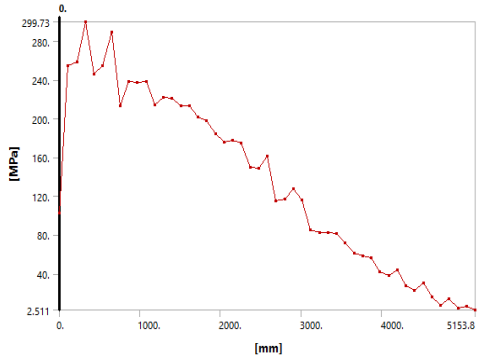

Figure 5.153. Equivalent Stress at section 1.2 skin 4 core 6 (Mach 0.8)

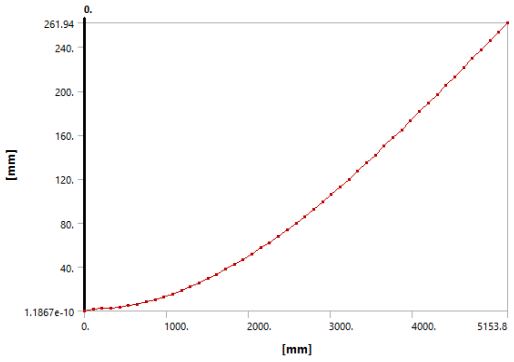

Figure 5.154. Variation of deformation at section 1.2 skin 4 core 6 (Mach 0.8)

5.2.4. Wing. 6 Cells

The determination of displacements and stress using the different structural modeling are presented here. The finite element modeling was used by import the pressure distribution and applied on the wing structure .it corresponds with the real case this give the true picture of deformation and stresses on the wing skin.

The effects of design parameters of the wing structure are discussed as follows.

- Effects of skin thickness.
- Effects of number of cells
- Effects of core thickness (invariably of skin thickness)

5.2.4.1. (Effects of Skin Thickness)

Using the skin= 2mm and core thickness=2mm, the maximum deformation= 149.83mm and the resulted Von Mises=208.83**MPa**

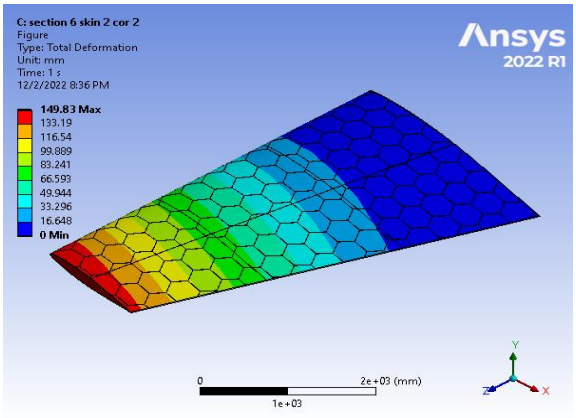

Figure 5.156. Contour Total Deformation at 6 cells cells skin 2 core 2 (Mach 0.4)

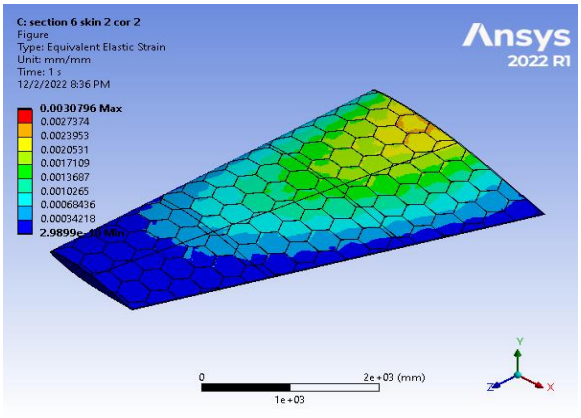

Figure 5.155. Contour Equivalent Stress at 6 cells cells skin 2 core 2 (Mach 0.4)

Increasing the skin thickness=3mm, the deformation = 104.24 mm and the resulted Von Mises =141.84 MPa mises=mm

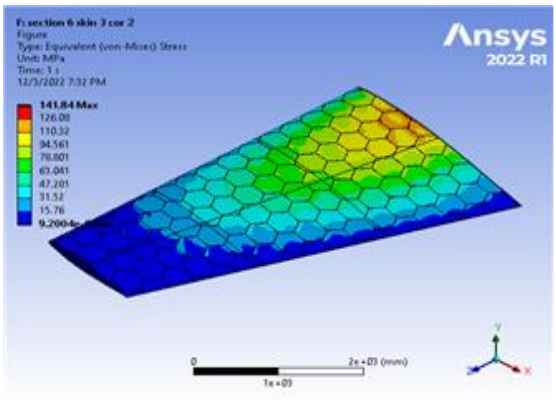

Figure 5.157. Contour Equivalent Stress at 6 cells skin 3 core 2 (Mach 0.4)

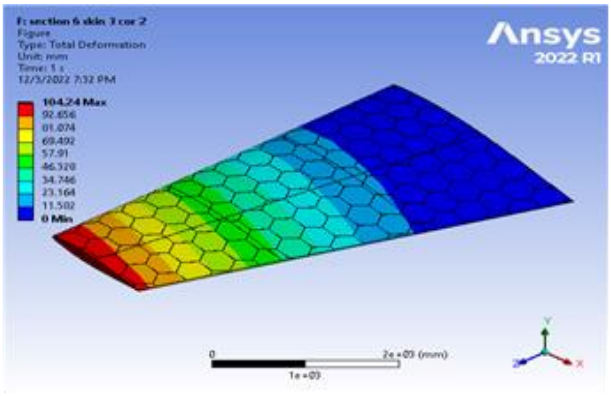

Figure 5.158. Contour Total Deformation at 6 cells skin 3 core 2 (Mach 0.4)

Table 5.4 shows the results of using different thickness (invariably of core) note in the Table 5.4 that some of the points in red failed because the value of the value exceeded Yield Strength=505 N/(mm)^2. And that the least mass was (210.46 Kg) and the larger mass was (451.26 Kg) in using Material (Al7075 T6). Table 5.4 shows us the change in the total Von Mises Stress was largest (765.07 MPa) at skin thickness (2mm), core (2mm), and Mach 0.8 and which failed, while the lowest was stress (100.77 MPa) at a skin thickness of (4mm), core (6mm) and Mach0.4. Also, this Table 5.4 shows that the largest Equivalent strain of (0.0011286 mm /mm) occurs in the model with The skin thickness (4mm) and core (6mm) at Mach 0.8, while the least deviation is (0.001417mm/mm) obtained in the model with a skin thickness (2mm) and core (6mm) at Mach 0.4.

Table 5.4. Wing. 6 cells at angle of attack **12**°

Mach No	Skin thickness(mm)	Core thickness(mm)	Max deformation (mm)	Von Mises stress (MPa)	Equivalent strain (mm/mm)	Mass (kg)
	2	2	149.83	208.83	0.00308	210.46
	3	2	104.24	141.84	0.002064	268.93
	4	2	80.478	113.23	0.001575	328.02
	2	4	138.66	203.51	0.002887	273.77
	3	4	98.149	136.93	0.001962	331.6
	4	4	76.558	104.97	0.001509	389.87
	2	6	129.37	196.4	0.002781	336.7
	3	6	93.145	130.62	0.001839	393.69
0.4	4	6	73.405	100.77	0.001417	451.26
Mach No	Skin thickness(mm)	Core thickness(mm)	Max deformation (mm)	Von Mises stress (MPa)	Equivalent strain (mm/mm)	Mass (kg)
	2	2	329.04	467.96	0.0069023	210.46
	3	2	228.96	321.24	0.0046238	268.93
	4	2	176.79	260.86	0.003631	328.02
	2	4	304.44	456.06	0.0064775	273.77
	3	4	215.53	307.49	0.0044095	331.6
	4	4	168.13	237.86	0.003391	389.87
	2	6	283.99	441.37	0.0065513	336.7
	3	6	204.5	294.99	0.004155	393.69
0.6	4	6	161.18	227.4	0.003184	451.26
Mach No	Skin thickness(mm)	Core thickness(mm)	Max deformation (mm)	Von Mises stress (MPa)	Equivalent strain (mm/mm)	Mass (kg)
	2	2	531.3	765.07	0.011286	210.46
	3	2	369.72	526.43	0.007557	268.93
	4	2	285.5	426.58	0.005938	328.02
	2	4	491.52	746.52	0.010595	273.77
	3	4	347.99	504.07	0.00723	331.6
	4	4	271.47	389.03	0.005558	389.87
	2	6	458.47	724.37	0.010264	336.7
	3	6	33.07	480.62	0.006771	393.69
0.8	4	6	260.24	372.02	0.00522	451.26

5.2.4.2. (Effects of Core Thickness)

Using the skin= 2mm and core thickness=2mm, the maximum deformation=149.83 mm and the resulted Von Mises=208.83MPa

the resulted von Increasing the skin thickness=3mm, the deformation = 104.24mm and the resulted von =141.84MPa

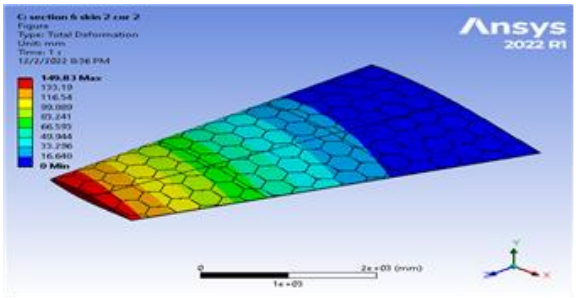

Figure 5.159. Contour Total Deformation at 6 cells skin 2 core 2 (Mach 0.6)

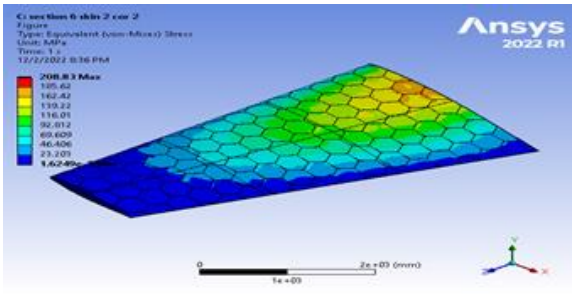

Figure 5.160. Contour Equivalent Stress at 6 cells skin 2 core 2(Mach 0.6)

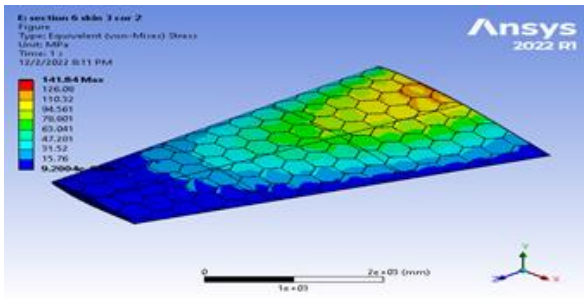

Figure 5.162. Contour Equivalent Stress at 6 cells skin 3 core 2(Mach 0.6)

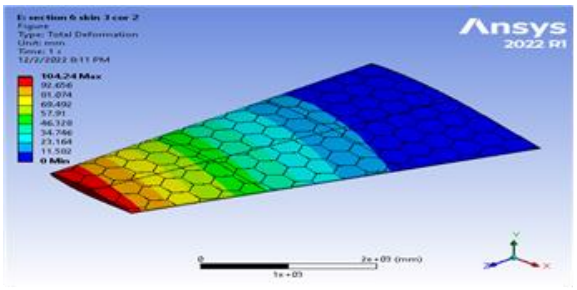

Figure 5.161. Contour Total Deformation at 6 cells skin 3 core 2 (Mach 0.6)

Table 5.5. Wing. 6 cells at angle of attack **12**°

Mach No	skin thickness(mm)	Core thickness(mm)	Max deformation (mm)	Equivalent stress (MPa)	Equivalent strain (mm/mm)	Mass (kg)
0.4	2	2	149.83	208.83	0.00308	210.46
	2	4	138.66	203.51	0.002887	273.77
	2	6	129.37	196.4	0.002781	336.7
	3	2	104.24	141.84	0.002064	268.93
	3	4	98.149	136.93	0.001962	331.6
	3	6	93.145	130.62	0.001839	393.69
	4	2	80.478	113.23	0.001575	328.02
	4	4	76.558	104.97	0.001509	389.87
	4	6	73.405	100.77	0.001417	451.26
Mach No	skin thickness(mm)	Core thickness(mm)	Max deformation (mm)	Equivalent stress (MPa)	Equivalent strain (mm/mm)	Mass (kg)
0.6	2	2	329.04	467.96	0.0069023	210.46
	2	4	304.44	456.06	0.0064775	273.77
	2	6	283.99	441.37	0.0065513	336.7
	3	2	228.96	321.24	0.0046238	268.93
	3	4	215.53	307.49	0.0044095	331.6
	3	6	204.5	294.99	0.004155	393.69
	4	2	176.79	260.86	0.003631	328.02
	4	4	168.13	237.86	0.003391	389.87
	4	6	161.18	227.4	0.003184	451.26
Mach No	skin thickness(mm)	Core thickness(mm)	Max deformation (mm)	Equivalent stress (MPa)	Equivalent strain (mm/mm)	Mass (kg)
0.8	2	2	531.3	765.07	0.011286	210.46
	2	4	491.52	746.52	0.010595	273.77
	2	6	458.47	724.37	0.010264	336.7
	3	2	369.72	526.43	0.007557	268.93
	3	4	347.99	504.07	0.00723	331.6
	3	6	330.17	480.62	0.006771	393.69
	4	2	285.5	426.58	0.005938	328.02
	4	4	271.47	389.03	0.005558	389.87
	4	6	260.24	372.02	0.00522	451.26

Mach No	skin thickness(mm)	Core thickness(mm)	Max deformation (mm)	Equivalent stress (MPa)	Equivalent strain (mm/mm)	Mass (kg)
0.4	2	2	149.83	208.83	0.00308	210.46
	2	4	138.66	203.51	0.002887	273.77
	2	6	129.37	196.4	0.002781	336.7
	3	2	104.24	141.84	0.002064	268.93
	3	4	98.149	136.93	0.001962	331.6
	3	6	93.145	130.62	0.001839	393.69

	4	2	80.478	113.23	0.001575	328.02
	4	4	76.558	104.97	0.001509	389.87
	4	6	73.405	100.77	0.001417	451.26
Mach No	skin thickness(mm)	Core thickness(mm)	Max deformation (mm)	Equivalent stress (MPa)	Equivalent strain (mm/mm)	Mass (kg)
	2	2	149.83	208.83	0.00308	210.46
	2	4	138.66	203.51	0.002887	273.77
	2	6	129.37	196.4	0.002781	336.7
	3	2	104.24	141.84	0.002064	268.93
0.4	3	4	98.149	136.23	0.001962	331.6
0.6	3	6	93.145	130.62	0.001839	393.69
	4	2	80.478	113.23	0.001575	328.02
	4	4	76.558	104.97	0.001509	389.87
	4	6	73.405	100.77	0.001417	451.26
Mach No	skin thickness(mm)	Core thickness(mm)	Max deformation (mm)	Equivalent stress (MPa)	Equivalent strain (mm/mm)	Mass (kg)
	2	2	329.04	467.96	0.0069023	210.46
	2	4	304.44	456.06	0.0064775	273.77
	2	6	283.99	441.37	0.0065513	336.7
	3	2	228.96	324.24	0.0046238	268.93
0.6	3	4	215.53	307.49	0.0044095	331.6
	3	6	204.5	294.99	0.004155	393.69
	4	2	176.79	260.86	0.003631	328.02
	4	4	168.13	237.86	0.003291	389.87
	4	6	161.18	227.4	0.003184	451.26
Mach No	skin thickness(mm)	Core thickness(mm)	Max deformation (mm)	Equivalent stress (MPa)	Equivalent strain (mm/mm)	Mass (kg)
	2	2	531.3	765.07	0.011286	210.46
	2	4	491.53	746.52	0.010595	273.77
	2	6	458.47	724.37	0.010638	336.7
	3	2	369.72	526.43	0.007557	268.93
0.8	3	4	347.99	504.07	0.00723	331.6
	3	6	330.17	480.62	0.006771	393.69
	4	2	285.5	426.58	0.005938	328.02
	4	4	271.47	389.03	0.005558	389.87
	4	6	260.24	372.02	0.00522	451.26

Table 5.5 shows the results of using different thickness (invariably of core). note in the

Mach No	skin thickness(mm)	Core thickness(mm)	Max deformation (mm)	Equivalent stress (MPa)	Equivalent strain (mm/mm)	Mass (kg)
	3	4	215.53	307.49	0.0044095	331.6
	3	6	204.5	294.99	0.004155	393.69
Mach No	skin thickness(mm)	Core thickness(mm)	Max deformation (mm)	Equivalent stress (MPa)	Equivalent strain (mm/mm)	Mass (kg)
	4	2	176.79	260.86	0.003631	328.02
	4	4	168.13	237.86	0.003391	389.87
	4	6	161.18	227.4	0.003184	451.26
Mach No	skin thickness(mm)	Core thickness(mm)	Max deformation (mm)	Equivalent stress (MPa)	Equivalent strain (mm/mm)	Mass (kg)
	2	2	140.83	208.83	0.00308	210.46
	2	4	138.66	203.51	0.002887	273.77
	2	6	129.37	196.4	0.002781	336.7
0.4	2 / 3	2	531.3 / 104.24	765.07 / 141.84	0.011286 / 0.002064	210.46 / 268.93
	2 / 3	4	491.52 / 98.149	746.52 / 136.93	0.010505 / 0.001962	273.77 / 331.6
	2 / 3	6	[illegible] / 93.143	[illegible] / 130.67	[illegible] / 0.001869	336.7 / 393.69
0.8	3 / 4	2	[illegible] / 80.478	[illegible] / 116.43	[illegible] / 0.001575	268.93 / 328.02
	3 / 4	4	347.99 / 76.558	504.07 / 104.07	0.00723 / 0.001509	331.6 / 389.87
	3 / 4	6	330.17 / 73.405	480.62 / 100.77	0.006771 / 0.001417	393.69 / 451.26
Mach No	skin thickness(mm)	Core thickness(mm)	Max deformation (mm)	Equivalent stress (MPa)	Equivalent strain (mm/mm)	Mass (kg)
	4	2	285.5	426.58	0.005938	328.02
	4	4	271.47	389.03	0.005558	389.87
0.6	4 / 2	6 / 2	260.24 / 329.64	372.02 / 467.96	0.00522 / 0.0069023	451.26 / 210.48

Table 5.5 that some of the points in red failed because the value of the value exceeded Yield Strength=505 N/(mm)^2. And that the least mass was (210.46 Kg) and the largest mass was (451.26 Kg) in using Material (Al7075 T6).

Mach No	skin thickness(mm)	Core thickness(mm)	Max deformation (mm)	Equivalent stress (MPa)	Equivalent strain (mm/mm)	Mass (kg)
	2	4	304.44	456.06	0.0064775	273.77
	2	6	283.99	441.37	0.0065513	336.7
	3	2	228.96	321.24	0.0046238	268.93
	3	4	215.58	307.49	0.0044095	331.6
	3	6	204.5	294.99	0.004155	393.69
	2	2	140.89	208.83	0.00308	210.46
	4	2	170.79	266.86	0.003631	328.02
	2	4	138.66	203.51	0.002887	273.77
	4	4	168.15	237.86	0.003391	389.87
	2	6	129.37	196.4	0.002781	336.7
	4	6	161.18	227.4	0.003184	451.26
0.4	3	2	104.24	141.84	0.002064	268.93
	3	4	98.149	136.93	0.001962	331.6
	3	6	93.145	130.62	0.001839	393.69
	2	2	531.3	765.07	0.011286	210.46
	4	2	80.478	113.23	0.001575	328.02
	2	4	491.52	746.52	0.010505	273.77
	4	4	76.558	104.97	0.001509	389.87
	2	6	458.07	720.37	0.010217	336.7
	4	6	73.405	100.77	0.001464	451.26
0.8	3	2	369.72	526.43	0.007557	268.93
	3	4	347.99	504.07	0.00723	331.6
	3	6	330.17	480.62	0.006771	393.69
0.6	2	2	329.04	467.96	0.0069023	210.46
	4	2	285.5	426.58	0.005938	328.02
	2	4	304.44	456.06	0.0064775	273.77
	4	4	271.47	389.03	0.005558	389.87
	2	6	283.99	441.37	0.0065513	336.7
	4	6	260.24	372.02	0.00522	451.26

Table 5.5 shows us the change in the total Von Mises Stress was largest (765.07 MPa) at skin thickness (2mm), core (2mm), and Mach 0.8 and which failed, while the lowest was stress (100.77 MPa) at a skin thickness of (4mm), core (6mm) and Mach0.4. Also, this

	3	2	228.96	321.24	0.0046238	268.93
	3	4	215.53	307.49	0.0044095	331.6
Mach No	skin thickness(mm)	Core thickness(mm)	Max deformation (mm)	Equivalent stress (MPa)	Equivalent strain (mm/mm)	Mass (kg)
	3	6	204.5	294.99	0.004155	393.69
	4	2	176.79	260.86	0.003631	328.02
	4	4	168.13	237.86	0.003391	389.87
	4	6	161.13	227.4	0.003184	451.26
	2	4	138.66	203.51	0.002887	273.77
Mach No	skin thickness(mm)	Core thickness(mm)	Max deformation (mm)	Equivalent stress (MPa)	Equivalent strain (mm/mm)	Mass (kg)
	2	6	129.37	196.4	0.002781	336.7
	3	2	104.24	141.84	0.002064	268.93
0.4	3	4	98.149	136.93	0.001902	331.6
	3	6	93.143	130.62	0.001839	393.69
	4	2	80.478	114.33	0.001674	328.02
	4	4	76.578	106.47	0.001509	389.87
	4	6	73.405	100.77	0.001417	451.26
0.8	3	4	347.99	504.07	0.00723	331.6
Mach No	skin thickness(mm)	Core thickness(mm)	Max deformation (mm)	Equivalent stress (MPa)	Equivalent strain (mm/mm)	Mass (kg)
	3	6	330.17	480.62	0.0067771	393.69
	4	2	285.5	426.58	0.005938	328.02
	4	4	271.47	389.03	0.005558	389.87
0.6	2	2	329.04	467.96	0.0065023	210.46
	4	6	260.24	372.02	0.00522	451.26

Table 5.5 shows that the largest Equivalent strain of (0.0011286 mm /mm) occurs in the model with The skin thickness (4mm) and core (6mm) at Mach 0.8, while the least deviation is (0.001417mm/mm) obtained in the model with a skin thickness (2mm) and core (6mm) at Mach 0.4.

The summary of the results which are extracted from the contours and shown in

	2	4	304.44	456.06	0.0064775	273.77
	2	6	283.99	441.37	0.0065513	336.7
	3	2	228.96	321.24	0.0046238	268.93
	3	4	215.53	307.49	0.0044095	331.6
	3	6	204.5	294.99	0.004155	393.69
	4	2	176.79	260.86	0.003631	328.02
	4	4	168.13	237.86	0.003391	389.87
	4	6	161.18	227.4	0.003184	451.26
Mach No	skin thickness(mm)	Core thickness(mm)	Max deformation (mm)	Equivalent stress (MPa)	Equivalent strain (mm/mm)	Mass (kg)
0.8	2	2	531.3	765.07	0.011286	210.46
	2	4	491.52	746.52	0.010595	273.77
	2	6	458.47	724.37	0.010264	336.7
	3	2	369.72	526.43	0.007557	268.93
	3	4	347.99	504.07	0.00723	331.6
	3	6	330.17	480.62	0.006771	393.69
	4	2	285.5	426.58	0.005938	328.02
	4	4	271.47	389.03	0.005558	389.87
	4	6	260.24	372.02	0.00522	451.26

Table 5.5. some cases fail to the maximum stresses developed compared to the yield stress at the used Material (Al7075 T6) when a stress ratio less than 1. They are labelled in red colour. even the masses are low compared to the used mass in A/C design.

5.2.4.3. (Effects of Number Cells)

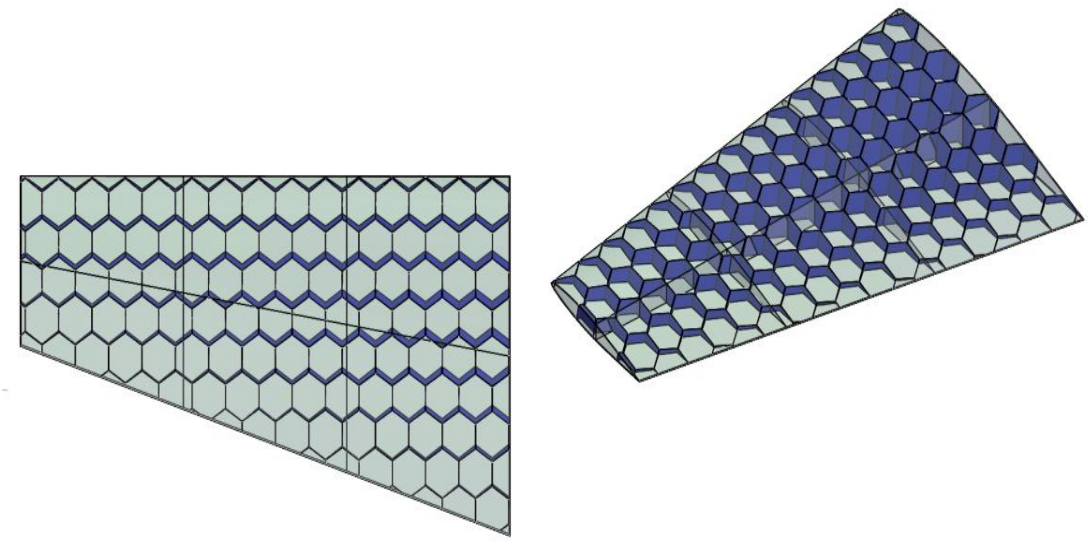

Figure 5.163. Wing .6 cells

5.2.4.4. MACH (0.4), (0.6), (0.8)

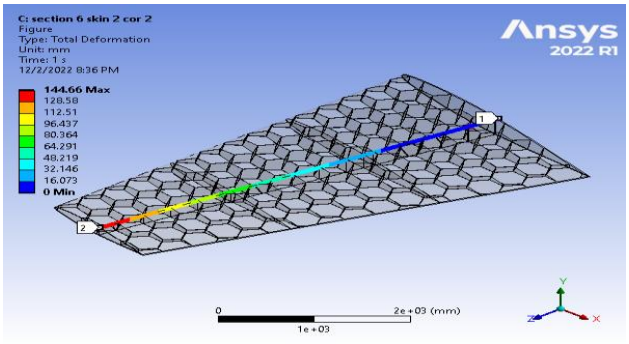

Figure 5.164. Contour Total Deformation at 6 cells skin 2 core 2 (Mach 0.4)

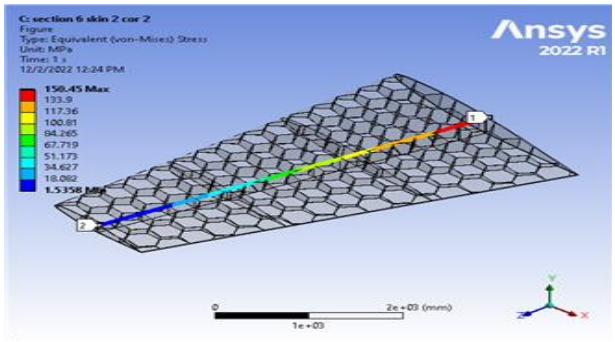

Figure 5.165. Contour Equivalent Stress at 6 cells skin 2 core 2 (Mach 0.4)

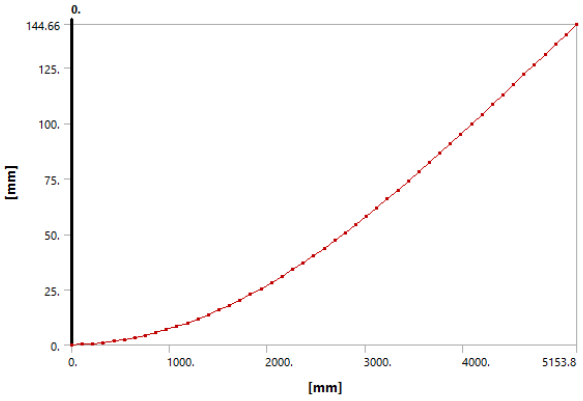

Figure 5.166. Variation of deformation at section 1.2 skin 2 core 2 (Mach 0.4)

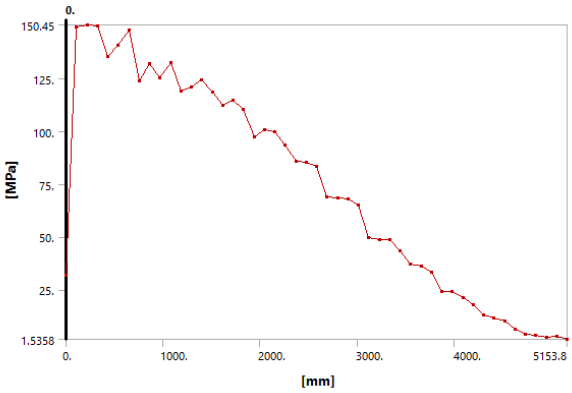

Figure 5.167. Equivalent Stress at section 1.2 skin 2 core 2 (Mach 0.4)

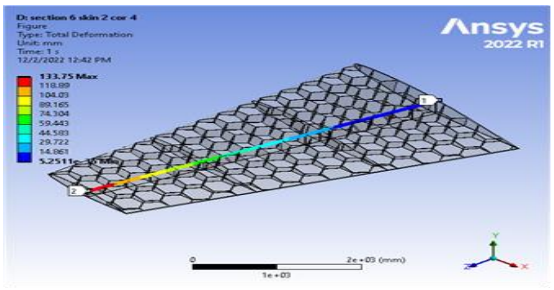

Figure 5.169. Contour Total Deformation at 6 cells skin 2 core 4 (Mach 0.4)

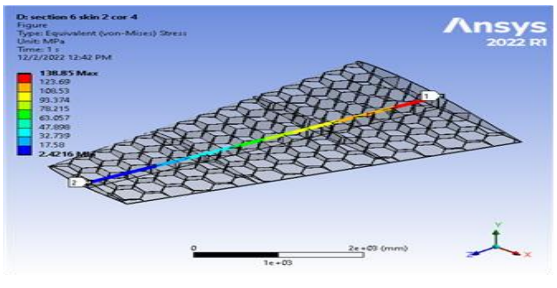

Figure 5.168. Contour Equivalent Stress at 6 cells skin 2 core 4 (Mach 0.4)

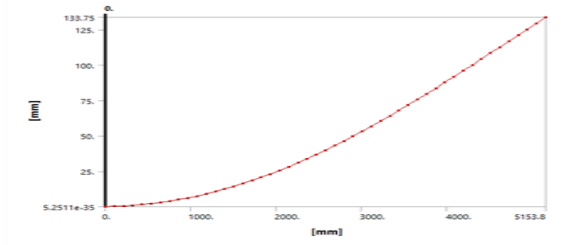

Figure 5.171. Variation of deformation at section 1.2 skin 2 core 4 (Mach 0.4)

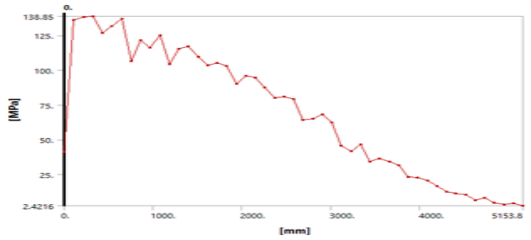

Figure 5.170. Equivalent Stress at section 1.2 skin 2 core 4 (Mach 0.4)

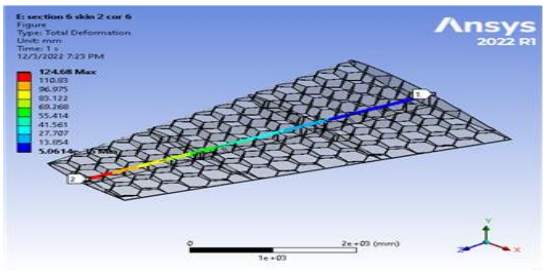

Figure 5.173. Contour Total Deformation at 6 cells skin 2 core 6(Mach 0.4)

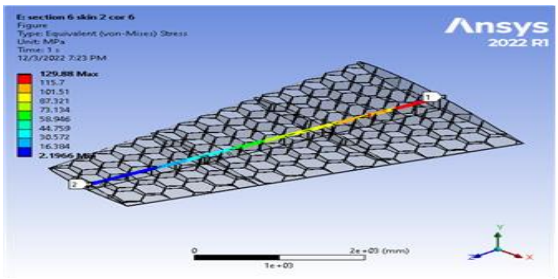

Figure 5.172. Contour Equivalent Stress at 6 cells skin 2 core 6(Mach 0.4)

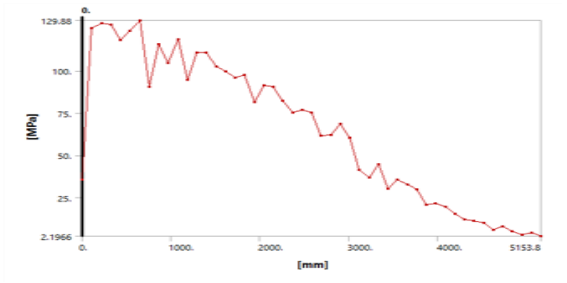

Figure 5.174. Equivalent Stress at section 1.2 skin 2 core 6(Mach 0.4)

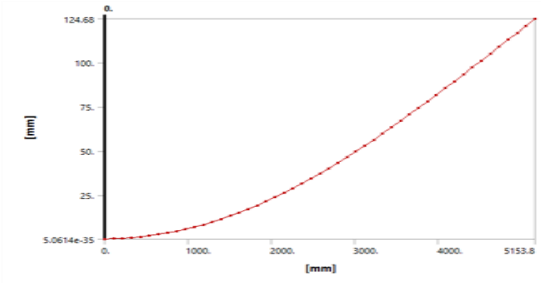

Figure 5.175. Variation of deformation at section 1.2 skin 2 core 6(Mach 0.4)

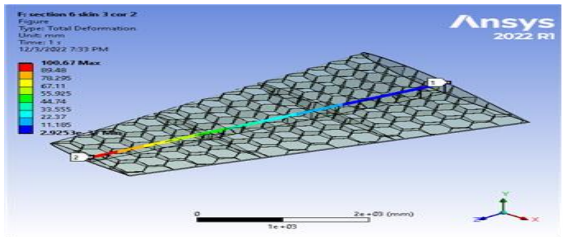

Figure 5.177. Contour Total Deformation at 6 cells skin 3 core 2 (Mach 0.4)

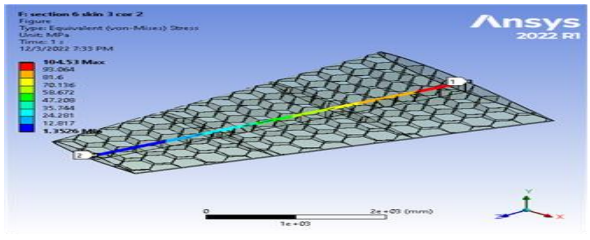

Figure 5.176. Contour Equivalent Stress at 6 cells skin 3 core 2 (Mach 0.4)

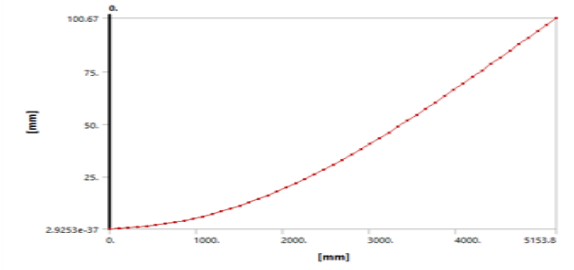

Figure 5.179. Variation of deformation at section 1.2 skin 3 core 2(Mach 0.4)

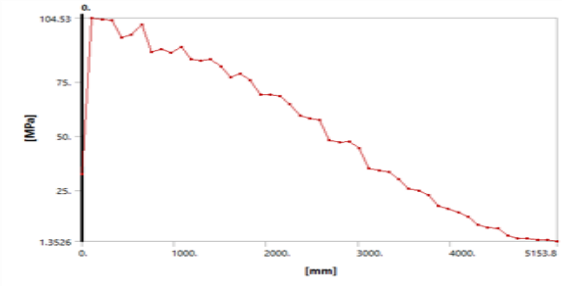

Figure 5.178. Equivalent Stress at section 1.2 skin 3 core 2 (Mach 0.4)

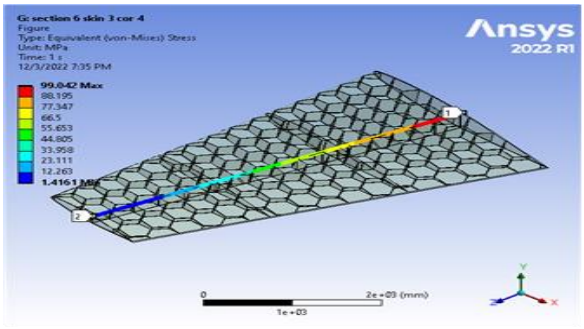

Figure 5.180. Contour Equivalent Stress at 6 cells skin 3 core 4 (Mach 0.4)

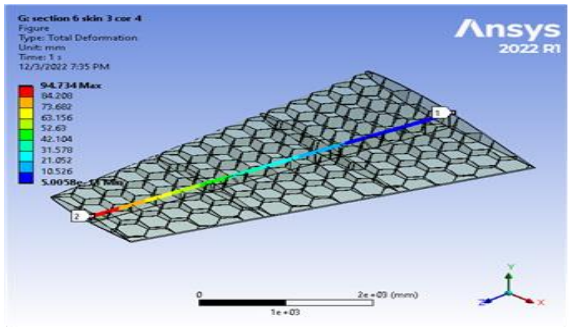

Figure 5.181. Contour Total Deformation at 6 cells skin 3 core 4 (Mach 0.4)

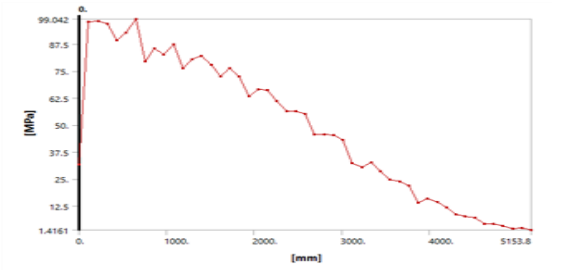

Figure 5.182. Equivalent Stress at section 1.2 skin 3 core 4 (Mach 0.4)

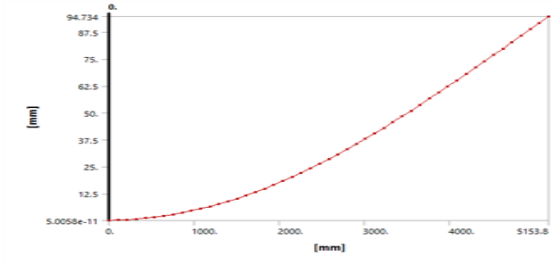

Figure 5.183. Variation of deformation at section 1.2 skin 3 core 4 (Mach 0.4)

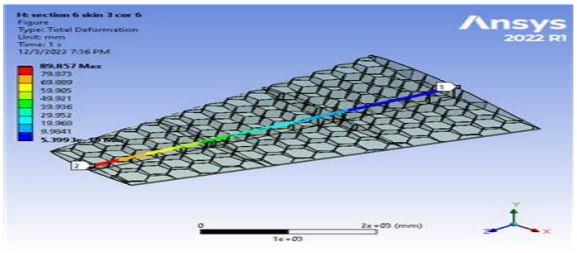

Figure 5.184. Contour Total Deformation at 6 cells skin 3 core 6 (Mach 0.4)

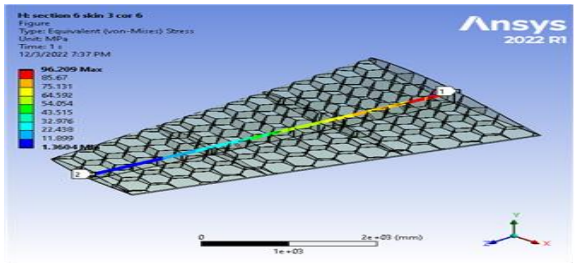

Figure 5.185. Contour Equivalent Stress at 6 cells skin 3 core 6 (Mach 0.4)

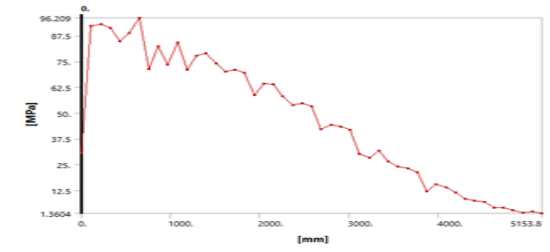

Figure 5.187. Equivalent Stress at section 1.2 skin 3 core 6 (Mach 0.4)

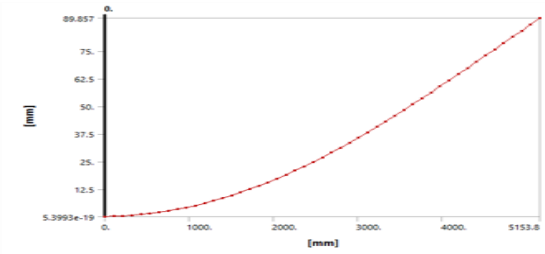

Figure 5.186. Variation of deformation at section 1.2 skin 3 core 6 (Mach 0.4)

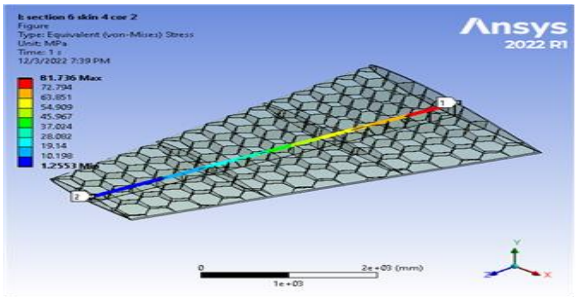

Figure 5.188. Contour Equivalent Stress at 6 cells skin 4 core 2 (Mach 0.4)

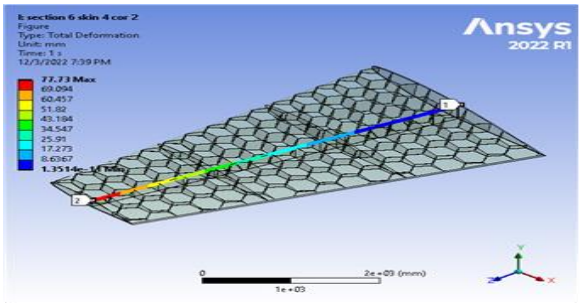

Figure 5.189. Contour Total Deformation at 6 cells skin 4 core 2 (Mach 0.4)

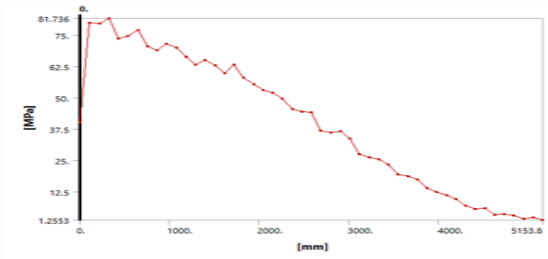

Figure 5.191. Equivalent Stress at section 1.2 skin 4 core 2 (Mach 0.4)

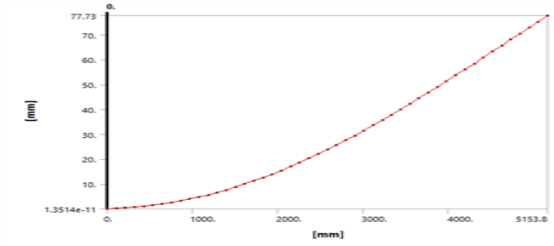

Figure 5.190. Variation of deformation at section 1.2 skin 4 core 2 (Mach 0.4)

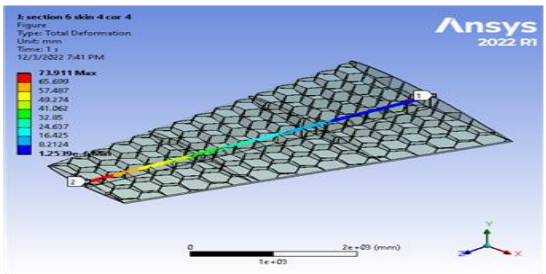

Figure 5.193. Contour Total Deformation at 6 cells skin 4 core 4 (Mach 0.4)

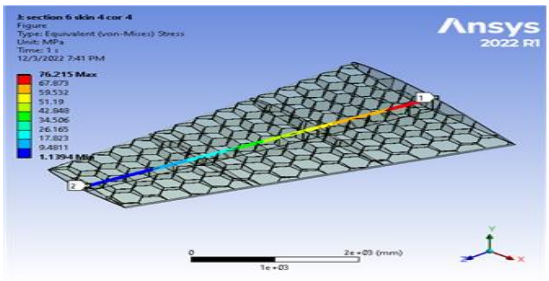

Figure 5.192. Contour Equivalent Stress at 6 cells skin 4 core 4 (Mach 0.4)

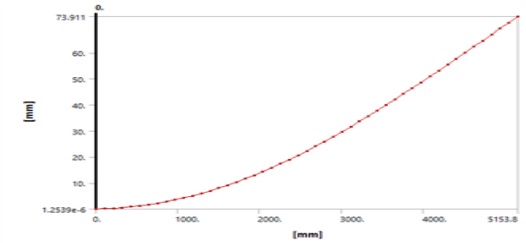

Figure 5.195. Variation of deformation at section 1.2 skin 4 core 4 (Mach 0.4)

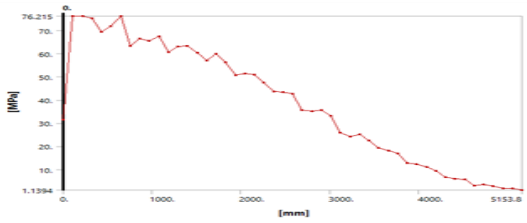

Figure 5.194. Equivalent Stress at section 1.2 skin 4 core 4 (Mach 0.4)

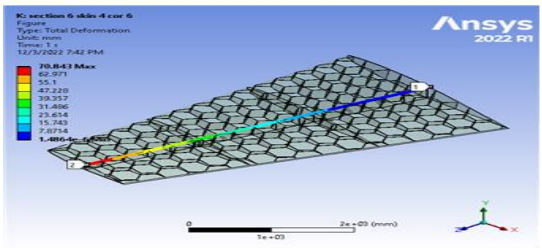

Figure 5.197. Contour Total Deformation at 6 cells skin 4 core 6 (Mach 0.4)

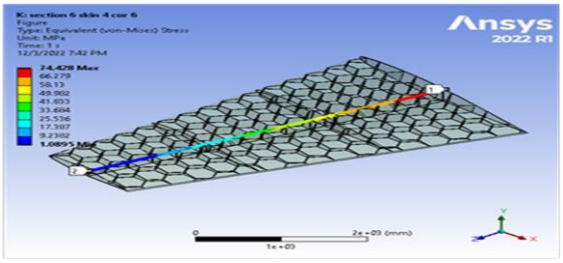

Figure 5.196. Contour Equivalent Stress at 6 cells skin 4 core 6(Mach 0.4)

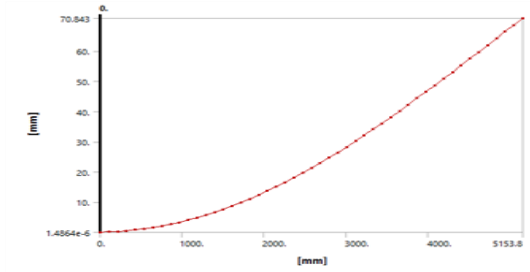

Figure 5.199. Variation of deformation at section 1.2 skin 4 core 6 (Mach 0.4)

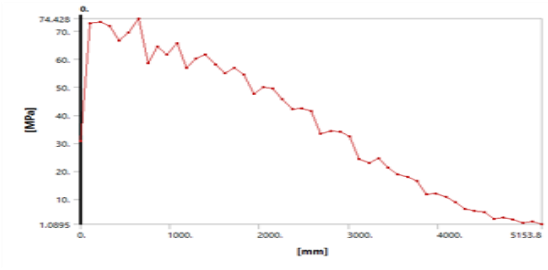

Figure 5.198. Equivalent Stress at section 1.2 skin 4 core 6 (Mach 0.4)

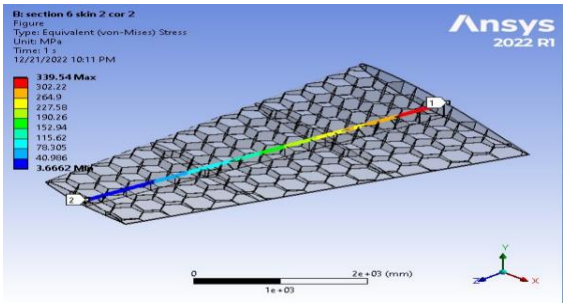

Figure 5.200. (Contour)Equivalent Stress at 6 cells skin 2 core 2 (Mach 0.6)

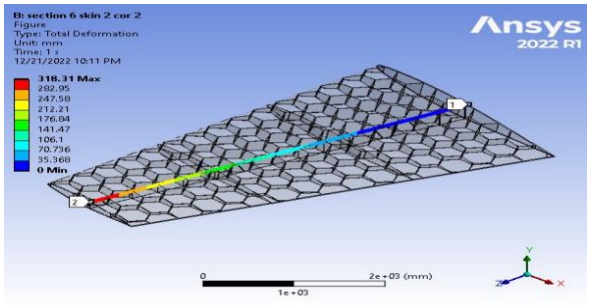

Figure 5.201. (Contour)Total Deformation at 6 cells skin 2 core 2 (Mach 0.6)

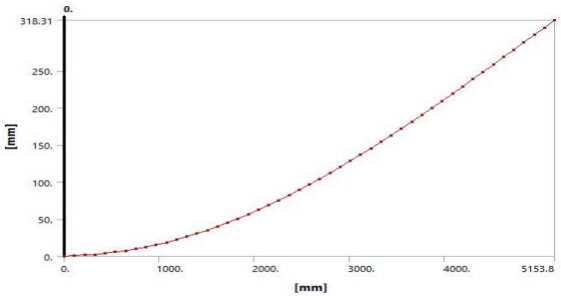

Figure 5.203. Variation of deformation at section 1.2 skin 2 core 2 (Mach 0.6)

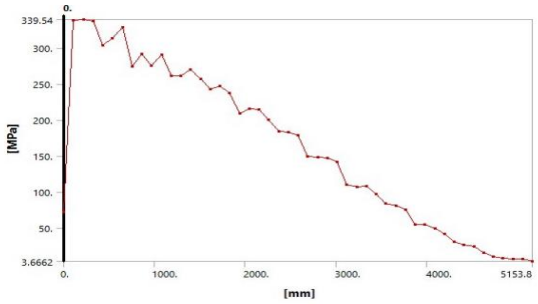

Figure 5.202. Equivalent Stress at section 1.2 skin 2 core 2 (Mach 0.6)

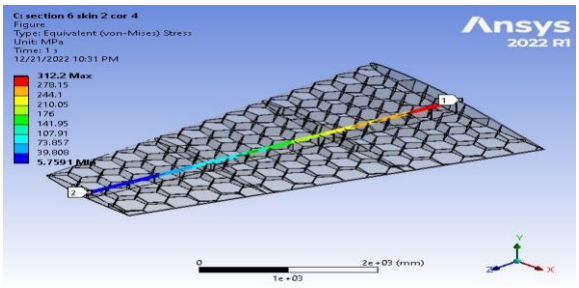

Figure 5.205. (Contour) Equivalent Stress at 6 cells skin 2 core 4 (Mach 0.6)

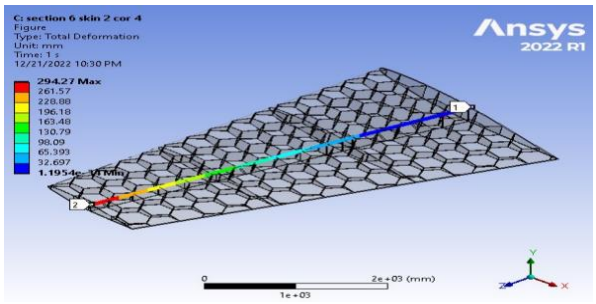

Figure 5.204. (Contour)Total Deformation at 6 cells skin 2 core 4 (Mach 0.6)

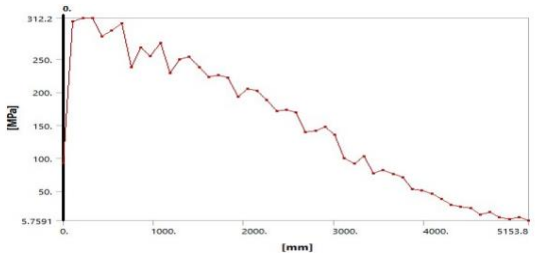

Figure 5.206. Equivalent Stress at section 0 skin 2 core 4 (Mach 0.6)

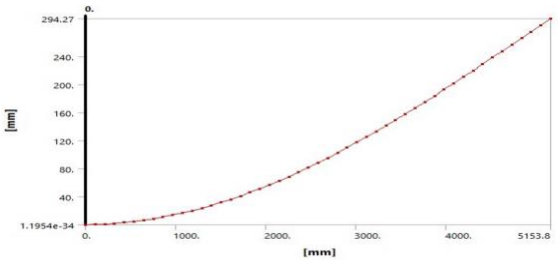

Figure 5.207. Variation of deformation at section 0 skin 2 core 4 (Mach 0.6)

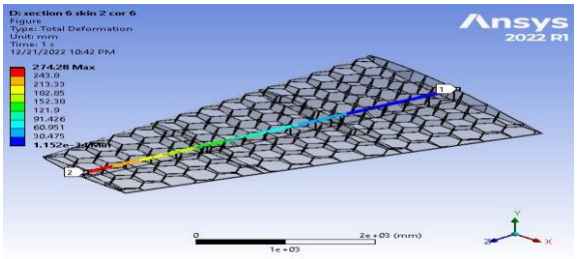

Figure 5.208.(Contour)Total Deformation at 6 cells skin 2 core 6 (Mach 0.6)

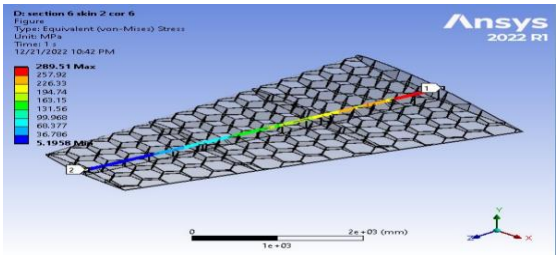

Figure 5.209. Contour Equivalent Stress at 6 cells skin 2 core 6 (Mach 0.6)

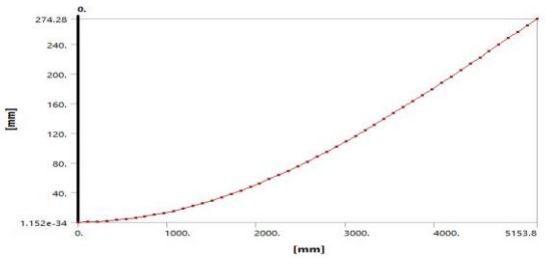

Figure 5.211. Variation of deformation at section 1.2 skin 2 core 6 (Mach 0.6)

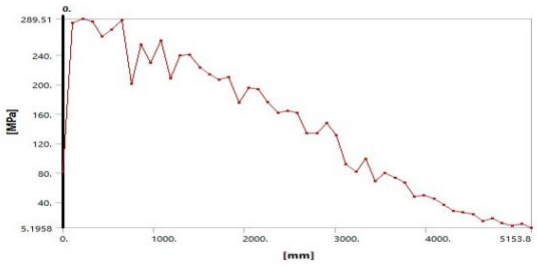

Figure 5.210. Equivalent Stress at section 1.2 skin 2 core 6 (Mach 0.6)

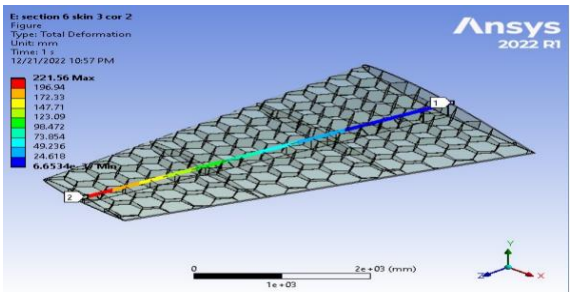

Figure 5.212. Contour Total Deformation at 6 cells skin 3 core 2 (Mach 0.6)

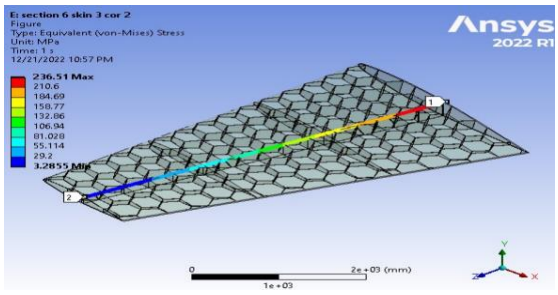

Figure 5.213. Contour Equivalent Stress at 6 cells skin 3 core 2 (Mach 0.6)

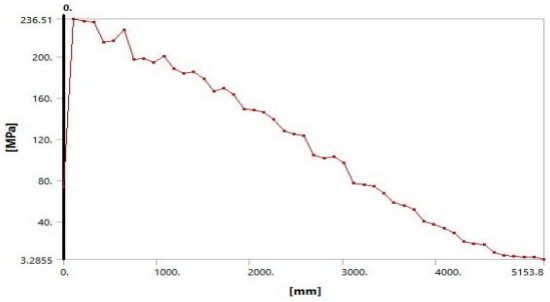

Figure 5.214. Equivalent Stress at section 1.2 skin 3 core 2 (Mach 0.6)

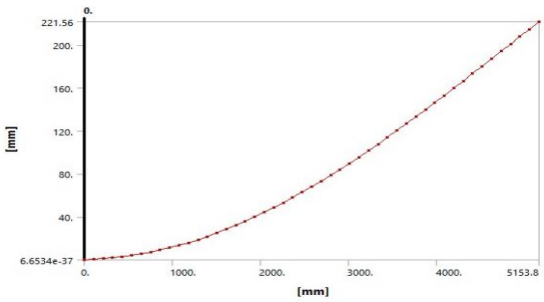

Figure 5.215. Variation of deformation at section 1.2 skin 3 core 2 (Mach 0.6)

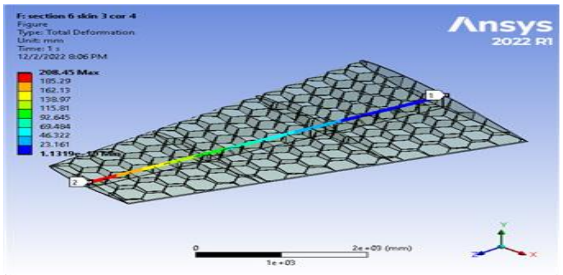

Figure 5.217. Contour Total Deformation at 6 cells skin 3 core 4 (Mach 0.6)

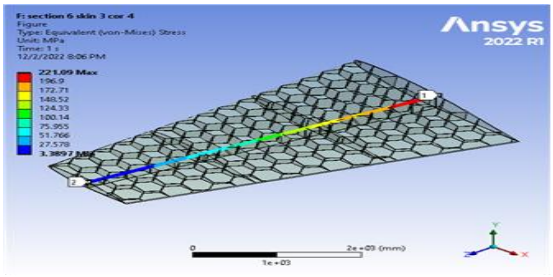

Figure 5.216. Contour Equivalent Stress at 6 cells skin 3 core 4 (Mach 0.6)

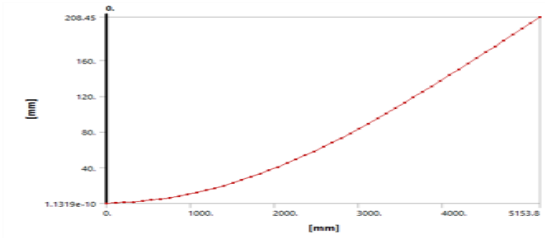

Figure 5.219. Variation of deformation at section 1.2 skin 3 core 4 (Mach 0.6)

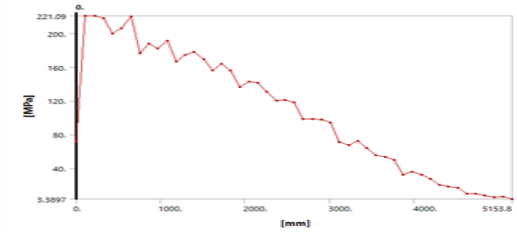

Figure 5.218. Equivalent Stress at section 1.2 skin 3 core 4 (Mach 0.6)

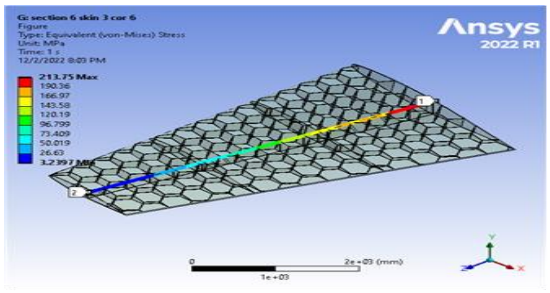

Figure 5.220. Contour Equivalent Stress at 6 cells skin 3 core 6 (Mach 0.6)

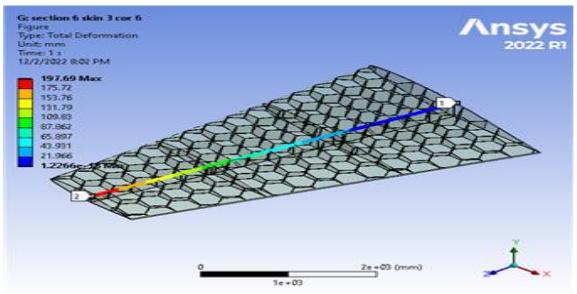

Figure 5.221. Contour Total Deformation at 6 cells skin 3 core 6 (Mach 0.6)

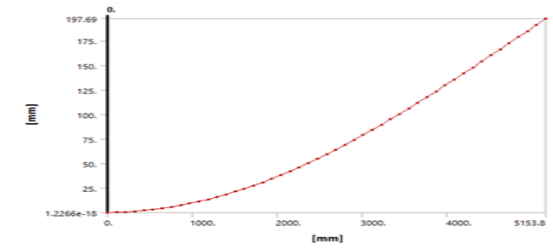

Figure 5.222. Variation of deformation at section 1.2 skin 3 core 6 (Mach 0.6)

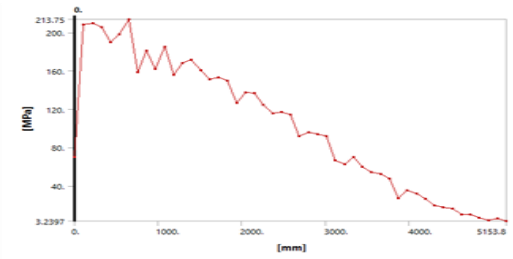

Figure 5.223. Equivalent Stress at section 0 skin 3 core 6 (Mach 0.6)

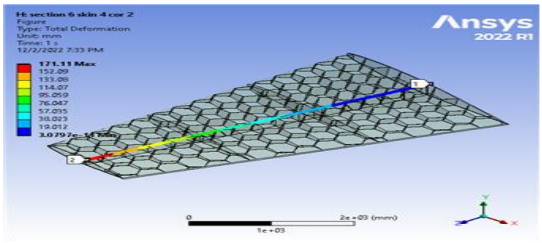

Figure 5.224. Contour Total Deformation at 6 cells skin 4 core 2 (Mach 0.6)

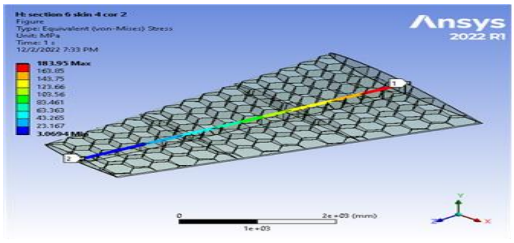

Figure 5.225. Contour Equivalent Stress at 6 cells skin 4 core 2(Mach 0.6)

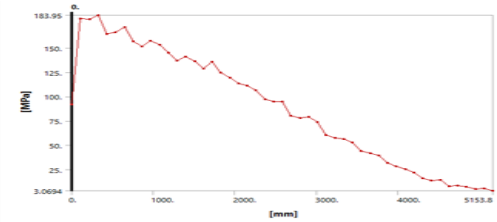

Figure 5.227. Equivalent Stress at section 1.2 skin 4 core 2 (Mach 0.6)

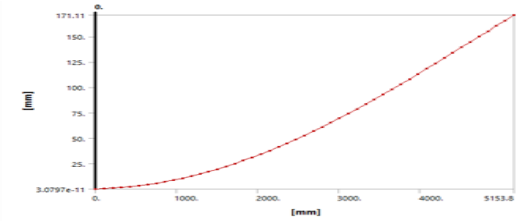

Figure 5.226. Variation of deformation at section 1.2 skin 4 core 2 (Mach 0.6)

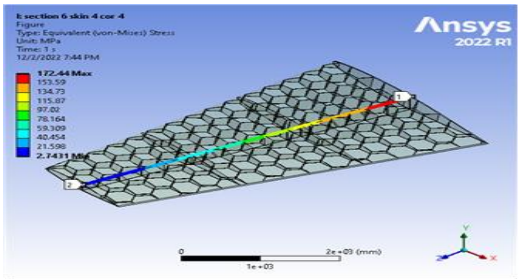

Figure 5.229. Contour Equivalent Stress at 6 cells skin 4 core 4 (Mach 0.6)

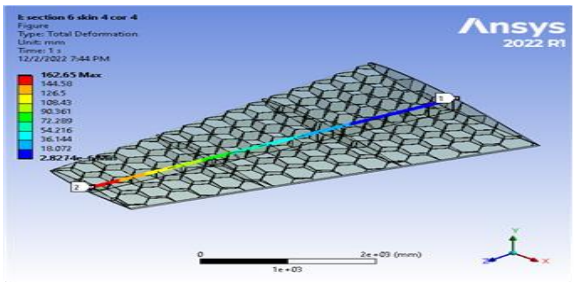

Figure 5.228. Contour Total Deformation at 6 cells skin 4 core 4 (Mach 0.6)

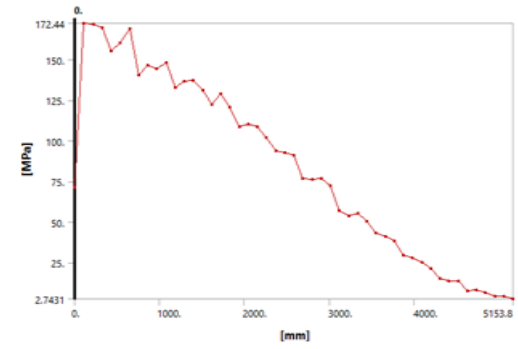

Figure 5.230. Equivalent Stress at section 1.2 skin 4 core 4 (Mach 0.6)

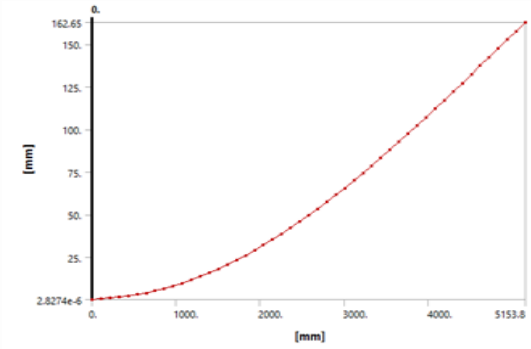

Figure 5.231. Variation of deformation at section 1.2 skin 4 core 4 (Mach 0.6)

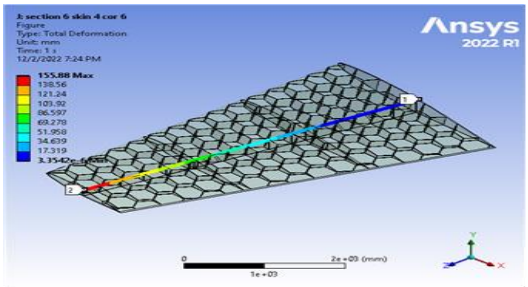

Figure 5.232. Contour Total Deformation at 6 cells skin 4 core 6 (Mach 0.6)

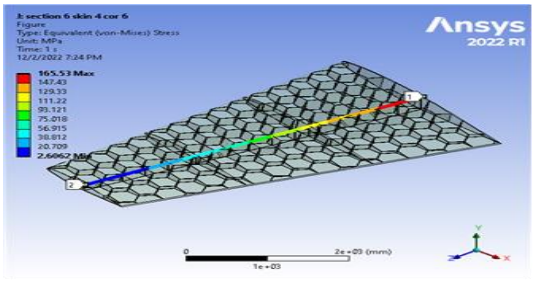

Figure 5.233. Contour Equivalent Stress at 6 cells skin 4 core 6 (Mach 0.6)

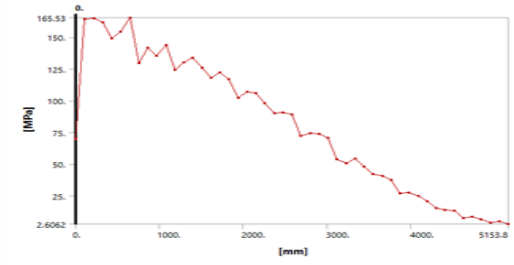

Figure 5.234. Equivalent Stress at section 1.2 skin 4 core 6 (Mach 0.6)

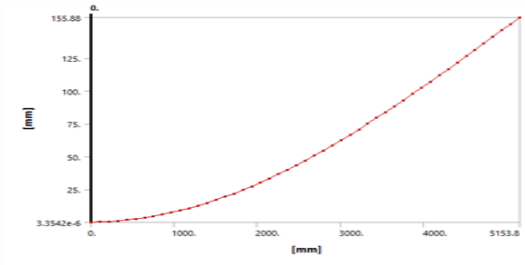

Figure 5.235. Variation of deformation at section 1.2 skin 4 core 6 (Mach 0.6)

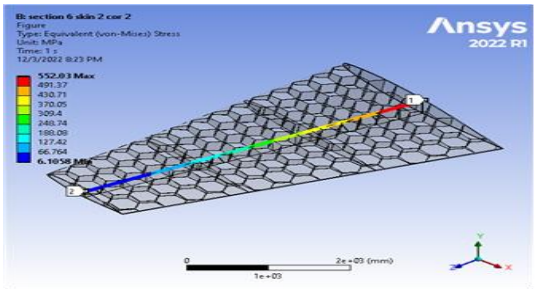

Figure 5.236. Contour Equivalent Stress at 6 cells skin 2 core 2 (Mach 0.8)

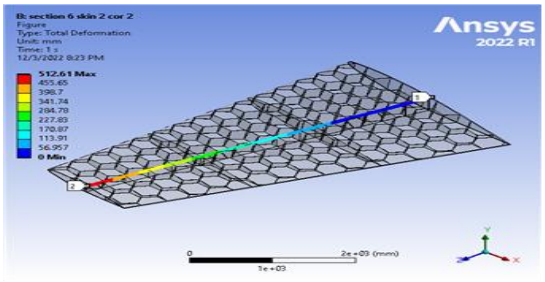

Figure 5.237. Contour Total Deformation at 6 cells skin 2 core 2 (Mach 0.8)

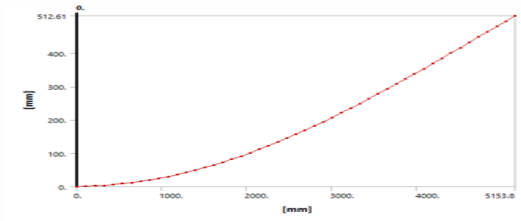

Figure 5.238. Variation of deformation at section 1.2 skin 2 core 2(Mach 0.8)

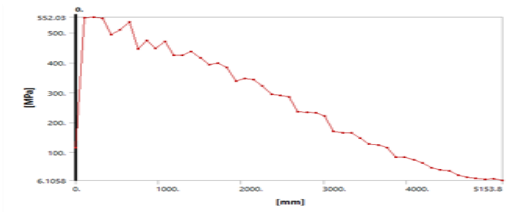

Figure 5.239. Equivalent Stress at section 1.2 skin 2 core 2 (Mach 0.8)

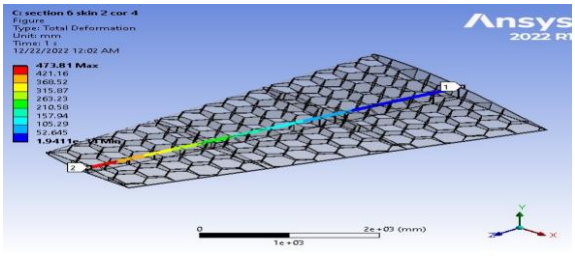

Figure 5.241. Contour Total Deformation at 6 cells skin 2 core 4 (Mach 0.8)

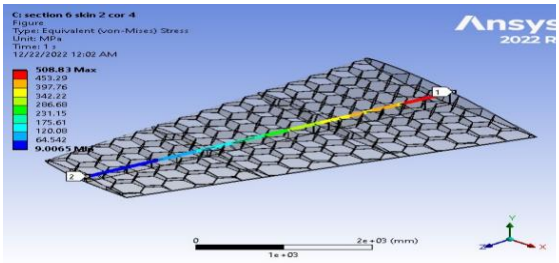

Figure 5.240. Contour Equivalent Stress at 6 cells skin 2 core 4 (Mach 0.8)

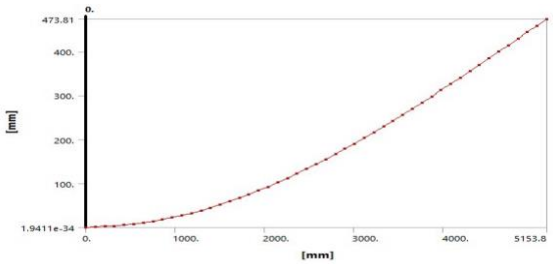

Figure 5.242. Variation of deformation at section 1.2 skin 2 core 4 (Mach 0.8)

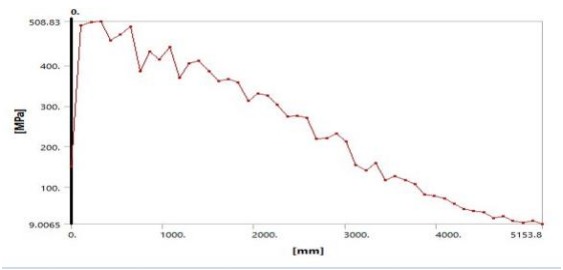

Figure 5.243. Equivalent Stress at section 1.2 skin 2 core 4 (Mach 0.8)

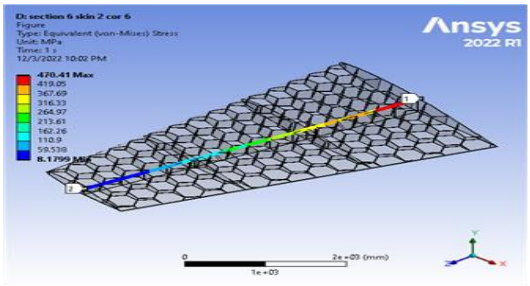

Figure 5.244. Contour Equivalent Stress at 6 cells skin 2 core 6 (Mach 0.8)

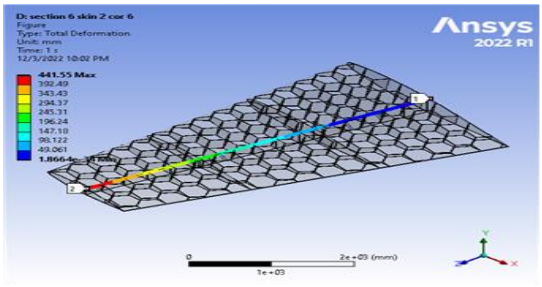

Figure 5.245. Contour Total Deformation at 6 cells skin 2 core 6 (Mach 0.8)

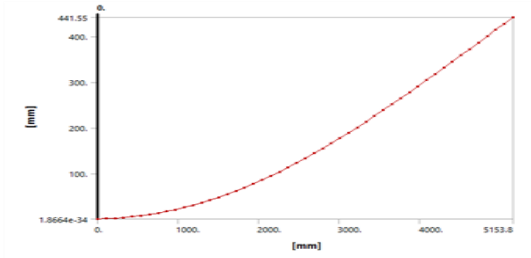

Figure 5.246. Variation of deformation at section 1.2 skin 2 core 6 (Mach 0.8)

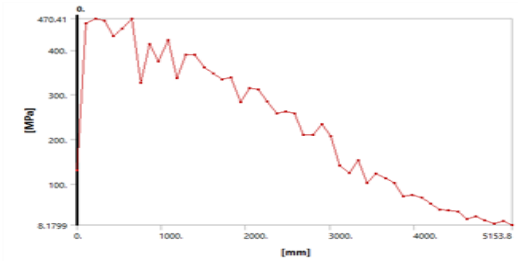

Figure 5.247. Equivalent Stress at section 1.2 skin 2 core 6 (Mach 0.8)

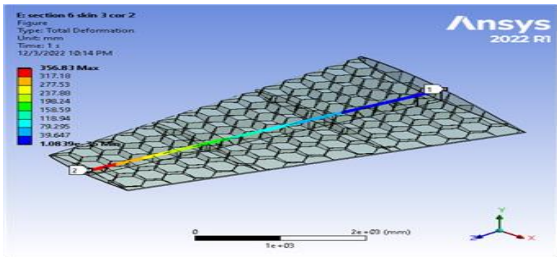

Figure 5.248. Contour Total Deformation at 6 cells skin 3 core 2 (Mach 0.8)

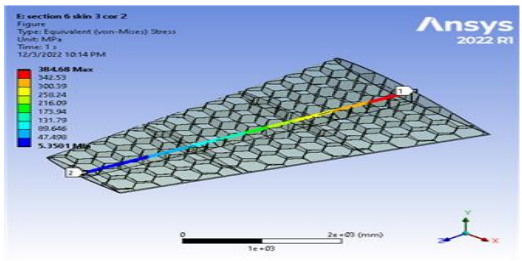

Figure 5.249. Contour Equivalent Stress at 6 cells skin 3 core 2 (Mach 0.8)

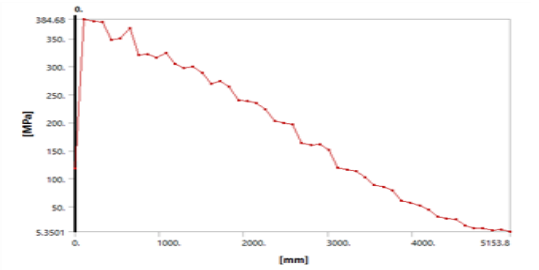

Figure 5.251. Equivalent Stress at section 1.2 skin 3 core 2 (Mach 0.8)

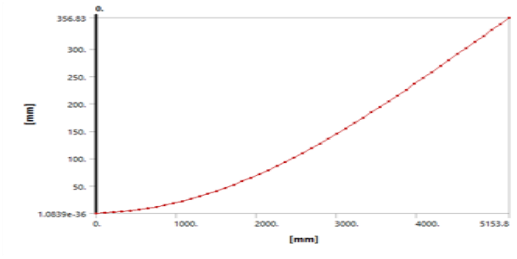

Figure 5.250. Variation of deformation at section 1.2 skin 3 core 2 (Mach 0.8)

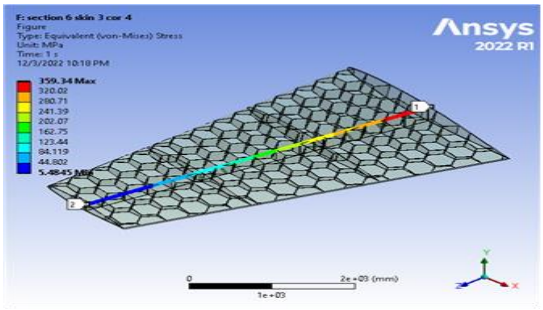

Figure 5.252. Contour Equivalent Stress at 6 cells skin 3 core 4 (Mach 0.8)

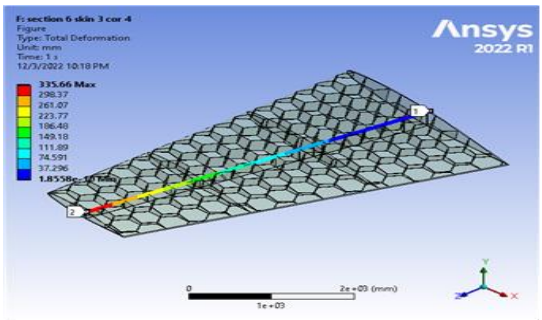

Figure 5.253. Contour Total Deformation at 6 cells skin 3 core 4 (Mach 0.8)

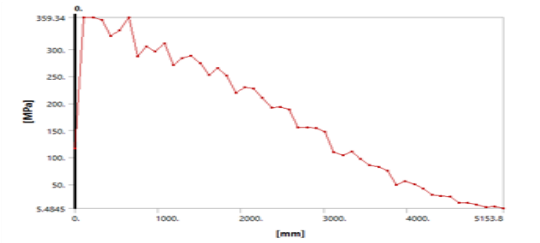

Figure 5.255. Equivalent Stress at section 1.2 skin 3 core 4 (Mach 0.8)

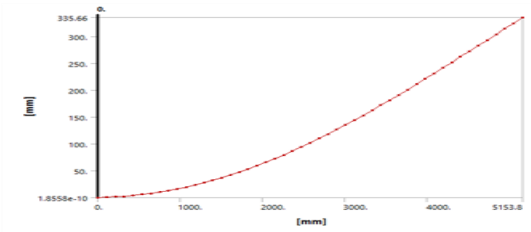

Figure 5.254. Variation of deformation at section 1.2 skin 3 core 4 (Mach 0.8)

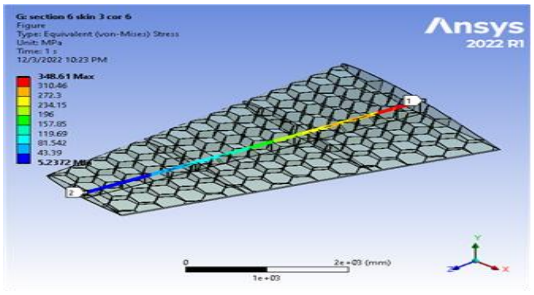

Figure 5.256. Contour Equivalent Stress at 6 cells skin 3 core 6 (Mach 0.8)

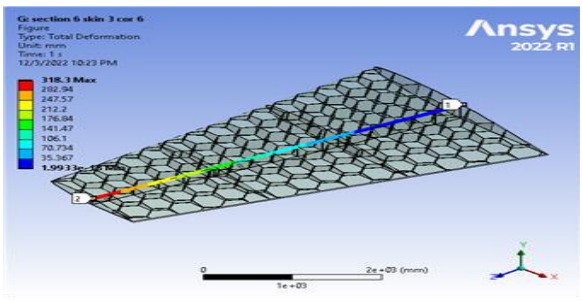

Figure 5.257. Contour Total Deformation at 6 cells skin 3 core 6 (Mach 0.8)

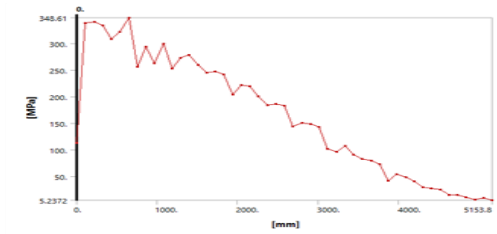

Figure 5.259. Equivalent Stress at section 1.2 skin 3 core 6 (Mach 0.8)

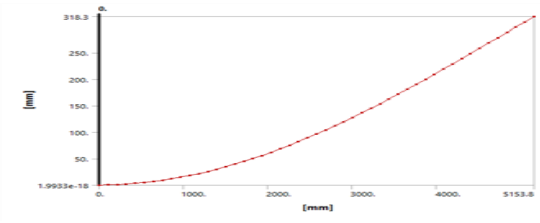

Figure 5.258. Variation of deformation at section 1.2 skin 3 core 6 (Mach 0.8)

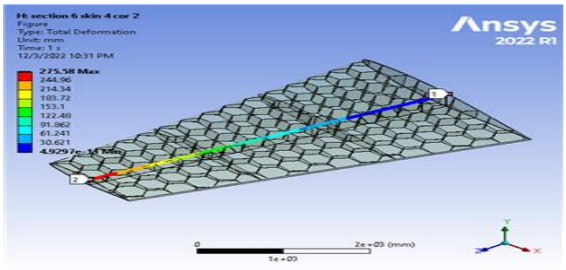

Figure 5.260. Contour Total Deformation at 6 cells skin 4 core 2 (Mach 0.8)

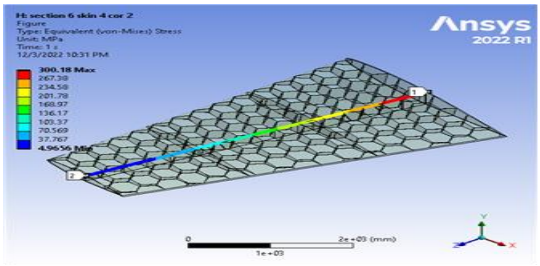

Figure 5.261. Contour Equivalent Stress at 6 cells skin 4 core 2 (Mach 0.8)

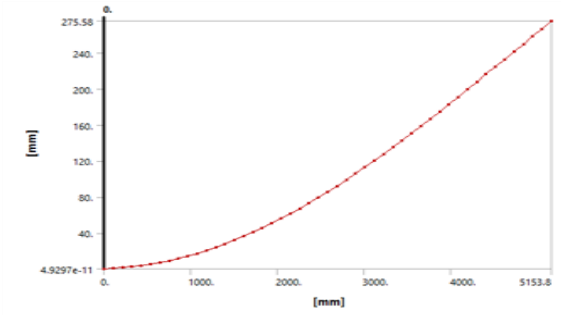

Figure 5.263. Variation of deformation at section 1.2 skin 4 core 2 (Mach 0.8)

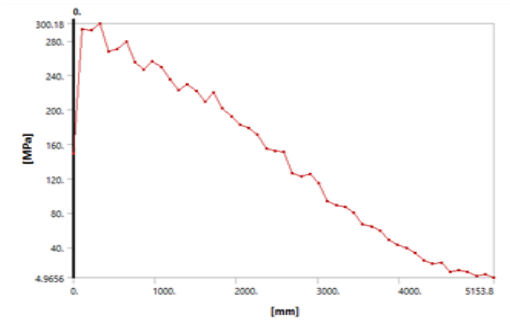

Figure 5.262. Equivalent Stress at section 1.2 skin 4 core 2 (Mach 0.8)

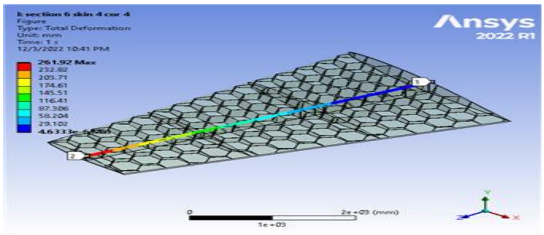

Figure 5.264. Contour Total Deformation at 6 cells skin 4 core 4 (Mach 0.8)

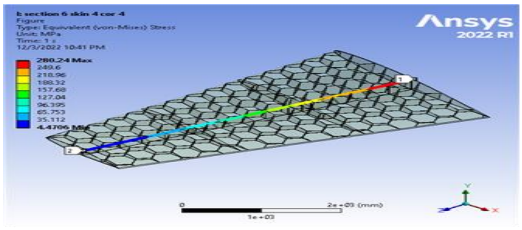

Figure 5.265. Contour Equivalent Stress at 6 cells skin 4 core 4 (Mach 0.8)

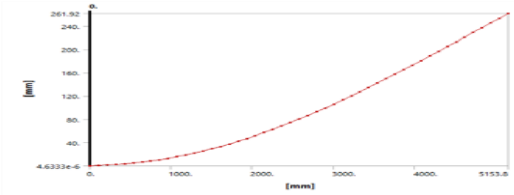

Figure 5.267. Variation of deformation at section 1.2 skin 4 core 4 (Mach 0.8)

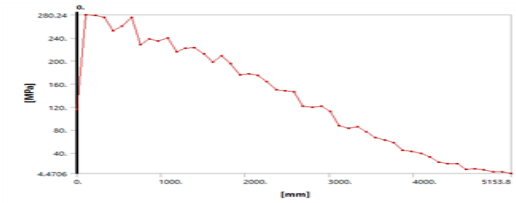

Figure 5.266. Contour Equivalent Stress at section 1.2 skin 4 core 4 (Mach 0.8)

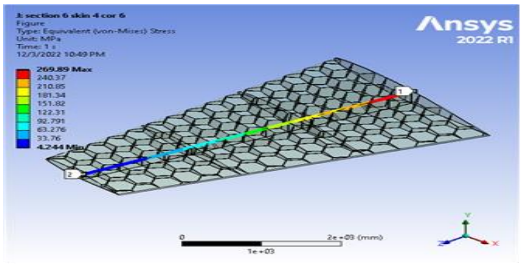

Figure 5.269. Contour Equivalent Stress at 6 cells skin 4 core 6 (Mach 0.8)

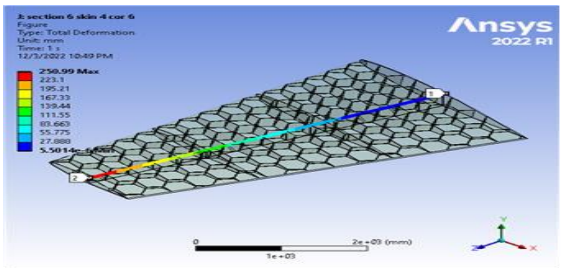

Figure 5.268. Contour Total Deformation at 6 cells skin 4 core 6 (Mach 0.8)

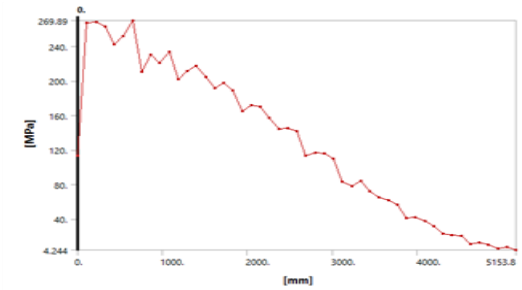

Figure 5.270. Equivalent Stress at section 1.2 skin 4 core 6 (Mach 0.8)

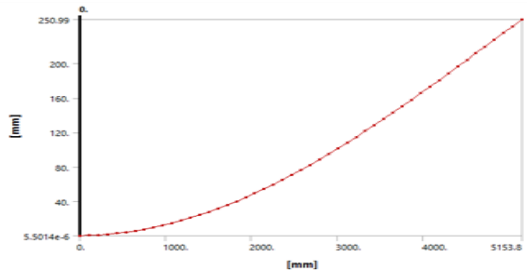

Figure 5.271. Variation of deformation at section 1.2 skin 4 core 6 (Mach 0.8)

5.2.5. Wing. 9 Cells

The determination of displacements and stress using the different structural modeling are presented here. The finite element modeling was used by import the pressure distribution and applied on the wing structure .it corresponds with the real case this give the true picture of deformation and stresses on the wing skin.

The effects of design parameters of the wing structure are discussed as follows.

- Effects of skin thickness.
- Effects of number of cells
- Effects of core thickness (invariably of skin thickness)

5.2.5.1. (Effects of Skin Thickness)

Using the skin= 2mm and core thickness=2mm, the maximum deformation=147.08 mm and the resulted Von Mises=208.96**MPa**

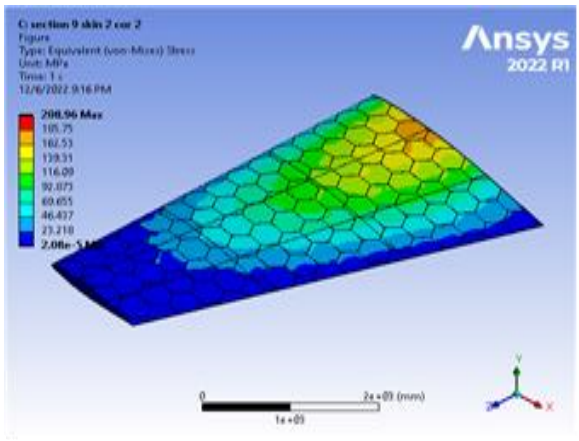

Figure 5.273. Contour Equivalent Stress at 9 cells skin 2 core 2 (Mach 0.4)

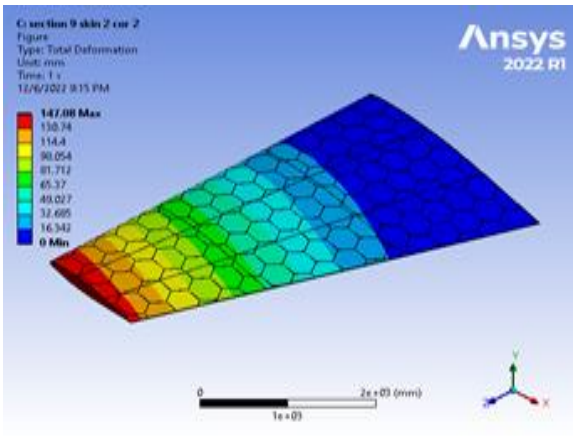

Figure 5.272. Contour Total Deformation at 9 cells skin 2 core 2 (Mach 0.4)

Increasing the skin thickness=3mm ,the deformation = 104.24 mm and the resulted Von Mises =141.84 MPa

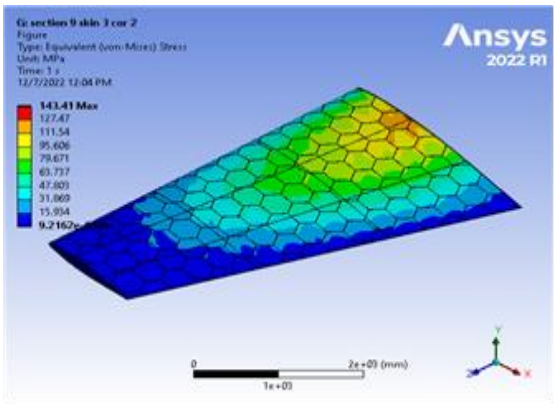

Figure 5.274. Contour Equivalent Stress at 9 cells skin 3 core 2 (Mach 0.4)

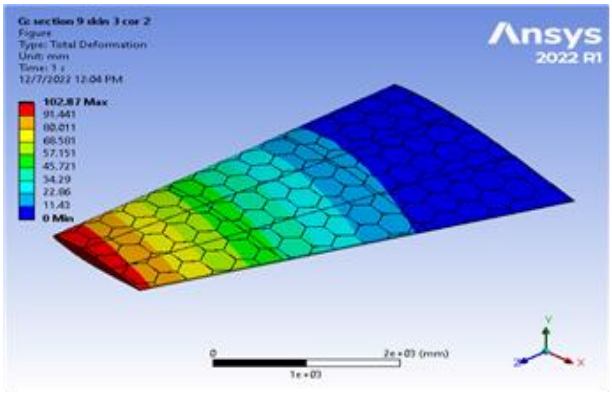

Figure 5.275. Contour Total Deformation at 9 cells skin 3 core 2 (Mach 0.4)

Table 5.6. Wing. 9 cells at angle of attack **12°**

Mach No	**Skin thickness (mm)**	**Core thickness (mm)**	**Max deformation (mm)**	**Von Mises stress (MPa)**	**Equivalent strain (mm/mm)**	**Mass (kg)**
0.4	2	2	147.08	208.96	0.002932	215.62
	3	2	102.87	134.41	0.00101	274.03
	4	2	79.621	111.26	0.001551	333.06
	2	4	134.95	273.45	0.0029942	283.98
	3	4	95.924	134.69	0.001944	341.69
	4	4	75.197	104.13	0.00149	399.84
	2	6	124.47	213.09	0.002994	351.85
	3	6	90.256	126.33	0.001808	408.67
	4	6	71.62	99.566	0.001391	466.04
Mach No	Skin thickness (mm)	Core thickness (mm)	Max deformation (mm)	Von Mises stress (MPa)	Equivalent strain (mm/mm)	Mass (kg)
0.6	2	2	322.98	471.27	0.006633	215.62
	3	2	225.94	324.75	0.004553	274.03
	4	2	174.9	252.4	0.003518	333.06
	2	4	296.29	531.58	0.0075368	283.98
	3	4	210.63	303.57	0.004369	341.69
	4	4	165.13	234.18	0.003353	399.84
	2	6	273.22	476.46	0.006699	351.85
	3	6	198.15	284.41	0.004071	408.67
	4	6	157.26	222.23	0.003106	466.04
Mach No	Skin thickness (mm)	Core thickness (mm)	Max deformation (mm)	Von Mises stress MPa)	Equivalent strain (mm/mm)	Mass (kg)
0.8	2	2	521.51	770.68	0.010839	215.62
	3	2	364.85	530.72	0.00744	274.03
	4	2	282.44	412.79	0.005754	333.06
	2	4	478.39	869.24	0.012324	283.98
	3	4	340.09	496.64	0.007114	341.69
	4	4	266.44	383.84	0.0054963	399.84
	2	6	441.12	779.15	0.010955	351.85
	3	6	319.92	465.42	0.006663	408.67
	4	6	253.9	362.45	0.005065	466.04

Table 5.6 shows the results of using different thickness (invariably of core). note in the Table 5.6 that some of the points in red failed because the value of the value exceeded Yield Strength=505N/$(mm)^2$. And that the largest mass was (215.62 Kg) and the lowest mass was (466.04 Kg) using in Material (Al7075 T6). Table 5.6 shows us the change in the total Von Mises Stress was largest (770.68 MPa) at skin

thickness (2mm), core (2mm), and Mach 0.8 which then failed, while the lowest was stress (99.566 MPa) at a skin thickness of (4mm), core (6mm) and Mach 0.4. Also, this Table 5.6 shows that the largest Equivalent strain of (0.012324 mm /mm) occurs in the model with the skin thickness (2mm) and core (4mm) at Mach 0.8, while the least deviation is (0.00101mm/mm) obtained in the model with a skin thickness (3mm) and core (2mm) at Mach 0.4.

5.2.5.2. (Effects of Core Thickness)

Using the skin= 2mm and core thickness=2mm, the maximum deformation=322.98 mm and the resulted Von Mises=471.27MPa

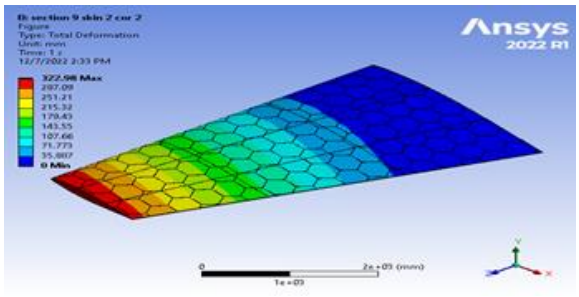

Figure 5.277.Contour Total Deformation at 9 cells skin 2 core 2 (Mach 0.6)

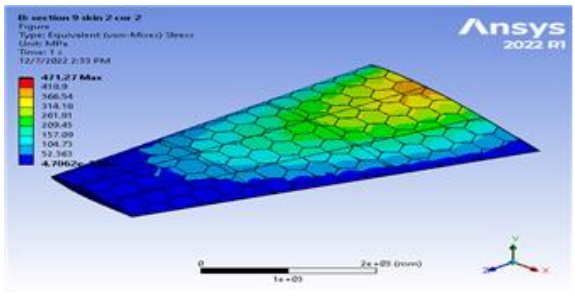

Figure 5.276. Contour Equivalent Stress at 9 cells skin 2 core 2(Mach 0.6)

Increasing the skin thickness=3mm, the deformation =225.94 mm and the resulted Von Mises =324.75Mpa

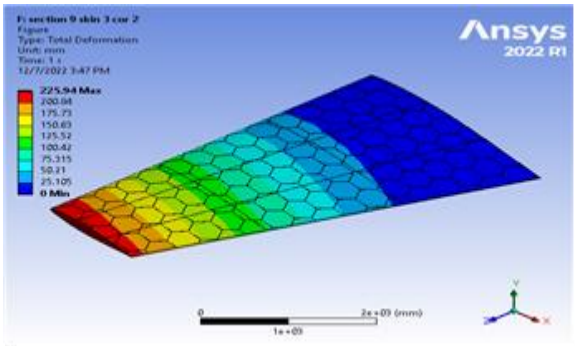

Figure 5.279. Contour Total Deformation at 9 cells skin 3 core 2 (Mach 0.6)

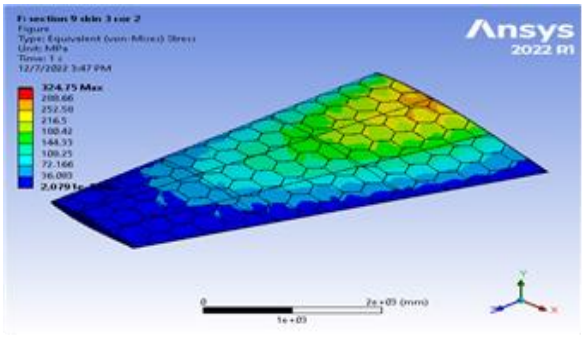

Figure 5.278. Contour Equivalent Stress at 9 cells skin 3 core 2(Mach 0.6)

Table 5.7. 9 cells at angle of attack **12°**

Mach No	**Skin thickness (mm)**	**Core thickness (mm)**	**Max deformation (mm)**	**Von mises stress (MPa)**	**Equivalent strain (mm/mm)**	**Mass (kg)**
0.4	2	2	147.08	208.96	0.002932	215.62
	2	4	134.95	273.45	0.0029942	283.98
	2	6	124.47	213.09	0.002994	351.85
	3	2	102.87	134.41	0.00201	274.03
	3	4	95.924	134.69	0.001944	341.69
	3	6	90.256	126.33	0.001808	408.67
	4	2	79.621	111.26	0.001551	333.06
	4	4	75.197	104.13	0.00149	399.84
	4	6	71.62	99.566	0.001391	466.04
Mach No	Skin thickness (mm)	Core thickness (mm)	Max deformation (mm)	Von mises stress (MPa)	Equivalent strain (mm/mm)	Mass (kg)
0.6	2	2	322.98	471.27	0.006633	215.62
	2	4	296.29	531.58	0.0075368	283.98
	2	6	273.22	476.46	0.0066987	351.85
	3	2	225.94	324.75	0.004553	274.03
	3	4	210.63	303.57	0.004369	341.69
	3	6	198.15	284.41	0.004071	408.67
	4	2	174.9	252.4	0.003518	333.06
	4	4	165.13	234.18	0.003353	399.84
	4	6	157.26	222.23	0.003106	466.04
Mach No	Skin thickness (mm)	Core thickness (mm)	Max deformation (mm)	Von mises stress (MPa)	Equivalent strain (mm/mm)	Mass (kg)
0.8	2	2	521.51	770.68	0.010839	215.62
	2	4	478.39	869.24	0.12324	283.98
	2	6	441.12	779.15	0.010955	351.85
	3	2	364.85	530.72	0.00744	274.03
	3	4	340.09	496.64	0.007114	341.69
	3	6	319.92	465.42	0.006663	408.67
	4	2	282.44	412.79	0.005754	333.06
	4	4	266.63	383.84	0.0054963	399.84
	4	6	253.9	362.45	0.005065	466.04

Table 5.7 hows the results of using different thickness (invariably of core). note in the Table 5.7 that some of the points in red failed because the value of the value exceeded Yield Strength=505 N/$(mm)^2$. And that the least mass was (215.62 Kg) and the largest mass was (466.04 Kg) in using Material (Al7075 T6) Table 5.7 shows us the change in the total Von Mises Stress was largest (770.68 MPa) at skin thickness (2mm), core (2mm), and Mach 0.8 and which failed, while the lowest was stress (99.566 MPa) at a skin thickness of (4mm), core (6mm) and Mach0.4. Also, this Table 5.7 shows that the largest Equivalent strain of (0.012324 mm /mm) occurs in the model with the skin thickness (2mm) and core (4mm) at Mach 0.8, while the least deviation is (0.00101mm/mm) obtained in the model with a skin thickness (3mm) and core (2mm) at Mach 0.4.

The summary of the results which are extracted from the contours and shown in Table 5.7 some cases fail to the maximum stresses developed compared to the yield stress at the used Material (Al7075 T6) when a stress ratio less than 1. They are labelled in red colour. even the masses are low compared to the used mass in A/C design.

5.2.5.3. (Effects of Number Cells)

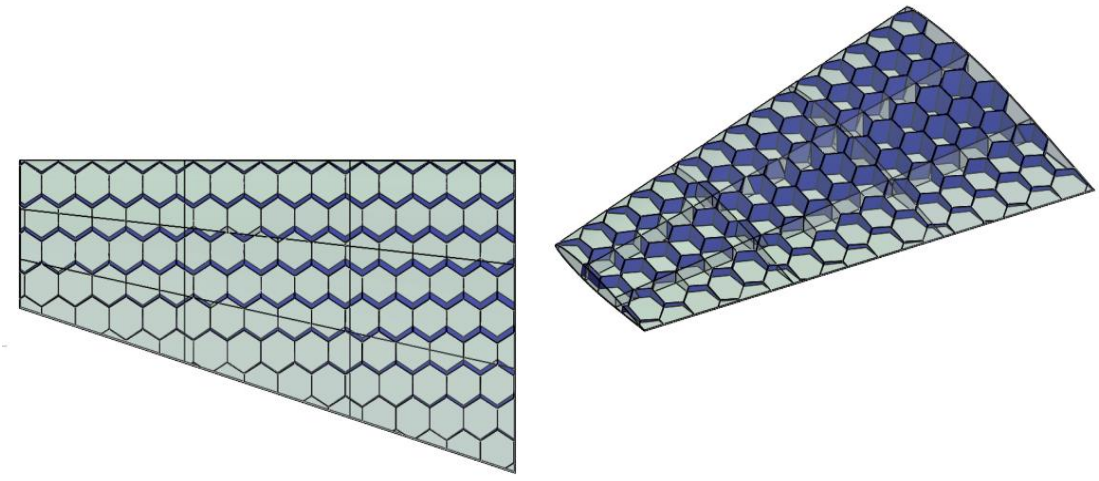

Figure 5.280. Contour wing 9 cells

5.2.5.4. MACH (0.4), (0.6). (0.8)

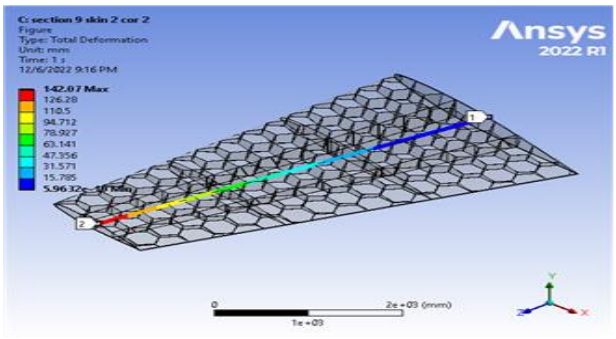

Figure 5.282. Contour Total Deformation at 9 cells skin 2 core 2 (Mach 0.4)

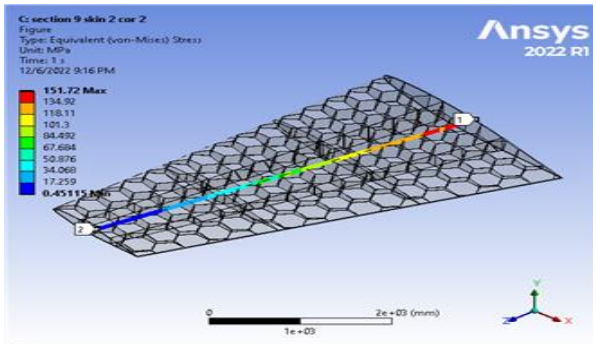

Figure 5.281. Contour Equivalent Stress at 9 cells skin 2 core 2 (Mach 0.4)

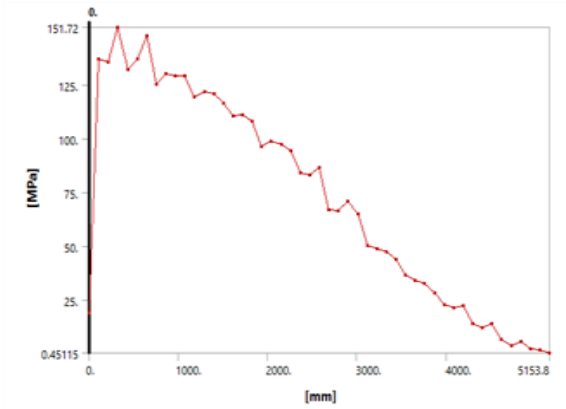

Figure 5.284. Equivalent Stress at section 1.2 skin 2 core 2 (Mach 0.4)

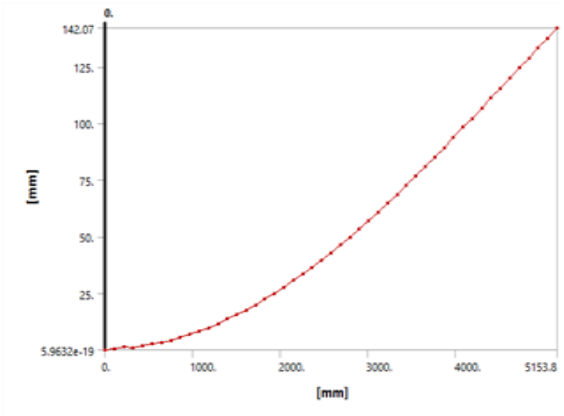

Figure 5.283. Variation of deformation at section 1.2 skin 2 core 2 (Mach 0.4)

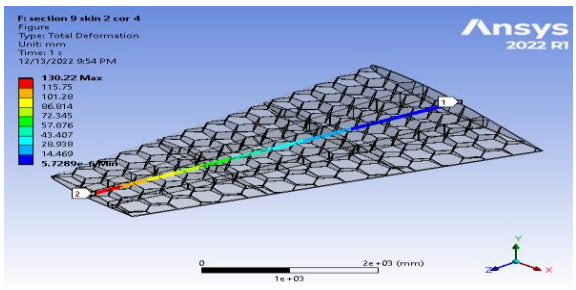

Figure 5.285. Contour Total Deformation at 9 cells skin 2 core 4 (Mach 0.4)

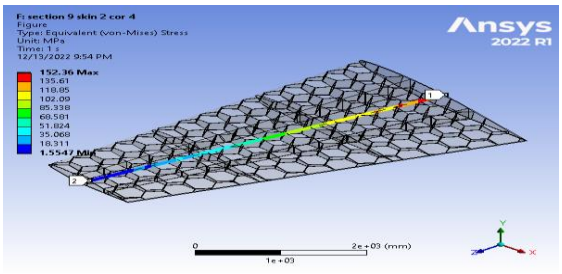

Figure 5.286. Contour Equivalent Stress at 9 cells skin 2 core 4 (Mach 0.4)

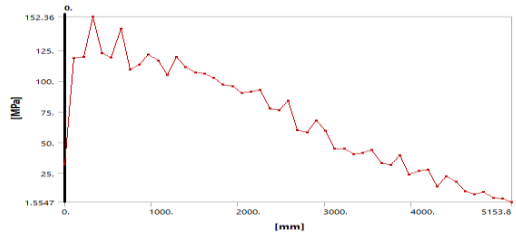

Figure 5.287. Equivalent Stress at section 1.2 skin 2 core 4 (Mach 0.4)

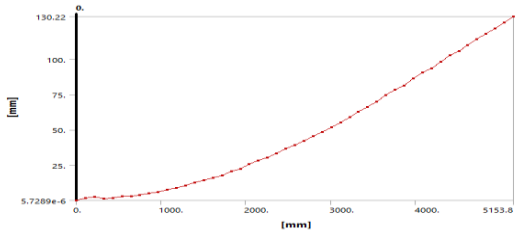

Figure 5.288. Variation of deformation at section 1.2 skin 2 core 4 (Mach 0.4)

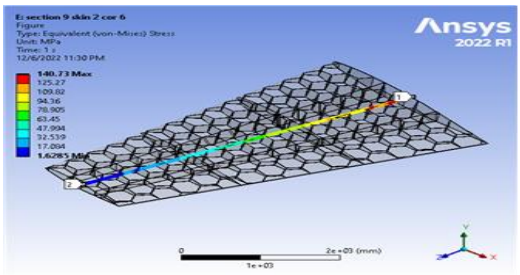

Figure 5.289. Contour Equivalent Stress at 9 cells skin 2 core 6(Mach 0.4)

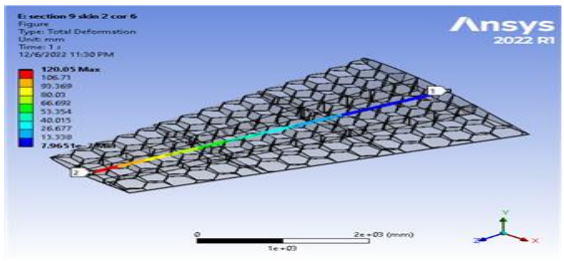

Figure 5.290. Contour Total Deformation at 9 cells skin 2 core 6(Mach 0.4)

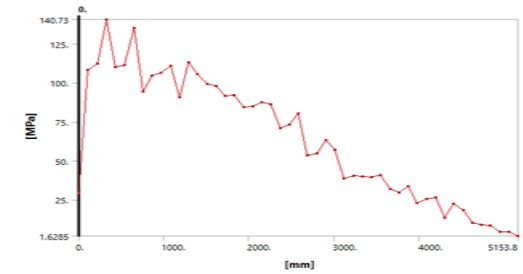

Figure 5.292. Equivalent Stress at section 1.2 skin 2 core 6(Mach 0.4)

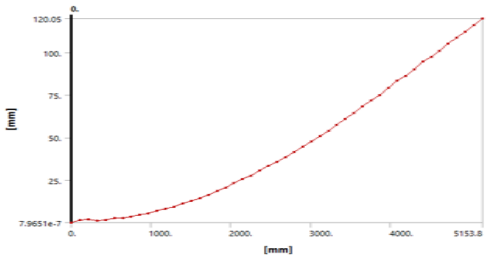

Figure 5.291. Variation of deformation at section 1.2 skin 2 core 6(Mach 0.4)

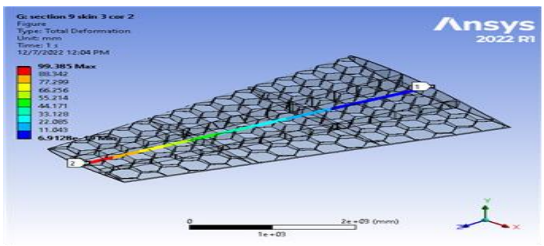

Figure 5.293. Contour Total Deformation at 9 cells skin 3 core 2 (Mach 0.4)

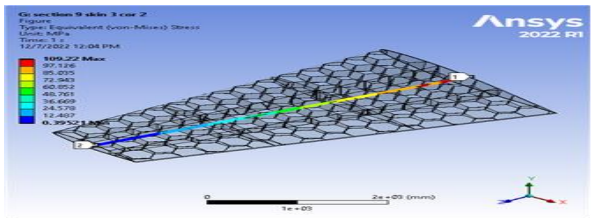

Figure 5.294. Contour Equivalent Stress at 9 cells skin 3 core 2 (Mach 0.4)

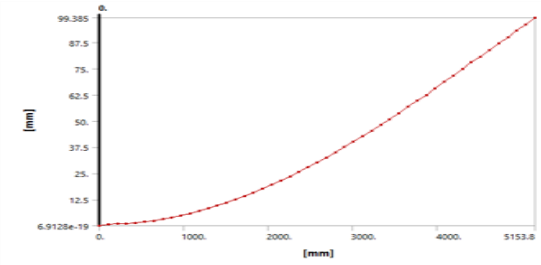

Figure 5.296. Variation of deformation at section 1.2 skin 3 core 2(Mach 0.4)

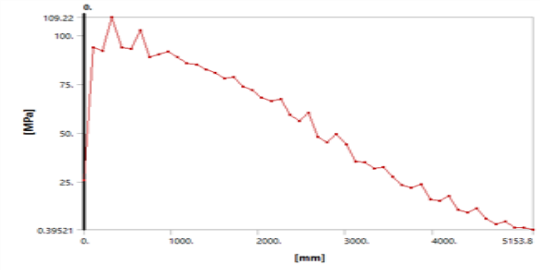

Figure 5.295. Equivalent Stress at section 1.2 skin 3 core 2 (Mach 0.4)

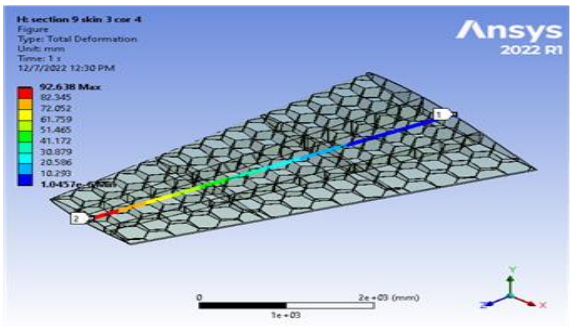

Figure 5.297. Contour Total Deformation at 9 cells skin 3 core 4 (Mach 0.4)

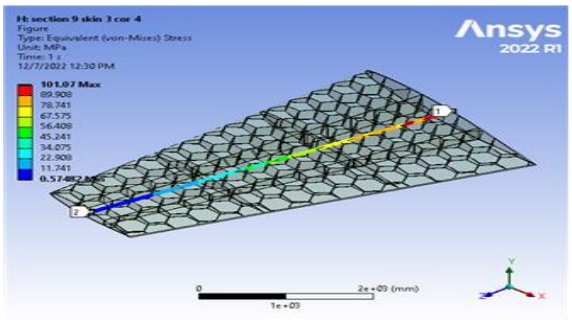

Figure 5.298. Contour Equivalent Stress at 9 cells skin 3 core 4 (Mach 0.4)

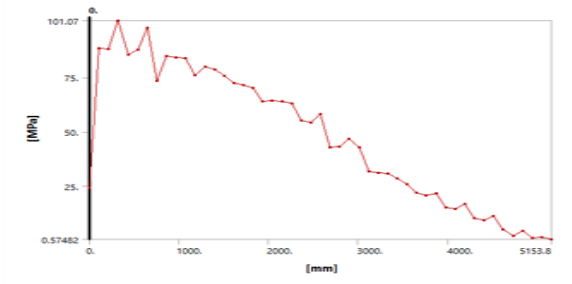

Figure 5.299. Equivalent Stress at section 1.2 skin 3 core 4 (Mach 0.4)

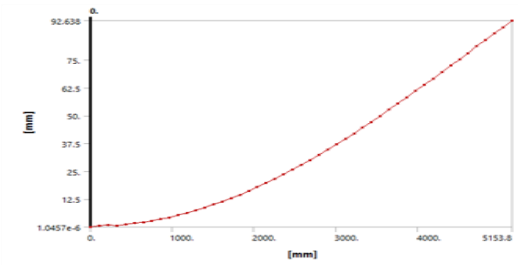

Figure 5.300. Variation of deformation at section 1.2 skin 3 core 4 (Mach 0.4)

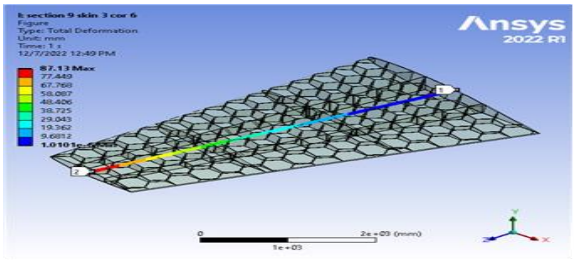

Figure 5.299. Contour Total Deformation at 9 cells skin 3 core 6 (Mach 0.4)

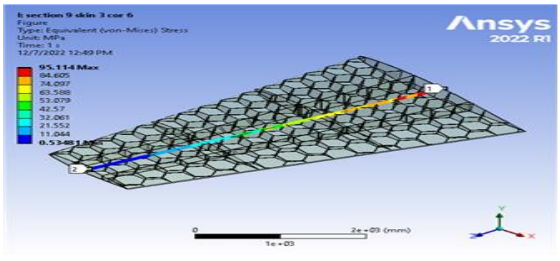

Figure 5.301. Contour Equivalent Stress at 9 cells skin 3 core 6 (Mach 0.4)

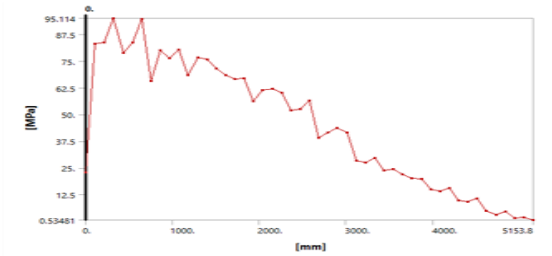

Figure 5.301. Equivalent Stress at section 1.2 skin 3 core 6 (Mach 0.4)

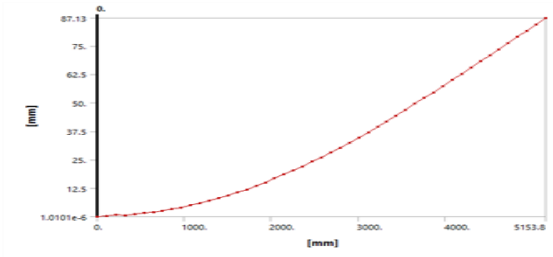

Figure 5.300. Variation of deformation at section 1.2 skin 3 core 6 (Mach 0.4)

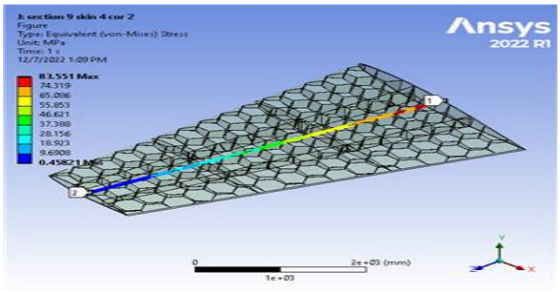

Figure 5.302. Contour Equivalent Stress at 9 cells skin 4 core 2 (Mach 0.4)

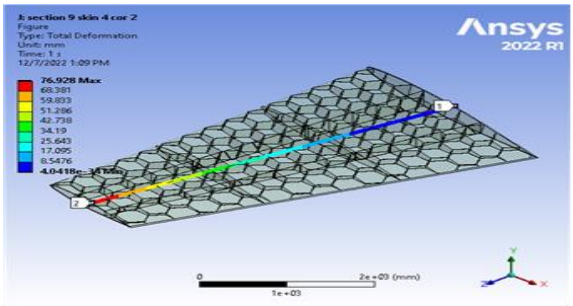

Figure 5.303. Contour Total Deformation at 9 cells skin 4 core 2 (Mach 0.4)

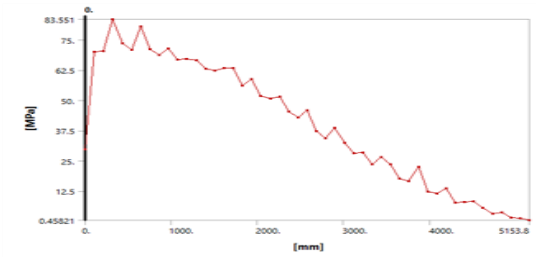

Figure 5.304. Equivalent Stress at section 1.2 skin 4 core 2 (Mach 0.4)

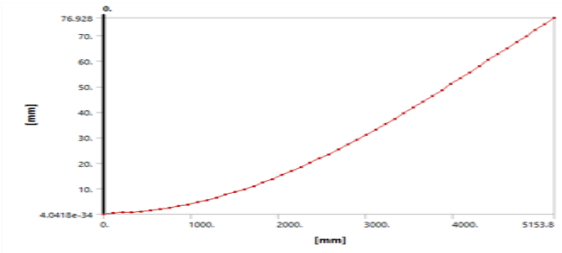

Figure 5.305. Variation of deformation at section 1.2 skin 4 core 2 (Mach 0.4)

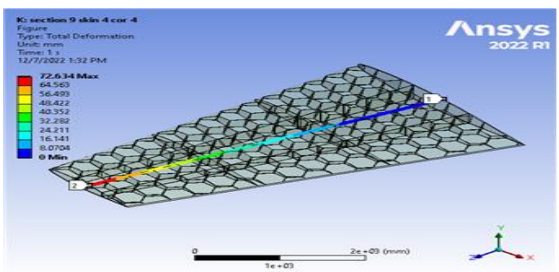

Figure 5.307. Contour Total Deformation at 9 cells skin 4 core 4 (Mach 0.4)

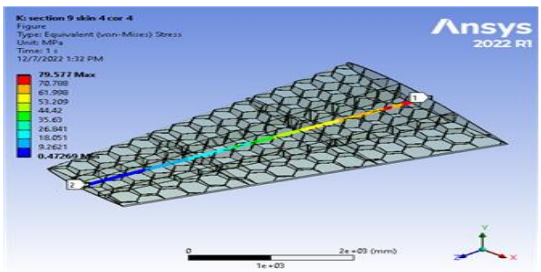

Figure 5.306. Contour Equivalent Stress at 9 cells skin 4 core 4 (Mach 0.4)

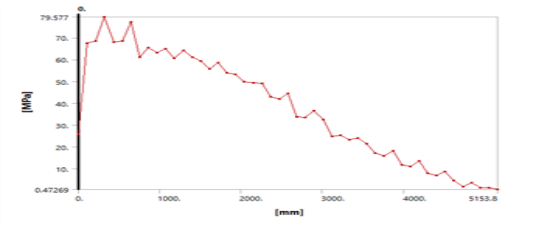

Figure 5.309. Equivalent Stress at section 1.2 skin 4 core 4 (Mach 0.4)

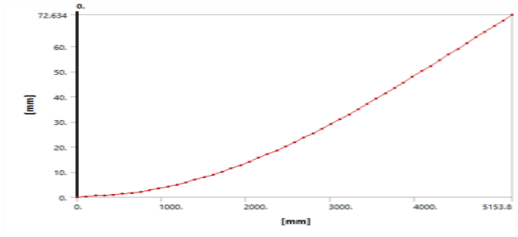

Figure 5.308. Variation of deformation at section 1.2 skin 4 core 4 (Mach 0.4)

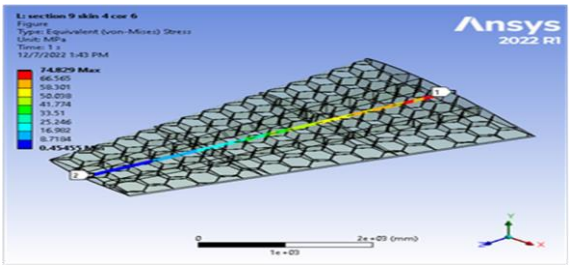

Figure 5.311. Contour Equivalent Stress at 9 cells skin 4 core 6(Mach 0.4)

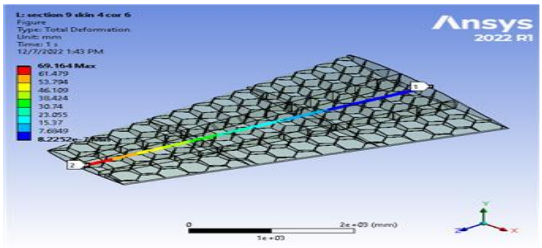

Figure 5.310. Contour Total Deformation at 9 cells skin 4 core 6 (Mach 0.4)

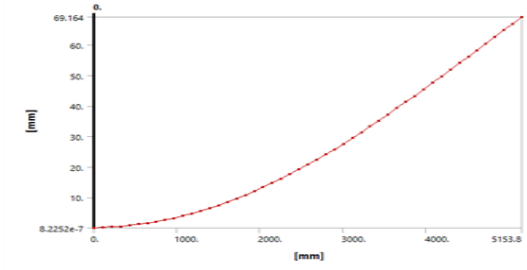

Figure 5.313. Variation of deformation at section 1.2 skin 4 core 6 (Mach 0.4)

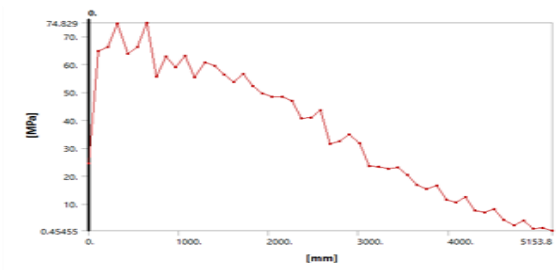

Figure 5.312. Equivalent Stress at section 1.2 skin 4 core 6 (Mach 0.4)

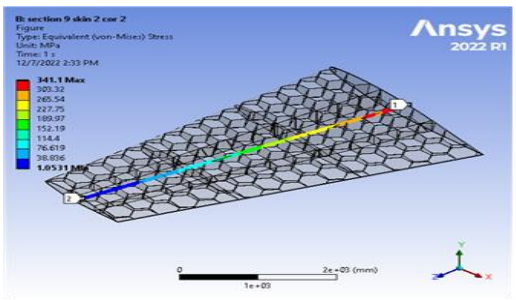

Figure 5.314. (Contour)Equivalent Stress at 9 cells skin 2 core 2 (Mach 0.6)

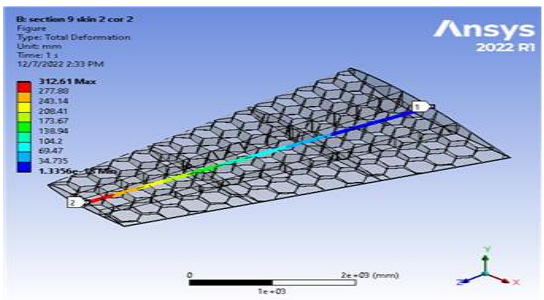

Figure 5.315. (Contour)Total Deformation at 9 cells skin 2 core 2 (Mach 0.6)

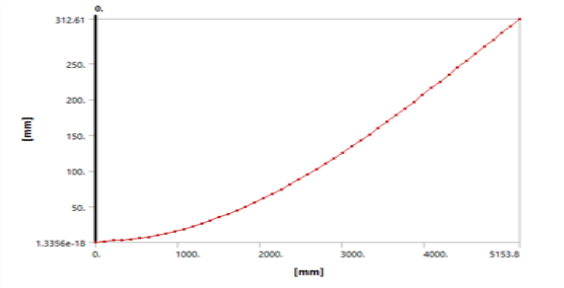

Figure 5.317. Variation of deformation at section 1.2 skin 2 core 2 (Mach 0.6)

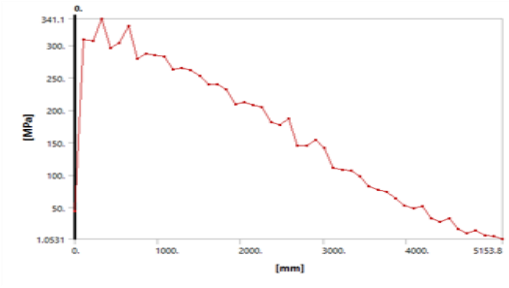

Figure 5.316. Equivalent Stress at section 1.2 skin 2 core 2 (Mach 0.6)

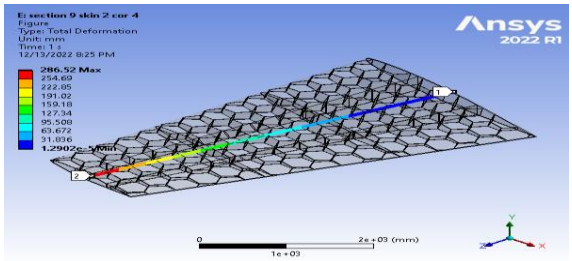

Figure 5.318. (Contour)Total Deformation at 9 cells skin 2 core 4 (Mach 0.6)

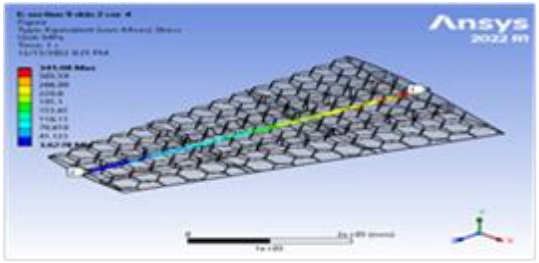

Figure 5.319. (Contour) Equivalent Stress at 9 cells skin 2 core 4 (Mach 0.6)

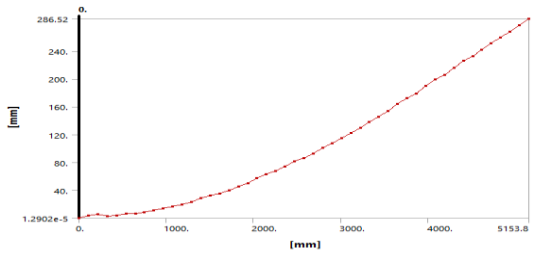

Figure 5.320. Variation of deformation at section 0 skin 2 core 4 (Mach 0.6)

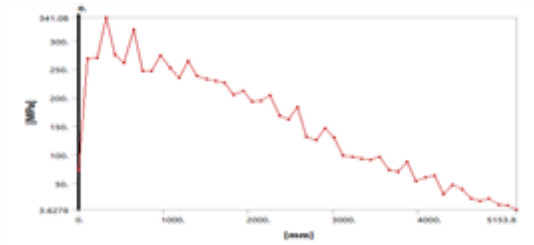

Figure 5.321. Equivalent Stress at section 0 skin 2 core 4 (Mach 0.6)

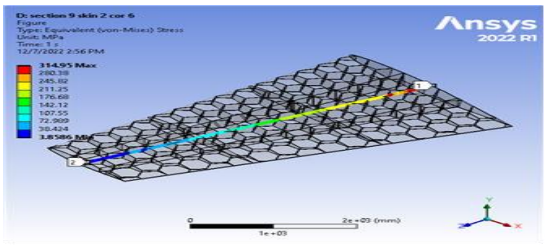

Figure 5.322. Contour Equivalent Stress at 9 cells skin 2 core 6 (Mach 0.6)

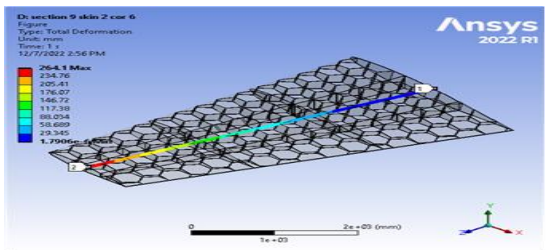

Figure 5.323.(Contour)Total Deformation at 9 cells skin 2 core 6 (Mach 0.6)

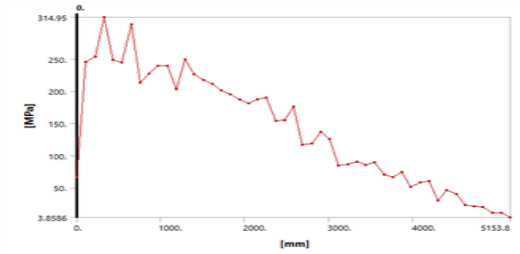

Figure 5.325. Equivalent Stress at section 1.2 skin 2 core 6 (Mach 0.6)

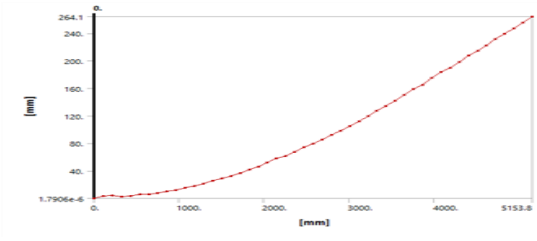

Figure 5.324. Variation of deformation at section 1.2 skin 2 core 6 (Mach 0.6)

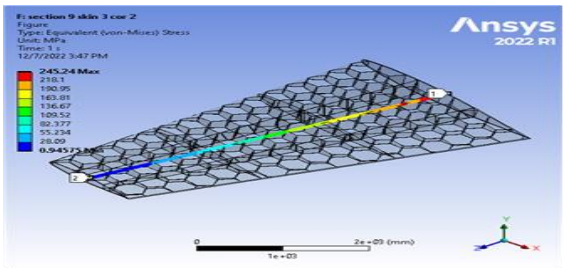

Figure 5.326. Contour Equivalent Stress at 9 cells skin 3 core 2 (Mach 0.6)

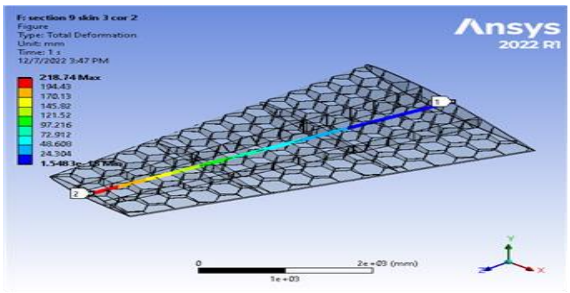

Figure 5.327. Contour Total Deformation at 9 cells skin 3 core 2 (Mach 0.6)

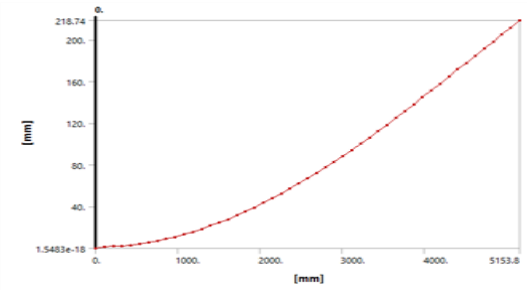

Figure 5.329. Variation of deformation at section 1.2 skin 3 core 2 (Mach 0.6)

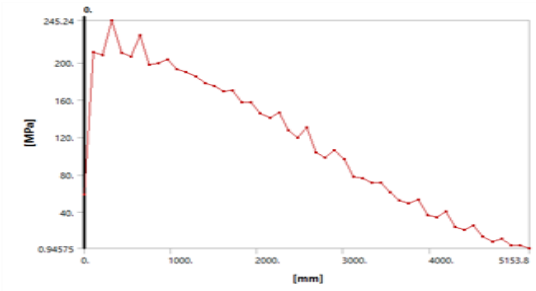

Figure 5.328. Equivalent Stress at section 1.2 skin 3 core 2 (Mach 0.6)

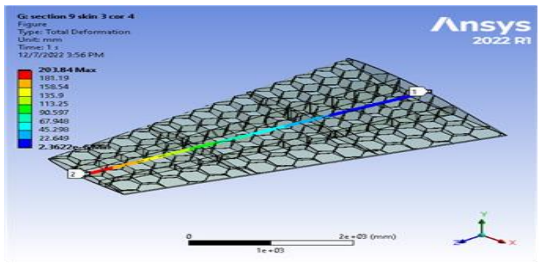

Figure 5.331. Contour Total Deformation at 9 cells skin 3 core 4 (Mach 0.6)

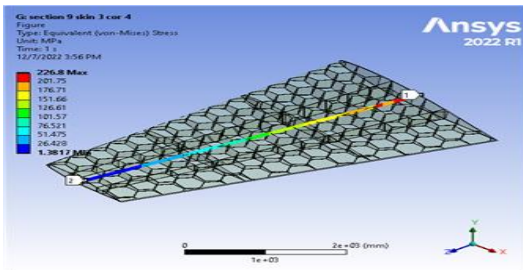

Figure 5.330. Contour Equivalent Stress at 9 cells skin 3 core 4 (Mach 0.6)

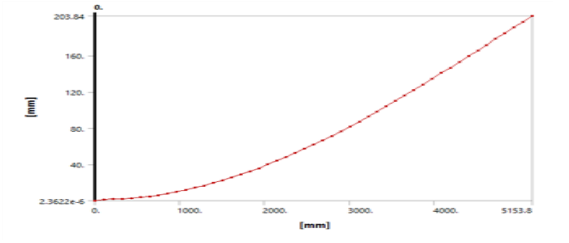

Figure 5.333. Variation of deformation at section 1.2 skin 3 core 4 (Mach 0.6)

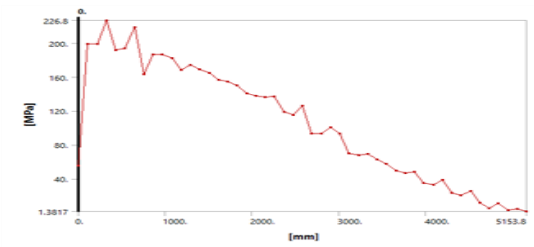

Figure 5.332. Equivalent Stress at section 1.2 skin 3 core 4 (Mach 0.6)

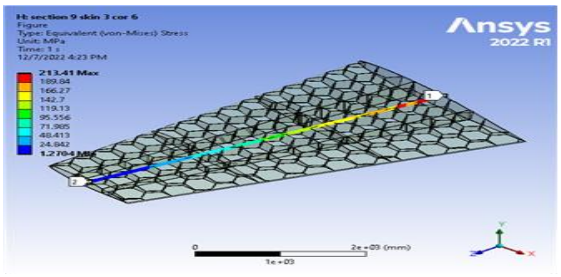

Figure 5.334. Contour Equivalent Stress at 9 cells skin 3 core 6 (Mach 0.6)

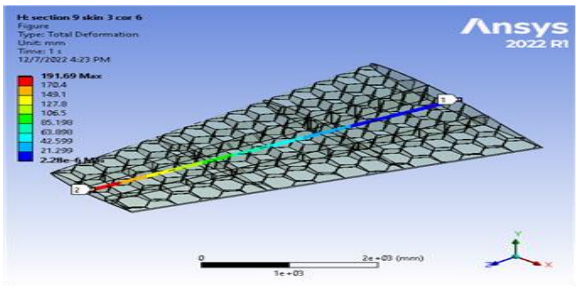

Figure 5.335. Contour Total Deformation at 9 cells skin 3 core 6 (Mach 0.6)

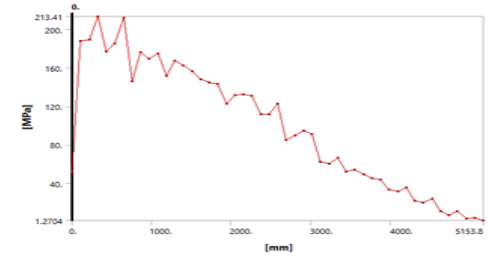

Figure 5.340. Equivalent Stress at section 0 skin 3 core 6 (Mach 0.6)

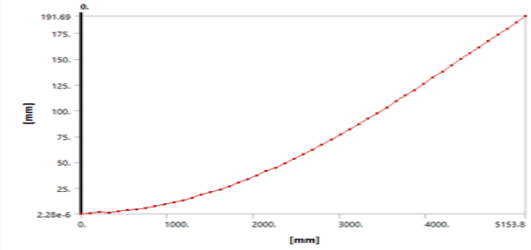

Figure 5.336. Variation of deformation at section 1.2 skin 3 core 6 (Mach 0.6)

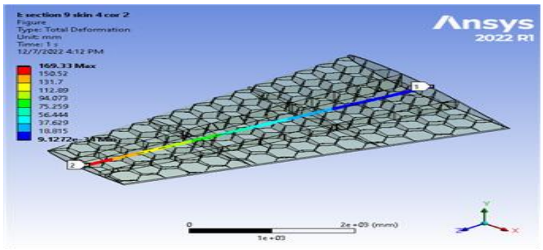

Figure 5.342. Contour Total Deformation at 9 cells skin 4 core 2(Mach 0.6)

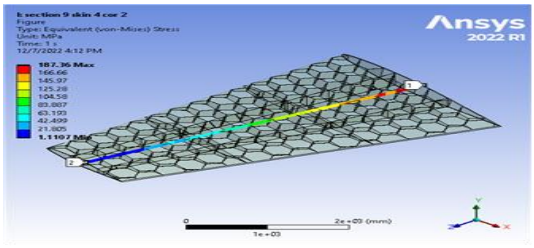

Figure 5.341. Contour Equivalent Stress at 9 cells skin 4 core 2(Mach 0.6)

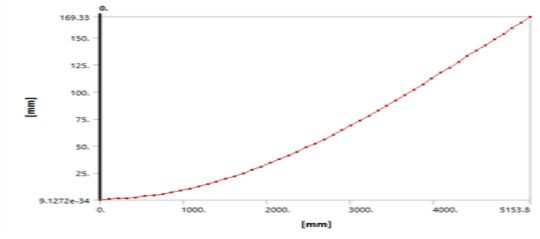

Figure 5.343. Variation of deformation at section 1.2 skin 4 core 2 (Mach 0.6)

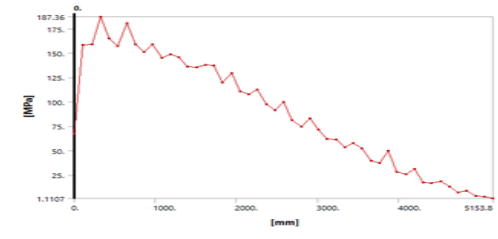

Figure 5.344. Equivalent Stress at section 1.2 skin 4 core 2 (Mach 0.6)

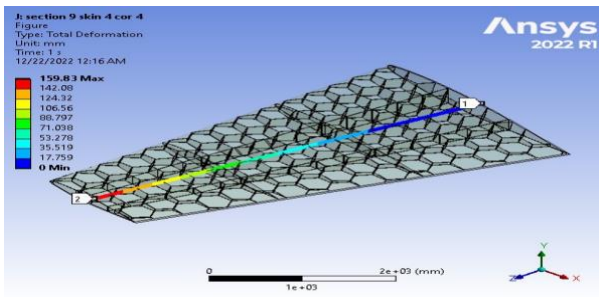

Figure 5.345. Contour Total Deformation at 9 cells skin 4 core 4 (Mach 0.6)

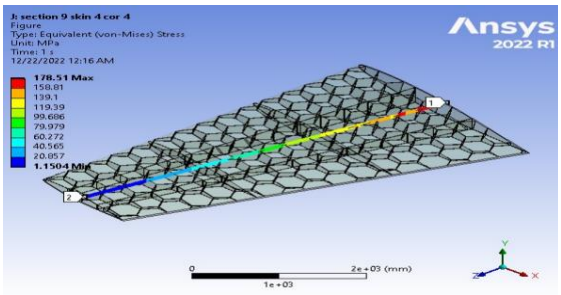

Figure 5.346. Contour Equivalent Stress at 9 cells skin 4 core 4 (Mach 0.6)

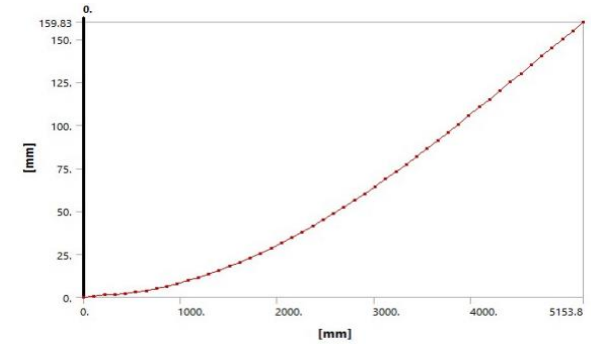

Figure 5.347. Variation of deformation at section 1.2 skin 4 core 4 (Mach 0.6)

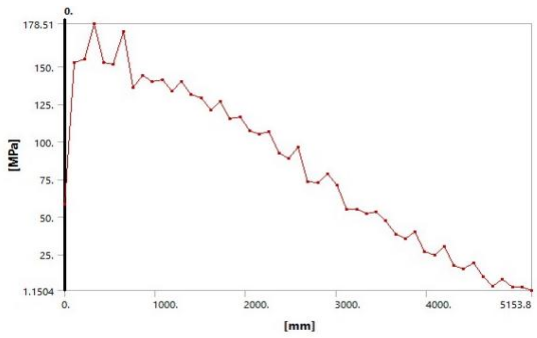

Figure 5.348. Equivalent Stress at section 1.2 skin 4 core 4 (Mach 0.6)

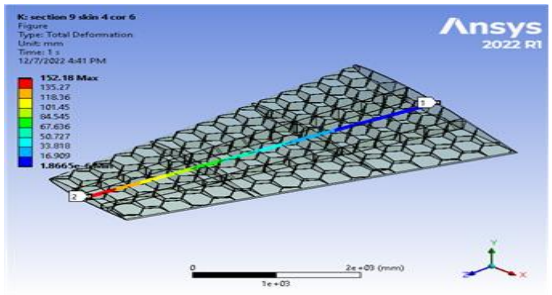

Figure 5.350. Contour Total Deformation at 9 cells skin 4 core 6 (Mach 0.6)

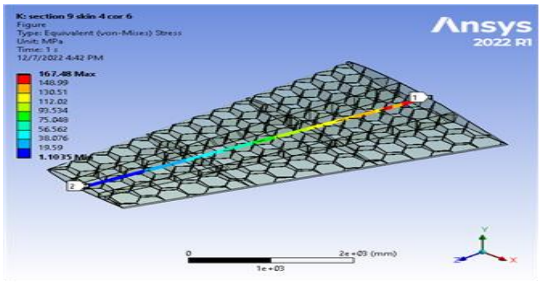

Figure 5.349. Contour Equivalent Stress at 9 cells skin 4 core 6 (Mach 0.6)

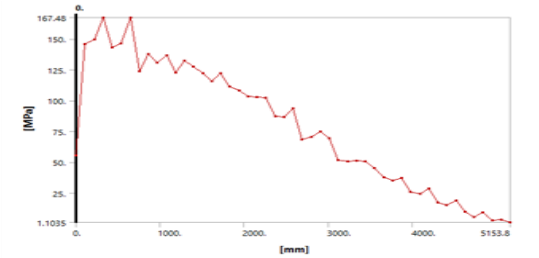

Figure 5.352. Equivalent Stress at section 1.2 skin 4 core 6 (Mach 0.6)6 (Mach 0.6)

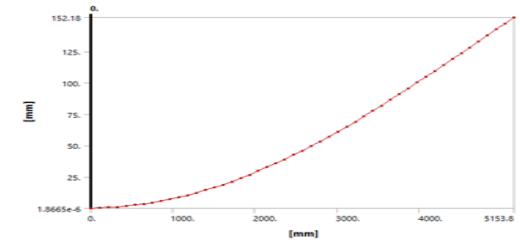

Figure 5.351. Variation of deformation at section 1.2 skin 4 core 6 (Mach 0.6)

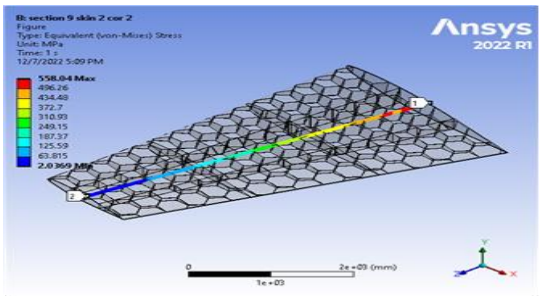

Figure 5.337. Contour Equivalent Stress at 9 cells skin 2 core 2 (Mach 0.8)

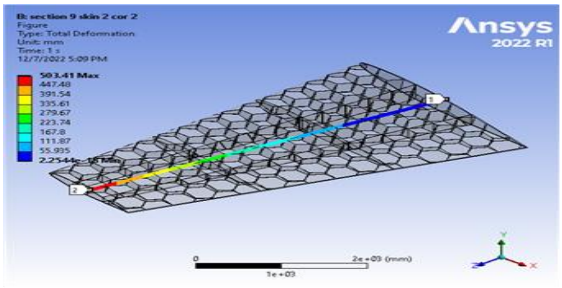

Figure 5.338. Contour Total Deformation at 9 cells skin 2 core 2 (Mach 0.8)

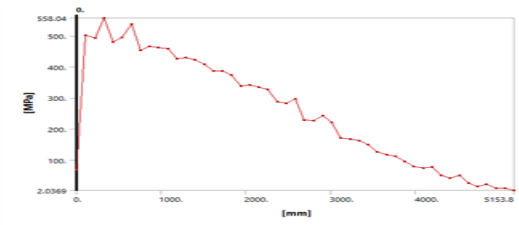

Figure 5.340. Equivalent Stress at section 1.2 skin 2 core 2 (Mach 0.8)

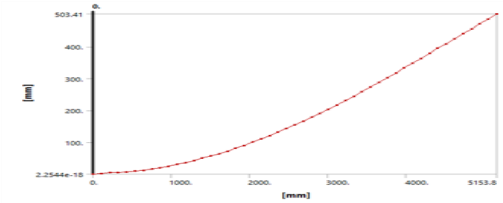

Figure 5.339. Variation of deformation at section 1.2 skin 2 core 2(Mach 0.8)

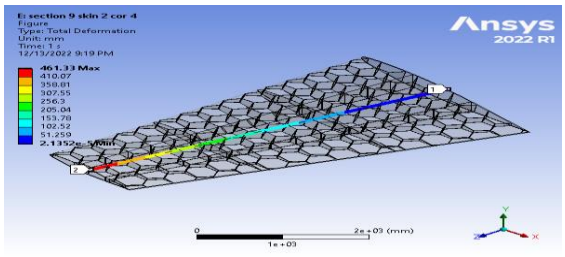

Figure 5.341. Contour Total Deformation at 9 cells skin 2 core 4 (Mach 0.8)

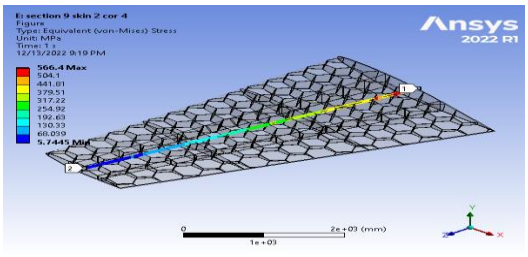

Figure 5.342. Contour Equivalent Stress at 9 cells skin 2 core 4 (Mach 0.8)

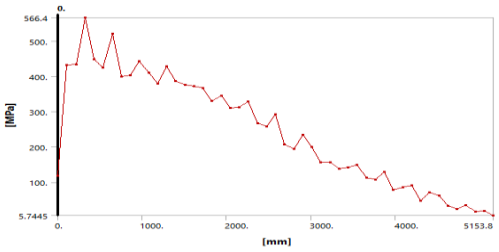

Figure 5.344. Equivalent Stress at section 1.2 skin 2 core 4 (Mach 0.8)

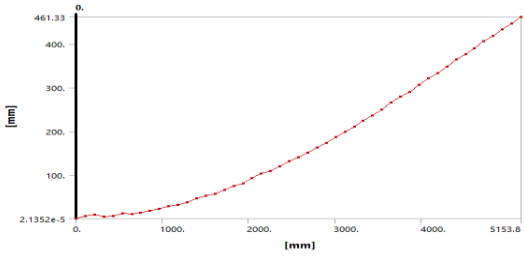

Figure 5.343. Variation of deformation at section 1.2 skin 2 core 4 (Mach 0.8)

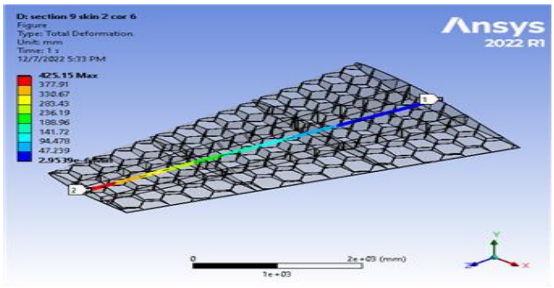

Figure 5.346. Contour Total Deformation at 9 cells skin 2 core 6 (Mach 0.8)

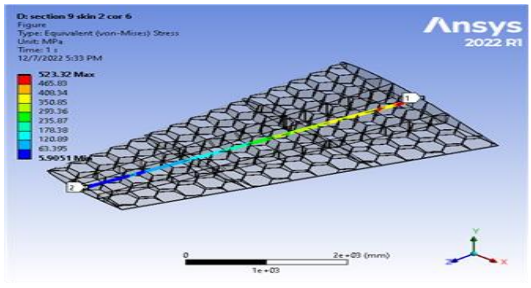

Figure 5.345. Contour Equivalent Stress at 9 cells skin 2 core 6 (Mach 0.8)

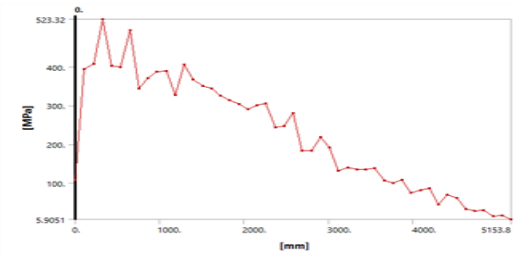

Figure 5.348. Equivalent Stress at section 1.2 skin 2 core 6 (Mach 0.8)

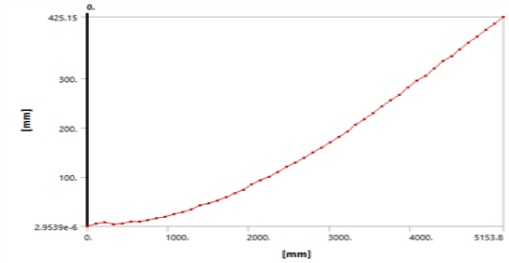

Figure 5.347. Variation of deformation at section 1.2 skin 2 core 6 (Mach 0.8)

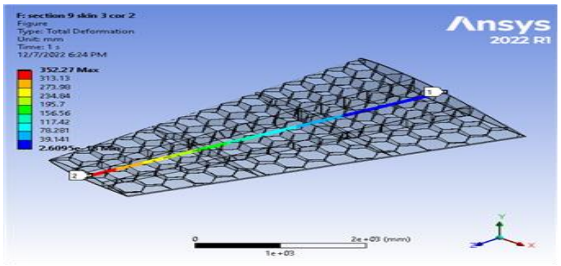

Figure 5.349. Contour Total Deformation at 9 cells skin 3 core 2 (Mach 0.8)

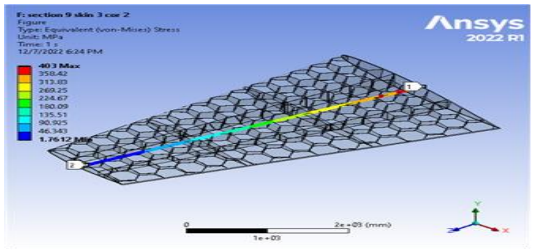

Figure 5.350. Contour Equivalent Stress at 9 cells skin 3 core 2 (Mach 0.8)

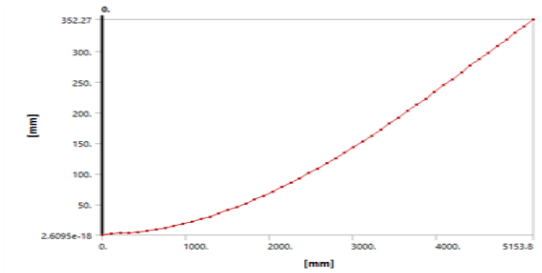

Figure 5.352. Variation of deformation at section 1.2 skin 3 core 2 (Mach 0.8)

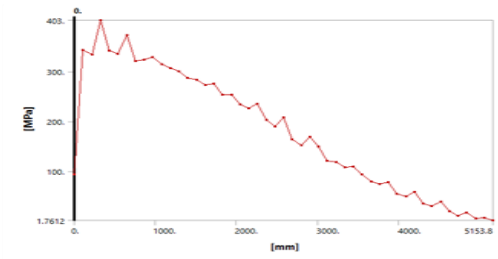

Figure 5.351. Equivalent Stress at section 1.2 skin 3 core 2 (Mach 0.8)

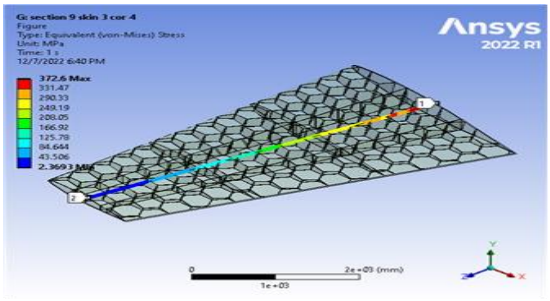

Figure 5.353. Contour Equivalent Stress at 9 cells skin 3 core 4 (Mach 0.8)

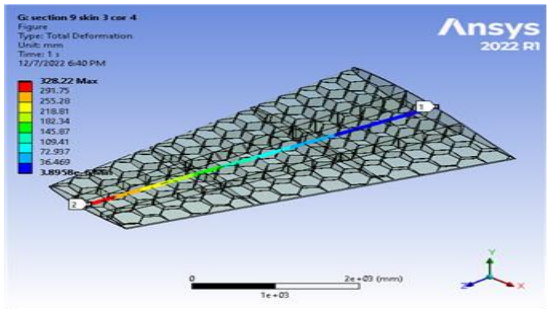

Figure 5.354. Contour Total Deformation at 9 cells skin 3 core 4 (Mach 0.8)

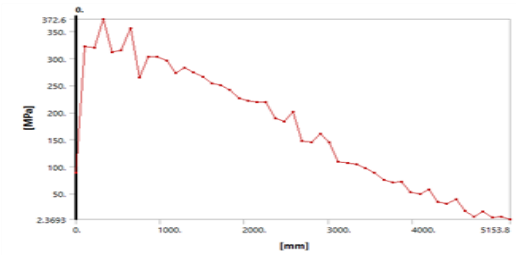

Figure 5.355. Equivalent Stress at section 1.2 skin 3 core 4 (Mach 0.8)

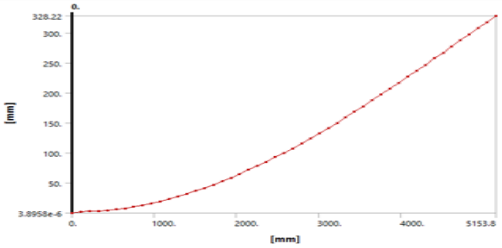

Figure 5.356. Variation of deformation at section 1.2 skin 3 core 4 (Mach 0.8)

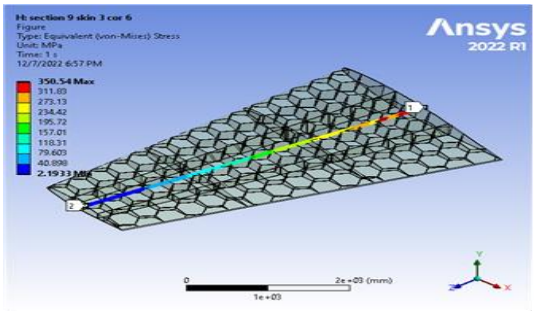

Figure 5.357. Contour Equivalent Stress at 9 cells skin 3 core 6 (Mach 0.8)

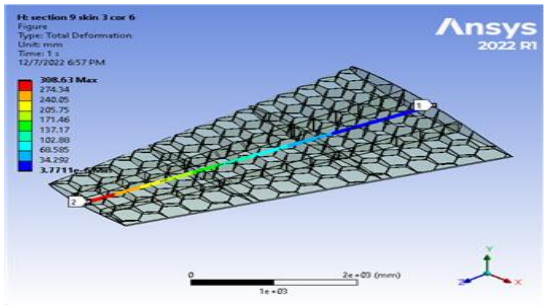

Figure 5.358. Contour Total Deformation at 9 cells skin 3 core 6 (Mach 0.8)

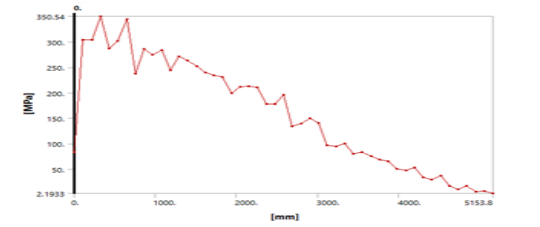

Figure 5.360. Equivalent Stress at section 1.2 skin 3 core 6 (Mach 0.8)

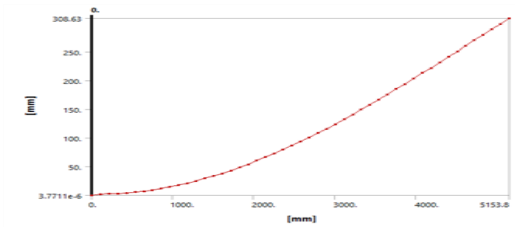

Figure 5.359. Variation of deformation at section 1.2 skin 3 core 6 (Mach 0.8)

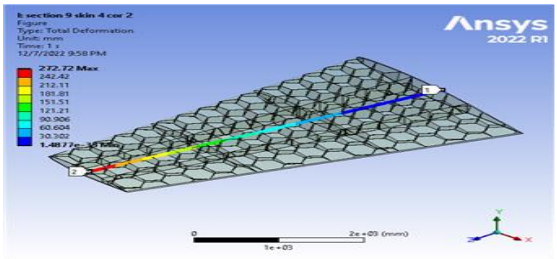

Figure 5.361. Contour Total Deformation at 9 cells skin 4 core 2 (Mach 0.8)

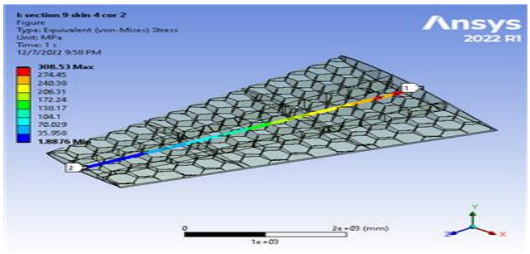

Figure 5.362. Contour Equivalent Stress at 9 cells skin 4 core 2 (Mach 0.8)

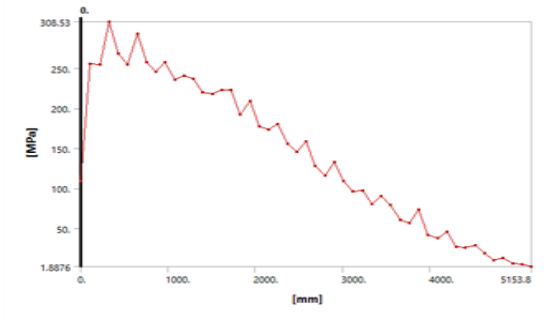

Figure 5.363. Equivalent Stress at section 1.2 skin 4 core 2 (Mach 0.8)

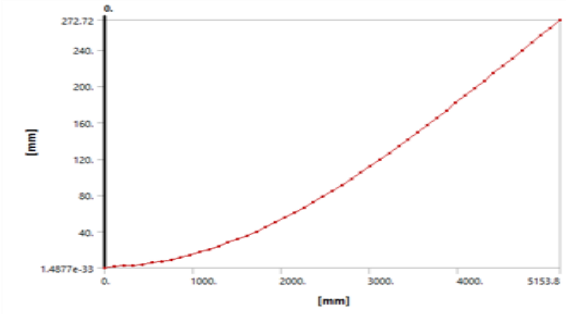

Figure 5.364. Variation of deformation at section 1.2 skin 4 core 2 (Mach 0.8)

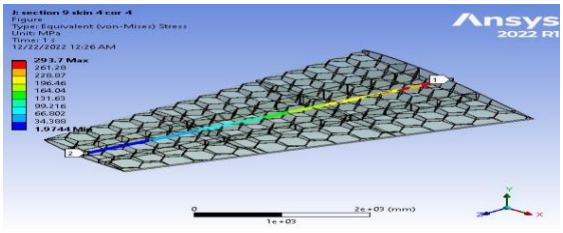

Figure 5.365. Contour Equivalent Stress at 9 cells skin 4 core 4 (Mach 0.8)

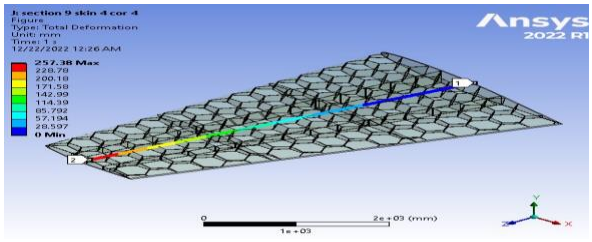

Figure 5.366. Contour Total Deformation at 9 cells skin 4 core 4 (Mach 0.8)

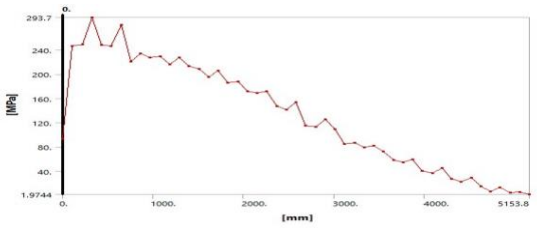

Figure 5.368. Contour Equivalent Stress at section 1.2 skin 4 core 4 (Mach 0.8)

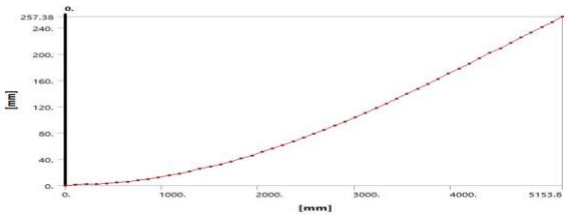

Figure 5.367. Variation of deformation at section 1.2 skin 4 core 4 (Mach 0.8)

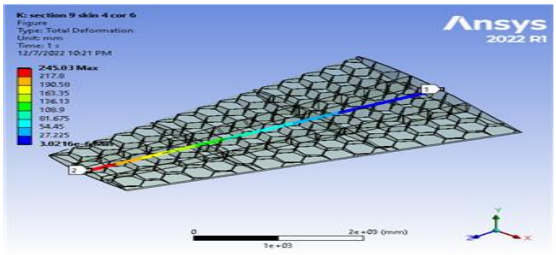

Figure 5.370. Contour Total Deformation at 9 cells skin 4 core 6 (Mach 0.8)

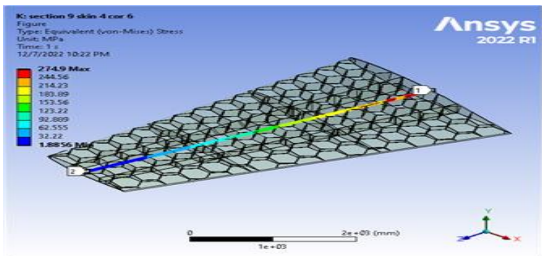

Figure 5.369. Contour Equivalent Stress at 9 cells skin 4 core 6 (Mach 0.8)

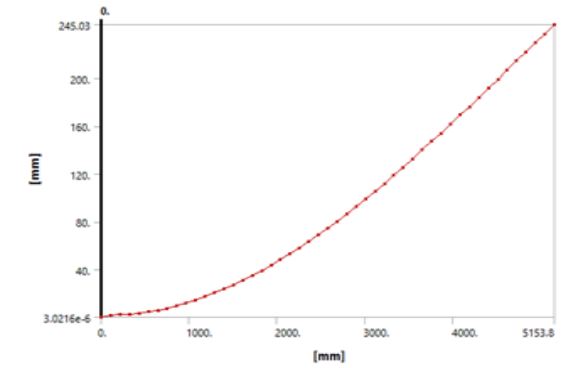

Figure 5.371. Variation of deformation at section 1.2 skin 4 core 6 (Mach 0.8)

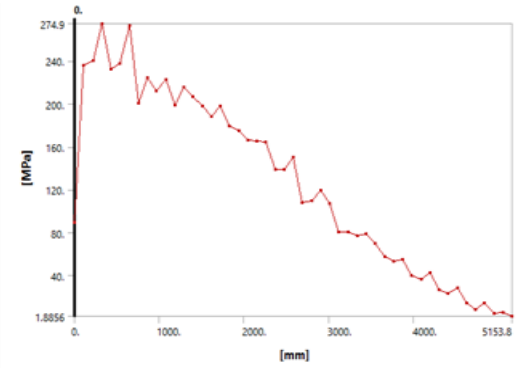

Figure 5.372. Equivalent Stress at section 1.2 skin 4 core 6 (Mach 0.8)

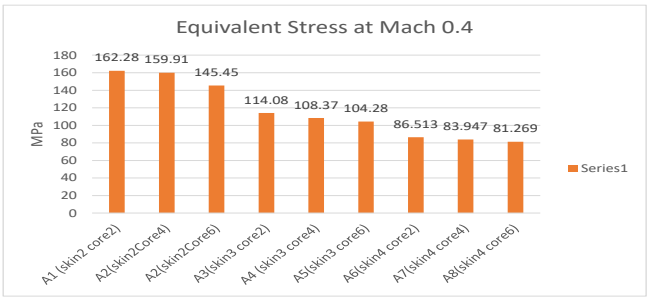

Figure 5.373. Equivalent Stress at one cell (Mach 0.4)

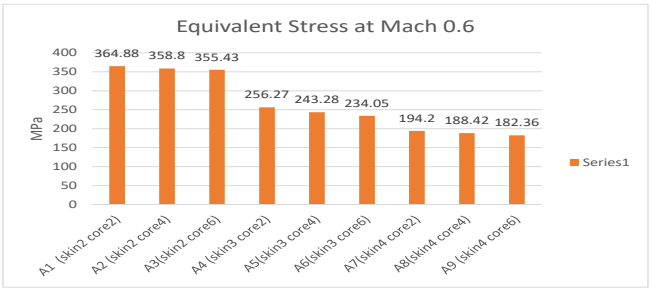

Figure 5.374. Equivalent Stress at one cell (Mach 0.6)

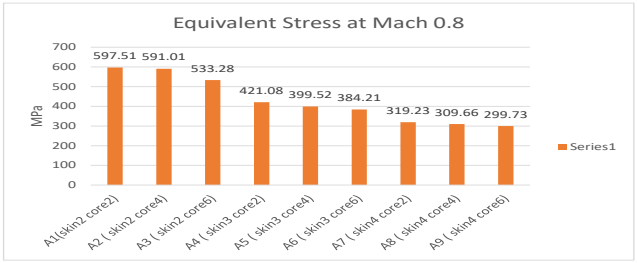

Figure 5.376. Equivalent Stress at one cell (Mach 0.8)

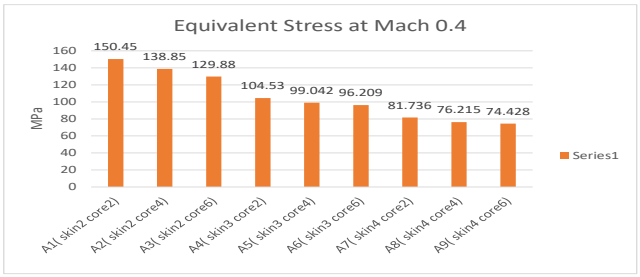

Figure 5.375. Equivalent Stress at 6 cells cells (Mach 0.4)

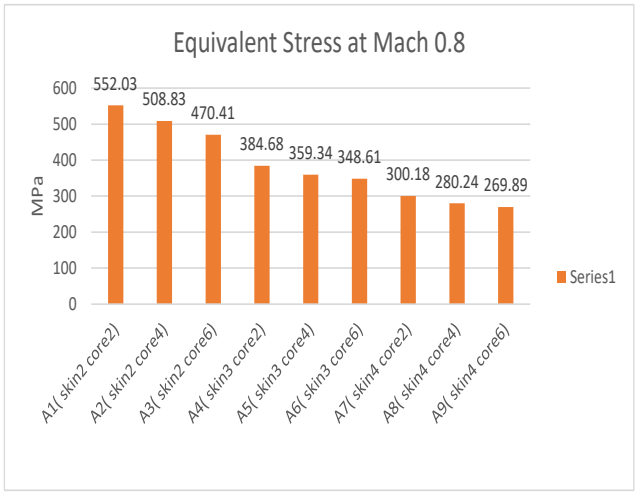

Figure 5.378. Figure 0.379. Equivalent Stress at 6 cells cells (Mach 0.8)

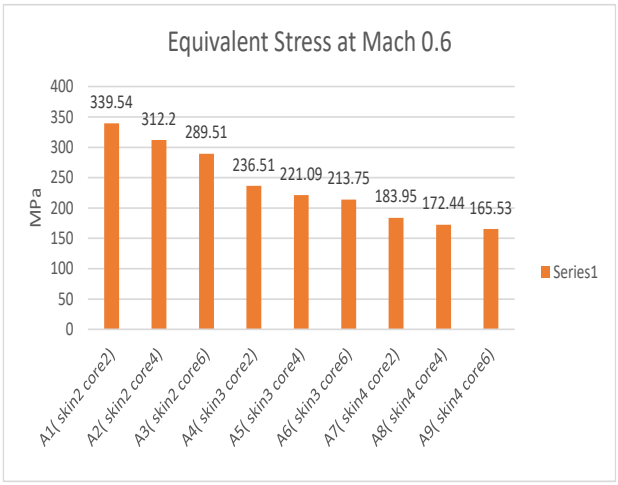

Figure 5.377. Equivalent Stress at 6 cells cells (Mach 0.6)

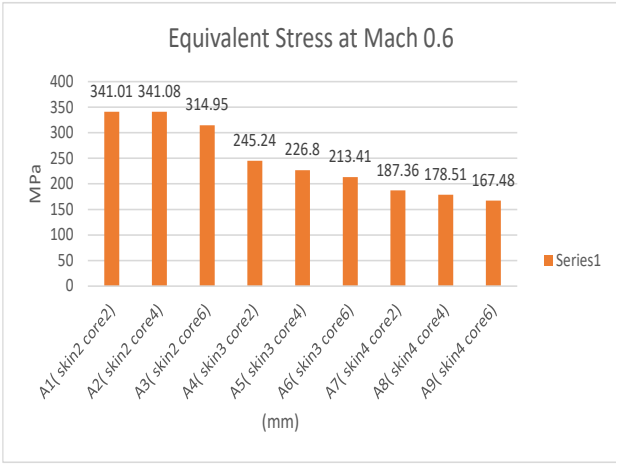

Figure 5.380. Equivalent Stress at 9 cells cells (Mach 0.6)

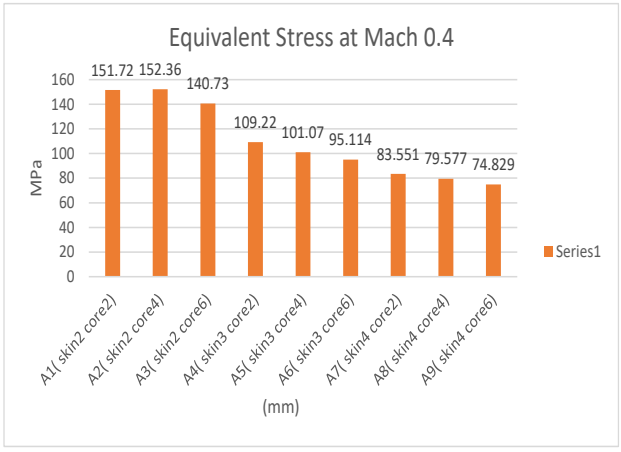

Figure 5.381. Equivalent Stress at 9 cells cells (Mach 0.4)

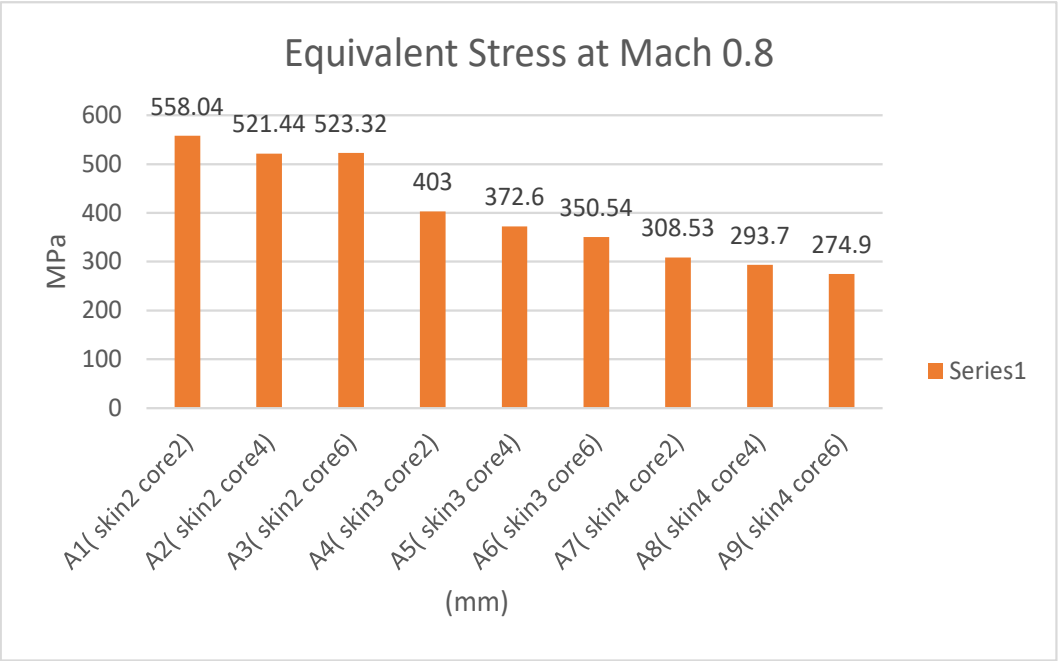

Figure 5.382. Equivalent Stress at 9 cells cells (Mach 0.8)

Table 5.8. Effects of strain thickness angle **12**° at One cell

Current work								M R Gargan [52]			
Mach No	skin thickness (mm)	Core thickness (mm)	Max deformation (mm)	Von mises stress (MPa)	Stress Ratio	Mass (kg)	Material	Skin thickness (mm)	Displacement (m)	Von.Mises stress (MPa)	Mass (Kg)
	2	2	338.84	473.87	1.066	200.21		1.5	0.056	460	414
	2	4	321.44	487.8	1.035	253.46		2	0.047	361	440
	2	6	308.4	515.52	0.979	306.56		2.5	0.041	298	467
	3	2	233.76	324.6	1.556	258.8		3	0.037	254	493
	3	4	223.74	316	1.598	311.5		3.5	0.032	221	520
	3	6	215.75	309.67	1.631	363.82					
	4	2	179.45	253.16	1.995	317.96	Al.Alloy				
	4	4	173.04	244.05	2.069	369.96	(7075				
0.6	4	6	167.95	235.52	2.144	421.71	.T6)				

5.3. COMPARISON STUDY

5.3.1. Case One

Wing skin thickness is an important factor, which should not be ignored during design Considering the thickness of the skin (2,3and 4) and core thickness (2,4 and 6) at Mach 0.6and angle 12 with several models that have been given the von miss stress, the tables show that the model in case No. (2) was chosen to be the case of The optimum in which a mass of (200.21), and thus the skin thickness of The optimal is (2mm). Table 5.8 shows us the change in the total Von Mises Stress is larger (515.52MPa) at skin thickness (2mm) and core (6mm), while the lowest stress (235.52) at a skin thickness of (4mm) and core (6mm). Table 5.8 shows that the largest stress ratio of (2.144) occurs in the model with A skin thickness is (4mm) and core (6mm), while the least stress ratio is (1.035) obtained in the model with a skin thickness (2mm) and core (4 mm). It can be concluded that the model whose skin thickness is (2mm) is the model's Optimal wing design.

While the result of Researcher Mohammed Romaydh Gargan was . Wing skin thickness should not be ignored during design and the rate of skin thickness can be considered from (1.5mm to 3.5) with several models have been trying it out. given von mises and the total wing mass, the tables show that the model in case No. (3) was chosen to be the case The optimum in which a mass of (254 Kg), and thus the thickness of the optimal crust is (3mm). Table 5.8 shows us the change in the total Von Mises Stress with total mass where get the most stress (460MPa) at skin thickness (1.5 mm), while the lowest stress (221MPa) at a skin thickness of (3.5mm). Table 5.8 shows that the largest displacement of (0.056) occurs in the model with The skin thickness (1.5mm), while the least deviation is (0.032) obtained in the model with a skin thickness (3.5mm) and core (6mm). It can be concluded that the model whose skin thickness is (3mm) is the model's Optimal wing design.

Table 5.9. Effects of strain thickness angle **12**° at 6 cells

Current work							M R Gargan [52]				
Mach No	skin thickness(mm)	Core thickness(mm)	Max deformation (mm)	Von mises stress (MPa)	Stress Ratio	Mass (kg)	Material	Skin thickness(mm)	Displacement(m)	V.mises (MPa)	Mass (Kg)
	2	2	329.04	467.96	1.079	210.46		1.5	0.056	460	414
	2	4	304.44	456.06	1.107	273.77		2	0.047	361	440
	2	6	283.99	441.37	1.144	336.7		2.5	0.041	298	467
	3	2	228.96	321.24	1.572	268.93		3	0.037	254	493
	3	4	215.53	307.49	1.642	331.6		3.5	0.032	221	520
	3	6	204.5	294.99	1.712	393.69					
	4	2	176.79	260.86	1.936	328.02	Al.Alloy				
	4	4	168.13	237.86	1.844	389.87	(7075				
0.6	4	6	161.18	227.4	2.221	451.26	.T6)				

5.3.2. Case Two

Wing skin thickness is an important factor, which should not be ignored during design Considering the thickness of the skin (2,3and 4) and core thickness (2,4 and 6) at Mach 0.6and angle 12 with several models that have been given the von miss stress, the tables show that the model in case No. (2) was chosen to be the case The optimum in which a mass of (210.46Kg), and thus the thickness of The optimal crust is (2mm). Table 5.9 shows us the change in the total Von Mises Stress is larger (467.96 MPa) at skin thickness (2mm) and core (2mm), while the lowest stress (227.4MPa) at a skin thickness of (4mm) and core (6mm). Table 5.9 shows that the largest stress ratio of (2.221) occurs in the model with The skin thickness is (4mm) and core (6mm), while the least stress ratio is (1.079) obtained in the model with a skin thickness (2mm) and core (2mm). It can be concluded that the model whose crust thickness is (2mm) is the model Optimal wing design.

While the result of Researcher Mohammed Romaydh Gargan was . Wing skin thickness should not be ignored during design and the rate of skin thickness can be considered from (1.5mm to 3.5) with several models have been trying it out. given von mises and the total wing mass, the tables show that the model in case No. (3) was chosen to be the case The optimum in which a mass of (254 Kg), and thus the thickness of The optimal crust is (3mm). Table 5.9 shows us the change in the total Von Mises Stress with total mass where get the most stress (460MPa) at skin thickness (1.5 mm), while the lowest stress (221MPa) at a skin thickness of (3.5mm). Table 5.9 shows that the largest displacement of (0.056) occurs in the model with The skin thickness (1.5mm), while the least deviation is (0.032) obtained in the model with a skin thickness (3.5mm) and core (6mm). It can be concluded that the model whose skin thickness is (3mm) is the model's Optimal wing design.

Table 5.10. Effects of strain thickness angle **12**° at 9 cells

Current work							M R Gargan [52]				
Mach No	skin thickness (mm)	Core thickness (mm)	Max deformation (mm)	Von mises stress (MPa)	Stress Ratio	Mass (kg)	Material	Skin thickness (mm)	Displacement (m)	V.mises (MPa)	Mass (Kg)
	2	2	322.98	471.27	1.0716	215.62		1.5	0.056	460	414
	2	4	296.29	531.58	0.949	283.98		2	0.047	361	440
	2	6	273.22	476.46	1.059	351.85		2.5	0.041	298	467
	3	2	225.94	324.75	1.555	274.03		3	0.037	254	493
	3	4	210.63	303.57	1.664	341.69		3.5	0.032	221	520
	3	6	198.15	284.41	1.776	408.67					
	4	2	174.9	252.4	2.001	333.06	Al.Alloy (7075 .T6)				
	4	4	165.13	234.18	2.157	399.84					
0.6	4	6	157.26	222.23	2.272	466.04					

5.3.3. Case Three

Wing skin thickness is an important factor, which should not be ignored during design Considering the thickness of the skin (2,3and 4) and core thickness (2,4 and 6) at Mach 0.6and angle 12 with several models that have been given the von miss stress, the tables show that the model in case No. 2) was chosen to be the case The optimum in which a mass of (215.62Kg), and thus the thickness of The optimal crust is (2mm). Table 5.10 shows us the change in the total Von Mises Stress is larger (471.27MPa) at skin thickness (2mm) and core (2mm), while the lowest stress (222.23 MPa) at a skin thickness of (4mm) and core (6mm). Table 5.10 shows that the largest stress ratio of (2.272) occurs in the model with The skin thickness is (4mm) and core (6mm), while the least stress ratio is (1.059) obtained in the model with a skin thickness (2mm) and core (6mm). It can be concluded that the model whose crust thickness is (2mm) is the model Optimal wing design.

While the result of Researcher Mohammed Romaydh Gargan was . Wing skin thickness should not be ignored during design and the rate of skin thickness can be considered from (1.5mm to 3.5) with several models have been trying it out. given von mises and the total wing mass, the tables show that the model in case No. (3) was chosen to be the case The optimum in which a mass of (254 Kg), and thus the thickness of The optimal crust is (3mm). Table 5.10 shows us the change in the total Von Mises Stress with total mass where get the most stress (460MPa) at skin thickness (1.5 mm), while the lowest stress (221MPa) at a skin thickness of (3.5mm). Table 5.10 shows that the largest displacement of (0.056) occurs in the model with The skin thickness (1.5mm), while the least deviation is (0.032) obtained in the model with a skin thickness (3.5mm) and core (6mm). It can be concluded that the model whose skin thickness is (3mm) is the model's Optimal wing design.

Through the above comparisons, it was found that the results reached are much better than the results of the other researcher. And the section the best in terms of design was section 6 cells.

PART 6

CONCLUSIONS AND RECOMMENDATIONS

From the discussions of the obtained results for aerodynamic and structural studies, the following points may be concluded.

6.1. CONCLUSIONS

PART 1. Aerodynamic investigations

The volume method coded in the ANSYS program package to predict the pressure distribution, which presented a direct approach for the computation of a three dimensional load distribution, for the selected wing configuration.

The following concluding remarks could be drawn.

- Increasing the angle of attack, increase the pressure distribution while the variation of the Mach number gives small change in the pressure distribution.
- A full pressure distribution pattern could be obtained using this method, which helps in pointing the maximum aerodynamic load (at lower wing root leading edge) and the minimum one (at lower wing tip trailing edge).
- The pressure distributions have shown good agreement with the verification case, hence the presented method which based on Volume method can be introduced as an accurate technique for computation the pressure distribution on the aerodynamic surface.

PART 2. Structural Analysis

Finite element technology was a way to maintain a complete analysis of wing structure design values. Using the program (ANSYS 2022R1) and the following points can be concluded as follows.

- We note that adding cells to the honeycomb increases its resistance (reducing stresses and deformations, and this is what makes the reinforced sheath necessary and important in designing wing structures to save the metals used in the design.
- Use (T6 . 7075 aluminum alloy) for both skin and core, giving the least weight to the wing structure.
- The selection of the structure material is not only based on the high resistance of the material but the weight of the material must also be considered. We note that using the alloy T6. 7075 used, it gives.

  a.The largest weight at one cell (421.71Kg) and less weight (200.2 Kg).

  b.The largest weight at 6 cells (451.26Kg) and less weight (210.46Kg).

  c.The largest weight at 9 cells (466.04Kg) and less weight (215.62Kg).
- We note that the effectiveness of the honeycomb in reducing stress is more than the effectiveness of the ribs and stringer.
- Finally, the finite element technique of a three.dimensional wing formed in the wing structure and the use of cells as stiffening elements was found to give good results and to determine the areas of most stress and suitable deformation at the limit (stress and deformation).
- The arrangement of using fail .

  a.The fail Von Mises at **One cell**, **Angle 12°.**Mach 0.6 ,skin thickness=2 and core thickness=6. at Mach 0.8 ,(skin thickness=2 ,core thickness=2) (skin thickness=2 ,core thickness=4), (skin thickness=2 ,core thickness=6), (skin thickness=3 ,core thickness=2), (skin thickness=3 ,core thickness=4).

  b. The fail Von Mises at **6 cells**, **Angle 12°.** at Mach 0.8 ,(skin thickness=2 ,core thickness=2) (skin thickness=2 ,core thickness=4), (skin thickness=2 ,core thickness=6), (skin thickness=3 ,core thickness=2), (skin thickness=3 ,core thickness=4).

c. The fail Von Mises at **9 cells**, **Angle 12°.** at Mach 0.8 ,(skin thickness=2 ,core thickness=2) (skin thickness=2 ,core thickness=4), (skin thickness=2 ,core thickness=6), (skin thickness=3 ,core thickness=2), (skin thickness=3 ,core thickness=4).

6.2. RECOMMENDATIONS

The following recommendations for future work are proposed.

- Testing this representation of the wing structure experimentally and comparing them with the current results.
- An aeroelastic study is necessary for the model suggested to be in industrial applications.
- study composite sandwich specimens using different core configurations or using functionally graded materials.
- Using advanced materials such as metamaterials and nanomaterials or natural fibers in the sandwich study.
- Repeat the current work on a specific scaled structure.

REFERENCES

1. Huenecke, K., "Modern Combat Aircraft Design", ***Naval Inst Press***, (1987).

2. Herrmann, A. S., Zahlen, P. C., and Zuardy, I., "Sandwich structures technology in commercial aviation", ***Sandwich Structures 7: Advancing With Sandwich Structures And Materials***, 13–26 (2005).

3. Worsfold, M., "The effect of corrosion on the structural integrity of commercial aircraft structure", (1999).

4. Sypeck, D. J., "Cellular truss core sandwich structures", ***Applied Composite Materials***, 12 (3): 229–246 (2005).

5. L.J. Gibson, M. F. A., "Cellular solids: structure & properties", (1988).

6. Vinson, J. R., "Sandwich structures: past, present, and future", Sandwich Structures 7: Advancing with Sandwich Structures and Materials, ***Springer***, 3–12 (2005).

7. Ashby, M. F. and Lu, T., "Metal foams: A survey", ***Science In China Series B: Chemistry***, 46 (6): 521–532 (2003).

8. Ashby, M. F., Evans, T., Fleck, N. A., Hutchinson, J. W., Wadley, H. N. G., and Gibson, L. J., "Metal Foams: A Design Guide", ***Elsevier***, (2000).

9. McCormack, T. M., Miller, R., Kesler, O., and Gibson, L. J., "Failure of sandwich beams with metallic foam cores", ***International Journal Of Solids And Structures***, 38 (28–29): 4901–4920 (2001).

10. Powers, S. A. and Sattler, D. F., "Rational Design of an Airfoil for a High-Performance Jet Trainer", ***Journal Of Aircraft***, 18 (7): 521–527 (1981).

11. Malone, J. B., "A subsonic panel method for iterative design of complex aircraft configurations", ***Journal Of Aircraft***, 19 (10): 820–825 (1982).

12. Cosentino, G. B. and Holst, T. L., "Numerical optimization design of advanced transonic wing configurations", ***Journal Of Aircraft***, 23 (3): 192–199 (1986).

13. Krantz, P. and Hedman, S. G., "Airfoil optimization", ***Journal Of Aircraft***, 23 (5): 355–356 (1986).

14. Appa, K., "Constant pressure panel method for supersonic unsteady airload analysis", ***Journal Of Aircraft***, 24 (10): 696–702 (1987).

15. Goorjian, P. M. and Guruswamy, G. P., "Transonic unsteady aerodynamic and aeroelastic calculations about airfoils and wings", ***Computers & Structures***, 30 (4): 929–936 (1988).

16. Mohammed, D. F., Ameen, H. A., and Mashloosh, K. M., "Experimental and numerical study of bending behavior for honeycomb sandwich panel with different core configurations", ***The Iraqi Journal For Mechanical And Material Engineering***, 16 (4): 315–328 (2016).

17. Sun, G., Huo, X., Chen, D., and Li, Q., "Experimental and numerical study on honeycomb sandwich panels under bending and in-panel compression", ***Materials & Design***, 133: 154–168 (2017).

18. Toradmal, K. P., Waghmare, P. M., and Sollapur, S. B., "Three-point bending analysis of honeycomb sandwich panels: experimental approach", ***International Journal Of Engineering And Techniques***, 3 (5): 3–7 (2017).

19. Matta, V., Kumar, J. S., Venkataraviteja, D., and Reddy, G. B. K., "Flexural behavior of aluminum honeycomb core sandwich structure", (2017).

20. Rao, K. K., Rao, K. J., Sarwade, A. G., and Chandra, M. S., "Strength analysis on honeycomb sandwich panels of different materials", ***International Journal Of Engineering Research And Applications (IJERA)***, 2 (3): 365–374 (2012).

21. Sahu, S. K., Badgayan, N. D., Samanta, S., Sahu, D., and Sreekanth, P. S. R., "Influence of cell size on out of plane stiffness and in-plane compliance character of the sandwich beam made with tunable PCTPE nylon honeycomb core and hybrid polymer nanocomposite skin", ***International Journal Of Mechanical Sciences***, 148: 284–292 (2018).

22. Arbintarso, E. S., Datama, H. F., Aviyanto, R. N. W., Prasetya, B., Purwokusumo, U., Aditiawan, B., Sangkoyo, P. P., and Adi, R. B. S., "The bending stress on GFRP honeycomb sandwich panel structure for a chassis lightweight vehicle", (2019).

23. Takagi, K. and He, J., "Compression characteristics of honeycomb sandwich panels to improve their impact resistances", (2017).

24. Al-Shammari, M. A. and Al-Waily, M., "Analytical investigation of buckling behavior of honeycombs sandwich combined plate structure", ***International Journal Of Mechanical And Production Engineering Research And Development***, 8 (4): 771–786 (2018).

25. Zhao, C., Zheng, W., Ma, J., and Zhao, Y., "The lateral compressive buckling performance of aluminum honeycomb panels for long-span hollow core roofs", ***Materials***, 9 (6): 444 (2016).

26. Sadiq, S. E., Jweeg, M. J., and Bakhy, S. H., "The effects of honeycomb parameters on transient response of an aircraft sandwich panel structure", (2020).

27. Harish, R. and Ramesh, S. S., "Vibration response analysis of honeycomb sandwich panel with varying Core Height", ***International Journal Of Emerging Technologies In Computational And Applied Sciences (IJETCAS)***, (5): 582–586 (2013).

28. Naresh, C., Chand, A. G., Kumar, K. S. R., and Chowdary, P. S. B., "Numerical investigation into effect of cell shape on the behavior of honeycomb sandwich panel", ***International Journal Of Innovative Research In Science, Engineering And Technology***, 2 (12): 8017–8022 (2013).

29. Zghal, S. and Nasri, R., "Experimental investigation for forced vibration of honeycomb sandwich beams", Advances in Acoustics and Vibration, ***Springer***, 223–233 (2017).

30. Uğur, L., Duzcukoglu, H., Sahin, O. S., and Akkuş, H., "Investigation of impact force on aluminium honeycomb structures by finite element analysis", ***Journal Of Sandwich Structures & Materials***, 22 (1): 87–103 (2020).

31. Griškevičius, P., Zeleniakienė, D., Leišis, V., and Ostrowski, M., "Experimental and numerical study of impact energy absorption of safety important honeycomb core sandwich structures", ***Materials Science***, 16 (2): 119–123 (2010).

32. Sakar, G. and Bolat, F. C., "The free vibration analysis of honeycomb sandwich beam using 3D and continuum model", ***International Journal Of Mechanical And Mechatronics Engineering***, 9 (6): 1077–1081 (2015).

33. Marythraza, M., Anitha, D., Dash, P. K., and Ravi Kumar, P., "Vibration analysis of honeycomb sandwich panel in spacecraft structure", ***International Journal Of Mechanical And Production Engineering Research And Development***, 8 (3): 849–860 (2018).

34. Bai, Z., Zhao, Y., Ma, W., and Tian, H., "Modal analysis for small satellite system with finite element method", (2008).

35. Abbadi, A., Tixier, C., Gilgert, J., and Azari, Z., "Experimental study on the fatigue behaviour of honeycomb sandwich panels with artificial defects", ***Composite Structures***, 120: 394–405 (2015).

36. "L-39’’Flight Technical Book’’", (1986).

37. Abbott, I. H. and Von Doenhoff, A. E., "Theory of wing sections dover publications", ***New York***, (1959).

38. Stollery, J. L., "Aerodynamics, Aeronautics and Flight Mechanics", Proceedings of the Institution of Mechanical Engineers, Part G: Journal of Aerospace Engineering, ***John Wiley & Sons***, 63–64 (1997).

39. Bertin, J. J. and Smith, M. L., "Aerodynamics for Engineers, Prentice-Hall", ***Inc., New Jersey***, (1998).

40. Houghton, E. L. and Carruthers, N. B., "Aerodynamics for Engineering Students. Third Edition.", ***Elsevier***, (1982).

41. Versteeg, H. K. and Malalasekera, W., "Computational fluid dynamics: the finite volume method", ***Harlow, England: Longman Scientific & Technical***, (1995).

42. Bruhn, E. F., "Analysis and Design of Flight Vehicle Structures", ***Tri-State Offset Company***, (1965).

43. Čalkovský, A., Pávek, J., and Daněk, V., "Konstrukce a Pevnost Letadel: 1. Díl", ***VA AZ***, (1984).

44. Zhang, C. Y., Liu, H., and Ma, Y. P., "Optimization of Aircraft Mid-Fuselage Structure Design Based on Parametric Modeling", (2014).

45. Choi, W.-H. and Kim, C.-G., "Broadband microwave-absorbing honeycomb structure with novel design concept", ***Composites Part B: Engineering***, 83: 14–20 (2015).

46. Lukkassen, D. and Meidell, A., "Advanced materials and structures and their fabrication processes", ***Book Manuscript, Narvik University College, HiN***, 2: 1–14 (2007).

47. Soliman, H., .

48. Gibson, L. J., Ashby, M. F., Schajer, G. S., and Robertson, C. I., "The mechanics of two-dimensional cellular materials", ***Proceedings Of The Royal Society Of London. A. Mathematical And Physical Sciences***, 382 (1782): 25–42 (1982).

49. Masters, I. G. and Evans, K. E., "Models for the elastic deformation of honeycombs", ***Composite Structures***, 35 (4): 403–422 (1996).

50. Ayoob, M., "VIBRATION ANALYSIS OF HONEYCOMB CORE SANDWICH PANELS USING A NEW SUGGESTED COMPOSITES", (2022).

51. Elsoni, T., "AERODYNAMIC AND STRUCTURAL DESIGN OF A JET TRAINER AIRCRAFT WING", (1999).

52. Gargan, M., "The Optimumal Structural Design of Aircraft Wing By Using Finite Element Method", (2001).

CURRICULUM VITAE

Ibtisam Jaafar Ismail, an aircraft mechanical engineer, graduated from the College of Engineering, University of Technology, Iraq. She obtained her bachelor's degree in 2019. She is currently studying for a master's degree at Karabük University in the field of mechanical engineering.